Predicted Scramjet Testing Capabilities of the Proposed RHYFL-X Expansion Tube

By

Benjamin S. Stewart

A thesis submitted to the University of Queensland

for the degree of Doctor of Philosophy

Division of Mechanical Engineering

October 2004

Produced in LaTeX 2_ε.

Except where acknowledged in the customary manner, the material presented in this thesis is, to the best of my knowledge, original and has not been submitted in whole or part for a degree in any university.

Benjamin S. Stewart

Abstract

For the Supersonic Combustion Ramjet (Scramjet) to be realized as a viable hypersonic propulsion option, significant testing must be performed in test flows which duplicate those that would be experienced during anticipated atmospheric flight. The expense associated with real flight tests necessitates that ground-based testing play a significant role in the experimental development of the scramjet. Based on current, or even near-term technologies, the expansion tube concept offers superior physical simulation of hypersonic flow. This study investigates the potential performance capabilities of a large-scale, high-performance free-piston driven expansion tube based on the RHYFL shock tunnel project. The predictions are focused specifically on the ability of the RHYFL-X expansion tube to generate sub-orbital scramjet testing conditions and are obtained through one-dimensional and axisymmetric simulations of this proposed facility.

To validate the simulation techniques and approximations used to model the flow in the RHYFL-X expansion tube, simulations of a currently operating expansion tube, X2, are presented. These one-dimensional and axisymmetric simulations initially assumed equilibrium chemistry. The driver gas conditions after the two-stage compression process were obtained via a combination of numerical and experimental analyses. An accurate knowledge of the driver length at the point of primary diaphragm rupture was required for sound agreement with experimental results. The inertial effect of the secondary diaphragm was also examined for different X2 operating conditions. Results show that a hold-time imposed on the secondary diaphragm improved agreement with experimental data.

The effects of finite-rate chemistry on the air test gas of two standard operating conditions in the X2 facility were also investigated. A 5 species, 17 reaction model of air was used in

inviscid one-dimensional simulations of a 6.8 km/s condition and a 9.7 km/s condition. By comparison with equilibrium simulations of the same conditions it was seen that finite-rate chemistry effects can be significant in conditions where test gas dissociation occurs prior to the unsteady expansion. For the higher enthalpy condition, the significant dissociation of the air test gas caused by the faster primary shock, combined with the more severe unsteady expansion process, resulted in a test flow highly influenced by nonequilibrium phenomena. The low primary shock speeds required to produce atmospheric static temperatures in the final test flow of the proposed RHYFL-X expansion tube was shown to result in negligible, if any, dissociation of the test gas prior to expansion. Even assuming the worst case scenario of a completely frozen expansion, these minimal dissociation levels prior to expansion indicate that the three RHYFL-X operating conditions investigated would have test flows essentially dissociation free.

Results from one-dimensional and axisymmetric simulations of the RHYFL-X expansion tube indicate that this proposed facility would be capable of generating true Mach number testing conditions over the intended scramjet flight trajectory, while inheriting the short test times and limited core flow diameters associated with expansion tubes. Simulated pressures well in excess of those that would be experienced during flight indicate that this facility would offer the unique capability of duplicating freestream conditions required for accurate aerodynamic, heating and combustion testing of integrated scramjet models. The use of a nozzle was also investigated for increasing the diameter of the core test flow. While seeing moderate increases in core flow diameter, the viscous axisymmetric simulations also displayed the desirable characteristic of increasing the duration of steady flow.

List of Publications

[1] Stewart, B.S., Morgan, R.G. and Jacobs, P.A., "Rocketdyne Hypersonic Flow Laboratory as High-Performance Expansion Tube for Scramjet Testing", *Journal of Propulsion and Power*, Volume 19, No. 1, Jan-Feb 2003.

[2] Hayne, M.J., Mee, D.J., Gai, S.L., Stewart, B.S. and Morgan, R.G., "Flow establishment over rearward-facing steps in high ethalpy flows", *The 24th International Symposium on Shock Waves*, Beijing, China, July 11-16 2004.

[3] Stewart, B.S., Jacobs, P.A. and Morgan, R.G., "Finite-Rate Chemistry Simulations of the X2 Expansion Tube", *University of Queensland, Division of Mechanical Engineering*, Research Report Number: 2003/10, October 2003.

[4] Stewart, B.S., Hayne, M., Jacobs, P.A. and Morgan, R.G., "Flow Establishment in Large-Scale High-Performance Expansion Tubes", *Presented at the 11th AIAA/AAAF International Space Planes and Hypersonics Systems and Technologies Conference*, (Paper 5239) 29 Sept - 4 Oct 2002, Orleans, France.

[5] Stewart,B.S., Morgan, R.G. and Jacobs, P.A., "Scramjet Testing in the Proposed RHYFL-X Expansion Tube", *Presented at the 8th International Workshop on Shock-Tube Technology*, 11-14 Sept 2002, Bangalore, India.

[6] Stewart, B.S., Jacobs, P.A. and Morgan, R.G., "The Starting Process of an Expansion Tube Nozzle", *Proceedings of the Twenty-third International Symposium on Shock Waves*, Published by the University of Texas, Arlington, F. K. Lu (Ed.). 23-27 July, 2001, Fort Worth, USA.

[7] Stewart, B.S. and Morgan, R.G., "Establishment of Test Conditions in the RHYFL-X Facility", *Presented at the 37th AIAA/ASME/SAE/ASEE Joint Propulsion Conference and Exhibition.* (Paper 4843) 8-11 July, 2001, Salt Lake City, USA.

[8] Stewart, B.S. and Jacobs, P.A., "Simulation of the starting process of a Hypersonic Nozzle on an Origin 2000", *Presented at the HPC-ASIA 2001 High-Performance Computing Conference (Poster Presentation).* 24-28 Sept, 2001, Gold Coast, Australia.

[9] Stewart, B.S., Jacobs, P.A., and Morgan, R.G., "The RHYFL Facility as a High Performance Expansion Tube for Scramjet Testing", *Presented at the 21st AIAA Advanced Measurement and Ground Testing Technology Conference.* (Paper 2595) 19-22 June, 2000, Denver, USA.

Acknowledgements

First and foremost I want to express my sincerest thanks to my supervisors Professor Richard Morgan and Dr Peter Jacobs. Richard's knowledge of all things hypersonic combined with Peter's computer and programming prowess has offered the unique opportunity to obtain direct tutelage from two at the forefront of their fields. My deep gratitude to both of you.

I would like to thank Rowan Gollan for his assistance with his finite-rate chemistry package and the Gemini computer server. Thanks also to Michael Hayne for his assistance with the X2 experiments and to Kevin Austin for proof-reading my thesis when I could no longer bare to look at it. The help and support from the staff of the Department of Mechanical Engineering was greatly appreciated during this thesis, particularly Valerie Hutchinson, Rose Clements, Elizabeth Schelbach, Steve Kimball, Dave Griffin and John Peters.

The facilities provided by the Australian Partnership for Advanced Computing (APAC, Canberra) and UQ's High Performance Computing Group were invaluable in the completion of this thesis. I would like to acknowledge the financial support provided by the Australian Research Council in the form of an Australian Postgraduate Award (with Industry), as well as the UQ Scholarships Office for providing a Completion Scholarship in the final stages. A thankyou also goes to Russ Morrison and Malcolm Jenkins from WBM Engineering, the commercial partner for the ARC SPIRT Collaborative Research Grant - "Conversion of RHYFL shock tunnel into an expansion tube".

I thank my family, as well as Simonne's, for their support and understanding. And finally, a HUGE thankyou goes to Simonne - your love, encouragement and support has saved me from insanity, and my computer(s) from the hard end of a sledgehammer, on more than one occasion.

Contents

List of Figures

List of Tables

Nomenclature

1D	One-dimensional
2D	Two-dimensional (axisymmetric)
a	Sound speed, m/s
A	Area, m^2
A_f	Reaction constant
B_f	Reaction constant
C_f	Correction factor
Cp	Specific heat (constant pressure), J/(kg.K)
d	diameter, m
D/T	Driver gas/Test gas interface
Expt	Experiment
F_1	Driver function
f	Sound speed ratio, a_3/a_2
h	heat transfer coefficient, $W/m^2\,K$
h	enthalpy
H	Total or Stagnation Enthalpy, MJ/kg
k	Thermal conductivity, $W/m\,K$
k_f	Forward reaction rate
L	length, m

m	mass unit, kg
m	mole fraction
M	Mach number
MW	Molecular Weight
No	Number
P	Pressure, Pa
P_r	Prandt number
q	Heat transfer rate, W
q	Gas property
R	Gas constant
R_u	Universal Gas Constant
t	Time, s
T/A	Test gas/Accelerator gas Interface
T	Temperature, K
T_{D_f}	Activation energy
u	velocity
V	Volume, m^3
X, Y, Z	Cartesian coordinates, m

Greek

γ	Ratio of specific heats
λ	Compression ratio
ρ	Density, kg/m^3
Φ	Performance Measure

Subscripts

∞	Free-stream flow conditions
0	Stagnation conditions
1	Initial test gas
2	Shock processed test gas

3	Expanded driver gas
4	Compressed driver gas
5	Initial Accelerator gas
6	Shock processed accelerator gas
7	Expanded test gas
A	Accelerator tube
c	Chemical
D	Driver tube
f	Final state
fill	Fill conditions
i	Initial state
max	maximum
P	Pitot
s	Static
S	Shock Tube

Acronyms

APAC	Australian Partnership for Advanced Computing
CEA	Chemical Equilibrium with Applications (NASA)
CFD	Computational Fluid Dynamics
CFL	Courant-Friedrichs-Levy
CPU	Central Processing Unit
C-J	Chapman-Jouget
GLOM	Gross Lift Off Mass
IMOC	Inviscid Method of Characteristics
LEO	Low Earth Orbit
MARIAH	Magnetohydrodynamic Accelerator Research into Advanced Hypersonics
MHD	Magnetohydrodynamic
NASA	National Aeronautics and Space Administration (USA)

RDHWT	Radiantly Driven Hypersonic Wind Tunnel
RHYFL	Rocketdyne Hypersonic Flow Laboratory
RLV	Reusable Launch Vehicle
R&D	Research and Development
SID	Shock-Initiated Driver
SSTO	Single Stage To Orbit
xt	Space-time

Chapter 1

Introduction

In 1957, Russia launched the first artificial satellite (Sputnik) into orbit, marking the start of the "Space Age". Fuelled by the Cold War, the subsequent space-race between the Soviet Union and the United States further accelerated achievements in this field. Some of the major space-related milestones achieved in the 18 years following Sputnik are illustrated in Figure 1.1. These include the first probe on the moon (Luna 2), the first man in space (Yuri Gagarin), the first man on the moon (Neil Armstrong), the first earth space-station (Salyut 1) and the first lander on Mars (Viking 1). Following the success of the Apollo moon missions, manned access to space has concentrated on servicing low earth orbit (LEO). The payload delivery business has provided numerous launcher configurations and 1981 saw the successful first flight of the space-shuttle, a partially reusable launch system. The space-shuttle has now been employed to access space for around 23 years and is intended to keep flying until the International Space Station (ISS) is completed in 2010. The Columbia shuttle disaster in February 2003 grounded the shuttle fleet and necessitated the use of the Russian Soyuz launch vehicle to recover crew from the International Space Station (ISS). The Soyuz launch system is derived from the R-7 ballistic missile which was developed in the 1950's. This stagnation of space-related achievements and activities over the past 20 years is primarily due to the substantial financial expense of carrying a payload into space. In order for the exploration, utilization and, ultimately, the colonization of space to become a financially viable concept, the high cost associated with getting into space, which currently demands

around $US10,000 to $US20,000 per kg depending on launch system, must be dramatically reduced.

1.1 Space Access

The high cost associated with attaining an orbit around the Earth can be attributed mainly to the fact that current launch systems require the fuel oxidizer to be carried on-board the launch vehicle. In Figure 1.2, the mass percentages of various components of the US Space Shuttle illustrates the large percentage (approximately 31%) that liquid oxygen makes up of the Gross Lift Off Mass (GLOM) of around 2000 tonnes. It would constitute a significant weight saving if this oxygen could be obtained from the atmosphere through the use of an *air-breathing* propulsion system, such as the scramjet engine, to provide acceleration up to, or near, orbital speeds.

The potential of the hypersonic, air-breathing engine concept was first recognised in the late 1950's [6], offering an alternative to the traditional cryogenic propulsion systems. An air-breathing engine obtains fuel oxidizer (oxygen) directly from the atmosphere through which it flies, as seen with gas turbine and ramjet engines. The scramjet, or Supersonic Combustion RAMJET, is a hypervelocity, air-breathing engine which has the potential to greatly reduce the cost associated with the delivery of a payload to orbit [7]. The dramatic reduction in the amount of oxidizer needed to be carried would result in a weight reduction of the associated structure required to house the oxidizer. For the same overall GLOM, these weight savings would allow for a number of considerable benefits. It would allow for a more robust and potentially fully reusable launch vehicle, eliminating the expense associated with large expendable components. Payload gains relative to the GLOM would also be possible, greatly reducing the cost per mass of delivering a payload to orbit. Predicted mass percentages of a scramjet powered launch vehicle [1] are illustrated in Figure 1.3. The combination of structure, guidance and payload of a scramjet powered vehicle would constitute around 28% of the GLOM as opposed to only 14% for the space-shuttle. With due consideration to the structural mass required for a reusable scramjet powered vehicle, this suggests a significant increase in the percentage of payload.

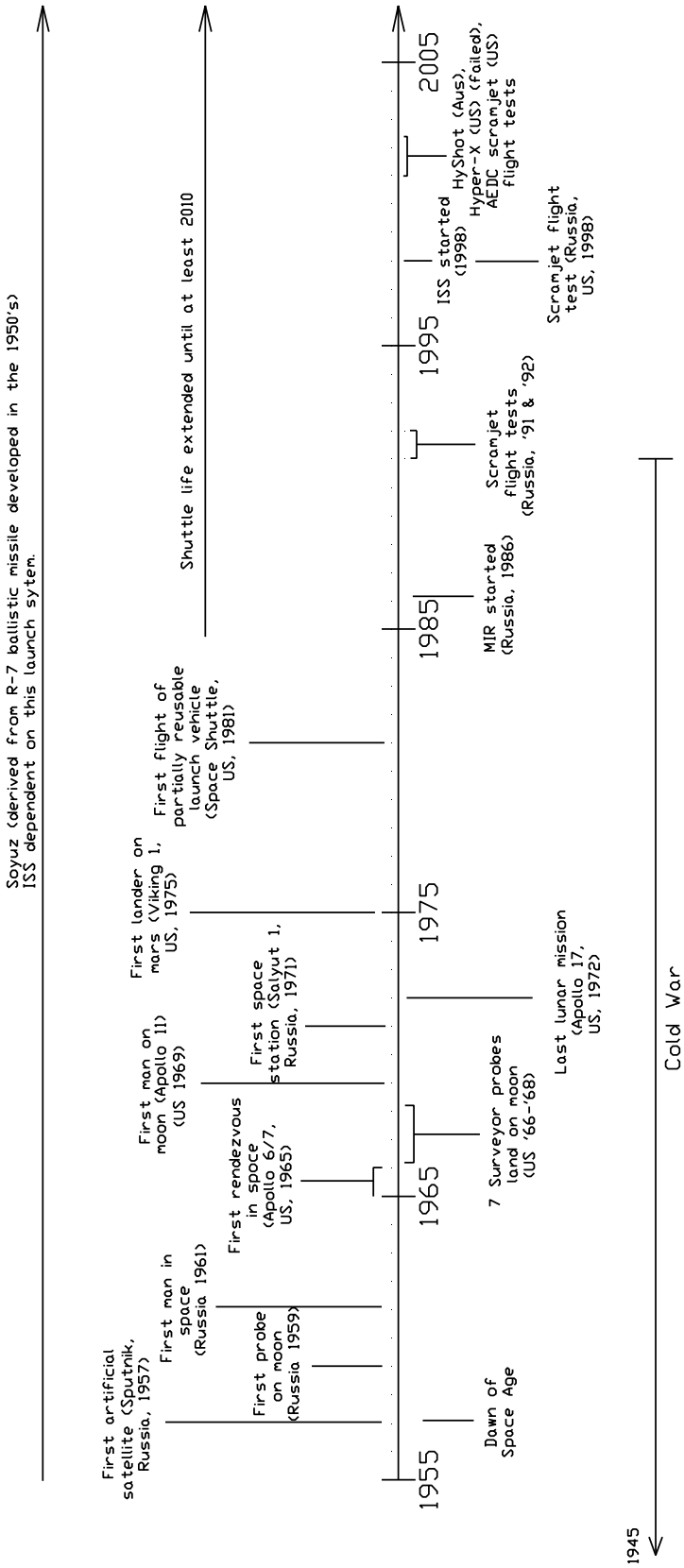

Figure 1.1: Time-line of significant space-related milestones.

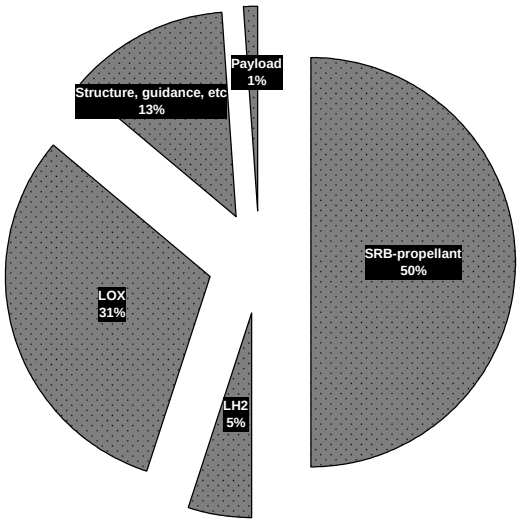

FIGURE 1.2: Mass percentages of space-shuttle Gross Lift Off Mass.

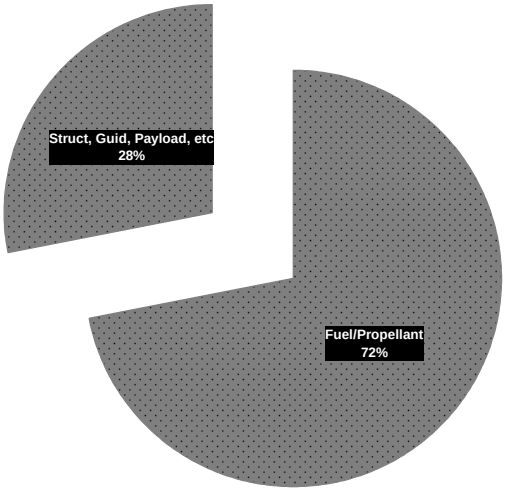

FIGURE 1.3: Predicted mass percentages of scramjet-powered launch vehicle [1].

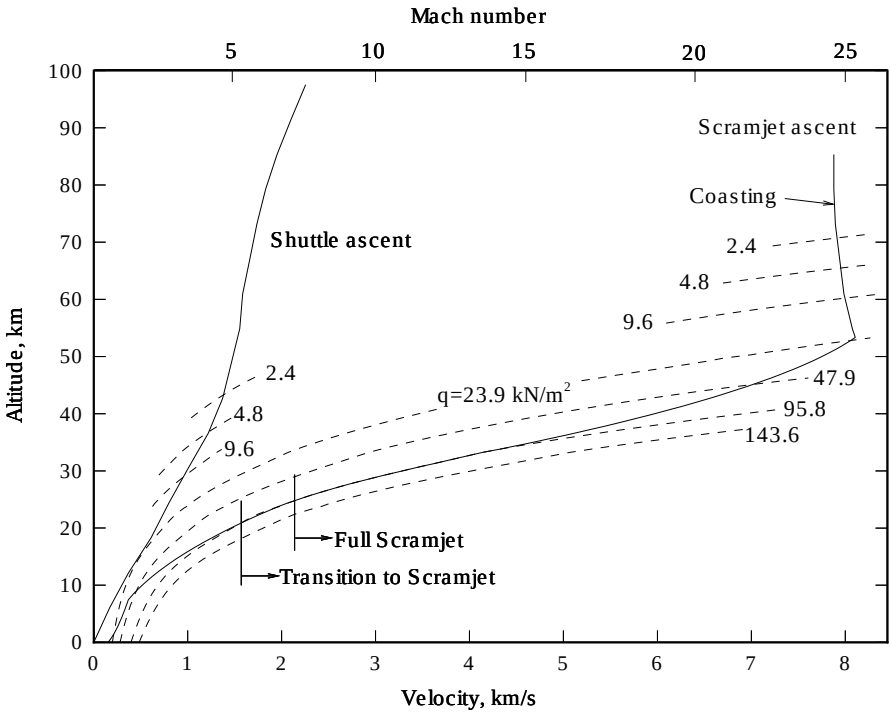

Figure 1.4: A proposed scramjet flight trajectory (adapted from Billig[2]).

One implication of the air-breathing nature of the scramjet concept is that the vehicle must fly at very high speeds ($>$ Mach 5) in the lower, more dense atmosphere ($\sim 25-40\,km$) in order to obtain enough oxygen for combustion requirements. A typical proposed flight trajectory of a scramjet powered launch vehicle is shown in Figure 1.4. This hypersonic flight regime would subject the craft to significantly higher stagnation pressures and temperatures [8] than would be experienced by a more conventionally powered vehicle such as the space shuttle. This in turn leads to greater thrust requirements due to the increase in aerodynamic drag, whilst the increased thermal loads will result in greater structural complexity and vehicle weight. Figure 1.5 shows the total pressure that would be experienced by a scramjet powered vehicle following the flight trajectory in Figure 1.4. Also shown in this figure is the total pressure experienced during orbital reentry and reentry of the Apollo capsule. The extreme pressure requirements demand extensive testing on all aspects of the highly integrated scramjet/airframe vehicles if the scramjet is to become a viable propulsion

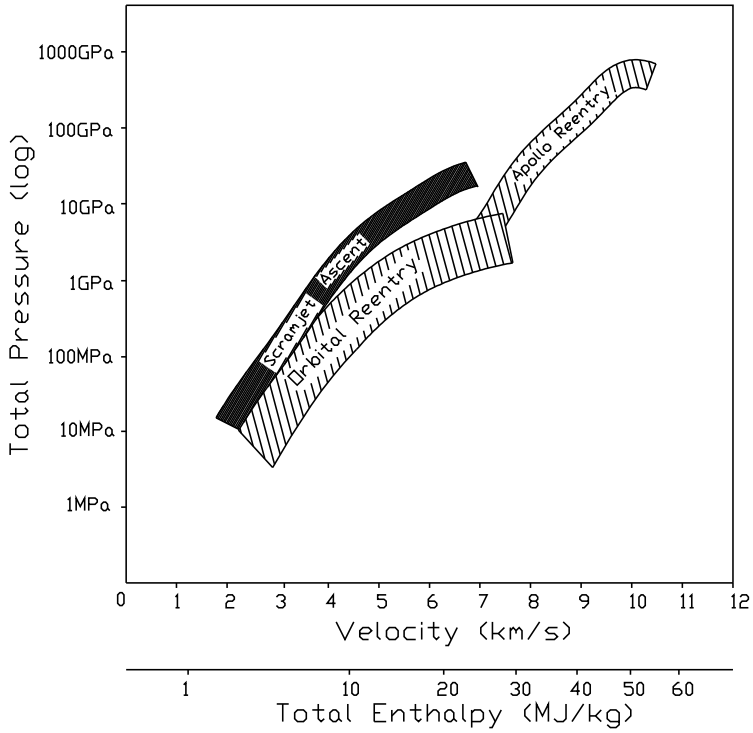

FIGURE 1.5: Total pressure (based on isentropic stagnation of the flow with equilibrium chemistry) associated with an anticipated scramjet ascent trajectory compared with orbital and Apollo reentry trajectories.

system for a Single Stage to Orbit Reusable Launch Vehicle (SSTO RLV). By matching various similitude parameters, accurate simulation of certain phenomena can be conducted in test conditions that differ to the true flight conditions. Such parameters include the Reynolds Number ($\frac{\rho u l}{\mu}$), the hypersonic similarity parameter ($M\theta$), the binary scaling parameter (ρl), the product $\rho^2 l$ and the matching of the total enthalpy (H_0). However, the only way to simulate all flight phenomena in a particular test is to fully duplicate all the freestream properties.

Traditionally, wind tunnels have offered a relatively cheap, quick and safe means of evaluating and modifying various aerodynamic shapes and models to arrive at a certain design. These designs are then usually refined and verified through a series of flight tests. However, the high costs associated with hypersonic flight reduces the feasibility of flight tests and thus places far greater emphasis on the crucial role of ground-based testing for the

evaluation and refinement of hypersonic flight-craft designs.

The generation of suitable hypersonic flow conditions in a ground-based test facility is a very challenging task. As flow speeds exceed around 2 km/s, continuous, or even intermittent wind tunnels are not feasible due to both excessive power requirements [1] and the fact that current material technologies prohibit the prolonged containment of gas at the extreme stagnation conditions associated with hypervelocity flow. To generate these high enthalpy conditions in the laboratory, short duration (or pulse) facilities have been developed. One such facility is the free-piston driven shock tunnel which has been utilized for hypersonic research since the early 1960's [9] and has been the experimental mainstay for scramjet testing since the early 1980s [10, 11]. However, the principles of operation of this facility restrict its flow generation capabilities to flows which simulate the lower-enthalpy end of the scramjet's proposed flight envelope.

Though different types of facilities have been used for testing various aspects of scramjet operation, it is generally recognised that the expansion tube is the only facility (based on current or near term technologies) which has the potential to produce test flows which simulate true in-flight conditions over the intended range of scramjet flight [9, 12]. By operating in expansion tube mode with a detonation driver, NASA's HYPULSE facility[13, 14] is used for scramjet testing at up to Mach 15 flight enthalpy with a flow velocity of 4.8 km/s and total pressure of 2.7 MPa [15, 16]. Though matching the flight enthalpy, "flight simulation is not exactly matched... because of facility limitations" (Rogers *et al*[15]). Through the generation of high driver sound speeds, a large-scale high-performance free-piston driver offers a means by which the flow generation capabilities of an expansion tube may be increased. But being a large, highly-stressed, highly-engineered pressure vessel, the capital cost of a free-piston driver exceeds the combined cost of all the other components of the facility [17, 18]. As a consequence, the full potential of the free-piston driven expansion tube concept has not been realized thus far.

[1] Test conditions corresponding to flight at 2 km/s at an altitude of 20 km has an energy requirement of approximately 400 MW per square meter of test section

1.2 The Rocketdyne Hypersonic Flow Laboratory (RHYFL)

An opportunity to increase the current ground-based hypervelocity testing capabilities lies in the components that were manufactured for the Rocketdyne Hypersonic Flow Laboratory (RHYFL) [19, 20] in 1989. Figure 1.6 compares the size of the RHYFL shock tunnel design to some other major ground based facilities from around the world. The RHYFL facility was originally designed as a large-scale reflected shock tunnel to enable full-size testing of the National Aero-Space Plane (NASP) scramjet engines. However, the NASP project was cancelled in 1990 after 100's of tonnes of hardware had been fabricated at a cost of ten's of millions of dollars. These major components for the RHYFL facility are now in storage and Chinitiz [9] was first to speculate on the performance that could be achieved if it were reconfigured to operate as an expansion tube. Of particular interest is the use of the large free-piston driver which features a 250 MPa maximum design burst pressure and a significant 9:1 area ratio between the driver and shock tube. This expensive, high-performance driver assembly weighs around 400 tonnes, has a length of 47 m, an inside diameter of 600 mm and a piston mass of 1750 kg. The coupling of this free-piston driver to a large expansion tube derived from the RHYFL hardware, would result in an unprecedented hypervelocity testing facility (RHYFL-X).

1.3 Objectives and Overview

This thesis explores the idea of utilising a large-scale high-performance free-piston driven expansion tube for the purpose of scramjet testing. In particular, it investigates the use of the hardware that was fabricated for the RHYFL shock tunnel project in making such a facility. The primary objective is to determine the range and quality of test conditions that could be expected from this proposed facility and to ascertain the suitability of these expected flows for the testing of scramjet-integrated hypersonic flight vehicles. Towards this end, the thesis is organised as follows:

Chapter 2 presents the principals behind the operation of various types of wind tunnels.

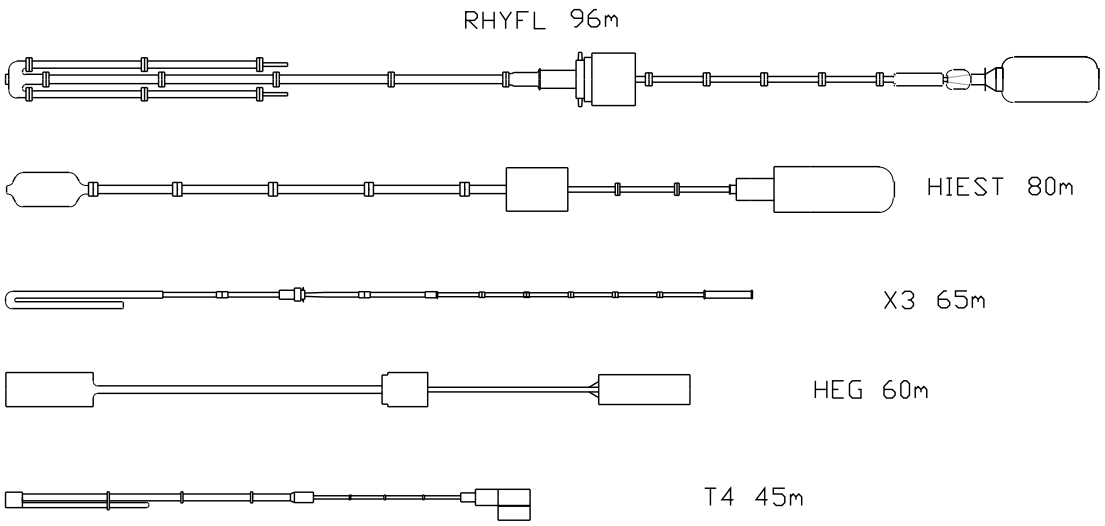

Figure 1.6: The original RHYFL design compared with other large hypersonic wind-tunnels.

It is shown that the free-piston expansion tube is the only facility, based on current or near term technologies, with the theoretical potential of being able to generate test flows with properties matching those that would be experienced by a scramjet during atmospheric flight.

Chapter 3 is a validation and verification of the numerical techniques employed to model expansion tube flow. The reliable simulation of the transient flow within an expansion tube is by no means a trivial task. As the proposed RHYFL-X facility is a large-scale expansion tube, a reliable simulation technique is required that is computationally feasible. Various modelling techniques are investigated for not only their capability of being able to adequately simulate expansion tube flow, but also their computational practicality in attaining performance estimates of large scale facilities. Detailed simulations of the X2 expansion tube are compared with experimental results to obtain confidence in the numerical codes and techniques.

The effects of finite-rate chemistry in expansion tube flow is examined in Chapter 4. The

one-dimensional flow simulation code *L1D* is used with a 5 species, 17 reaction finite-rate chemistry model of air to simulate different operating conditions of the X2 expansion tube. The finite-rate chemistry simulations are compared with simulations that assume equilibrium chemistry to ascertain the importance of including finite-rate chemistry phenomena in simulations of various expansion tube operating conditions.

Chapter 5 presents the performance predictions for the proposed RHYFL-X facility. Analytical methods are presented to attain a first order estimate of the initial fill conditions required for three proposed operating conditions. One-dimensional and axisymmetric simulations are then performed to refine these operating conditions and provide estimates of the test flow conditions and test times. Also reported is the diameter of the core flow and the levels of test gas dissociation that could be expected in the RHYFL-X expansion tube. The predicted hypersonic flow generation capabilities of this proposed facility is summarized and compared to what would be required for full duplication of hypersonic atmospheric flight.

The design and implementation of a nozzle placed at the end of an expansion tube is investigated in Chapter 6. As the cross-sectional area of test flow in a standard expansion tube is limited to the inside diameter of the acceleration tube, the concept of a hypersonic nozzle placed at the end of the acceleration tube section is of interest. Inviscid axisymmetric simulation results are presented to verify a contoured nozzle design obtained using a Method of Characteristics procedure. Viscous simulations were also performed to examine the ability of the nozzle to expand a hypersonic short-duration flow to uniform exit conditions. This chapter also examines the effect that the start-up process of such a nozzle has on the short test times inherent with expansion tube operation.

Chapter 7 outlines and summarizes the findings, conclusions and recommendations for the use of a large-scale expansion tube based on the RHYFL shock tube design for generating hypersonic flows for the purpose of scramjet testing.

Chapter 2

Hypersonic Test Facilities

The term *hypersonic* refers to a flow where the Mach number is greater than around 5 [21]. Thus a hypersonic flow can be generated readily by expanding a reservoir of gas to a low temperature and hence low sound speed. While the flow would be considered hypersonic, the actual velocity of the flow may not be that substantial. In this case, the energies associated with this flow will be well below that of atmospheric flight at corresponding Mach numbers. The term hypervelocity however refers to flows with very high velocities. If the flow is sufficiently hot, and therefore has a high sound speed, a hypervelocity flow is not necessarily hypersonic.

2.1 Intermittent/Continuous Test Facilities

There are types of facilities which can produce essentially continuous hypersonic testing conditions. These 'blow-down' type facilities are based on the principle of adding the energy to the test gas prior to an isentropic expansion through a nozzle. Figure 2.1 shows a generic layout of a hypersonic blow-down wind-tunnel. These facilities offer a convenient means of generating flows with hypersonic Mach numbers in test sections which have diameters of the order of several metres. They are however, severely limited in the total enthalpies and pressures they can generate. As mentioned in the previous chapter, hypervelocity flow fields have such high energy levels that it is impractical to power a continuous or even intermittent facility that targets these conditions. Aside from the huge energy requirements,

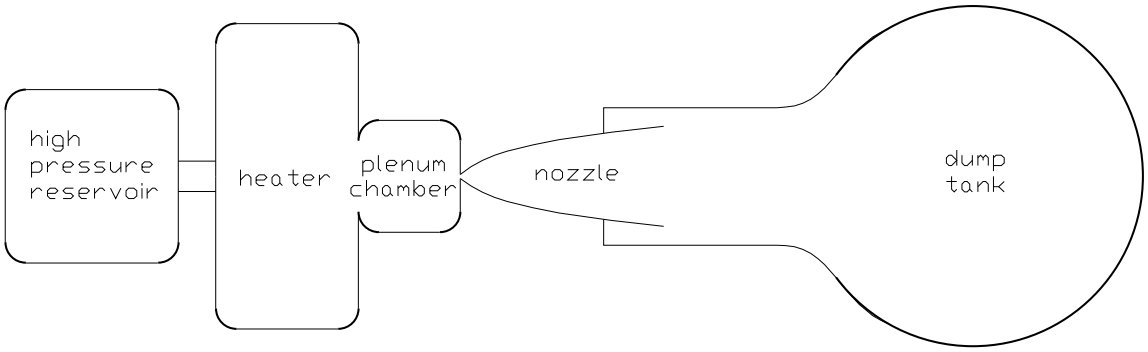

FIGURE 2.1: Schematic diagram of a continuous blow-down wind-tunnel facility.

these facilities are required to contain the test gas at, or near, the stagnation conditions prior to expansion. For this reason the total temperatures and pressures of these facilities are restricted to around 1500 K and 15 MPa respectively. These values are well below the total temperature and pressures needed for full duplication of high speed atmospheric flight.

One type of intermittent facility that can generate the enthalpy levels associated with hypersonic flight is the arcjet wind-tunnel, sometimes referred to as Hot-Shot tunnels [22]. These facilities have been used for the last 4 decades [23, 24] to generate high-enthalpy flows, primarily for the testing of thermal protection systems (TPS), but also for investigating catalytic recombination of atoms on surfaces and combustion in hypersonic air-breathing engines [25]. A typical arcjet wind-tunnel, illustrated in Figure 2.2, consists of a set of electrodes housed in separate electrode chambers with a constrictor tube linking the two. The second, or down-stream, electrode acts as the reservoir and a place for the gas to reach uniform conditions before the subsequent expansion through the nozzle. The test gas is introduced both from the upstream electrode chamber and the constrictor wall and then flows out through the nozzle. When a DC power supply is applied across the two electrodes, an electric discharge passes through the test gas flowing in the constrictor tube. It is this electric discharge that heats the test gas prior to nozzle expansion. Studies [24, 26] have shown that reservoir temperatures for these facilities reach the order of 10,000 degrees. At these temperatures, which resemble the stagnation point temperature of high speed scramjet

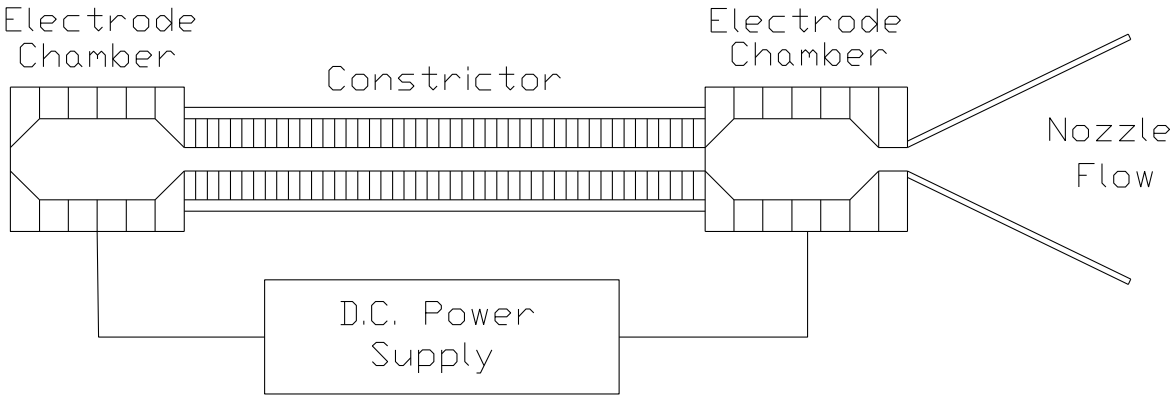

Figure 2.2: Schematic diagram of an arcjet wind-tunnel facility.

flight, the gas undergoes considerable excitation of internal degrees of freedom, dissociation and ionization. As the gas experiences rapid expansion, there is not sufficient time for the recombination reactions to complete and thus arcjet test flows are characterized by significant chemical and thermal non-equilibrium. These high-temperature real-gas phenomena alter aerodynamic properties of a vehicle [22], heat transfer characteristics [26] and combustion phenomena [27] when compared to atmospheric flight. As the pressure in the chambers of the arcjet wind-tunnels become too large, the current that heats the test gas prior to expansion is extinguished. Due to this, the arcjet wind tunnels have total pressure limitations equally severe, if not more so, than blow-down facilities. So while arcjet wind-tunnel facilities offer a convenient means of generating flows with enthalpy levels corresponding to hypervelocity flight, their severe total pressure limitations and test gas dissociation and ionization result in test conditions unsuitable for accurate aerothermodynamic and combustion

experiments on a scramjet vehicle.

Related to the arcjet wind-tunnel, is the concept of the Electrothermal Wind-Tunnel (EWT) (for further discussion see Ref. [9]). This facility introduces high pressure liquid air which is subsequently vaporized by the electric discharge. By this means, pressures of the order of gigapascals could be generated, with total temperatures around 10,000 K. Massive power requirements (of the order of gigaWatts) and severe material limitations, however, relegate this facility to a long-term concept. There are also ideas of using the EWT as the first stage of a two stage concept utilizing a magnetohydrodynamic (MHD) flow-accelerator as the second stage [28]. While this may be categorised as a 'nearer-term' concept [9], it still requires technology and processes that have not been demonstrated in order to create the total enthalpy and total pressure flows experienced in hypersonic atmospheric flight. The Radiantly Driven Hypersonic Wind Tunnel / Magnetohydrodynamic Accelerator Research into Advanced Hypersonics (RDHWT/MARIAH II) research program, sponsored by the US Air Force, is a program associated with the evaluation of a facility concept for generating true flight conditions in the Mach number range of 8 to 15 with test times greater than 1 s [29]. This concept involves a number of significantly challenging technologies such as an ultra-high-pressure air supply ($\sim$2 GPa), supersonic thermal energy addition (laser/electron beam) and MHD velocity augmentation. Substantial R&D is required in all these areas before this hypersonic wind-tunnel concept could be realized as a hypersonic testing facility.

In summary, based on current proven technologies, intermittent and continuous facilities are not capable of generating suitable test flows that match those associated with hypersonic atmospheric flight. To be able to more closely match the total enthalpies and pressures associated with high speed flight, short duration, or 'pulse' facilities have been developed.

2.2 Pulse Facilities

There exist a number of short-duration, or *pulse* facility concepts that are currently used in investigating various aspects of high-speed aerothermodynamics [1]. There are also a number

[1] The term aerothermodynamics is used to encompass aero-dynamic and aero-heating characteristics, as well as various physical processes associated with high speed flow.

of ways in which the energy is generated to drive these facilities. Each driver and facility has varying capabilities and characteristics and the choice of a driver/facility combination is determined by the consideration of several key aspects:

- Cost: Capital and operating costs vary significantly between the different types of facilities and drivers. With the current financial environment relating to hypersonics, the various costs are perhaps the most influencing factors in determining the overall type of facility.

- Test Flow Quality: Another major aspect dictating the decision is the capability of the facility/driver combination of generating the desired test-flow conditions. That is, the ability to generate flow conditions that are as close as possible to the ones that would be experienced during flight.

- Test Flow Duration: Test-flow duration can vary by several orders of magnitude ($\sim$1.0e-5 – 1.0e-2 seconds) between the different types of hypervelocity short-duration testing facilities. Different model configurations and/or effects (such as recirculating flows, combustion, shear stress, etc) require different times for the flow to fully establish. Longer test times are desirable so that steady-state flow conditions can be achieved over as large a model as possible. The short test times can also be considered as beneficial as testing at these very high energies would require active cooling of all components if the tests were to last longer than a fraction of a second.

- Test Section Size: Due to various operating principles, different facilities create varying cross-sectional areas of test flow. In conjunction with longer test times, a larger area of test flow results in the ability to test larger models, which reduces the extent to which uncertain scaling parameters need to be used when applying experimental results to full size applications.

Also of concern are factors such as the physical size and weight of the overall structure, the turn-around time of the facility, and the man-power and expertise required to operate it. As the majority of the hardware for the proposed RHYFL-X facility has already been designed and fabricated, the following section investigates the cost-independent capability of

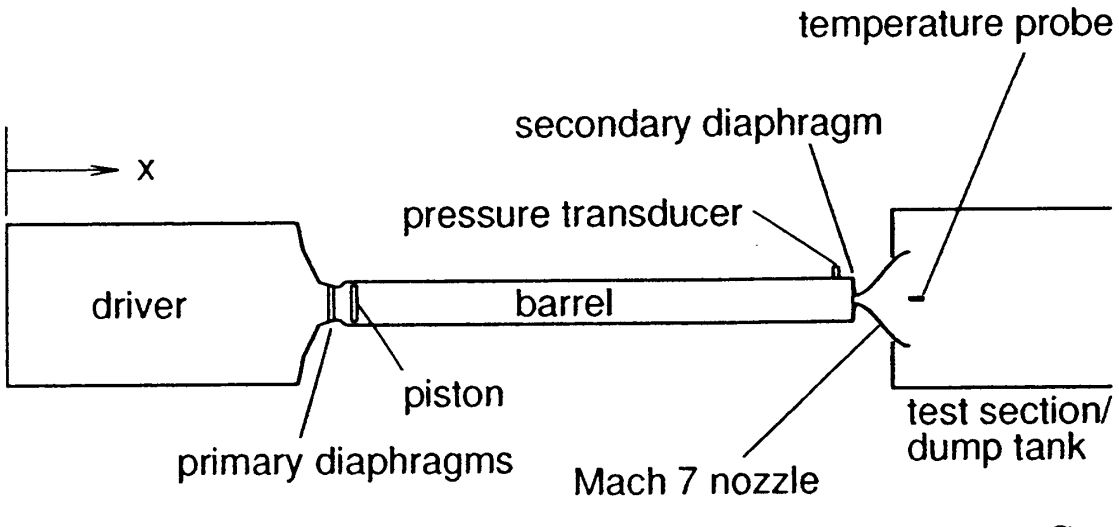

FIGURE 2.3: Schematic diagram of the Oxford University Gun Tunnel (from Buttsworth [3]).

various pulse facilities and driver types for producing hypersonic flows suitable for scramjet testing.

2.2.1 The Gun Tunnel

The concept of the gun tunnel, which is a type of "free piston compressor tunnel" [5], has been around since the early 1960's [30]. Free piston compressor tunnels work on the concept of using a high pressure reservoir to accelerate a piston down a tube containing the test gas. This piston action compresses and heats the test gas. The test gas is then expanded to hypersonic conditions from an essentially stagnated condition through a nozzle at the end of the tube. Through the use of this nozzle, a facility of this nature can have typical test section diameters of several hundred millimeters. Figure 2.3 is a schematic diagram of the Oxford University Gun Tunnel [3].

A gun tunnel uses a light piston and hence a fast piston stroke (*i.e.* piston speed generates shock waves) to non-isentropically compress the test gas (as opposed to facilities which use a heavier piston travelling at slower speeds [31]). This non-isentropic compression process results in a higher test gas temperature than would otherwise be possible via an isentropic

process. This method of adding energy to the test gas coupled with the fact that the stagnation properties are not physically realized for as long, enables an increase in stagnation properties to the vicinity of 2500 K and 20 MPa. The penalty for the higher stagnation conditions is a significant decrease in test time when compared to continuous or intermittent facilities. These stagnation conditions however are still well short of the stagnation temperatures and pressures associated with hypersonic atmospheric flight which can reach well over 10,000 K and 10 GPa respectively. Typical test times for a gun tunnel are of the order of 10 ms.

2.2.2 The Shock Tunnel

The shock tunnel was invented over a century ago and has been an experimental mainstay of hypersonic ground-based research for the majority of that time. Rather than using a mechanical means to compress the test gas, the shock tube concept utilizes a strong shock travelling down a tube of test gas to compress and heat it. (The means by which this strong shock is generated is the topic of the section later in this chapter) There are two main operating modes for a shock tunnel which will be discussed in the following sections: 1) the non-reflected mode, and 2) the reflected mode.

The Non-Reflected Shock Tube

In a non-reflected shock tube, the shock wave that propagates down the shock tube accelerates the test gas to some velocity whilst also increasing its pressure and temperature. The length of test flow between the shock and the test-gas/driver-gas interface can be limited by Mirel's effect where, after a certain distance along the shock tube, mass-loss to the boundary layer results in the length of this slug of test-gas remaining constant irrespective of how long the shock tube is. The test flow then passes over the test-model which is placed at the end of the shock tube. A non-reflected shock tube can be operated with a nozzle placed on the end of the shock tube segment to increase the diameter of the core flow. Various techniques have been employed [32] to aid the starting process of such nozzles in the short test times inherent with these facilities. A major disadvantage of the non-reflected shock tunnel is the short

test times - typically in the range of 10 to 100 microseconds. The x-t diagram in Figure 2.4 illustrates the principal wave processes that occur during ideal operation of a non-reflected shock tube.

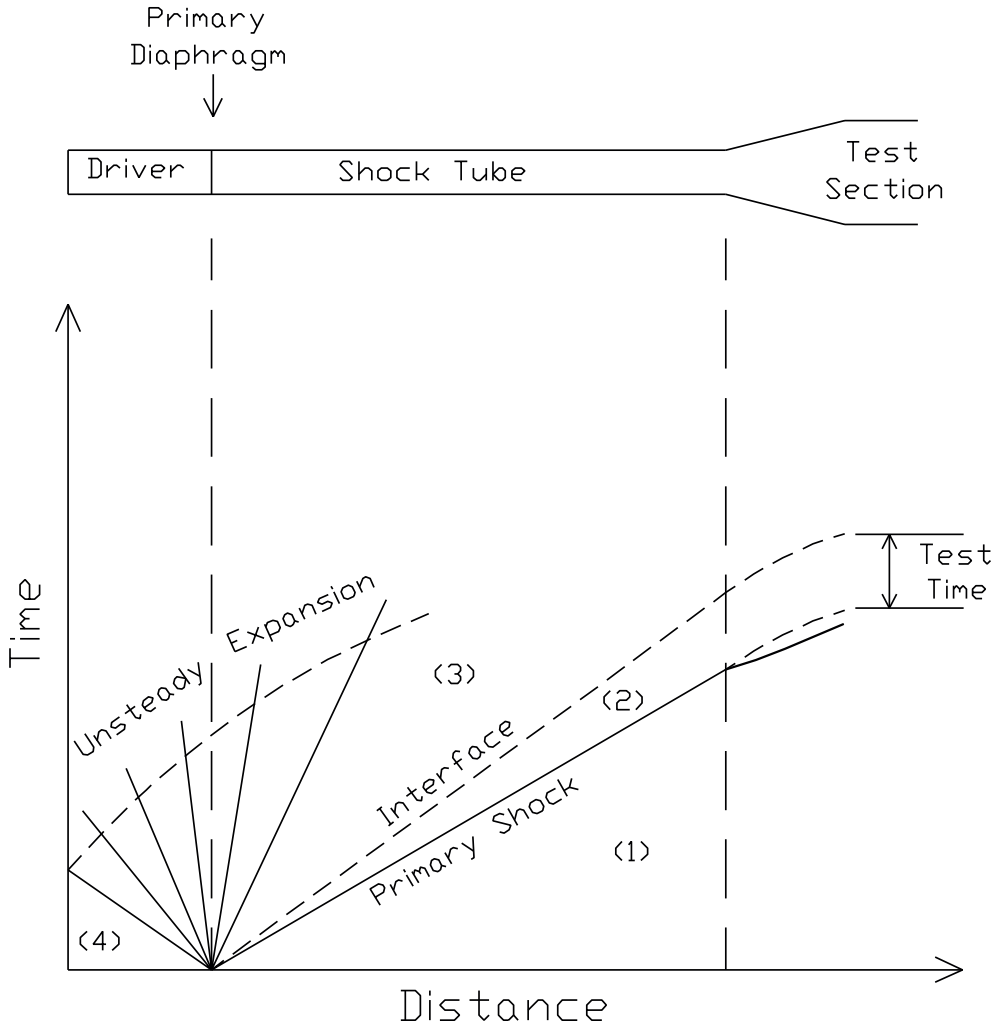

FIGURE 2.4: Schematic diagram of a non-reflected shock tunnel with corresponding xt-diagram.

With the use of a free-piston driver (discussed later in the chapter) the non-reflected shock tube is capable of speeds in excess of 10 km/s. Because all the energy in a shock tunnel is added to the test flow via a shock wave, significant dissociation occurs as the shock speed increases. Test flows produced by non-reflected shock tubes have characteristically low Mach numbers due to the high temperature of the shock processed test gas. At the higher

shock speeds, the temperature of the test gas is such that a dissociated plasma is formed which is unsuitable for aerodynamic testing.

The Reflected Shock Tunnel

The initial part of operation of a reflected shock tunnel is the same as for that of a non-reflected shock tunnel in that a shock is driven along a length of tube containing the test gas. When the shock reaches the end of this shock tube however there is an end plate with a small orifice in it that leads to the nozzle. The shock reflects off this end-plate, bringing the test gas to rest. This region of high-pressure, high-temperature stagnated gas is the supply region, or reservoir, for the subsequent expansion through the nozzle. Because the flow is stagnated in the reflected shock tunnel, the pressures and velocities attainable in these facilities are lower than that achievable in a comparable non-reflected shock tube. As the simulated flight speed starts to increase so too does the dissociation of the test gas, resulting in experimentally obtained results that would differ from those that would be experienced during flight [33]. As it is unclear as to what or how much of an effect the dissociation has, it is difficult to compensate for the dissociation when analyzing experimentally obtained results. Flow velocities approaching orbital velocities can be generated in a free-piston reflected shock tube [34], but, again, the severe dissociation and ionization of the test gas at these speeds would results in dubious aerothermodynamic testing capabilities. Reflected shock tubes also suffer from test gas contamination by the driver gas at these high speeds.

Figure 2.5 shows an x-t diagram of the primary wave processes that occur during the operation of a reflected shock tunnel. The total pressure and temperature of the final test flow is governed by the stagnation conditions achieved in the nozzle supply region prior to expansion. Currently available materials limit this stagnated region to pressures and temperatures of the order of 200 MPa and 8000 K respectively, though typical operating conditions are well below these values. Facilities that use sacrificial components are capable of stagnation conditions somewhat larger than this [35]. For accurate aerothermodynamic testing, test conditions must replicate those that would be experienced during flight. During the scramjet's proposed flight trajectory, it will experience stagnation pressures up to ten's

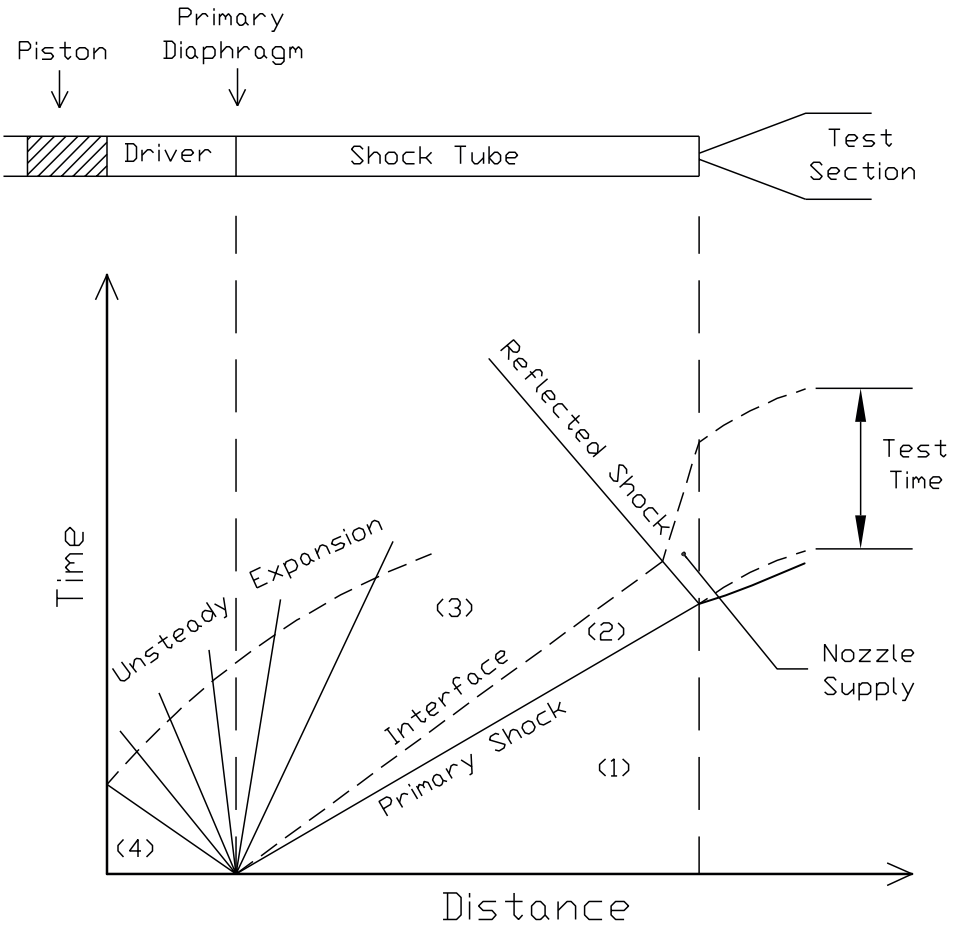

FIGURE 2.5: Schematic diagram of a reflected shock tunnel with corresponding xt-diagram.

of gigapascals. So while the reflected shock tunnel can generate total pressures matching those of low hypersonic flight speeds, it is still orders of magnitude below what is required for true Mach number testing of the scramjet over its full intended flight envelope (Figure 5.20, Chapter 5).

Operating in reflected mode results in test times that are an order of magnitude longer than those of a non-reflected shock tube (typically several milliseconds) but shorter than that of a gun-tunnel. Unlike a gun-tunnel, a reflected shock tunnel does not have a mechanical means of separating the driver gas and the test gas. The arrival of the reflected shock wave at the driver/test gas interface causes 'jetting' of the driver gas forward along the walls of

the shock tube. It is this premature arrival of the driver gas in the test flow, known as driver-gas contamination [36], which dictates the length of useful test flow. As the shock speed increases, this driver-gas contamination becomes worse until the test time decreases to a point where it may become no longer useful [34].

From this discussion it is evident that the total pressure and dissociation limitations of the reflected shock tunnel results in test flows that will not accurately simulate aerothermodynamic characteristics of vehicles at high hypersonic flight speeds. So while shock tunnels offer a convenient means of producing high enthalpy, high Mach number flows, an alternative hypersonic flow generation technique is required if the accurate simulation of the high energy, high total pressure flows associated with the scramjet are to be achieved.

2.2.3 The Expansion Tube

The expansion tube was first postulated in the 1950's [37] as a means for creating high-enthalpy flow conditions without the total pressure and flow dissociation problems inherent with other testing facilities. Figure 2.6 shows an x-t diagram of an expansion tube during ideal operation. The expansion tube consists of three main sections. 1) the driver section, 2) the shock tube section and 3) the acceleration, or expansion, tube section. An expansion tube is simply a variation of a shock tunnel where the steady expansion nozzle is replaced with a length of tube called an acceleration tube. The primary shock wave propagates down the shock tube until it reaches a thin diaphragm which initially separates the shock tube from the acceleration tube. This light secondary diaphragm shears off upon the arrival of the shock resulting in a high pressure, high temperature slug of gas in a moving frame of reference. The pressurized test gas then expands via an unsteady expansion into the low pressure acceleration tube.

The unsteady expansion which propagates back upstream into the slug of test gas (but still moving downstream in a laboratory frame of reference because the slug of gas is supersonic) adds substantial energy to the flow [38]. Consider an elemental slug of test gas that passes through an unsteady expansion fan centred around the secondary diaphragm. As work is equal to the force multiplied by the distance over which this force acts, the work

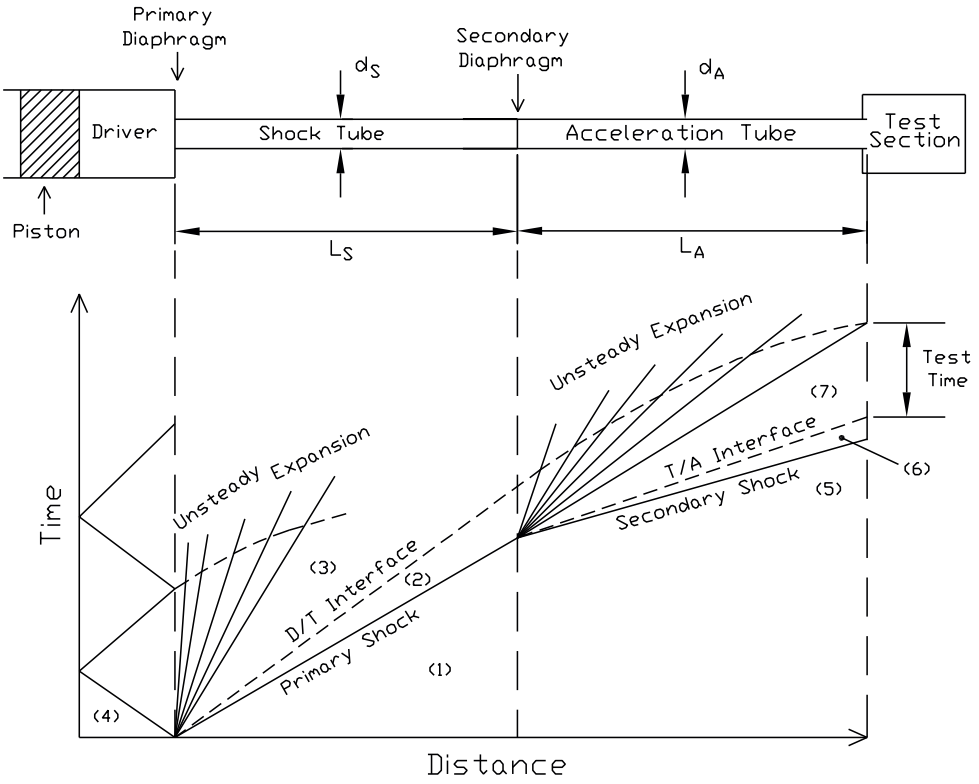

FIGURE 2.6: Schematic diagram of an expansion tube with corresponding xt-diagram.

done by the leading edge of this gas slug on the slug in front of it is proportional to the pressure drop across the expansion fan integrated with respect to the distance across which this pressure drop occurs. As the trailing edge of this elemental slug of gas will pass through the unsteady expansion at a later time, the pressure drop will be the same but the distance over which it happens will be larger. This results in positive net work being done on the considered slug of gas, and hence an increase in energy of the slug. This process is known as the "energy multiplication" effect of an unsteady expansion [39] and it significantly increases the total pressure and enthalpy of the test gas. Using the notation in Figure 2.6, Equations 2.1 and 2.2 give the perfect-gas total pressure and enthalpy ratios across the unsteady expansion

centered at the secondary diaphragm [40]:

$$\frac{P_{07}}{P_{02}} = \left[\frac{1+\frac{\gamma_2-1}{2}M_2}{1+\frac{\gamma_2-1}{2}M_7}\right]^{\frac{2\gamma_2}{\gamma_2-1}} \left[1+\frac{1}{\gamma_2}\right]^{\frac{\gamma_2}{1-\gamma_2}} \left[1+\frac{(\gamma_2-1)M_7^2}{2}\right]^{\frac{\gamma_2}{\gamma_2-1}} \tag{2.1}$$

$$\frac{H_{07}}{H_{02}} = \frac{\gamma_2(\gamma_2-1)}{\gamma_2+1}\left[\frac{1}{\gamma_2-1}+\frac{M_7^2}{2}\right]\left[\frac{1+\frac{\gamma_2-1}{2}M_2}{1+\frac{\gamma_2-1}{2}M_7}\right]^2 \tag{2.2}$$

Because of the strong primary shock, the Mach number of the shock-processed test gas (M_2) is approximately constant for all operating conditions and can be estimated from the following equation from Morgan [40]:

$$M_2 \approx \sqrt{\frac{2}{(\gamma_2-1)\gamma_2}} \tag{2.3}$$

Figure 2.7 is plot of the total pressure and enthalpy gains across an unsteady expansion. This figure indicates that as the expanded test gas reaches a Mach number of around 15, the gain in total pressure of a perfect gas approaches a factor of 60. This is accompanied with the potential to increase the total enthalpy by a factor of 3. Once the energy is added to the flow via the unsteady expansion process, the flow is never stagnated, so the large stagnation conditions are never physically realized. This means that the expansion tube concept does not suffer from the fundamental dissociation and total pressure limitations of other facilities. Independent of driver considerations, the expansion tube is the only ground-based testing facility with the potential capability of being able to create suitable test flows with total pressures and enthalpies required for full simulation of hypersonic scramjet powered vehicles up to orbital speeds.

A penalty to be paid for the unsteady flow processes of an expansion tube is the very short periods of steady test flow. These test times are typically of the order of 10's to 100's of microseconds for currently operating facilities. Section 2.4 outlines the waves processes which govern the test time in an expansion tube.

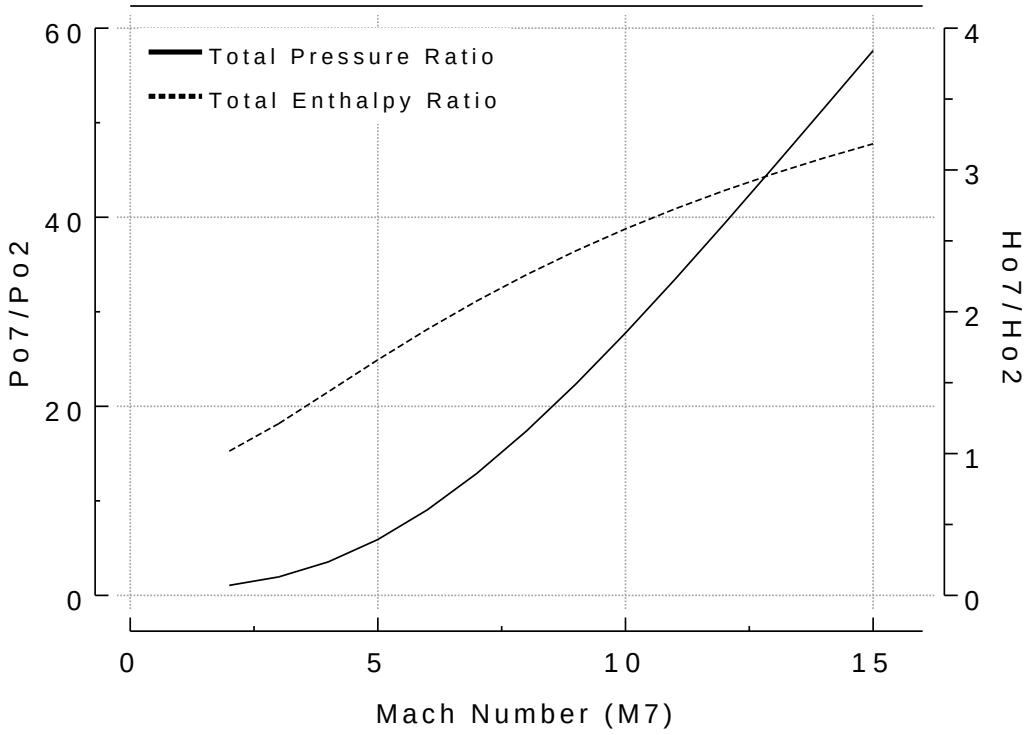

FIGURE 2.7: Perfect-gas total pressure and enthalpy gains across an unsteady expansion. Notation from Figure 2.6. γ_2=1.4.

2.3 Driver Types

The driver is the source of energy that is required to generate test flows in a wind tunnel. For a continuous facility such as a blow-down wind tunnel, the driver could typically be a large reservoir of high-pressure gas at room temperature. This large reservoir would expand through a converging-diverging nozzle to the desired conditions whilst being maintained at a certain pressure via a compressor. This type of facility would have a Mach number limit of approximately 4 due to the limitations on the stagnation temperature for this type of facility and the possibility of condensation of the oxygen in the expanded test flow. As the simulated flow energies increase, energy can be added to the test gas prior to expansion via methods such as electrical resistance heating, arc heating, hot pebble beds and vitiated air techniques. These facilities have to be operated intermittently as the larger energy and pressures requirements reach levels that can not be maintained for long durations. As reported

earlier, the massive amounts of energy required to continuously generate flow above about 2km/s, combined with limitations associated with containment of the stagnation conditions, lead to the development of pulsed facilities. For these pulsed facilities there are a number of different methods by which the energy is produced to drive the facility. Two approaches that are used the most widely for generating high energy driver conditions for pulse facilities are the detonation driver and the free-piston driver.

2.3.1 Detonation Driver

In a detonation driver, energy is released from the rapid combustion of a detonable mixture in the driver section. A detonation wave travels along the tube as a free-running Chapman-Jouget (C-J) wave, increasing the pressure and temperature of the driver gas. This high pressure, high temperature driver gas is what drives the shock down the shock tube. A light primary diaphragm can be used because the initial pressure in the driver tube is only around 1/20th of the post detonation pressure. The driver pressures achievable by detonation drivers are only limited to the pressure rating of the driver tube. Detonation drivers, however, are restricted in the types of gases that can be used in the driver. They are therefore substantially limited in the range of driver sound speeds that can be generated (the impact of the driver sound speed on expansion tube test flows is discussed later in this chaper as well as in Chapter 6). There a 2 main ways of operating a detonation driver - with a forward running detonation and a reverse running detonation.

Forward detonation

In the "forward detonation" mode, the detonation wave is used to initiate combustion at the breech end of the driver. This then travels downstream towards the diaphragm as a free-running Chapman-Jouget (C-J) wave, as used in the HYPULSE Shock-Initiated Driver (SID) [41]. This imparts a forward velocity on the gas prior to expansion and thus has an energy advantage over a driver with stagnant conditions at diaphragm rupture. Operating in this manner however, the expansion waves reflect off the back of the driver tube earlier and can quickly catch up to the primary shock. This interaction could disrupt the shock-processed test gas and cause attenuation of the primary shock. Figure 2.8 is a schematic

diagram of a shock-induced forward-detonation driver coupled to a shock tube [4]. In this

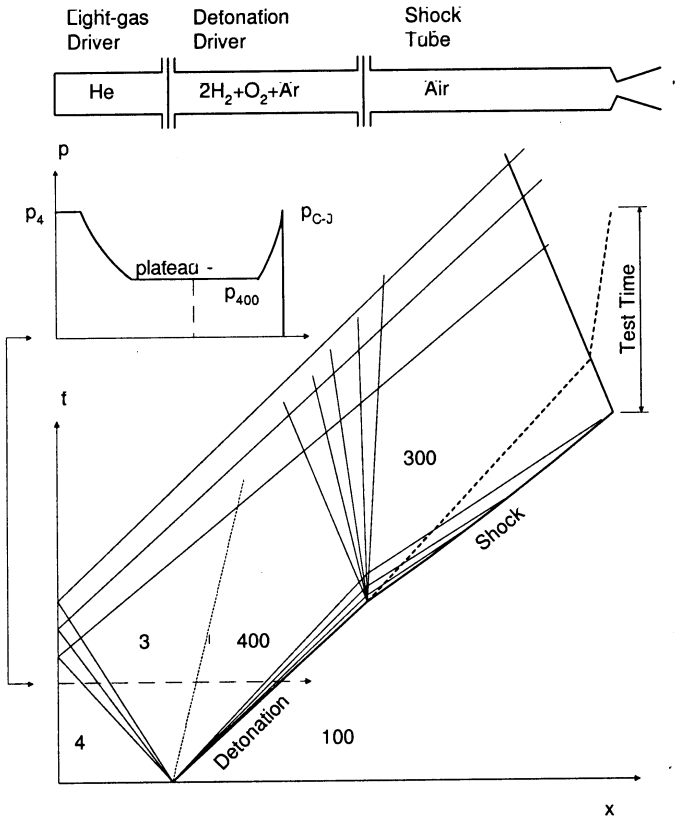

FIGURE 2.8: Schematic diagram of a forward-detonation driver linked to a shock tube with a corresponding xt-diagram (from Bakos [4]).

case the detonation is initiated by a shock that is created by the high-pressure section of helium adjacent to the detonation tube. This prolongs the time required for the expansion waves to catch up to the primary shock.

Reverse detonation

In the reverse mode, the detonation is initiated at the primary diaphragm station, with the C-J wave then travelling upstream towards the breech end. In this way, a longer duration of steady driver conditions at the primary diaphragm station is achieved until the arrival of the reflected C-J wave from the other end of the driver tube. This mode of operation imparts a velocity to the gas opposite to that which it will ultimately be travelling down the tube.

As a result of this, an energy loss will occur through the steady expansion that is required to bring the gas to a stationary state before accelerating it in the required direction.

2.3.2 Free-Piston Driver

The free-piston driver concept was developed by Stalker in the early 1960's [42]. A reservoir of high-pressure gas is used to accelerate a heavy piston from rest down a driver tube, subsequently compressing the driver gas. The momentum of the heavy piston results in an overshoot in pressure at which point the primary diaphragm ruptures and a shock wave propagates into the test gas on the other side of the diaphragm. Figure 2.9 is a schematic diagram of the RHYFL free-piston driver coupled to a shock tube segment. To avoid primary

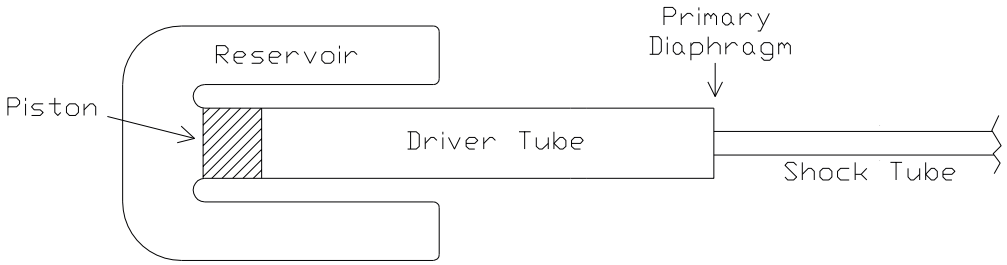

Figure 2.9: Schematic diagram of the RHYFL free-piston driver coupled to a shock tube.

shock attenuation, the driver gas slug must be sufficiently long at the moment of diaphragm rupture such that the disturbances from the reflection of the expansion fan do not catch up with the shock-processed test gas. Tuned operation of the piston means that the piston still has sufficient forward momentum at the point of diaphragm rupture such that the rupture pressure is maintained for a longer period of time. However, this requires a significant area ratio at the primary diaphragm station so that *tuning* occurs at manageable piston speeds. This large area ratio means that the whole driver assembly must be significantly larger in diameter than the shock tube and greatly increases the cost of the overall facility. Tuned operation of a free-piston driver does however result in a smaller slug of driver gas being needed at diaphragm rupture to drive a certain length shock tube.

A major advantage of the free-piston driver is that any gas or combination of gases can be used as the driver gas. The driver gas composition can be tailored to result in a certain driver sound speed at rupture and/or a desired compression ratio. This results in a very versatile driver capable of a wide range of driver conditions. Due to the versatility of this type of driver and the high rupture pressures that are possible, the free-piston driver remains the cost-independent driver-of-choice [17] when generating high velocity flow. However, a free-piston driver is a highly stressed pressure vessel that has to be carefully engineered to withstand large velocities and extreme dynamic loading, large pressures and temperatures, and the possibility of high-energy impacts, in a repetitive operating environment. This results in the capital cost of the free-piston driver being the significant portion of the overall cost of an entire facility. This coupled with the fact that the expansion tube has only recently been accepted as a hypersonic testing facility capable of generating suitable test flows, means that the full potential of a large high-performance free-piston driven expansion tube has yet to be realized.

Double-Driver Arrangement

An expansion tube can be operated with either one or two driver sections. A double-driver (or compound driver) expansion tube [43, 44] consists of a second driver section which is placed between the primary driver and the shock tube. Figure 2.10 is a schematic diagram of such a double-driver arrangement. When the primary diaphragm ruptures, a shock is

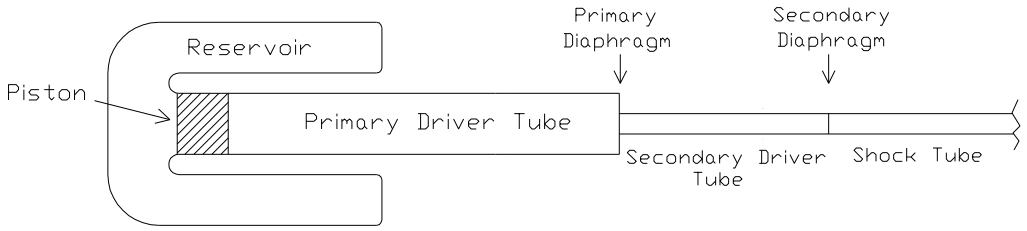

FIGURE 2.10: Schematic diagram of double driver arrangement coupled to a shock tube segment.

initiated that travels down this secondary driver tube section. Running in an over-tailored mode results in the driver gas in the second section having a higher temperature, and hence

sound speed, than would be possible with only one driver. By operating in this mode, test flows with significantly higher total pressures and enthalpies are possible.

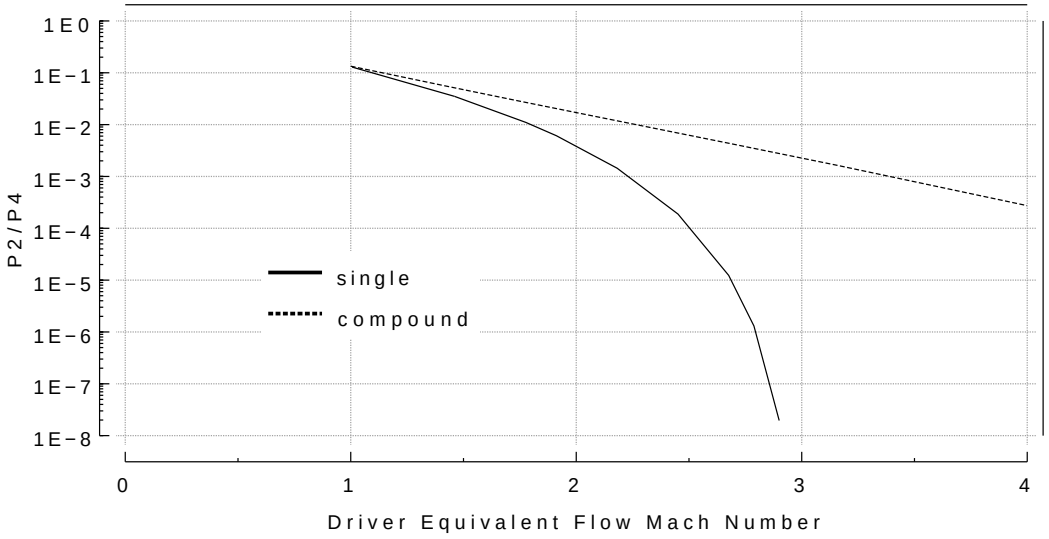

Figure 2.11: Comparison of single and compound drivers using helium as the driver gas and assuming no area ratio between driver and driven sections. P2 = pressure of shock processed test gas, P4 = driver rupture pressure.

Figure 2.11 (adapted from Morgan [39, 45]) plots the *driver-equivalent flow Mach number* versus the pressure ratio P2/P4 using perfect-gas relations. The calculations use helium as the driver gas and assuming no area ratio between the driver and driven sections.. The driver-equivalent flow Mach number is the flow speed of the shock processed test gas normalised by the driver sound speed at rupture. The pressure ratio P2/P4 is the pressure of the shock processed test gas (P2) normalised by the rupture pressure of the driver gas (P4). It is evident from this figure that the compound driver offers a significant pressure ratio advantage over the single driver at driver-equivalent flow Mach numbers higher than around 2. Below these conditions however there is little benefit, if any, to be had by using this more complicated mode of operation. Due to the wave processes that govern the test time in expansion tubes, the use of a compound driver also results in a shorter test time for a given size facility. When targeting scramjet flight conditions up to orbital velocities, the shock speed through the test gas must be kept low in order to result in static temperatures of the expanded test gas in the vicinity of atmospheric levels (explained in the following section). This leads to low speeds

of the shock-processed test gas which in turn means driver-equivalent flow Mach numbers of no more than around 1.5. For this reason, only a single-driver configuration will be used in simulations and predictions for the scramjet testing capabilities of the proposed facility.

2.4 Operation of a Free-Piston Driven Expansion Tube

As with any transient wave-driven facility, the lengths of the various sections of an expansion tube must be optimized in order to achieve the maximum test time. As these wave speeds change, so too do the optimum section lengths and the amount of steady test time available. This section will examine the wave processes responsible for both creating the test flow and governing the available test time in a free-piston driven expansion tube.

2.4.1 Single Driver Expansion Tube

The unsteady flow of an expansion tube is initiated by the rupturing of the primary diaphragm. Figure 2.12 shows a more detailed version of the xt-diagram presented in Figure 2.6. The large area ratio at the primary diaphragm location results in choked flow (Mach Number = 1) at the area transition which prevents the unsteady expansion fan propagating upstream into the driver. This is a desired feature as it provides increased performance capabilities of the expansion tube. Figure 2.13 shows the benefits in terms of pressure obtained by using a large area ratio at the throat compared to a constant area driver/shock tube coupling for a driver gas with $\gamma = 1.67$. This figure shows the Performance Measure, Φ, which is defined by

$$\Phi = \frac{\frac{P_3}{P_4} \text{ for } \frac{A_D}{A_S} \gg 1}{\frac{P_3}{P_4} \text{ for } \frac{A_D}{A_S} = 1}$$

where P_3 is the expanded driver gas pressure, P_4 is the rupture pressure, A_D is the inside area of the driver tube and A_S is the inside area of the shock tube ($\frac{A_D}{A_S} \gg 1$ implies chocked flow at the throat). This parameter is plotted for varying values of the driver equivalent Mach number, M_*. For low values of M_* there is a theoretical 3 fold nose-to-tail pressure

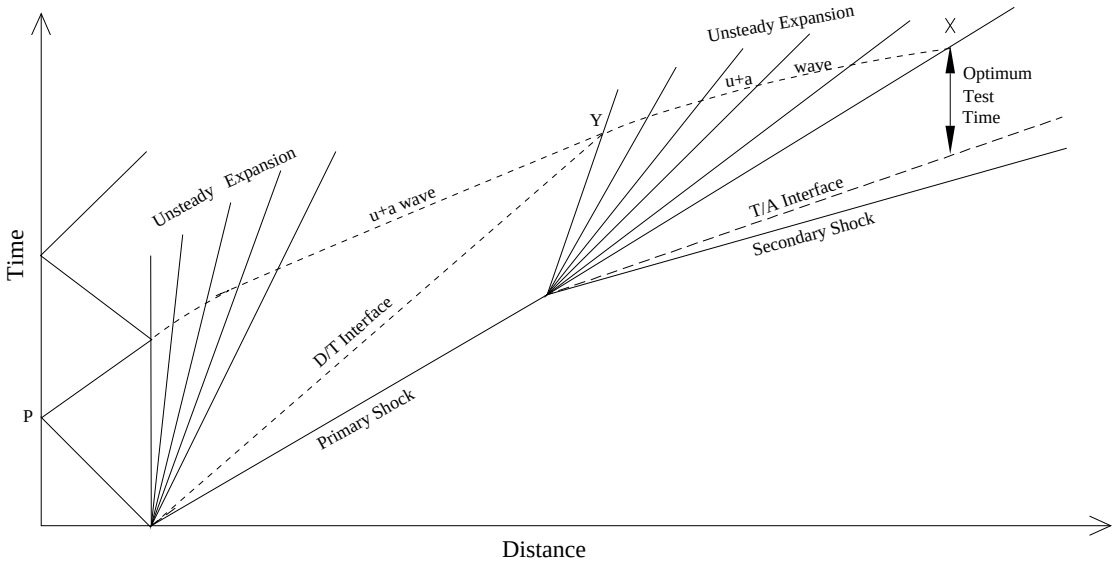

Figure 2.12: An x-t diagram of ideal expansion tube operation.

advantage of having a significant area ratio between the driver and shock tube compared to a constant area driver/shock tube segment. The pressure advantage associated with the large area ratio is seen to increase rapidly for larger values of M_*. There is approximately an order of magnitude benefit with regards to pressure for conditions with an M_* of around 2.2.

The expansion wave generated by the primary diaphragm rupture travels back upstream through the driver gas until it reaches, in the case of a free piston driver, the head of the piston (point P in Figure 2.12). The expansion wave is reflected and travels back downstream towards the diaphragm station. At this point, the interaction between the reflected expansion wave and the tail of the unsteady expansion fan generates a disturbance wave which travels upstream through the gas at the local sound speed. In a laboratory frame of reference this wave would appear to be travelling at a speed equal to the sound speed plus the local flow speed, hence they are known as '$u + a$' waves, where u is the flow velocity and a is the sound speed. When the driver gas / test gas interface (D/T Interface) reaches the upstream edge of the unsteady expansion fan ($u - a$ waves centred at the secondary diaphragm station),

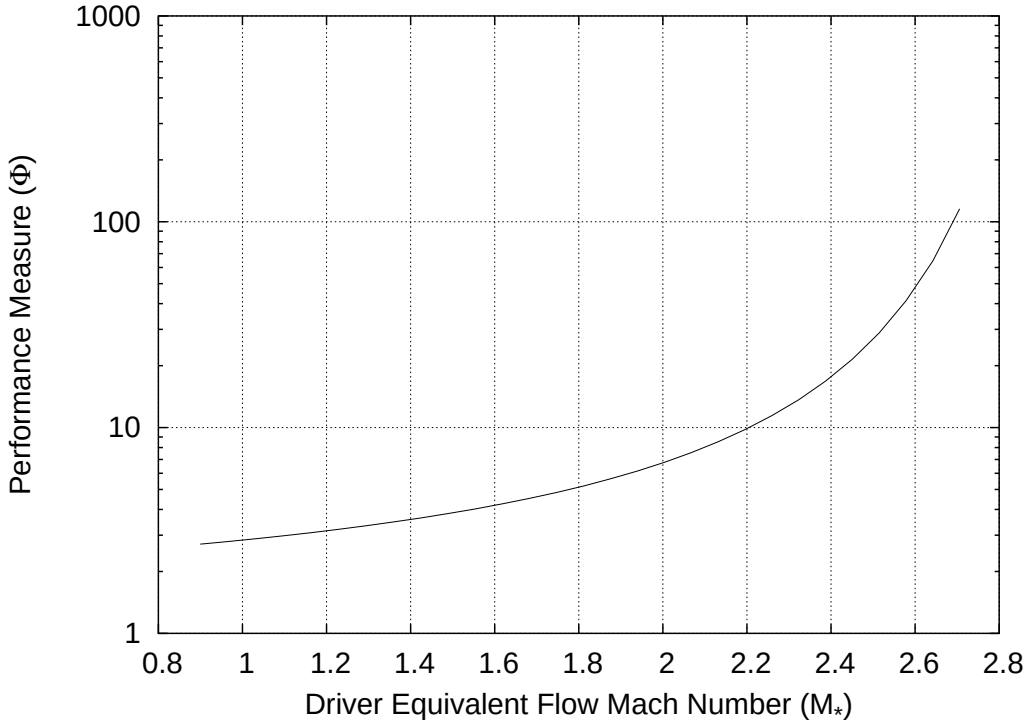

FIGURE 2.13: Performance measure, Φ, as a function of driver equivalent Mach number, M_*, indicating the pressure benefits of a large area-ratio driver compared to a constant area driver.

it too generates a $u + a$ disturbance wave which travels downstream through the test gas. The optimum length of the shock tube would be such that the $u + a$ wave generated at the primary diaphragm location arrives at the upstream edge of the unsteady expansion fan at the same time as the driver/test gas interface (point Y). The $u + a$ wave generated by this interaction then travels downstream through the unsteady expansion, catching up to the expanded test gas and eventually terminates the test time. The optimum acceleration tube length would be such that the downstream edge of the unsteady expansion fan and the $u+a$ wave arrive at the test section at the same time (point X). The test time in Figure 2.12 is the time between the test gas/accelerator gas interface (T/A Interface) and point X. If the acceleration tube was made shorter than this, the test time would be truncated by the early arrival of the unsteady expansion. If made longer, the $u+a$ wave would disrupt the test flow first. Note that althought these flow proceses occur both for the ideal inviscid case as well as for the real gas situation, the viscous effects will alter the speeds of the waves relative to

the inviscid approximation.

Typical test times for currently operating expansion tubes are in the range of 10's to 100's of microseconds. From the above analysis it is evident that, for a given condition, the optimum lengths of the different sections would change depending on the length of the driver gas slug at diaphragm rupture. The longer the driver rupture pressure can be maintained, the longer the optimum tube sections will be, resulting in longer test times.

There are two regions in the operational cycle of an expansion tube where the test flow is accelerated, the first being via the primary shock and the second being via the unsteady expansion. As a result of this there is a theoretically infinite number of ways to achieve a given final flow speed. The final test flow conditions depend not only on the driver conditions at rupture but also on the primary shock speed. For example, consider a condition that has a desired test flow velocity of 6 km/s, representing the approximate upper region of intended scramjet flight. Figure 2.14 is plot of the density of the test gas as a function of the primary shock speed for a fixed final flow speed of 6 km/s (The computer programs written to generate the data for the graphs in this chapter are included in Appendix D). This analysis has been based on perfect-gas properties and ideal expansion tube operation, and has ignored phenomena such as viscous effects and the sound speed buffer requirement across the D/T Interface. As the calculations have assumed perfect gas properties, the final shock speed of 7217 m/s was noticeably higher than the flow speed (6 km/s). The calculations have also assumed the RHYFL design rupture pressure of the primary diaphragm of 250 MPa and Mach one flow at the throat due to large area ratio between the driver and driven section. The driver gas was set as helium at an arbitrary temperature of 500 K with air as the test and accelerator gases initially at 296 K. Figure 2.14 illustrates that the test flow density varies significantly over the range of possible primary shock speeds. If maximum density was desired for this condition, the fill conditions would be chosen such that a primary shock speed of around 3.1 km/s would result. Figure 2.15 shows the static temperature of the test flow for the same 6 km/s condition. This indicates that the temperature of test flow rapidly increases as the primary shock speed increases which results in an essentially linear increase in sound speed, a, with primary shock speed. Unlike the density and pressure, the

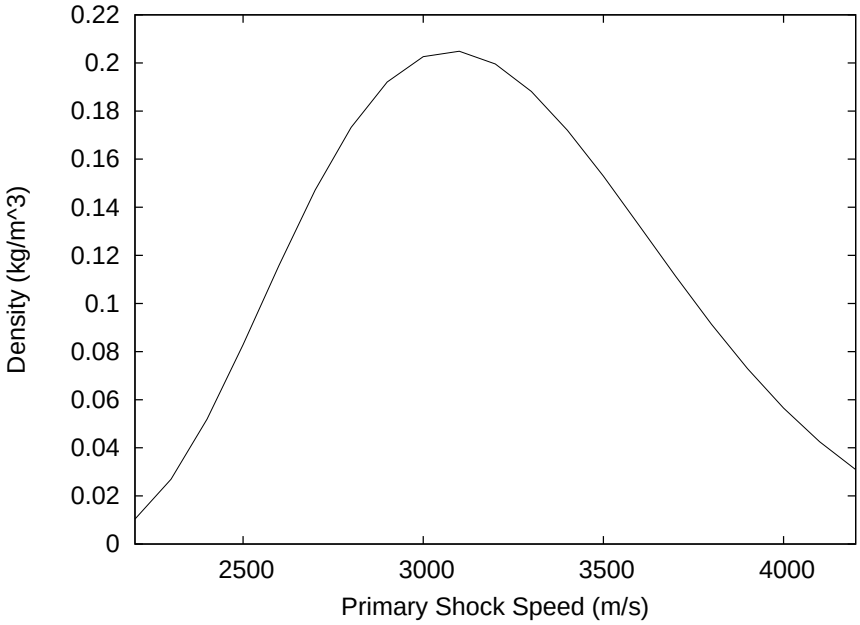

FIGURE 2.14: Test flow density versus primary shock speed for a final flow velocity of 6 km/s based on perfect gas calculations.

test gas temperature is independent of the driver gas conditions at rupture and, for a fixed final flow/shock speed, is only dependent on the speed of the primary shock. In order to achieve true Mach number conditions (*i.e.* matching Mach number and flow velocity), the sound speed, and hence temperature, must be equal to that of atmospheric conditions. At altitudes associated with anticipated scramjet flight at 6 km/s, the temperature of the air is in the vicinity of 230 K. To achieve this test flow temperature in an expansion tube with a final test flow velocity of 6 km/s, Figure 2.15 indicates that primary shock speeds of around 2.4 km/s will be necessary. Figure 2.14 shows that this shock speed will result in a significant reduction in the test flow density compared to the density that would be obtained with a shock speed of around 3.1 km/s.

The isentropic total pressure of an ideal test flow is proportional to the Mach number to the 7th power ($P_o \propto M^7$). As the test flow sound speed increases linearly with primary shock speed for a fixed final flow speed, the Mach number of the test flow decreases linearly as the primary shock speed is increased. This results in a rapid drop in total pressure of the final test flow as the primary shock speed increases. Figure 2.16 shows this significant

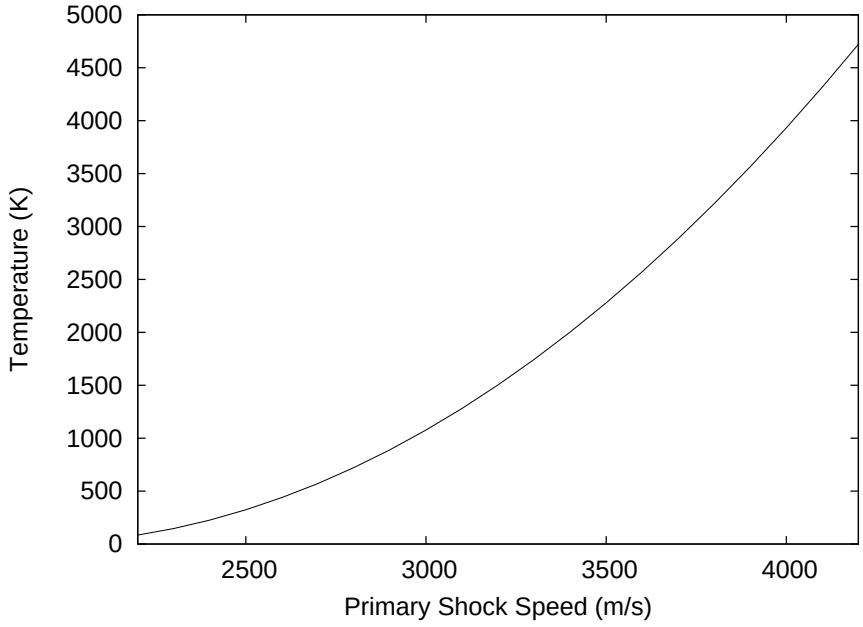

Figure 2.15: Test flow temperature versus primary shock speed for a final flow velocity of 6 km/s based on perfect gas calculations.

decrease in total pressure as the primary shock speed is increased for a fixed final flow speed of 6 km/s. The total pressure on this graph has been normalized by the rupture pressure of 250 MPa.

This analysis illustrates that while a given final shock speed can be generated by a theoretically infinite number of primary shock speeds, there is only one primary shock speed that will result in a particular test flow temperature and velocity. While the free piston driver is capable of generating high sound speeds, Paull [46] discovered that an expansion tube should be operated with a sound speed buffer across the expanded driver gas / compressed test gas interface (*i.e.* across region 3 to 2 in Figure 2.6). This criterion requires that there be at least a 20% increase in sound speed across this interface to reduce the downstream propagation of noise generated in the driver. As a given primary shock speed sets the sound speed in the shock processed test gas (region 2), this also governs what the expanded driver sound speed must be (region 3).

Still working with the aforementioned example of generating a flow of 6 km/s with a

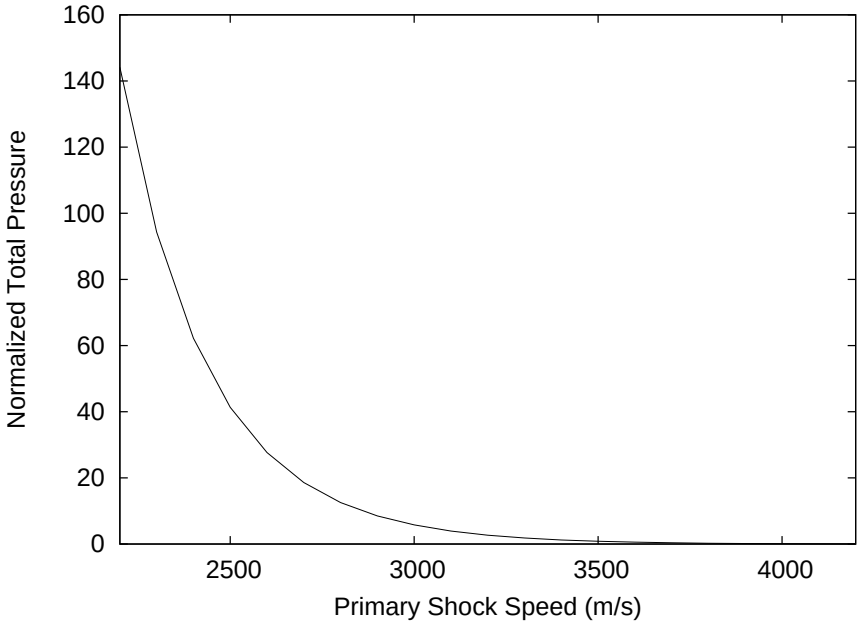

FIGURE 2.16: Test flow total pressure versus primary shock speed for a final flow velocity of 6 km/s based on perfect gas calculations. Total pressure has been normalized by the driver rupture pressure.

static temperature of ∼230 K, it was seen that a primary shock speed of around 2.4 km/s was needed. This shock speed through air at ambient temperature results in a sound speed of the shock processed air test gas, a_2, of around 957 m/s (assuming equilibrium chemistry). The sound speed of the driver gas can now be estimated from the following equation from Morgan [40]

$$a_4 = a_2 \, M_2 \, \frac{f}{F_1} \left[\frac{\gamma_2(\gamma_2 - 1)}{2} + \frac{\gamma_4 - 1}{2} \right]^{\frac{1}{2}}$$

where $F_1 \approx 1$ is a function pertaining to the driver geometry and $f = a_3/a_2 < 0.8$ to avoid noise transmission to the test gas. M_2, the Mach number of the processed test gas, is approximately constant for all operating conditions and can be estimated by Equation 2.3. Applying this perfect gas analysis results in a driver sound speed of around 1130 m/s for targeting a 6 km/s true flight condition. This flow speed represents the approximate upper bounds of what a scramjet would be expected to achieve in atmospheric flight and lower

flight speeds would require lower desired driver sound speeds.

Helium is a commonly used driver gas in free piston drivers because of its high sound speed. Because a sound speed of 1130 m/s corresponds to helium at a temperature of only 368 K it will not be feasible to use helium in a free piston driver when targeting flight conditions in an expansion tube while satisfying Paull's sound speed buffer criteria. The compression process would result in temperatures much higher than this. However, a benefit of the free-piston driver is that any gas, or mixture of gases can be used as the driver gas. In this way a gas mixture can be used that, for a suitable compression ratio for a large free piston driver, gives the desired sound speed at the point of primary diaphragm rupture. The use of a suitable driver gas when targeting high speed atmospheric flight conditions will be examined further in Chapter 5.

2.4.2 Compound-Driver Expansion Tube

As an expansion tube driven with a compound driver has an additional section, there is an extra degree of freedom when targeting a given final shock speed. This adds to the complexity of the overall operation of the expansion tube. Figure 2.17 plots the density of the test gas of a 6 km/s test flow generated in a compound-driver expansion tube versus the shock speed in secondary driver (Shock 1) and the shock speed in shock tube (Shock 2). As for the previous section, these perfect gas calculations have used the RHYFL design conditions of 250 MPa burst pressure of the primary diaphragm and Mach 1 flow at the throat. Again helium at 500 K was the driver gas with air as the both test and accelerator gases at 296 K. This figure shows how the density is strongly dependent on the choice of both shock speeds. Figure 2.18 is a plot of the final test flow temperature and shows that the final test flow temperature is a function only of the speed of the shock in the shock tube (Shock 2). The projection of the temperature curve in Figure 2.18 on to the Shock 2/Temperature plane would result in a trace identical to that obtained for the final test flow temperature for a singe driver expansion tube shown in Figure 2.15.

As the preceding examples of generating a test flow with a velocity of 6 km/s and a temperature of ∼230 K with both a single and a compound driver utilized the same driver

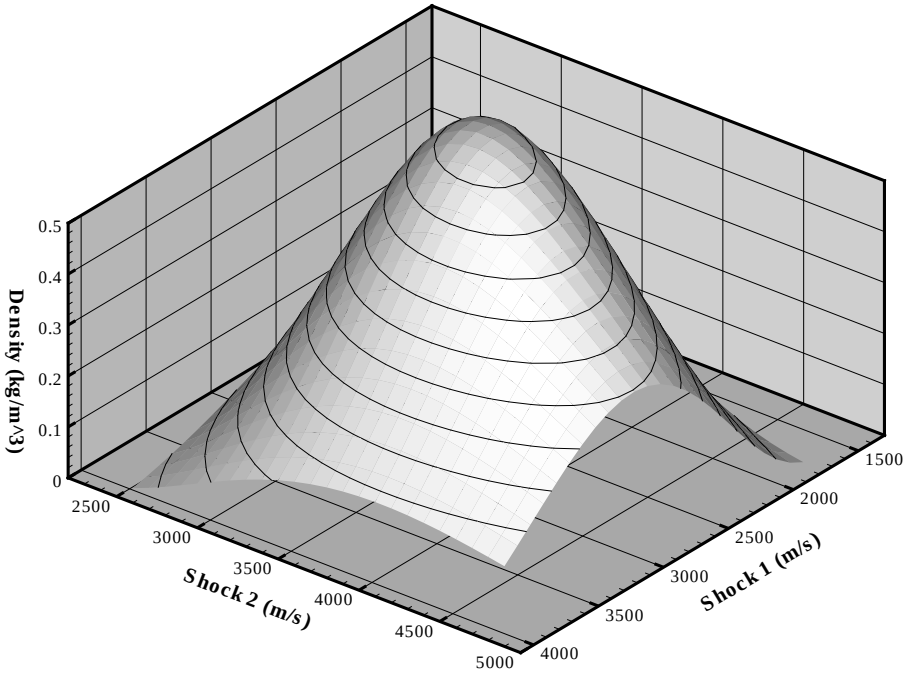

FIGURE 2.17: Test gas density versus shock speed in secondary driver (Shock 1) and shock speed in shock tube (Shock 2) for a final flow speed of 6 km/s based on perfect gas calculations.

conditions, it is worth noting the difference in the density in the final test flow between the two methods. For both driver configurations it was shown that a shock of ∼2.4 km/s in the shock tube was needed to give a test flow static temperature of approximately 230 K. Figure 2.14 indicates that for the driver conditions chosen (Helium at 250 MPa and 500 K), a single driver perfect-gas expansion tube would produce a 6 km/s test flow with a density of $0.052\,kg/m^3$. For a compound driver targetting the same test flow velocity and static temperature, a density of $0.075\,kg/m^3$ would be possible if the secondary driver shock speed (Shock 1) was set to 2.2 km/s while still maintaining the 2.4 km/s shock speed in the shock tube. Figure 2.17 indicates that this combination of shock speeds required to provide the correct test flow temperature at 6 km/s results in a density far from the maximum possible value of almost $0.5\,kg/m^3$. For this example, the compound driver configuration can theoretically generate a 40% higher density test flow for the same test flow speed and temperature

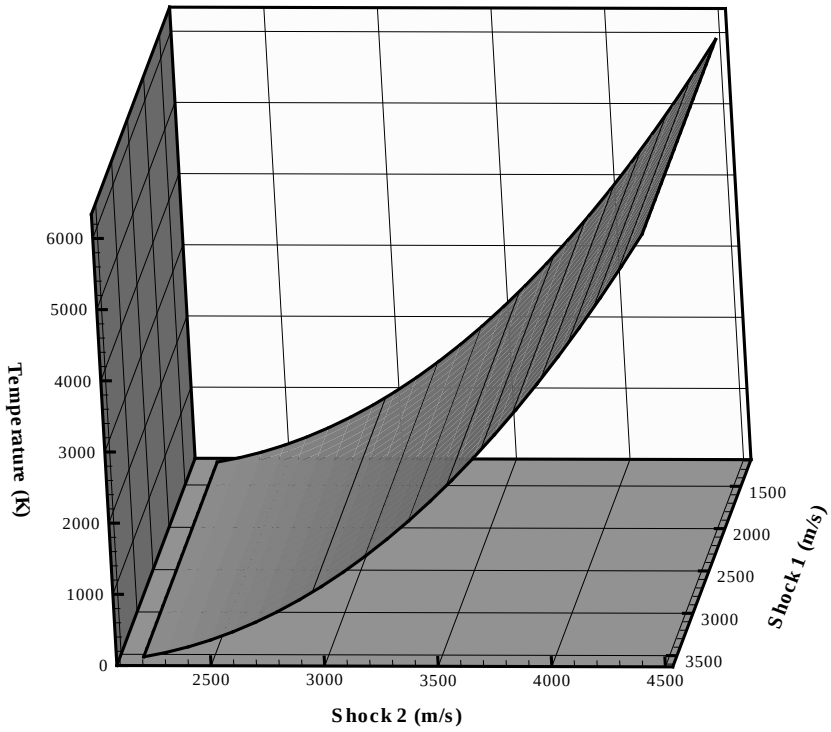

Figure 2.18: Test gas temperature versus shock speed in secondary driver (Shock 1) and shock speed in shock tube (Shock 2) for a final flow speed of 6 km/s based on perfect gas calculations.

when compared to the single driver configuration.

This condition represents the upper enthalpy region of anticipated scramjet testing conditions and has a driver-equivalent flow Mach number of 1.5. Lower enthalpy conditions would have lower driver-equivalent flow Mach numbers meaning that the advantage of the compound driver would diminish at lower testing enthalpies (see Figure 2.11). The minimal advantage in the nose-to-tail pressure ratio gained by using a compound driver at these low driver-equivalent Mach numbers is outweighed by the added complexity of such a configuration and, as stated previously, has resulted in this thesis focusing on the use of a single driver expansion tube for generating scramjet testing conditions.

2.4.3 Test Section Size

Unlike more conventional hypersonic testing facilities such as shock tubes and blow-down tunnels, an expansion tube does not require a nozzle to expand the test gas to the desired conditions. For this reason, the test section of a standard expansion tube is limited to the inside diameter of the tube. As the cost associated with building such a facility increases rapidly with tube diameter, the test section of expansion tubes are typically quite small - ranging from 10's of millimeters in diameter to 182.6 mm for the X3 expansion tube[47].

An opportunity to increase the available testing cross-section in an expansion tube is created through the use of a nozzle placed at the end of the acceleration tube. This nozzle would expand the flow to a larger area, allowing the testing of larger models. When sub-scale models are tested, certain scaling laws are used in an attempt to compensate for the smaller model. One commonly used is the binary scaling parameter which is the product of the density and a characteristic length of the model. As models approach actual size, the measurements and predictions become less reliant on these uncertain scaling parameters. This is beneficial for modelling systems in which there are multiple, interacting processes that scale differently with model size. For scramjet combustion experiments, testing at full, or near full size with duplicated flow composition is required for accurate residence times and combustion phenomena [48]. Increased model size also has benefits associated with instrumentation, force measurement and visualization techniques.

There are a number of possibilities for nozzle shapes, arrangements and positions for use with expansion tubes. Conical nozzles offer a simple means of expanding a flow but result in a diverging flow in the test section. Contoured nozzles, known also as "flow-straightening nozzles", are more involved in their design and are intended to result in a parallel flow after expansion. These nozzle shapes can be implemented as either 'skimmer' type nozzles or full capture nozzles. Skimmer type nozzles have an entrance to the nozzle which has a smaller diameter than the acceleration tube diameter. In this way only the core flow is captured in the nozzle, hence expanding a uniform flow. The full capture nozzle begins at the same diameter on the tube and expands the entire flow, including the boundary layer. There are also a number of possibilities in regard to where the nozzle is positioned in an expansion

tube arrangement [49]. In the current work, the use of a full capture nozzle is investigated at the end of the acceleration tube segment of an expansion tube (Figure 2.19).

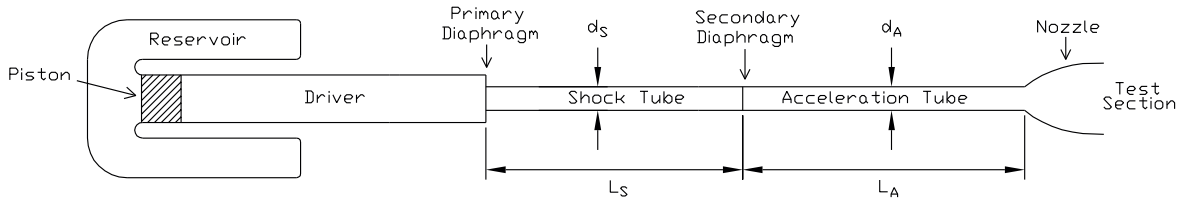

Figure 2.19: Schematic diagram of the proposed RHYFL-X expansion tube with a contoured nozzle placed at the end of the acceleration tube.

A nozzle placed at the end of an expansion tube would have hypersonic conditions at the entrance to the nozzle. This type of hypersonic nozzle differs from a more conventional wind-tunnel nozzle that expands a stagnated supply region of gas to the desired conditions. Because of the short test times inherent with expansion tubes it is imperative that the characteristics of the starting process of such a nozzle are understood. Chapter 6 presents an investigation into the design of a hypersonic nozzle placed at the end of the acceleration tube section of an expansion tube to expand the flow and increase the test section size.

2.5 Summary

This chapter has outlined the operating principles of various hypersonic ground-based testing facilities. It has shown that while continuous hypersonic blowdown wind tunnels offer a convenient means of testing large models at hypersonic Mach numbers, they fundamentally lack the ability to generate the high energies needed for simulation of hypersonic atmospheric flight. To generate higher energies, pulse facilities have been developed, with the most common of these being the free piston driven reflected shock tunnel. These facilities offer a relatively cheap, quick and reliable means by which hypersonic flow speeds corresponding to the low enthalpy end of the predicted scramjet flight trajectory can be generated but are fundamentally limited by the fact that the test flow is stagnated prior to expansion. When

aiming at higher flight speeds, test flows produced by reflected shock tubes inherently suffer from substantial dissociation and a deficiency in total pressure when compared to atmospheric flight at the same velocity. These deficiencies would result in measured performance parameters in the laboratory that differ from those that would be experienced during flight. To enable accurate simulation of the flight characteristic of a scramjet powered vehicle, a different method of flow generation is required that can produce true flight conditions.

It was shown that ideal operation of an expansion tube avoids the stagnation of the energized test flow and therefore provides a theoretical opportunity to produce dissociation-free test conditions which represent those that would be experienced by a scramjet over its entire flight envelope. The full potential of a free-piston driven expansion tube has never been realized due to the large cost associated with the construction of a large high-performance free-piston driver. The utilization of a large free-piston driver built as part of the RHYFL project offers an ideal opportunity to construct such a facility. This chapter has outlined the major operational principles and characteristics of a free-piston driven expansion tube. The superior flow generation capabilities of the expansion tube has associated disadvantages when compared to other testing facilities. There are valid concerns regarding the establishment of the flow over the test article in the short test times associated with expansion tube flow and the small test section area inherent with standard expansion tubes also limits the size of the models that can be tested.

The next chapter presents the numerical models, techniques and assumptions used to simulate expansion tube flow and ultimately predict the performance capability of the proposed RHYFL-X facility. These simulation techniques are validated and verified by simulating the X2 expansion tube located at the University of Queensland.

Chapter 3

Expansion Tube Modelling

3.1 Introduction

The primary motivation for this chapter is to investigate and validate the numerical modelling techniques that will be used to predict the performance capabilities of the RHYFL-X expansion tube. Adequately modelling the flow characteristics inside a hypervelocity pulse facility is a challenging task as the flow can be influenced by strong shocks, high temperature effects, chemical kinetics, gas interfaces and viscous interactions [50]. The length scales associated with some of these various flow phenomena are around five to six orders of magnitude smaller than that of the length of the facility. This means that while the proposed facility is of the order of 80 m in length, the grid resolution must be sufficiently fine to resolve the small scale physics. Validation simulations were performed of the currently-operational free-piston expansion tube, X2, located at the University of Queensland. Accurate reproduction and prediction of the flow within this expansion tube instills confidence in the predictions made for the proposed RHYFL-X facility.

3.2 Modelling Tools & Techniques

3.2.1 Previous

Axisymmetric Navier-Stokes codes have been utilised in the past to model the unsteady flow processes which occur throughout expansion tube operation. Jacobs [51] used an axisymmetric modelling technique in an attempt to identify some of the basic mechanisms responsible for the noisy test flow seen in certain experiments in NASA Langley's HYPULSE facility. This facility does not have the significant added complexity of a free-piston driver. The simulations took up to 50 hrs of CPU time on a single processor of a Cray-YMP supercomputer and achieved reasonable agreement with results from established experimental conditions. Axisymmetric simulations were also performed by Wilson etal [52] of the HYPULSE facility, incorporating finite-rate chemistry. Utilising the experimentally obtained primary shock speed, only a section of the shock tube was incorporated in Wilson's simulations. The simulations still required 70 hrs of CPU time on a Cray C90 and did not achieve a grid-independent solution. So, while it could be argued that the full axisymmetric approach may be justified when investigating certain flow characteristics of established experimental conditions in smaller facilities, the magnitude of computational expense deems this method inappropriate for determining the performance envelope of a proposed large-scale facility.

Because of the computational expense of axisymmetric simulations, one-dimensional flow simulation techniques have also been employed to model expansion tube flow. Wilson [50] used a one-dimensional Eulerian code to model the flow in the HYPULSE facility. In this simulation the driver temperature was determined by choosing a temperature which gave a simulated primary shock speed equal to that found experimentally. The simulated static pressures in the test flow were 40% higher than that measured in the expansion tube, indicating a significantly higher simulated final shock speed than that found from experiment. More recently, Sasoh etal [53] used a one-dimensional simulation technique to predict the flow conditions in the JX-1 expansion tube [1] and incorporated the free-piston compression of the driver gas. Due to the complex, multi-dimensional flow phenomena associated with

[1] The JX-1 expansion tube is located at the Shock Wave Research Centre, Tohoku University.

expansion tube flow, these numerical results struggled to attain even qualitative agreement with experimental results.

3.2.2 Current

A method by which shock tubes and expansion tubes have been modelled in the past is to begin by obtaining the primary shock speed from experimental results and then compute the post-shock test gas conditions. These conditions are then used as an input flow condition for the axisymmetric simulation of the acceleration tube section. This technique has two major disadvantages in relation to the current work. Firstly, it is not predictive as it is using the experimentally obtained primary shock speed to calculate inflow conditions to the acceleration tube. To enable reliable performance predictions of a proposed facility, the entire expansion tube needs to be adequately modelled. Secondly, expansion tube test flows can be significantly altered by $u + a$ disturbance waves that originate upstream, and subsequently propagate downstream into the test gas. The major $u + a$ waves that can disrupt the test flow have two primary sources: one is when the expansion fan in the driver gas caused by the rupture of the primary diaphragm reflects off the head of the piston, the other is the interaction of the driver gas/test gas (D/T) interface and the trailing edge of the unsteady expansion fan, which ultimately terminates the test time. By using the post-shock conditions as a steady inflow boundary condition to the acceleration tube, any disturbances originating upstream of the secondary diaphragm would not be captured. This may not be crucial in facilities that are not heavily influenced by driver attenuation. However, in free-piston facilities such as the X2 expansion tube where a small driver length at primary diaphragm rupture is believed to have a significant effect on the final flow properties, all upstream influences must be captured for accurate reproduction of the final flow properties.

In order to be able to capture these disturbance waves that alter the test flow in an axisymmetric simulation of the acceleration tube, a special boundary condition was incorporated into the Multi-Block Compressible Navier-Stokes solver *MB-CNS* [54–56] where a time-varying input can be used as the inflow. In this way, the flow in the low speed, high

density portion of the expansion tube (*i.e.* the driver and shock tube where the multidimensional effects are assumed to have an insignificant effect on the flow) can be modelled one-dimensionally with the flow history being recorded at the secondary diaphragm. This flow history at the secondary diaphragm can then be used as an inflow file for the axisymmetric simulation, thus capturing any disturbances originating upstream that propagate downstream into the test flow. This combination of one-dimensional and axisymmetric simulations to model the expansion tube process will be referred to as *hybrid* simulations.

3.3 X2 Two-Stage Piston Compression Process

The X2 expansion tube utilizes a two-stage compression process with a compound piston to compress the driver gas to rupture conditions [57]. This driver configuration reduces the overall length of the compression tube when compared to a more conventional free-piston driver. The compound piston arrangement consists of a lighter carrier piston and a heavier inner piston. The light outer piston, driven by a high pressure reservoir, carries the inner heavier piston for the first stage of the compression process. After a certain distance the outer piston hits a buffer and is stopped, allowing the inner piston to continue down the second stage compressing the driver gas to rupture conditions. Figure 3.1 illustrates the X2 driver assembly and shows the different stages of the compression process. The piston movement and flow processes that occur from (ii) to (iii) in Figure 3.1 will be referred to as the transition process.

The two-stage compression process has been modeled previously by Doolan [5] by considering the two different stages of compression separately in a simplified one-dimensional simulation using *L1D*. The technique neglected the more complicated flow processes that occur during the transition process. While the simulated pressure was in relatively good agreement with experimental pressure traces, the simulation noticeably over-predicted the temperature of the final driver-gas slug by around 50%. This indicated that there may be significant heat losses occurring in the transition process that could be responsible for the discrepancy between experiment and simulation. With the aim of achieving an improved,

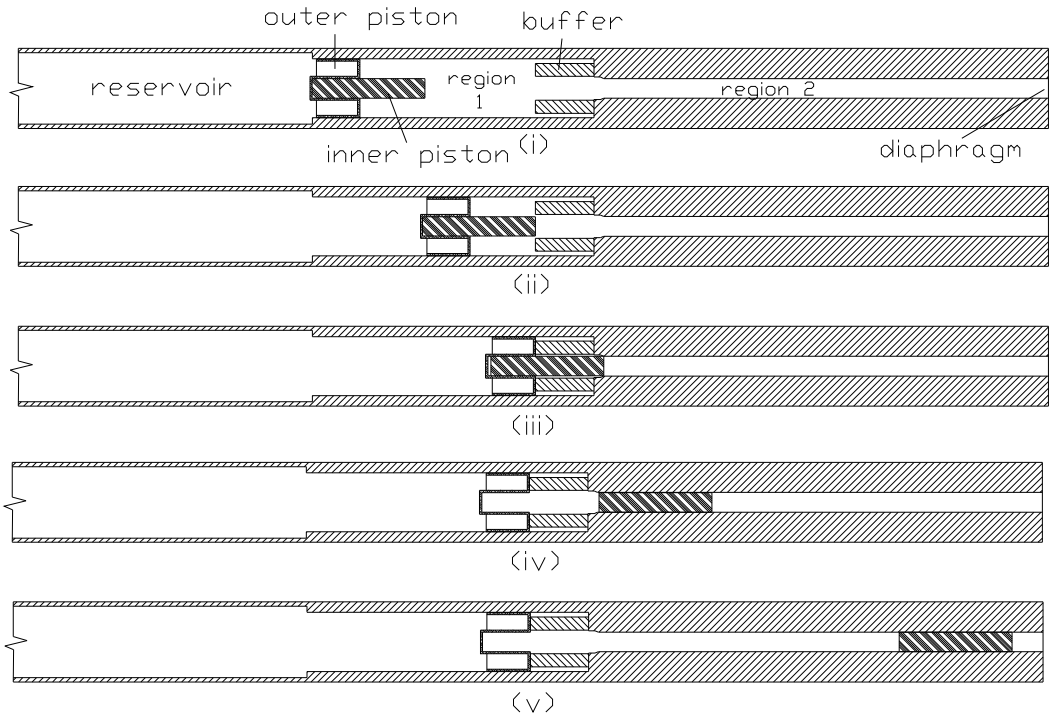

Figure 3.1: Schematic diagram of the X2 driver assembly with the piston at different stages of the compression process.

reliable simulation technique of the X2 compression process, a quasi-steady-state perfect-gas flow simulation program, *X2_transition.c*, was written by the author to model the flow processes and heat transfer that occur during this complex transition process. As the X2 facility was constructed to validate principals and designs that were to be used for a much larger expansion tube, X3, the simulation technique developed for X2 could also be utilized in evaluation of this larger facility.

For small displacements of the piston, the X2_transition.c program calculates the resultant gas properties both around the protruding inner piston and in the region ahead of the inner piston (Figure 3.1(ii)). The mass flow rate and flow velocity between the two regions can then be calculated, allowing the estimation of the heat transfer rate to the inner piston and buffer material using Newton's law of cooling [58]:

$$q = hA(T_w - T_\infty) \tag{3.1}$$

where the heat transfer rate, q, is related to the temperature difference between the wall (T_w) and the gas (T_∞)), the area (A) and the heat transfer coefficient (h). The heat transfer coefficient was estimated using flat plate empirical relations from Holman [58]:

$$h_{laminar} = 0.332 \, \frac{\rho \, C_p \, u}{P_r^{2/3} \, Re^{1/2}} \tag{3.2}$$

$$h_{turbulent} = \frac{k \, P_r^{1/3}}{x} \, \left[0.037 \, Re^{0.8} - 871 \right] \tag{3.3}$$

where P_r and Re are the Prandtl and Reynolds number respectively. The transition Reynolds number (with respect to the distance x that the inner piston has travelled inside the buffer) is taken to be 5×10^5. This program was used to simulate the amount of driver gas that passes through the small gap between the piston and the buffer during the transition process and to estimate the heat transfer to both the buffer and piston during this process. The Transition.c program is included in Appendix D.

3.3.1 Previous Blanked-off Driver Tests

Doolan performed 'blanked-off' tests of the X2 driver where a thick primary diaphragm was installed so that the driver gas obtains its maximum possible pressure without rupturing the diaphragm. The compression ratios were measured and, combined with the peak pressure and the initial conditions, allowed the calculation of driver gas bulk temperature [5] for each condition. These temperatures agreed well with temperatures based on the primary shock speeds of tests done with the rupture of the primary diaphragm. Table 3.1 outlines the initial conditions for 3 of the driver tests performed and Table 3.2 presents the results obtained from the experiments and the current simulations incorporating the X2_transition.c program.

A simplified geometry of the X2 compression process is solved using *L1D* up to where the transition process begins. The averaged flow properties of the driver gas at this stage are

Table 3.1: Description of driver conditions used in the blanked-off driver tests. See Ref [5] for details on the experimental data.

	Driver Gas	Reservoir Fill (MPa)	Driver Fill (kPa)
Condition A	Helium	1.3	50
Condition B	Helium	1.3	45
Condition C	Helium	1.4	40

Table 3.2: Comparison of experimental and current simulation (Sim) results for the blanked-off driver tests.

	Peak Pressure (MPa)		Final Temperature (K)			Final Slug Length (mm)	
	Expt	Sim	Expt	Isent[a]	Sim[b]	Expt	Sim
Condition A	24.0	22.1	2003	3512	2404	138	177
Condition B	25.8	25.9	2065	3777	2663	118	150
Condition C	39.1	38.1	2245	4671	3227	83	111

[a]Based on the pressure ratio
[b]Average across final compressed gas slug

then used in X2_transition.c to calculate the average flow properties after the piston transition (the start of the second stage of compression). These values are then placed back into *L1D* to solve the rest of the compression. The peak pressures obtained from the simulations for these conditions show good agreement with those from Doolan's experiments. The final temperatures however are still noticeably over-estimated. The differences in these temperatures are seen to increase as the compression ratio increases. For Condition A, the simulated temperature is 20% higher than that calculated based on the bulk temperature method and the Condition C temperature is around 45% over-estimated. The under-estimation of the final pressure in Conditions A and C also means that these temperature discrepancies would be increased if the compression ratios were matched. This is suggesting that there are still substantial losses that are occurring during the compression cycle that are not being captured by the simulations. The final gas slug lengths are also consistently over-estimated by approximately 30%. This consistent over-estimation of the length of the compressed driver gas can be attributed to a number of causes: one being the difference between the simulated

and experimental peak pressures. When the simulated peak pressure is lower than that measured during experiment, the simulated length of the compressed gas will be longer. While being responsible for maybe 4 or 5% of the discrepancy depending on the condition, this does not account for the relatively large difference (around 25 to 30%) between the two sets of values. Another contributing fact could be gas leakage past the seals of the piston. As the simulations do not account for any gas leakage around the piston, any leakage that does occur during operation would result in a shorter final slug length that is not captured numerically. The final slug length discrepancies can also be attributed to the modelling of the transition process. If more gas is allowed to flow into the second stage during the modelling of the transition process than actually happens in practice, a longer final compressed slug of gas would result. This would also be responsible for the under-estimation of the peak pressure in Conditions A and C.

These results illustrate that the complex two-stage compression process utilized on the X2 free piston expansion tube generates temperatures that appear to be noticeably lower than achieved using numerical techniques. These differences in the driver gas temperature at the point of primary diaphragm rupture would alter simulation results when compared to experimental results even if the simulations exactly modelled the flow processes during the rest of the expansion tube cycle. If the capabilities of a proposed facility was dependent on the maximum temperature that could be generated by the driver, the accurate modelling of the compression process would be required to allow an accurate prediction of the flow-generation capabilities. However, when targeting test flows with sub-orbital velocities and atmospheric static properties, it has already been shown that the proposed RHYFL-X expansion tube would require driver sound speeds at rupture well below those capable of even modest free piston drivers. With such a large driver margin available, it is not necessary to obtain accurate simulations of the free-piston compression process for the RHYFL-X facility. In practice it would be a matter of tuning driver parameters such that the required sound-speed was achieved. For this reason, the simulations of the X2 expansion tube presented in this thesis will not include the compression process. Rather, they will start from the moment of primary diaphragm rupture. The driver temperature in the simulations will be set such

that the resulting primary shock speed equals that measured in experiment.

The first X2 condition simulated in Section 3.4 was performed by Palmer [59] when the facility was recently commissioned (1999). It used similar driver conditions as the experiments performed by Doolan. Therefore the length of the final compressed driver gas slug length can be calculated using

$$\frac{P_f}{P_i} = \lambda^\gamma$$

for slight variations in driver compression ratio (where λ is the volumetric compression ratio). The rest of the X2 conditions simulated however have been conducted more recently, after modification of the X2 piston, and hence require new driver experiments to determine the compressed driver length.

3.3.2 Piston Modification

During the transition stage of the compression process, the driver gas in region 1 is forced through the relatively small gap between the inner piston and the buffer into region 2. As well as the losses incurred during this process, it also restricts the amount of gas which is transfered to region 2. By limiting the amount of gas in region 2, the final slug length at the point of rupture is also limited. By reducing the length that the inner piston protrudes from the outer piston, the heat losses during this transition could be minimized as well as allowing more gas to flow into region 2 for the second stage of compression. This would theoretically increase the length of the driver gas at the point of primary diaphragm rupture and also slightly increase the temperature at this point.

The limiting distance that the piston could move back in the outer carrier piston was such that it would not interfere with the opening characteristics of the diaphragm which initially separates the reservoir from the driver tube. The outer piston was modified so that the inner piston sat an additional 166 mm further back in the outer piston, reducing the amount protruding out the front of the outer piston from 306 mm to 140 mm. Figure 3.2 illustrates the modification made to the piston arrangement in an attempt to increase the length of driver gas at rupture and to reduce the amount of heat-transfer occurring during

the transition process. A new series of driver tests were performed to determine the final driver gas slug length for both the standard and modified pistons.

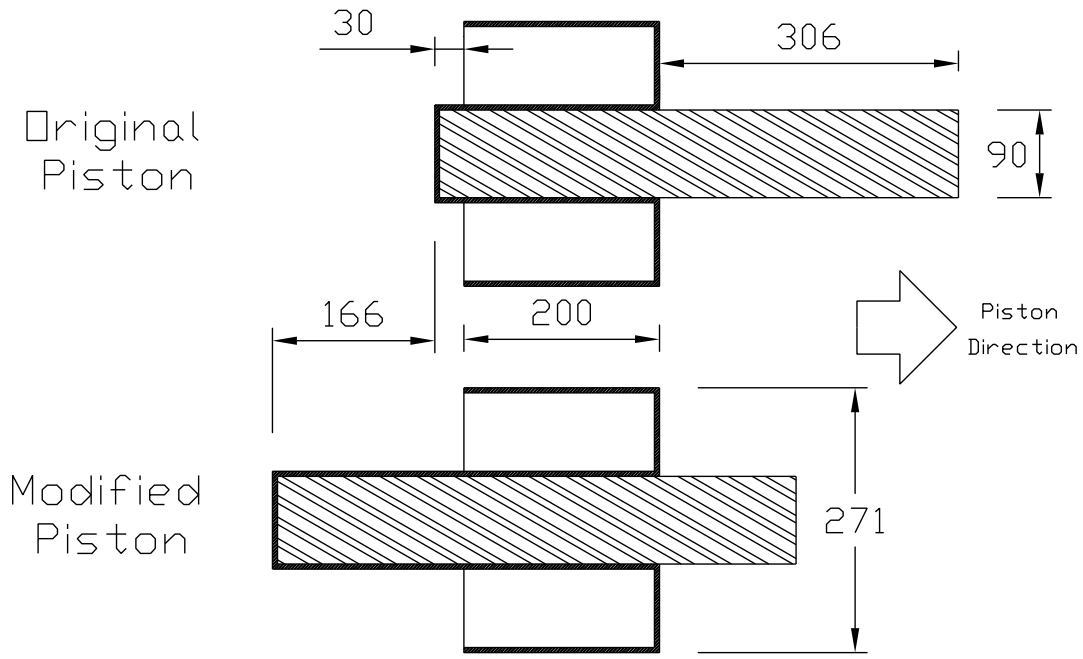

FIGURE 3.2: Schematic diagram of the original and modified compound piston for the X2 expansion tube. Dimensions are in millimetres

3.3.3 Current X2 Driver Experiments

If the slug of driver gas at the instant of primary diaphragm rupture is of insufficient length attenuation of the shocks will be experienced. If the slug length in the experiment is sufficiently long such that this does not occur, the precise length of the driver is not required in the simulations. As is shown later, the flow in the X2 facility is affected by disturbances caused by the insufficient length of driver gas at diaphragm rupture. Hence, the length of the driver gas slug at the point of diaphragm rupture must be known to enable accurate simulations of the facility. New blanked-off driver tests were performed to determine the length of compressed gas at rupture for both the original and modified piston designs.

The tests involved using a 4 mm-thick steel primary diaphragm that would not burst during the shot. In this way, when fired, the piston would compress the gas until it stopped, then travel backwards slightly before being stopped by the brakes. To measure the closest distance that the piston gets to the diaphragm during compression, lengths of ∼2 mm thick solder were inserted into the nylon buffer which is positioned just in front of the primary diaphragm. (This nylon buffer is to prevent the piston slamming into the diaphragm station when it is unintentionally driven too hard.) The solder would plastically deform allowing the measurement of how far the piston stops in front of the diaphragm and hence the length of driver gas at the point of rupture. Out of the five tests that were performed, three were for the standard piston used in X2 Conditions 1 and 2 (Section 3.4) and the other two tests were with the new modified piston which was used in Conditions 3 and 4. All tests used air in the reservoir and helium in the driver tube. Table 3.3 lists the initial condition for these tests.

Table 3.3: Description of driver conditions used in the current blanked-off driver tests.

	Piston	Reservoir Fill MPa	Driver Fill kPa
Driver Test 1	standard	1.6	57.5
Driver Test 2	standard	1.6	52.4
Driver Test 3	standard	1.6	52.4
Driver Test 4	modified	1.6	52.4
Driver Test 5	modified	n/a	52.4

Table 3.4: Results of current blanked-off driver tests.

	Max Pressure (MPa)	Pressure ratio (P_{max}/P_{fill})	Final Distance (mm)
Driver Test 1	31.1	541	105
Driver Test 2	38.1	727	88
Driver Test 3	38.0	725	89
Driver Test 4	34.0	649	103
Driver Test 5	29.4	561	110

The results from Driver Tests 1 to 3 show that the length of compressed driver gas at

the point of primary diaphragm rupture is around 13-16% less than that obtained for the modified piston for a given compression ratio. The modified piston (Driver Tests 4 and 5) had the effect of allowing more gas to flow into the region 2 (Figure 3.1 (i)) during the transition period due to the reduced protrusion length of the inner piston. This increase of mass in the second stage of compression resulted in an increase in length of the final compressed driver gas slug by approximately 5%. The smaller effective compression ratio of the modified piston meant that the piston needed to be driven harder initially to reach the same final pressure. This meant higher speeds at the point of impact with the buffer and plastic deformation of the outer piston resulted. The outer piston needed to be re-machined after every several shots when using the modified piston.

The simulations of the X2 facility incorporate the final driver slug lengths obtained from these experiments and use perfect-gas isentropic relations for small differences in the compression ratios. The remainder of this chapter examines the validity of using this modelling technique for simulating expansion tube flows by modelling various operating conditions of the X2 expansion tube.

3.4 Hybrid Simulations of the X2 Expansion tube

3.4.1 Condition 1

The first X2 condition modelled was a 7.2 km/s equivalent flight speed condition [2]. The operating conditions for this shot are outlined in Table 3.5. This particular condition is one that was used by Palmer when the facility was quite new. All stated conditions for this shot including primary and secondary shock speeds and static and Pitot pressures were obtained from Palmer's work [59]. Only 200μs were available for this condition for both the static and Pitot pressure traces at the end of the acceleration tube. Neely and Morgan [43] stated that equilibrium calculations more accurately modelled the unsteady expansion process in an expansion tube, so all simulations initially assume equilibrium chemistry. The equilibrium calculations for both the one-dimensional and axisymmetric simulations use curve-fits for

[2] The shot number was not available for this condition

Table 3.5: Initial conditions for X2 Condition 1.

Reservoir Fill (air)	1.55 MPa
Driver Fill (helium)	48 kPa
Shock Tube Fill, p_1 (air)	7.5 kPa
Accelerator Tube Fill, p_5 (air)	46.6 Pa
Primary Diaphragm Rupture Pressure, p_4	24 MPa
Secondary Diaphragm Rupture Pressure	∼45 kPa
Primary Shock Speed (expt)	3.8 km/s
Secondary Shock Speed (expt)	6.4 km/s

the equilbirum gas properties rather than solving the actual chemical reactions. The effects of non-equilibrium chemistry in expansion tube flow are investigated in Chapter 4.

The temperature of the helium driver gas at the instant of primary diaphragm rupture is determined by matching the primary shock speed with that measured from experimental pressure traces taken at known locations along the shock tube. The stated primary shock speed for this condition near the end of the shock tube was 3.8 km/s. A temperature of 2100 K at rupture gave a shock speed of 3.8 km/s using the one-dimensional code, *L1D*.

The length of the driver gas slug at rupture was determined using results obtained from driver-tests performed by Doolan. These driver-tests and the expansion tube experiments were performed when the facility was first commissioned. The driver length used for this condition was 125 mm. The experiments for all other operating conditions that are modelled in this section have been performed more recently. As there has been a noticeable difference in the operation of the X2 facility over this period of time, the compressed driver lengths for the other operating conditions were determined from the new blanked-off driver tests.

Driver Attenuation

The ideal operation of an expansion tube is based on the fact that the driver is of sufficient length such that the $u + a$ wave created by the interaction of the expansion waves and the head of the piston does not catch up to the shock processed test gas. Figure 3.3 indicates the insufficient length of the driver at rupture for this condition. The expansion wave that travels back up into the driver gas upon rupture of the primary diaphragm, reflects off the

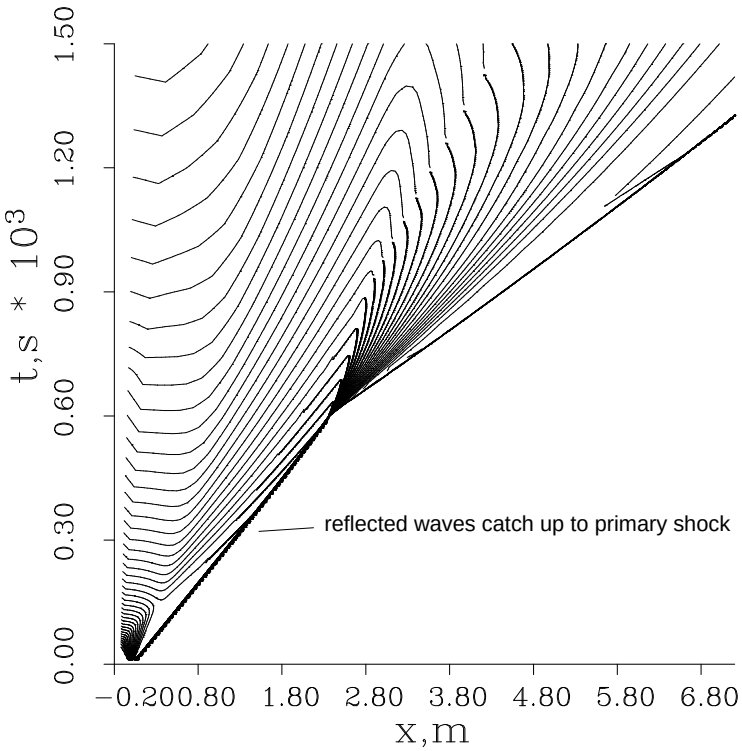

FIGURE 3.3: An xt-diagram produced from viscous *L1D* simulation results of the X2 expansion tube for Condition 1. Contours are of pressure on a logarithmic scale.

piston and then travels forward as a $u + a$ wave. These disturbance waves catch up to the primary shock approximately half way down the shock tube and lead to attenuation of the primary shock.

Figure 3.4 shows the effect that this insufficient driver length has on the test gas pressure. At 200μs (S1 in Figures 3.4 and 3.5), a steady region of shock-processed test gas can be seen behind the shock. The interface between the test gas and expanded driver gas can be identified by the small glitch in the trace. 150μs later however (S2 in Figures 3.4 and 3.5), the reflected waves have caught up to the shock and there is now no steady test gas behind the shock. This is associated with attenuation of the shock speed, and after another 150μs (S3) this reduced shock speed is evident by the lower post-shock static pressure level. This 12-13% reduction in static pressure indicates a 7-8% attenuation in shock speed. Figure 3.5 is an xt-diagram for just the shock tube segment of Figure 3.3 and indicates the times at

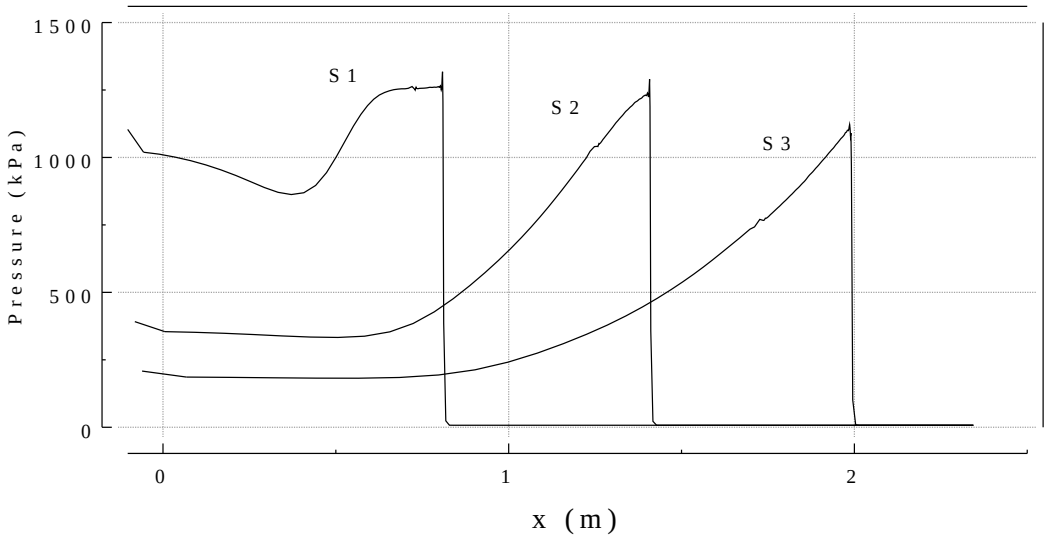

Figure 3.4: Plots of pressure along the shock tube at t=200μs (S1), t=350μs (S2) and t=500μs (S3).

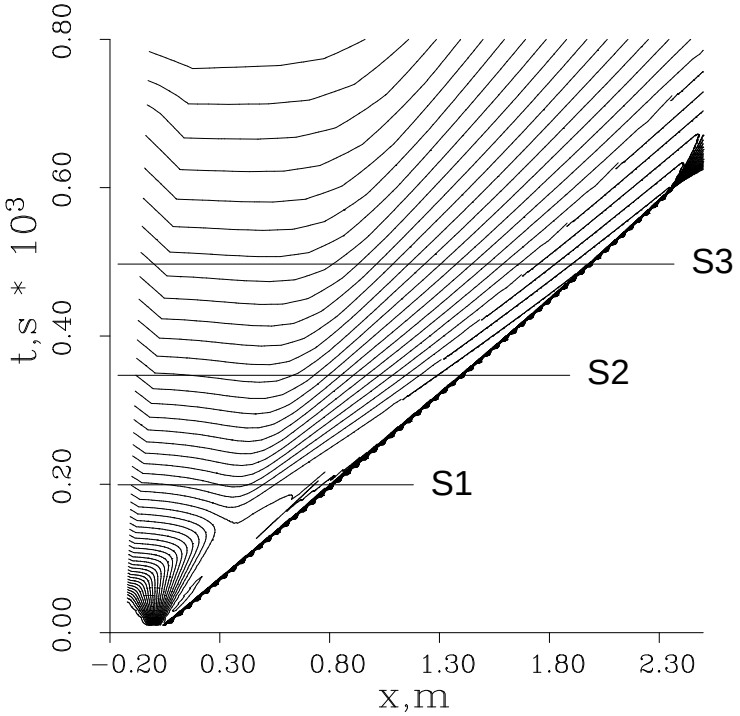

Figure 3.5: An x-t diagram of the X2 shock tube produced from *L1D* simulation results of Condition 1.

which the traces for Figure 3.4 were obtained.

Sound Speed Buffer

As mentioned previously, there is a criterion by Paull [46] stating that there should be a sound speed increase across the interface between the expanded driver gas and the shock processed test gas to minimize the propagation of noise into the test flow. *L1D* was used to estimate the driver-gas rupture temperature by matching the primary shock speed with that measured from experimental results. When the same initial conditions were used in an axisymmetric simulation using *MB-CNS*, the initial shock speed was the same, but was 5% faster than the *L1D* result by the end of the acceleration tube. Both the one-dimensional and axisymmetric simulations assumed ideal behaviour of the primary diaphragm.

The sound speed history was recorded at 3 locations, x=0.194 m, x=0.875 m and x=1.875 m, along the shock tube in both the one-dimensional and axisymmetric simulations. Figure 3.6 is a plot of these traces and shows the very good agreement between the two simulations techniques. The later arrival of the shock at x=1.875 m is indicative of the slightly slower

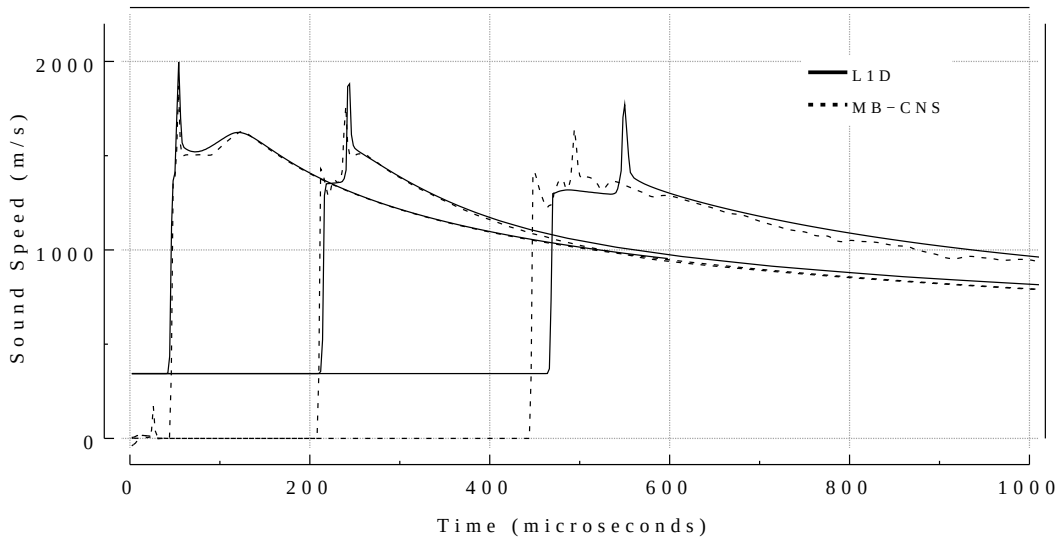

FIGURE 3.6: Sound speed histories recorded at x=0.194 m, x=0.875 m and x=1.875 m along the shock tube for both the viscous one-dimensional (*L1D*) and viscous axisymmetric (*MB-CNS*) simulations. The zero values for the *MB-CNS* results prior to shock arrival are due to the way data is recorded by this program.

shock speed obtained in the one-dimensional simulation. Although the one-dimensional analysis can not resolve the more complex flow behaviour there is excellent agreement between the shape and characteristics of the traces. Though difficult to see on the first set of traces due to the time scale used to fit all traces on the same graph, there is a small region of shock processed test gas, then a spike, followed by the expanded driver gas. This is more apparent on the second and third sets of traces where there is larger region of shock-processed test gas. The spike in the sound speed occurs in the expanded driver gas immediately after the interface in both simulations. Initially this was thought to be due to the conduction of heat from the hot shock-processed test gas into the cool expanded driver gas. A small increase in temperature of the helium driver gas would result in a noticeable increase in sound speed due to the large values of gamma and R for helium. However, this spike appears to be a numerical artifact rather than a physical phenomenon. The spike is only one cell thick and it does not increase in magnitude with time as one would expect if it was conduction of energy from the hot test gas. Rather, it stays the same width (in cell count) and slightly decreases in magnitude. The severe discontinuity of gas properties at the primary diaphragm location at the point of rupture causes difficulties in calculating the properties of the cells directly adjacent to the diaphragm location. This is discussed further in Chapter 5. Irrespective of this spike, it is still evident that the sound speed of the shock processed test gas is below that of the expanded driver gas, therefore contravening Paull's requirements for minimizing noise.

Hybrid Simulations of X2 Condition 1

As mentioned previously, a combination of one-dimensional and axisymmetric flow simulation techniques were used to model the flow within the expansion tube. The one-dimensional code used was *L1D* which is a Lagrangian code utilizing a control-mass approach. This means that the mesh elements move along with the flow as opposed to control-volume codes where the mesh is fixed. The geometry consisted of a 0.125 m helium driver gas slug linked to a 2.35 m slug of air test gas in the shock tube. The air test gas and accelerator gas were assumed to remain in chemical equilibrium with properties obtained from the CEA program [60]. Though a one-dimensional code, the tube diameter of 85 mm still needs to be

specified so that correct shear-stress and heat-flux values are computed. The viscous effects are modeled using a friction factor which is computed as a function of the local Reynolds number assuming fully-developed pipe-flow. The driver gas was divided into 30 cells that were clustered towards the diaphragm. This clustering was to try and minimise the size of the expanded cells. The test gas slug consisted of 300 cells spread over the length of the shock tube. The simulation was solved and the history of gas properties at the end of the shock tube were recorded. This history file was then used as a time-varying inflow boundary condition to the axisymmetric code, *MB-CNS*.

For the axisymmetric simulation, an acceleration tube equal to the dimensions of the X2 acceleration tube section (5.1 m in length and a radius of 42.5 mm) was used. Laminar boundary layers were assumed for this, and all simulations relating to the X2 expansion tube. The acceleration tube was split up into four equal length sections so that it could be solved in parallel using 4 of the 64 R14000 600 MHz CPU's which make up the University of Queensland's SGI Origin 3000 supercomputer. Initially a grid of 300x14 cells was used in each 1.275 m segment giving a total of 16800 cells. This was then doubled in each direction to have a grid of 600x28 cells in each section (67200 in total). For the 300x14 mesh the shock velocity started at 6775 m/s and attenuated by around 5% to 6408 m/s. This is in very good agreement with the experimentally determined shock speed of 6.4 km/s. This simulation required around 7.3 hrs of CPU time on the Origin 3000 facility to solve to a simulation time of 1.5 ms. When the mesh was doubled, the simulation time increased to almost 54 hours but the shock speed decreased by less than 1%. This insignificant change in shock speed is evident in Figure 3.7 which shows very little difference in the pressure levels measured on the wall near the end of the tube.

Figure 3.8 shows the Pitot pressure traces obtained from simulations with the two different levels of mesh refinement. These show slightly more variation between the two simulations (up to 5% at the peaks). The mesh could be doubled again in both directions in order to try and establish a totally grid independent solution. This would result in a simulation however that would take the order of 600-700 hours of CPU time. These simulation times may be justified when attempting to rigorously describe the flow in an established condition in a

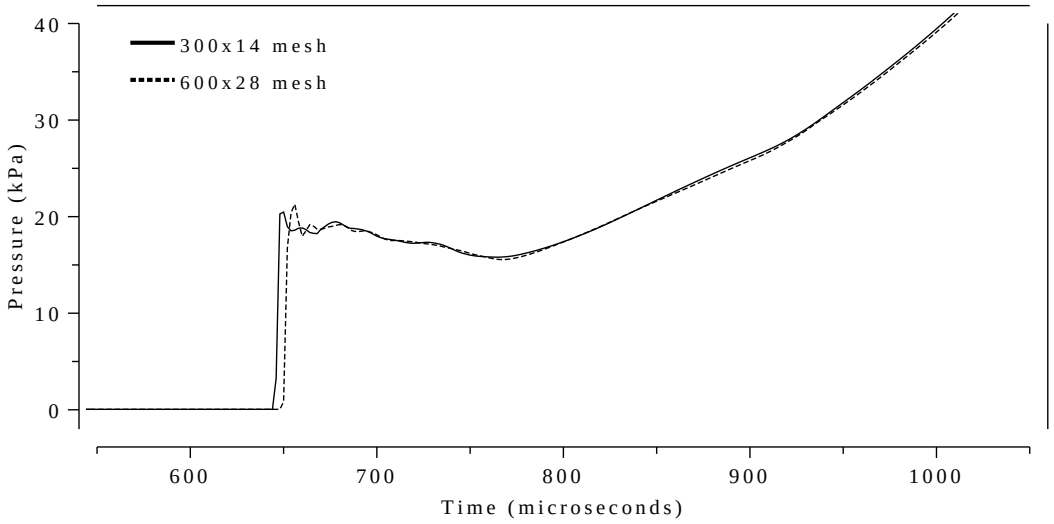

Figure 3.7: Static pressure histories from the viscous axisymmetric simulations of the acceleration tube for X2 Condition 1. Comparison between the two mesh densities: 300x14 cells and 600x28 cells.

smaller facility the size of X2, but the aim of this work is to verify the use of a simulation technique that can be used to determine the performance envelope of large facilities with cross-sectional areas 10 times that of the X2 facility. Because of this, a mesh as coarse as possible is desired that still gives sufficiently accurate results.

The small time steps associated with these simulations are due to the small cells in the boundary layer against the wall. For the 300x14 cell simulation, the time steps were around 3.1e-8 seconds (31 nanoseconds). When the amount of cells were doubled for the 600x28 cell simulation, the time steps were approximately halved to 13.5 nanoseconds. To avoid the small time steps in the boundary layer, the amount of radial cells was set at 14 and 600 cells were retained in the axial direction per block. This resulted in a simulation time that was reduced by a factor of 3.6 to around 15 hrs when compared to the 600x28 cell simulation. The shock velocity changed by a fraction of a percent, and Figures 3.9 and 3.10 show the small differences in static and Pitot pressure.

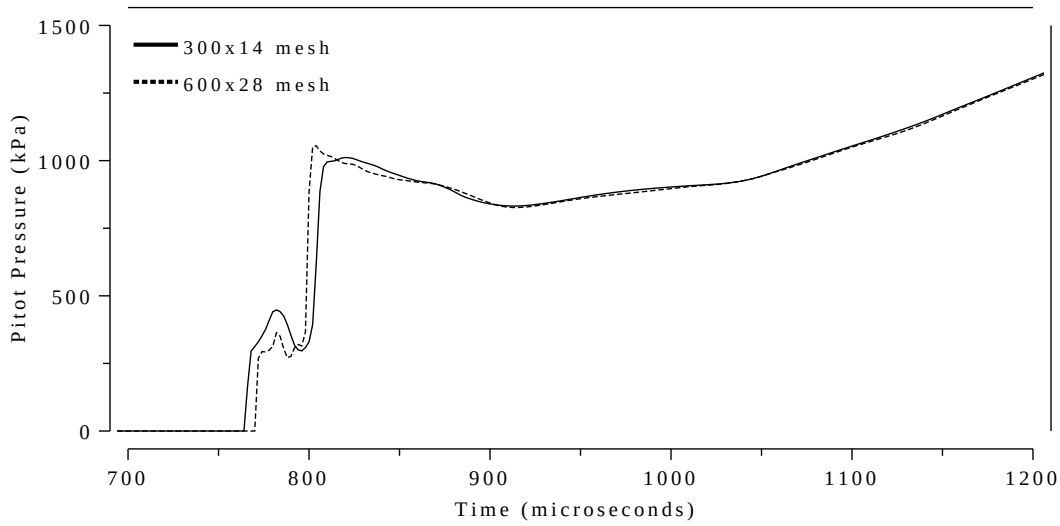

FIGURE 3.8: Pitot pressure histories from the axisymmetric simulations of the acceleration tube for X2 Condition 1. Comparison between the two mesh densities: 300x14 cells and 600x28 cells.

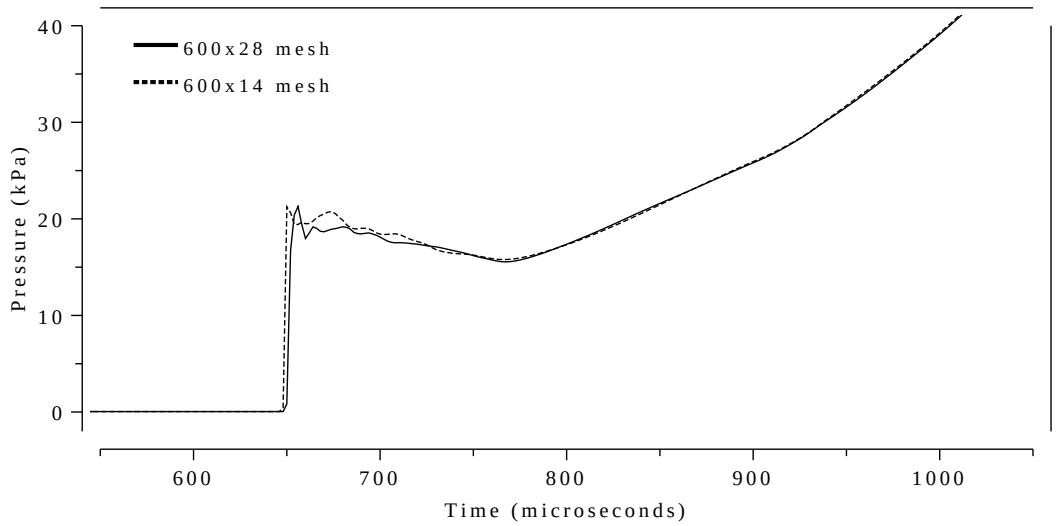

FIGURE 3.9: Static pressure histories from the axisymmetric simulations of the acceleration tube for X2 Condition 1. Comparison between the two mesh densities: 600x28 cells and 600x14 cells.

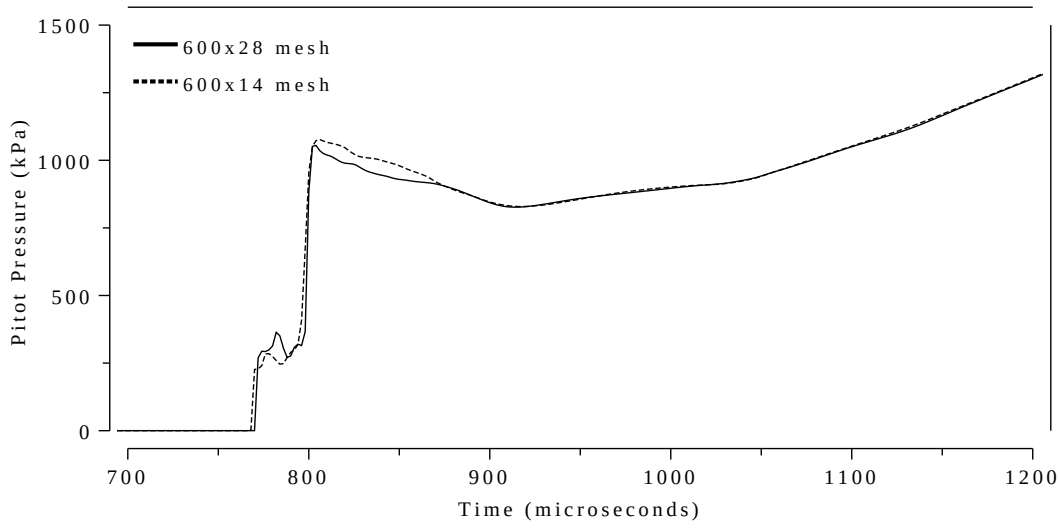

Figure 3.10: Pitot pressure histories from the axisymmetric simulations of the acceleration tube for X2 Condition 1. Comparison between the two mesh densities: 600x28 cells and 600x14 cells.

The small discrepancies that can be seen are in the vicinity of the accelerator/test gas interface where mass-loss from the shock-processed accelerator gas to the boundary layer occurs (this interface is evident by the sudden large jump in Pitot pressure in Figure 3.10). Though this indicates that the decreased cell resolution in the radial direction is not capturing the mass-loss to the boundary layer as well as the simulation with 28 cells across the radius, the general levels and shapes of both the static and Pitot pressure traces are in very good agreement with no noticeable difference 70μs after the test gas reaches the test section. Given the small difference between the two simulations but the large reduction in computation time, the 600x14 mesh will be used in X2 simulations to compare with experiment.

Hybrid Simulation Results Compared with Experiment

Figures 3.11 and 3.12 are plots of the experimental and simulated static and Pitot pressure levels obtained from X2 Condition 1. On these figures, the timescale has been set so that the shock arrivals coincide on a timescale corresponding to the simulations. Figure 3.11 shows the experimental static pressure trace taken on the wall a distance of 4.33 m downstream of the secondary diaphragm which is 0.72 m from the exit of the 5.05 m acceleration tube. Plotted against the experimental pressure trace is the simulated static pressure history taken at the corresponding location on the wall. This figure shows good agreement between the simulation pressure and that measured experimentally. The decay in pressure which starts about 40μs after the flow arrives is a combination of the flow structure in this region and attenuation due to insufficient driver length. The effects of a longer slug of driver gas at primary diaphragm rupture are shown later in this chapter.

Figure 3.12 displays the simulated Pitot pressure history of a point in the core flow at the exit of the acceleration tube compared with that obtained experimentally. The traces show good agreement with the Pitot pressure levels of the shock-processed accelerator gas that arrives prior to the test gas. The start of the simulated expanded test gas is around 25% higher than that obtained experimentally, but then proceeds to decrease in value until reaching values corresponding to that found from experiment around 100μs after the arrival of the test gas. This lower experimental Pitot pressure than what is predicted from the

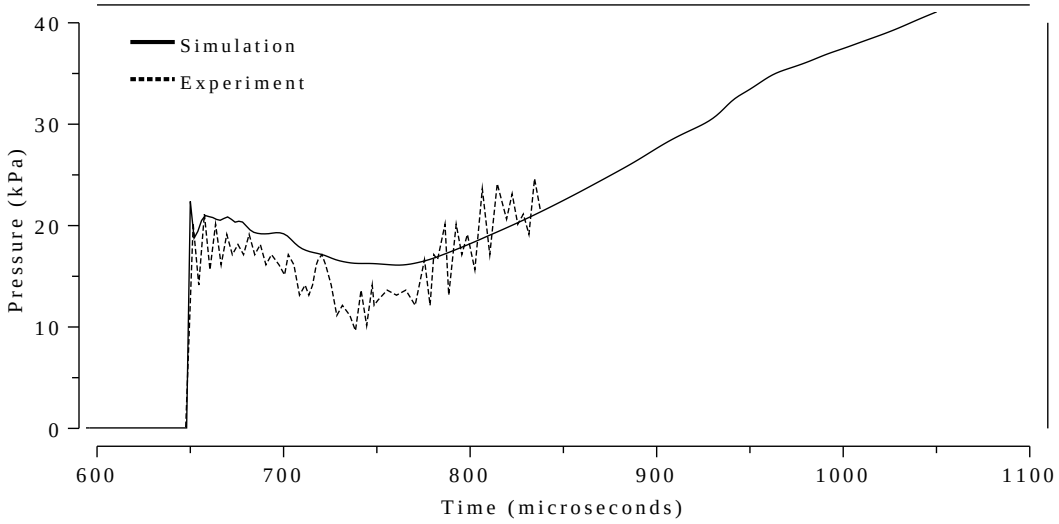

Figure 3.11: Static pressure history recorded on the wall 4.33 m along the acceleration tube for X2 Condition 1. Hybrid one-dimensional/axisymmetric viscous simulation results compared with experimental data.

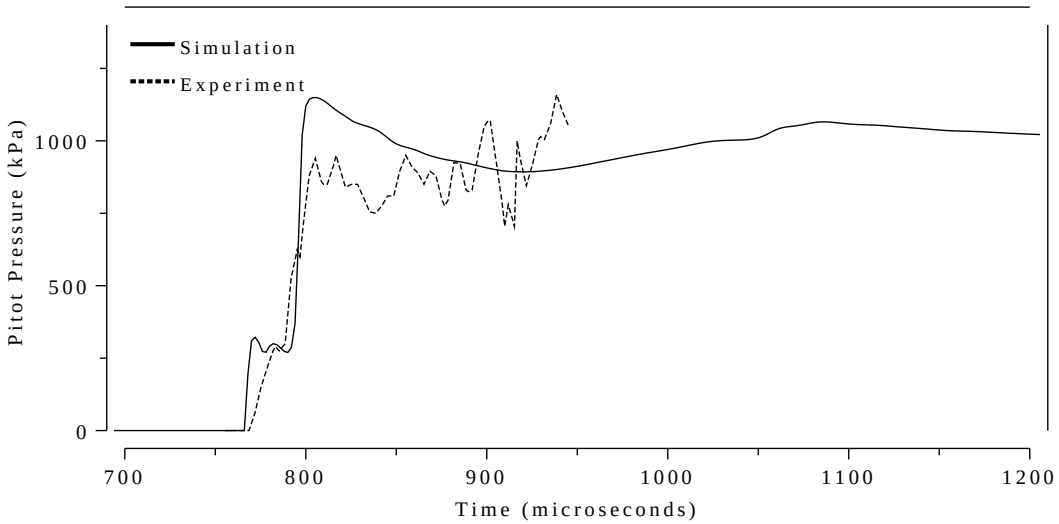

Figure 3.12: Pitot pressure history recorded at the exit of the acceleration tube for X2 Condition 1. Hybrid one-dimensional/axisymmetric viscous simulation results compared with experimental data.

simulation is thought to be due to the influence of the secondary diaphragm material which has not been included in the simulations thus far.

Influence of the Secondary Diaphragm

As depicted in the x-t diagram of Figure 2.6 (Chapter 2), the ideal operation of an expansion tube assumes the instantaneous rupture of all diaphragms and that they contribute no inertia to the flow. The thick primary diaphragm is surrounded by essentially stationary gas at the moment of diaphragm rupture and opens in a petalling manner thus contributing no inertia to the flow. This stagnant state of the gas surrounding this diaphragm at rupture and the fact that it contributes no inertia to the flow leads to the assumption that any effects caused by the finite opening time of the primary diaphragm will have an insignificant effect on the final test flow. For this reason the primary diaphragm will be modelled as a perfect diaphragm that disappears immediately upon rupture.

The light secondary diaphragm however, is sheared off upon arrival of the primary shock and has been shown to travel in a planar fashion downstream until beginning to fragment at a distance of approximately one-quarter of the tube diameter from the clamping position [61]. It is the presence of this diaphragm material which adds inertia to the flow and can hence reflect a shock into the oncoming gas. As the test flow originates from a small region of gas behind the secondary diaphragm, many studies (for example, [62–67]) have investigated the effects that the presence of the diaphragm material has on the final test flow properties. While it is generally agreed that the diaphragm does generate a reverse shock of some description, the strength, duration and effect of this shock is dependent on both the type and thickness of diaphragm material used as well as the flow conditions during the shot. The influence of this light secondary diaphragm has been found to be important for low-density superorbital conditions [44] but it is believed to have less influence for low-speed higher-density conditions. Experiments by Kendall [62] showed that as the mass of the diaphragm was reduced for a particular operating condition, the flow processes became closer to ideal. A simple means by which the inertia of the diaphragm can be approximated in a numerical analysis is by imposing a holding time on the diaphragm [68]. In this manner

the diaphragm is held in position for a finite time after the arrival of the primary shock which results in a reverse shock propagating back into the oncoming flow. Once the nominated hold time has expired the diaphragm is instantaneously removed. This method does not account for the extra inertia of the secondary diaphragm in the flow and therefore has the drawback of predicting an "*infinite rate of expansion for the gas particles initially close to the diaphragm*" [61].

To ascertain the effect that the secondary diaphragm can have on the final flow properties, an equilibrium simulation was again performed for Condition 1, but this time with a 10μs hold time imposed on the secondary diaphragm. Figure 3.13 shows the small increase in the static pressure of the test flow when the 10μs hold time is imposed on the secondary diaphragm. Also evident in this figure is a sudden pressure rise at $t\approx$930μs on the trace from the simulation which included the 10μs hold-time. This corresponds to a wave generated by the interaction of the driver gas/test gas interface with the reflected shock wave. When the interface, which has the higher density driver gas following it, hits the reflected shock wave, it causes a wave to travel downstream through the expanding test gas resulting in this sudden jump in pressure as it passes the test section. This can be seen in Figure 3.14 which is an xt-diagram generated from an inviscid one-dimensional simulation of this condition including the 10μs hold time on the secondary diaphragm. Note that the time and distance scales on this figure correspond to the rupture time and location, respectively, of the primary diaphragm. The hybrid simulation time originates (t=0) at the rupture of the secondary diaphragm. The wave generated by the interaction of the interface (solid black line, Figure 3.14) with the weakening reflected shock arrives at the test section at $t \approx$1.6ms, or 300μs after the arrival of the shock. When the diaphragm hold-time is not included, no reverse shock is formed and this jump in pressure is not experienced.

The slightly higher static pressure seen in Figure 3.13 is indicative of the 3% increase in the final shock speed which starts at around 6930 m/s and attenuates to around 6570 m/s. Figure 3.15 shows the 16% decrease in Pitot pressure resulting from the diaphragm hold time. The 10μs hold time placed on the secondary diaphragm results in a Pitot pressure of the exit core flow that is in good agreement to that found experimentally. The *echo* from

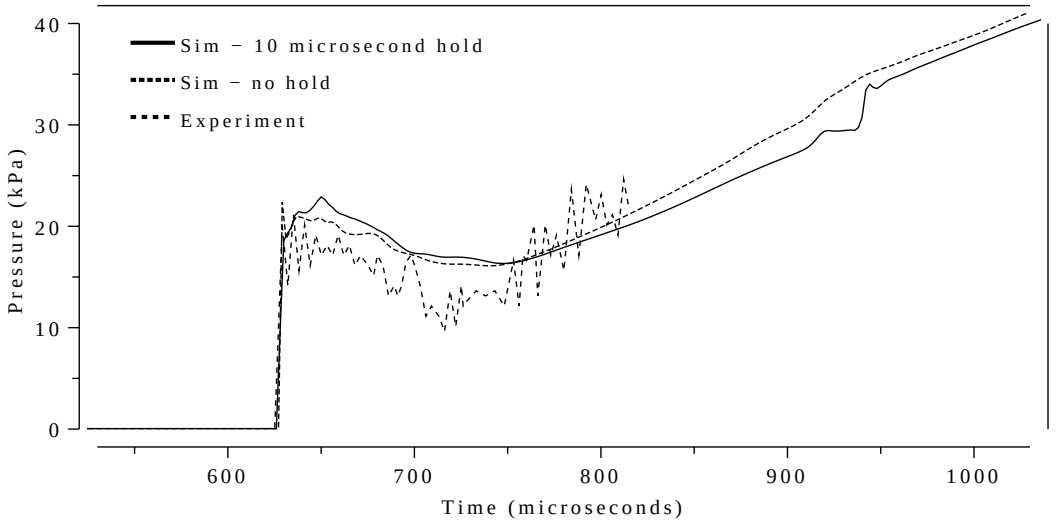

FIGURE 3.13: Static pressure history recorded on the wall 4.33 m along the acceleration tube for X2 Condition 1. Hybrid viscous simulation results (no hold-time and 10μs hold-time for secondary diaphragm) compared with experimental data.

the interface/reverse shock interaction can also be seen in this figure at $t\approx$1060μs. While simulations conducted for the current work, as well as by Hayne [69], have found that the final test flow properties are not very sensitive to diaphragm hold-time durations of between 10 and 40μs, increasing the hold-time does decrease the time between arrival of the shock and the aforementioned echo at the test section.

Assuming the small rise in shock speed and pressure to be negligible, the 16% reduction in Pitot pressure seen with the introduction of the 10μs hold time for the secondary diaphragm indicates a 16% decrease in density. With the pressure being assumed to remain the same, this corresponds to a 16% increase in the temperature of the test gas. Assuming a perfect gas, this increases the sound speed by 7.7% and hence reduces the Mach number by the same amount. The total pressure is strongly Mach number dependent, approximately to the power of 7 for perfect air with gamma of 1.4. This results in a reduction in total pressure by around 43%. As the Pitot pressure trace for the 10μs hold-time simulation agrees well with experiment, this indicates that the secondary diaphragm is reducing the total pressure for this condition by almost half compared to what would be achieved if the secondary diaphragm behaved ideally. With this being the case, it is crucial that the effect of the

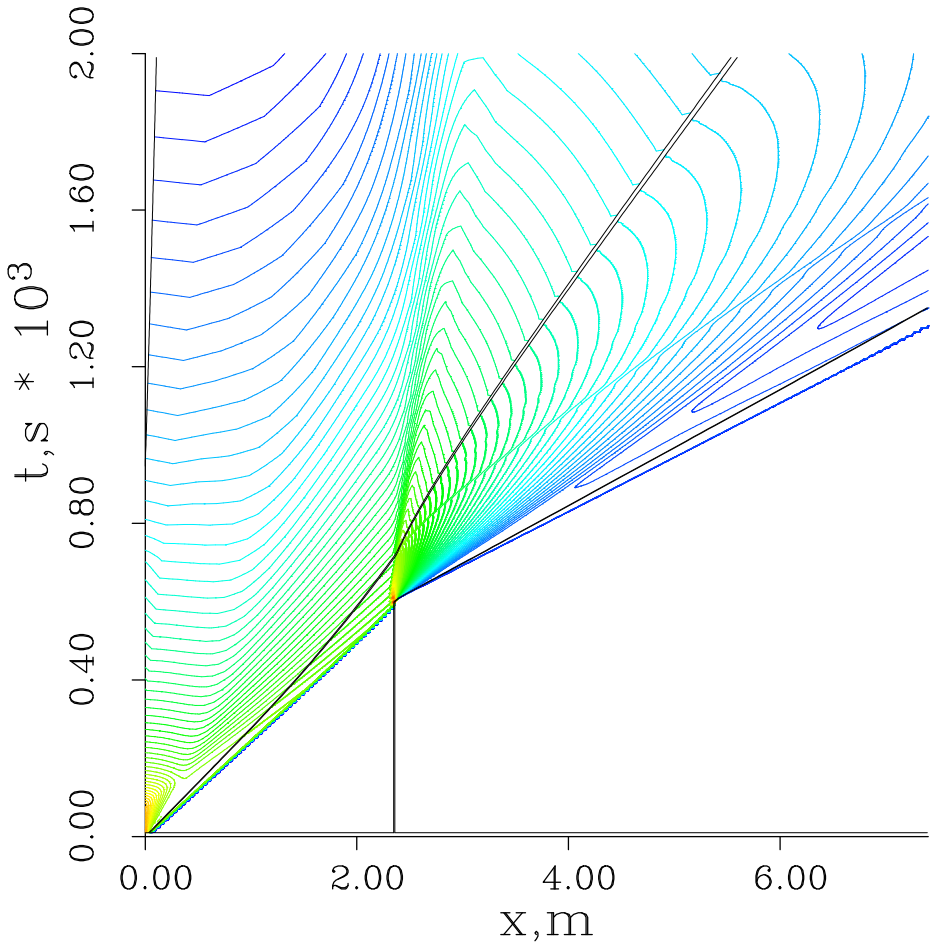

Figure 3.14: An xt-diagram of an inviscid one-dimensional simulation of Condition 1 including the 10μs hold-time on the secondary diaphragm. Solid black lines indicate interfaces between gas slugs.

secondary diaphragm is taken into account when simulating expansion tube flow and will therefore be used in the simulations presented in the remainder of the thesis. When the thickness of the secondary diaphragm is increased and/or the speed of the shot increases, the inertia of the diaphragm is believed to have more influence on the final flow properties. Condition 3 investigates an X2 condition that uses twice the thickness of material for the secondary diaphragm.

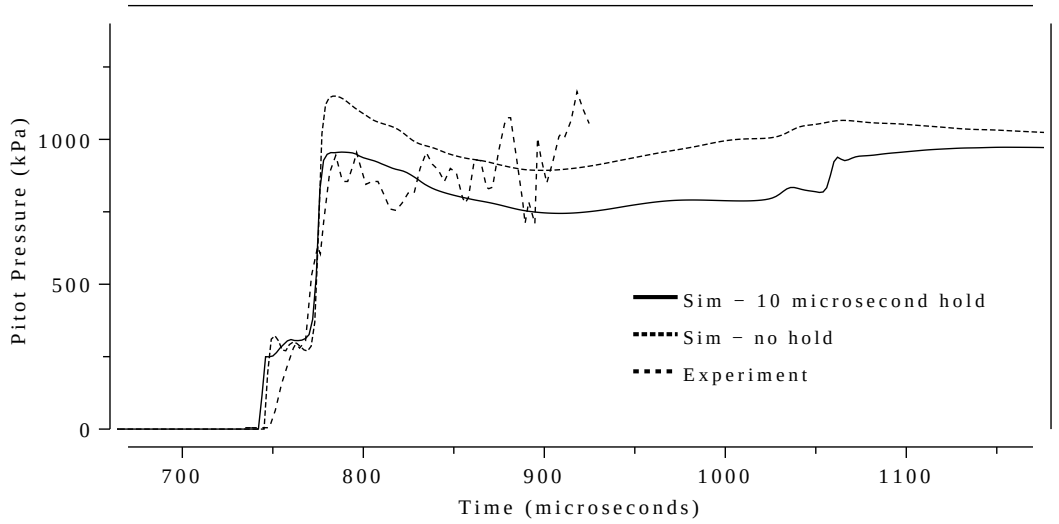

FIGURE 3.15: Pitot pressure history recorded at the exit of the acceleration tube for X2 Condition 1. Hybrid viscous simulation results (no hold-time and 10μs hold-time for secondary diaphragm) compared with experimental data.

Effects of Driver Decay

As shown earlier in this section, the X2 driver has as insufficient length of driver gas at the point of rupture to maintain a steady region of test gas behind the primary shock along the length of the shock tube. Simulations were performed to determine the magnitude of the effect that this driver decay has on the final flow properties. To determine this, simulations were performed with a driver gas slug length sufficiently long so that expansion waves can not reflect off the head of the piston and catch up to the primary shock. All other parameters were kept the same and the 10μs hold time was still imposed on the secondary diaphragm.

Figure 3.16 shows the 35% increase in static pressure obtained when a sufficiently long driver is used such that upstream disturbances do not disrupt the flow. The increase in static pressure is indicative of the 13% increase in the speed of the shock along the acceleration tube. Again, the times of shock arrival have been adjusted so that the traces can be directly compared. Figure 3.17 shows the 73% increase in Pitot pressure at the end of the acceleration tube. For an increase in flow velocity by 13% and an overall increase in ρu^2 ($\sim$ Pitot pressure) by 73%, the density must increase by around 35%. As this indicates that both the pressure

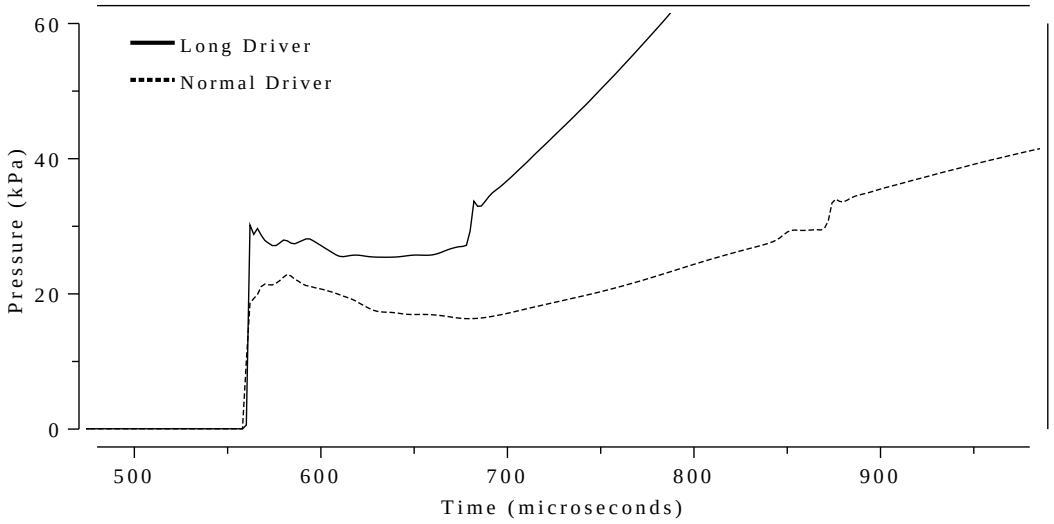

Figure 3.16: Static pressure history recorded on the wall 4.33 m down the acceleration tube from the Hybrid simulations of X2 Condition 1. Comparison of results using standard driver slug length at rupture (Normal Driver) and results using an increased length of driver gas at rupture (Long Driver).

and density increase by around 35%, the temperature must remain approximately constant. This 13% increase in flow velocity whilst maintaining a constant sound speed means that the Mach number also increases by 13%. Based on the same argument as presented earlier with perfect air with gamma of 1.4 this results in an increase of total pressure by over 300%. These results indicate the degree to which the X2 expansion tube is being affected by its short length of driver gas at rupture for this condition. The total pressure of the test flow is one third of what could be expected with a sufficiently long slug of driver gas at primary diaphragm rupture.

3.4.2 Condition 2: Shot 506

The second condition modelled had very similar nominal fill conditions as for the first condition and are as listed is Table 3.6. However, this shot utilised a modified piston that was designed to improve the performance of the two-stage driver. The length of the driver gas at primary diaphragm rupture was determined from data obtained from a new set of driver experiments outlined in Section 3.3.3. For the compression ratio used in this shot, a final

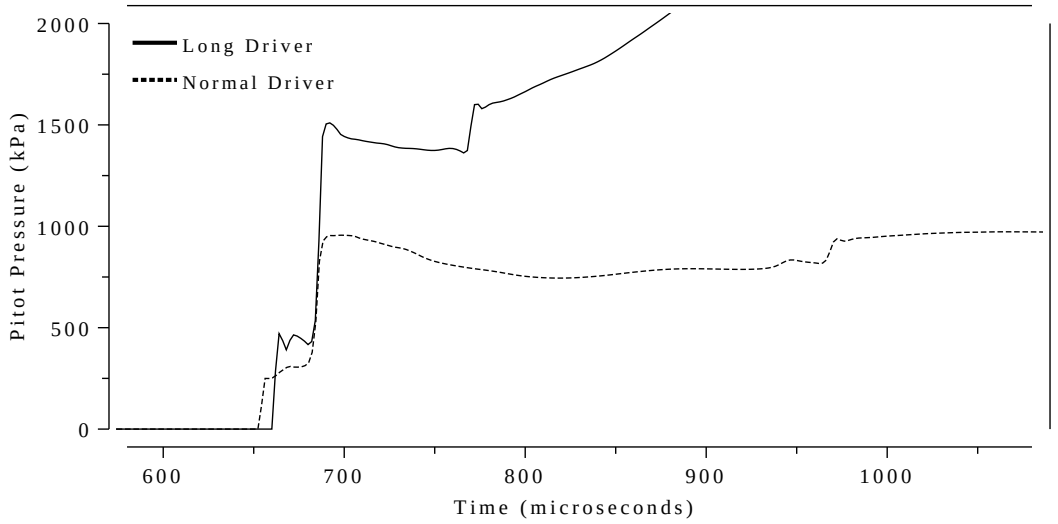

FIGURE 3.17: Pitot pressure history recorded on the wall 4.33 m down the acceleration tube from the Hybrid simulations of X2 Condition 1. Comparison of results using standard driver slug length at rupture (Normal Driver) and results using an increased length of driver gas at rupture (Long Driver).

Table 3.6: Initial conditions for X2 Condition 2: Shot 506.

Reservoir Fill (air)	1.55 MPa
Driver Fill (helium)	49.6 kPa
Shock Tube Fill, p_1 (air)	7.5 kPa
Accelerator Tube Fill, p_5 (air)	46.6 Pa
Primary Diaphragm Rupture Pressure, p_4	26 MPa
Secondary Diaphragm Rupture Pressure	∼45 kPa
Primary Shock Speed (expt)	3.9 km/s
Secondary Shock Speed (expt)	6.8 km/s

driver length of 115 mm was used in the simulations. The temperature of the driver gas at rupture was also set at 2100 K as that gave a simulated primary shock speed that matched the experimentally measured 3.9 km/s. Though the acceleration tube fill pressure was stated as being 46.6 Pa, comparison of the gauge with another gauge after the shots indicated a significant discrepancy between the two readings. As a fall-back, the secondary shock speed could be determined quite accurately by using the time of flight between pressure transducers at known locations along the tube wall. Using this shock speed at the end of the tube and

the post-shock pressure levels read from the pressure transducers, an initial pressure could be calculated. A pressure of 30 Pa was used in the acceleration tube for the simulations. 30 Pa will also be used for following simulations that all use a nominal fill pressure of 46.6 Pa. The simulation was performed as described for the simulation of Condition 1.

Figure 3.18 shows the agreement in static pressure between the one-dimensional simulation and experiment results at locations of 1.55 and 2.02 m down the shock tube. The

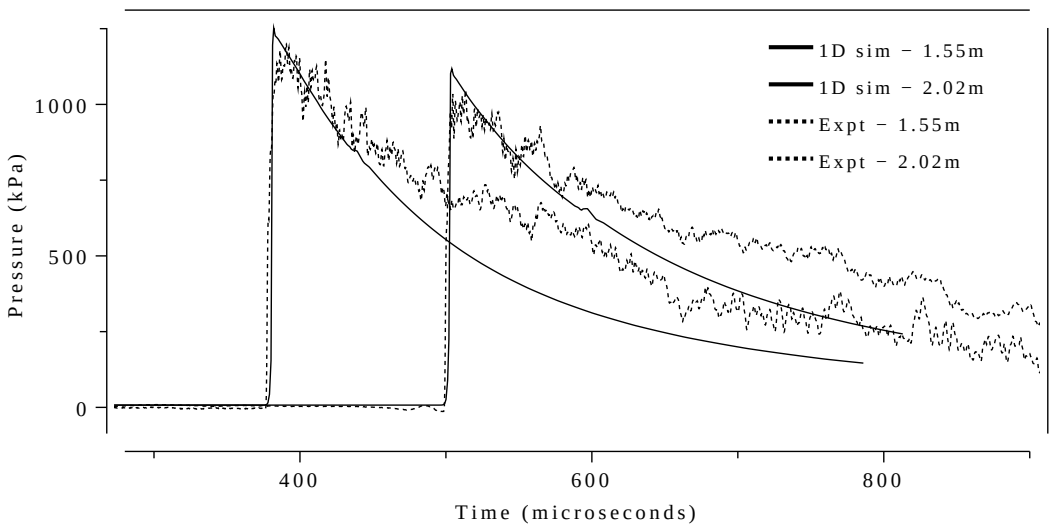

Figure 3.18: Static pressure history recorded at 1.55 m and 2.021 m along the shock tube for Condition 2. Comparison of viscous one-dimensional simulation results and experimental data (Shot 506).

peak values and initial decay agree well between simulation and experiment. However, after around 100μs at both locations, the simulated pressure seems to decay quicker than that seen in experiment. The simplified one-dimensional analysis assumes uniform conditions for the driver gas at rupture, that the piston has stopped completely at the point of rupture and remains stationary, and that the diaphragm opens instantaneously. It is encouraging that this idealized one-dimensional model agrees to this extent with what is observed experimentally. The secondary shock speed obtained from experiment for this condition started at around 7190 m/s and decayed to 6800 m/s at the end of the tube. This simulated shock speed started 2.9% higher than experiment at 7400 m/s and attenuated to 7070 m/s at the end of the acceleration tube, 4% higher than experiment.

Figure 3.19 is a comparison of the static pressure recorded on the wall of the expansion tube 2.15 m along the 5.05 m acceleration tube with what was obtained from the simulation. The initial pressure levels are in good agreement and the simulated pressure trace follows

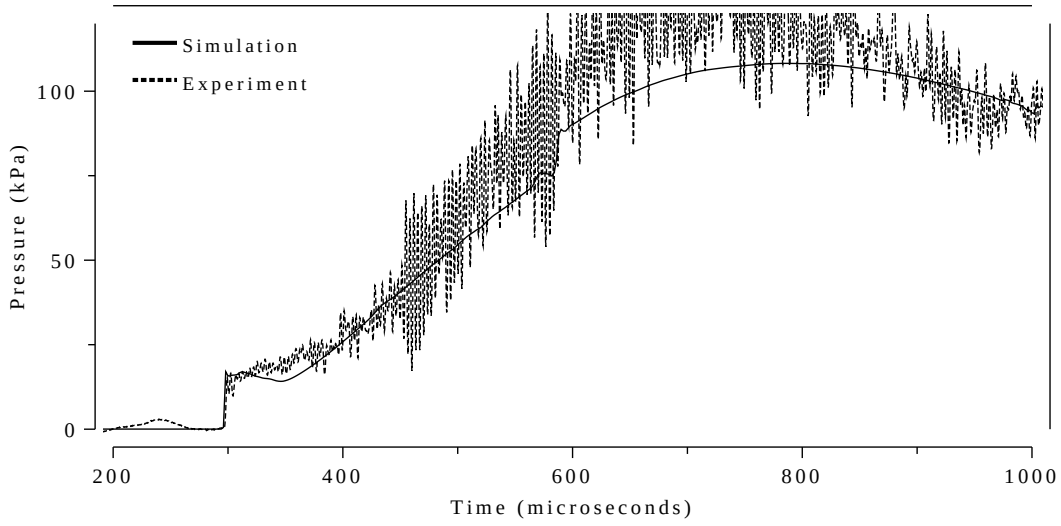

FIGURE 3.19: Static pressure history recorded at a point 2.15 m along the 5.05 m X2 acceleration tube. Comparison of viscous axisymmetric results (Hybrid simulation) and experimental data (Shot 506).

the shape of the experimental trace. Figure 3.20 is a plot of the experimental static pressure trace obtained on the wall 0.72 m from the end of the acceleration tube. Plotted against this is the static pressure traces obtained from the axisymmetric simulation at the same location. This plot demonstrates the excellent agreement between the experimental trace and what was obtained from simulation. It should be reiterated that these simulations have been based on minimizing computational requirements whilst still achieving sufficiently accurate agreement. The one-dimensional component of these Hybrid simulations requires negligible CPU time (around 30 seconds). The axisymmetric simulation of the acceleration tube was solved on the APAC National Facility which consists of 127 HP AlphaServer SC ES45 nodes, each with four 1 GHz processors. The simulation required 6.8 hours of CPU time to solve to a simulated time of 1.5 ms. If desired, a further refinement of the computational mesh could be afforded. This grid refinement would result in a slightly slower simulated shock speed and hence a slightly lower static pressure level, leading to an even closer agreement

with experiment.

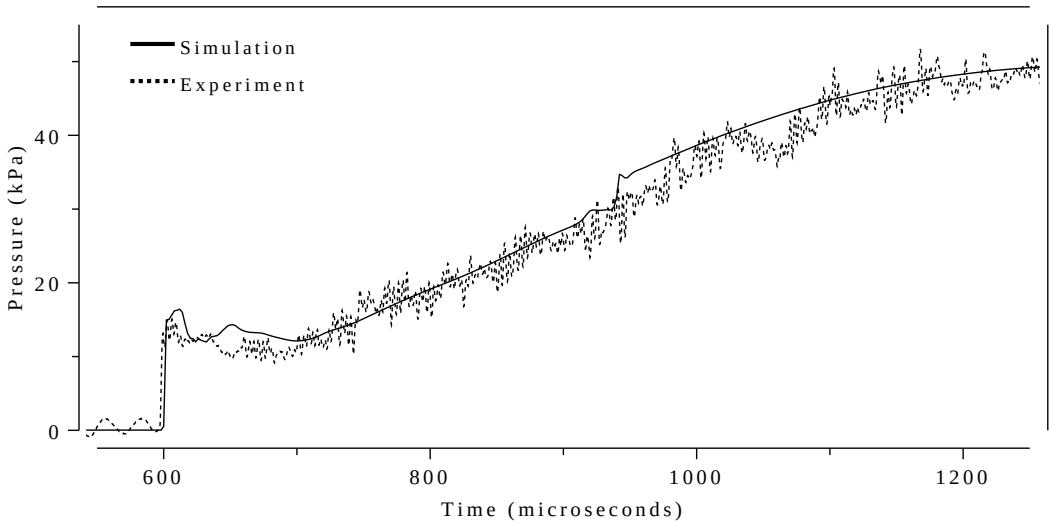

Figure 3.20: Static pressure history recorded at a point 0.72 m from the end of the 5.05 m X2 acceleration tube. Comparison of viscous axisymmetric results (Hybrid simulation) and experimental data (Shot 506).

Figure 3.21 shows the experimental Pitot pressure trace taken in the core flow at the exit plane of the acceleration tube compared with a trace obtained from the axisymmetric simulation. The bar gauge [70] used to measure the Pitot pressure is only designed to work until the reflected shock arrives back at the head of the gauge. For this reason, the experimental trace shown in Figure 3.21 is only useful for the first 80-85μs (as indicated in the figure). The simulated Pitot pressure level is in excellent agreement with the experimental trace during the useful measurement time of the gauge and then continues to maintain good agreement with the mean value of the experimental trace. There is also very good agreement with the level of initial shock processed accelerator gas.

3.4.3 Condition 3: Shot 393

The fill conditions for Condition 3, as shown in Table **??**, were similar to those for Condition 1 although twice the thickness of secondary diaphragm was used. The fill pressure for the accelerator tube was thought at the time to be the same as for Condition 1 (46.6 Pa) but

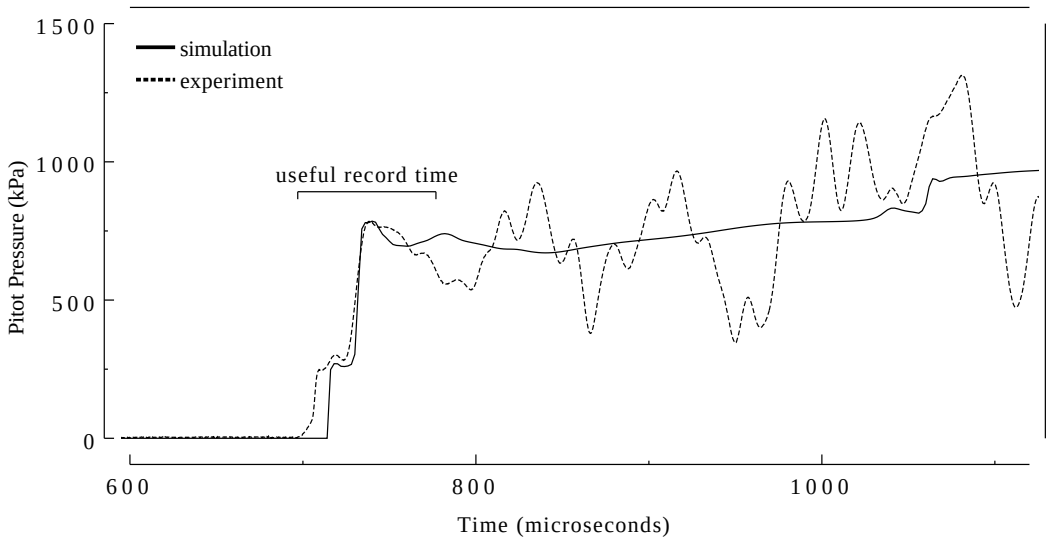

FIGURE 3.21: Pitot pressure history recorded at a point 0.72 m from the end of the 5.05 m X2 acceleration tube. Comparison of viscous axisymmetric results (Hybrid simulation) and experimental data (Shot 506). Useful record time of bar gauge indicated.

be relatively insensitive to the hold-time duration).

Figures 3.22 and 3.23 show the static and Pitot pressure traces obtained at the end of the acceleration tube. The initial simulated static pressure level in Figure 3.22 is in good agree-

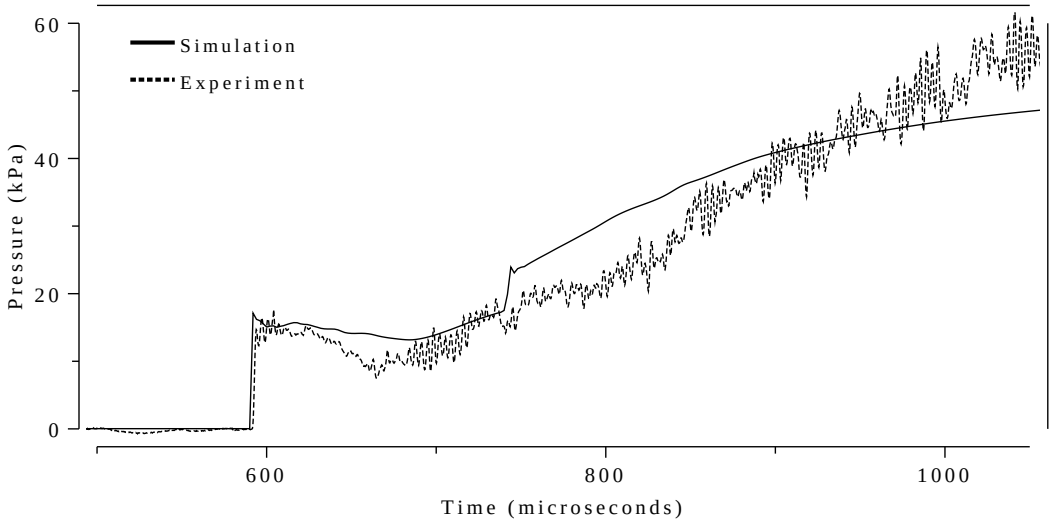

Figure 3.22: Static pressure history recorded at a point 0.72 m from the end of the 5.05 m X2 acceleration tube. Comparison of axisymmetric results (Hybrid simulation) and experimental data (Shot 393).

ment with experimental results. This is indicative of the fact that the simulated secondary shock speed was within 1% of the 6.9 km/s measured experimentally. More evident on both Figures 3.22 and 3.23 now is the jump in the corresponding property approximately 140μs after the shock arrives which is caused by the disturbance wave generated by the interaction of the D/T interface with the reflected shock. Because in practice the diaphragm shears off very quickly and is then accelerated rapidly downstream before fragmenting, the reverse shock generated in actual operation would not be as strong as that modelled numerically with the simplified diaphragm hold-time model. This would result in a weaker disturbance wave and a more dissipated increase in the gas properties rather than the sudden jump seen in the simulation results.

The initial level of simulated Pitot pressure agrees well with experiment, however the experimental level proceeds to drop rapidly by approximately 25% where the simulated Pitot

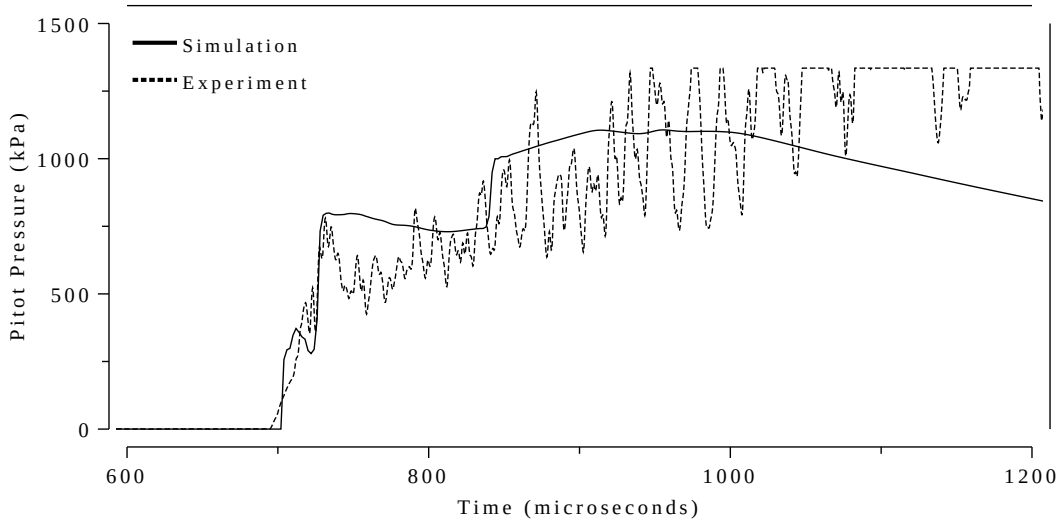

FIGURE 3.23: Pitot pressure history recorded at a point 0.72 m from the end of the 5.05 m X2 acceleration tube. Comparison of viscous axisymmetric results (Hybrid simulation) and experimental data (Shot 393).

pressure remains essentially constant. This discrepancy between experiment and numerical simulations is thought to be due to the increased influence of the heavier secondary diaphragm. The hold time of the secondary diaphragm in the simulation was increased to 30μs but this neglects the increased inertial effects of the extra diaphragm material. This increased inertia reduces the acceleration of the diaphragm material, and thus further hinders the energy cascade process of the unsteady expansion, resulting in a simulated Pitot pressure almost 40% higher than measured experimentally at a point 50μs after the shock arrives. These results suggest that while Hybrid simulation technique with the simplified diaphragm hold-time model offers a convenient and efficient means of accurately modelling the flow within an expansion tube for conditions using light secondary diaphragms, a more detailed diaphragm inertial model should be implemented in conditions where a thicker secondary diaphragm material is utilised.

3.4.4 Condition 4: Shot 833

Shot 833 was a high speed condition having a final shock speed of 9.7 km/s. Though this is well above the scramjet flight speeds of interest, the condition was modelled in order to

investigate phenomena associated with simulating high speed expansion tube flows. Table 3.8 outlines the initial fill conditions for Condition 4. As it has very similar driver conditions

Table 3.8: Initial conditions for X2 Condition 4: Shot 833.

Reservoir Fill (air)	1.6 MPa
Driver Fill (helium)	53.6 kPa
Shock Tube Fill, p_1 (air)	2.4 kPa
Accelerator Tube Fill, p_5 (air)	0.933 Pa
Primary Diaphragm Rupture Pressure, p_4	26 MPa
Secondary Diaphragm Rupture Pressure	∼45 kPa
Primary Shock Speed (expt)	5.0 km/s
Secondary Shock Speed (expt)	9.7 km/s

to the other conditions, a driver temperature of 2100 K was used in the simulations with a driver gas slug length of 121 mm at rupture.

The primary shock speed calculated from experimental results was 5 km/s towards the end of the shock tube. The primary shock speed obtained from the one-dimensional simulation of the shock tube section was around 4% slower than this at 4800 m/s. The pressure

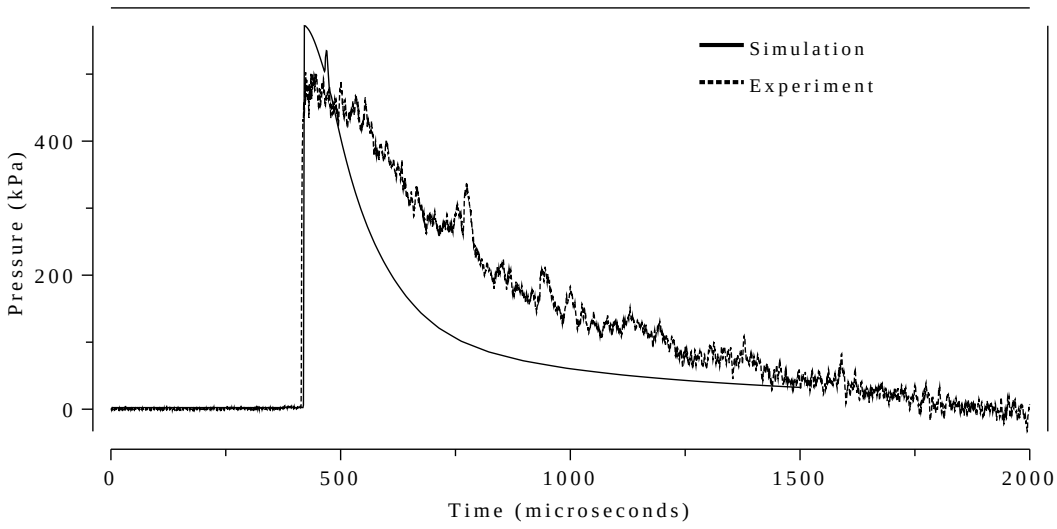

Figure 3.24: Static pressure history recorded at a point 2.02 m along the X2 shock tube. Comparison of viscous one-dimensional simulation results and experimental data (Shot 833).

towards the end of the shock tube was experimentally measured at being 490 kPa. To get

this post-shock pressure with a shock speed of 5 km/s, the fill pressure needed to be around 1.8 kPa using equilibrium chemistry - 25% less than the stated nominal fill pressure of 2.4 kPa. Despite this discrepancy, the stated nominal fill pressure of 2.4 kPa is used in the simulations of this condition. Figure 3.24 shows the one-dimensional simulated static pressure history recorded 2.02 m along the shock tube compared with that measured from experiment. Even though the experimental shock speed was slightly faster than the simulation, the measured pressure is 15% below what was simulated. This indicates that the actual fill pressure in the shock tube was lower than the stated nominal fill pressure.

Figure 3.25 shows a comparison between experiment and simulated static pressure histories recorded at 0.56 m, 1.06 m and 4.48 m along the acceleration tube. These traces indicate a reasonable agreement between experiment and simulation right along the length of the acceleration tube, especially considering the issues regarding the unreliable stated fill pressures. Both the experimental and simulated Pitot pressure traces taken at the exit of the

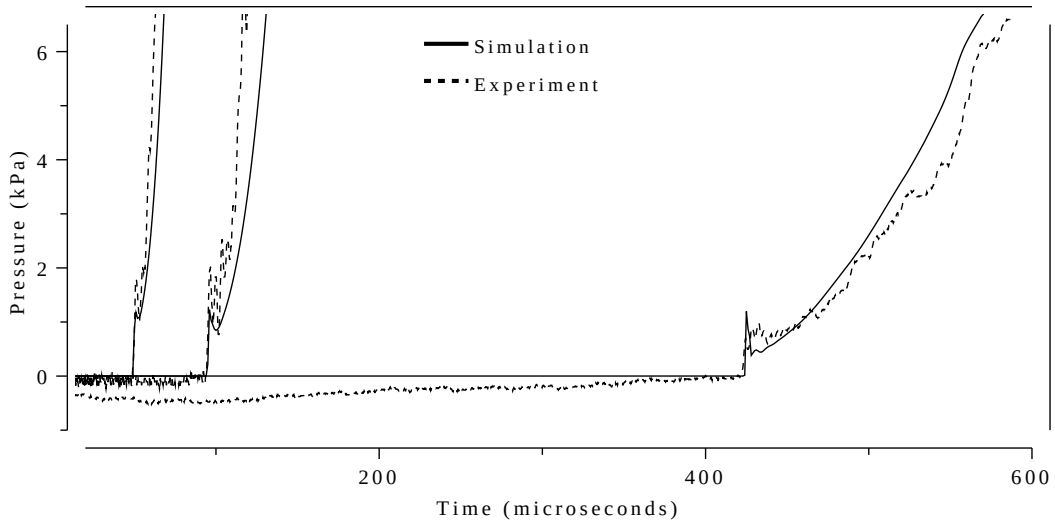

FIGURE 3.25: Static pressure histories recorded at points 0.56 m, 1.06 m and 4.48 m along the X2 acceleration tube. Comparison of viscous axisymmetric results (Hybrid simulation) and experimental data (Shot 833).

acceleration tube are plotted in Figure 3.26. It is evident from this graph that the simulated Pitot pressure is only between 35-45% of that measured experimentally. A grid-convergence study was performed for this simulation to determine the dependence of the solution on the

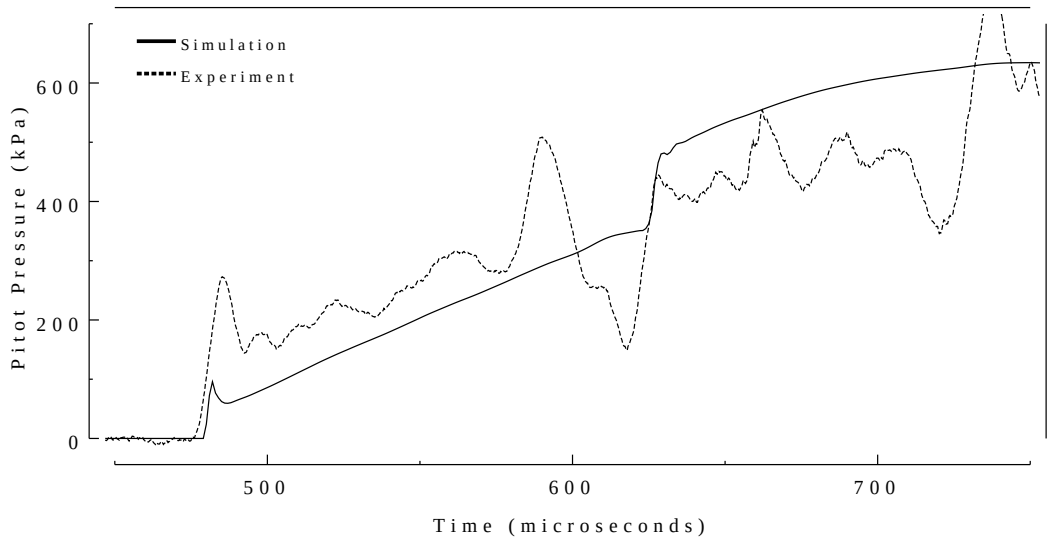

Figure 3.26: Pitot pressure history recorded at the exit of the X2 acceleration tube. Comparison of viscous axisymmetric results (Hybrid simulation) and experimental data (Shot 833).

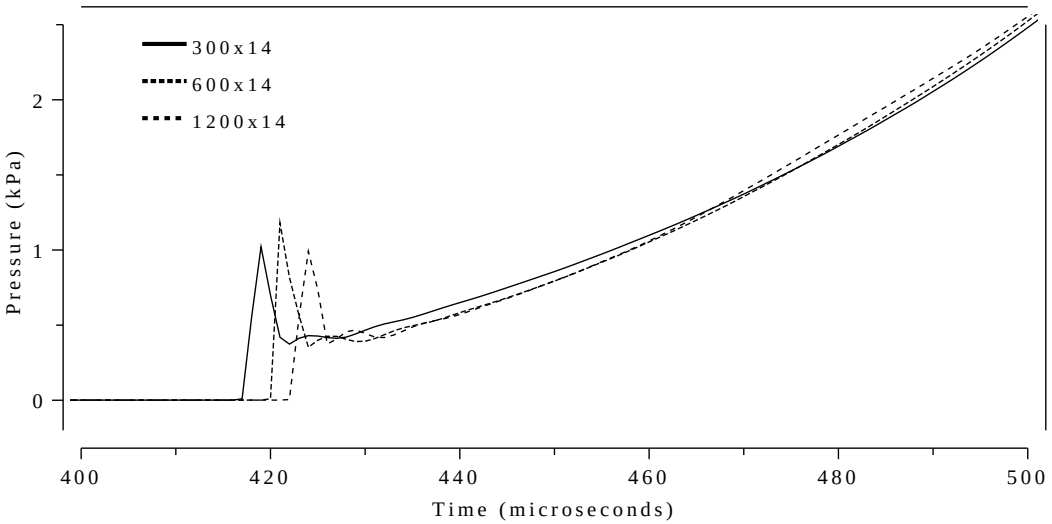

Figure 3.27: Simulated static pressure histories recorded at a point 0.72 m from the end of the 5.05 m X2 acceleration tube. Results from the three different grid-density simulations for Condition 4: 300x14 cells, 600x14 cells and 1200x14 cells.

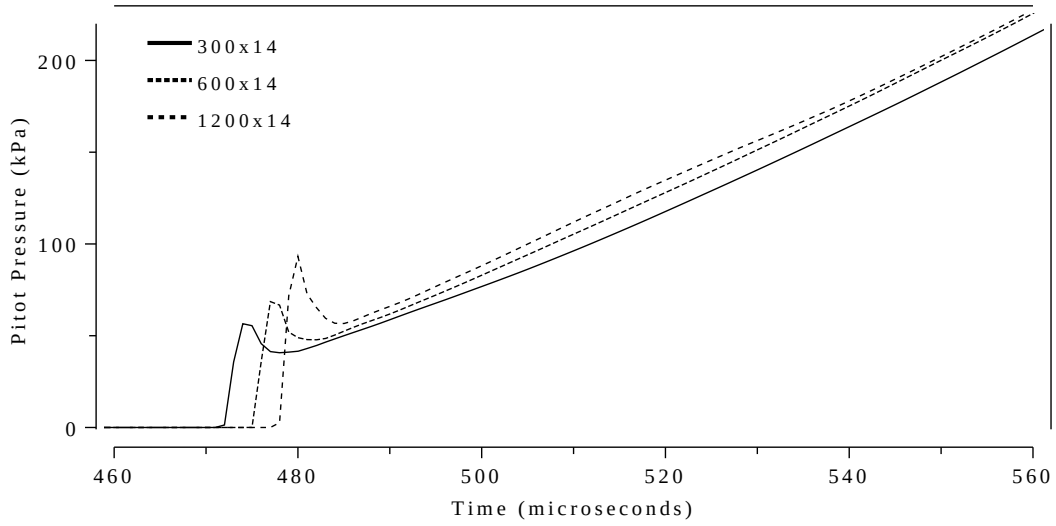

FIGURE 3.28: Simulated Pitot pressure histories recorded at the end of the 5.05 m X2 acceleration tube. Results from the three different grid-density simulations for Condition 4: 300x14 cells, 600x14 cells and 1200x14 cells.

grid. Keeping the cells across the diameter constant at 14, the cells along the longitudinal direction was first halved to 300 and then doubled to 1200. Figure 3.27 shows that the static pressure levels remain essentially constant between the three levels of mesh refinement. In support of this negligible change in static pressure is the very slight decrease in shock speed (<1%) as the mesh is refined. Figure 3.28 however shows a significant change in Pitot pressure between the 3 simulations, indicating that the solution has not achieved a fully grid independent solution. The level increases by approximately 18% between the most coarse mesh (300x14 cells) and the standard mesh (600x14 cells). The finest mesh (1200x14 cells) results in a further increase by around 18% in the Pitot pressure level. This finest-mesh simulation required almost 200 hrs on the Origin 3000 computer. Any further refinement of the mesh would result in computation times that become impractical. Just doubling the mesh again in the x-direction would require around 1 month of CPU time. The converged value of the test flow Pitot pressure can be approximated by

$$P_{\text{sim}} = P_{\text{conv}} + C\,\Delta x^n \tag{3.4}$$

where $C\,\Delta x^n$ is the error between the simulated Pitot pressure level, P_{sim}, and the converged value, P_{conv}. C is a constant determined by finding the best fit through the simulated data points and Δx is, in this case, the length of the computational cells in the x-direction. n is characteristic of the convergence of the code and has a value of between 1 and 2. The converged estimate (P_{sim} as Δx approaches zero) was insensitive ($\pm 5\%$) to values of n chosen within this range. A value of $n = 1.2$ gave a converged Pitot pressure (P_{conv}) of 57.5 ± 3.3 kPa as shown in Figure 3.29. This figure shows that although the Pitot pressure would increase somewhat as the mesh is refined, it is doubtful that lack of resolution alone would account for the large difference seen between simulated and experimental (164 kPa) Pitot pressure levels. A contributing factor in this difference is believed to be the effects of non-equilibrium chemistry which is investigated in Chapter 4 for both the low-enthalpy (Condition 2) and high-enthalpy (Condition 4) X2 operating conditions.

Neely and Morgan [43] have investigated chemistry effects for a 13 km/s air test gas condition in the X1 expansion tube. Though they state that equilibrium chemistry calculations, rather than calculations assuming frozen chemistry, more accurately describe the unsteady

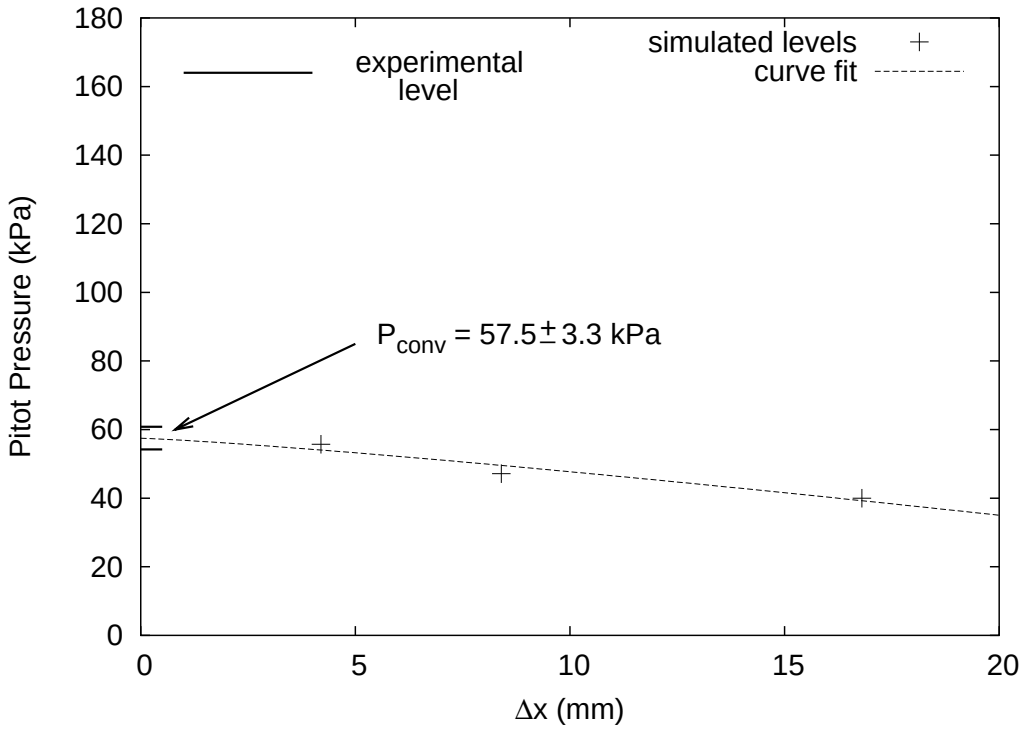

FIGURE 3.29: Approximation of the convergence of Pitot pressure for the high-enthalpy X2 condition as the mesh is refined.

expansion process, nonequilibrium effects are believed to play an influential role in the X2 condition modelled here. The X2 simulations presented so far have assumed that the chemistry reaches an equilibrium state during each time step. For the lower-speed section of the shock tube this may well be a valid assumption. The primary and reflected shocks cause certain levels of test flow dissociation and it is these dissociated species which may not have time to fully recombine through the rapid unsteady expansion to the levels to which equilibrium calculations predict. The resultant 'freezing' of the test gas would mean that the energy that has been used in the dissociation of the molecules (energy of formation) is not returned to the flow, resulting in a cooler expanded gas than would otherwise be obtained assuming equilibrium chemistry. In addition to this, the enthalpy multiplication effect of the unsteady expansion process only acts on the static component of the enthalpy rather than that in chemical form [71]. Even if the gas was allowed to fully recombine after the expansion, the enthalpy of the flow would be less than would be obtained in a flow that remains in chemical

equilibrium during the expansion process. It may be these non-equilibrium effects that are responsible for experimental Pitot pressures that are not being simulated accurately using equilibrium assumptions.

3.5 One-Dimensional Simulations

The previous section showed that a combination of one-dimensional and axisymmetric simulation techniques can be utilized to produce results that agree well with those found from experiment for the lower enthalpy conditions in the X2 expansion tube. While the shock speeds and static pressure levels were in reasonable agreement for the higher enthalpy condition, the simulated Pitot pressure level was under half that measured in experiment. These simulations required almost 200 hrs of CPU time for solutions that were not totally independent of the grid. These computation times maybe reasonable when attempting to fully describe the flow behaviour in a smaller facility, but when investigating the effects and trends of certain phenomena, a quick yet reliable means of modelling the flow within an expansion tube is required. This is even more critical when investigating the predicted operating capabilities of a large-scale facility. For this reason, the axisymmetric results presented previously will be compared to both viscous and inviscid one-dimensional simulations of the X2 facility assuming equilibrium chemistry.

3.5.1 Viscous Simulation: Condition 1

Figure 3.30 depicts the geometry used for the one-dimensional simulation of Condition 1. The initial section of the simulation up to the point of secondary diaphragm rupture is essentially the same as for the Hybrid simulations presented in the previous section. In addition, the full one-dimensional simulations have a 5.1 m acceleration tube (section (3) on Figure 3.30) placed on the end with a diameter of 85 mm. This acceleration tube is divided into 200 equally spaced cells. The cells in the shock tube (region 2) are now clustered towards the secondary diaphragm to minimise the size of the expanded test gas cells at the exit of the tube. A diaphragm with a 45 kPa rupture pressure is placed between the shock and

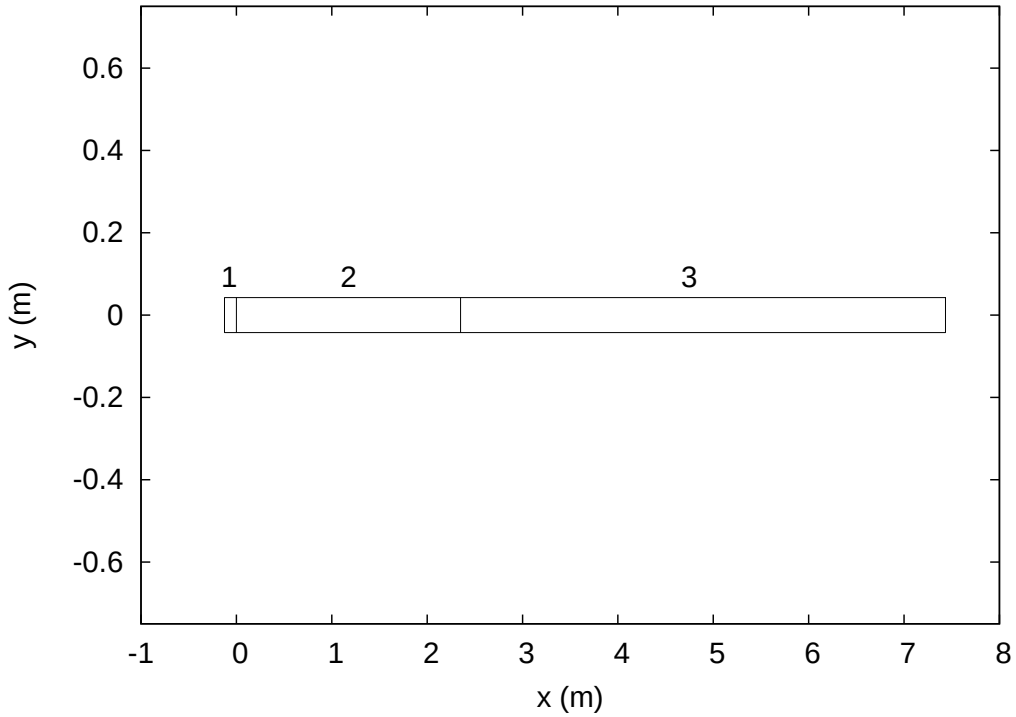

FIGURE 3.30: Geometry for the one-dimensional simulations (*L1D*) of X2 Condition 1.

accelerator tube. As in the Hybrid simulations, this diaphragm is held in place for 10μs once the shock arrives to simulate the inertia of the diaphragm material. The driver gas (region 1) was divided into 50 cells, clustered towards the primary diaphragm.

The shock speed in the acceleration tube started off within ∼1% of that from the axisymmetric simulation at 7027 m/s, but attenuated to 4% less (6320 m/s) than the axisymmetric simulation by the end of the acceleration tube. This extra attenuation can be attributed to the fact that, because it is one-dimensional, the shear at the walls is applied to the whole cell hence slowing the gas more than in an axisymmetric simulation where the wall shear is only applied to the very outer cells. This shock speed agrees very well (within ∼1%) with the experimental obtained shock speed of 6.4 km/s. Figure 3.31 shows a comparison of the pressure traces from the one-dimensional and axisymmetric equilibrium simulations. Also plotted in this figure is the static pressure trace obtained from experiment. This shows a good agreement in the levels between all three pressure traces. The pressure trace from the

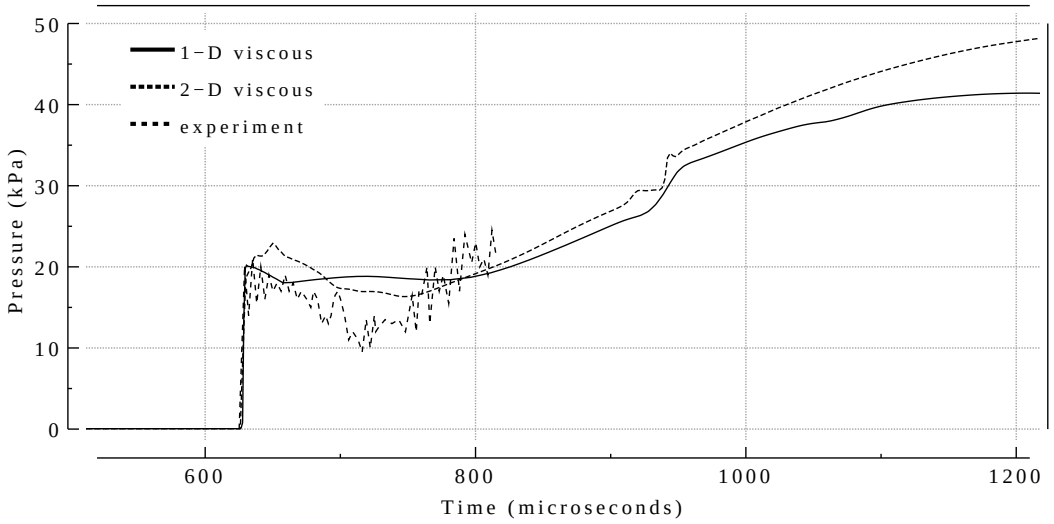

Figure 3.31: Static pressure history recorded 0.73 m from the end of the 5.05 m X2 acceleration tube. Comparison of results from one-dimensional (1-D) and axisymmetric (2-D) viscous simulations, and experimental data. (Condition 1).

L1D simulations however does not show the noticeable dip that can be seen in both the axisymmetric and experimental traces. This decrease in pressure is due to both driver-related attenuation and accelerator gas bleeding into the boundary layer. In Section 3.4.1 where the axisymmetric simulation incorporated a long-driver it was seen that there was only a small decrease in the static pressure after around 40μs. This small decrease is due to the mass-loss to the boundary layer and has been observed by Jacobs [72] and Wheatley [73] in previous expansion tube simulations. This mass-loss, which results in the test gas/accelerator gas interface velocity becoming approximately equal to the shock speed [74], forms a bulge in the boundary layer just upstream of the interface. It is this bulge that creates the region of core flow that has a higher velocity and lower pressure. The one-dimensional code can not model the radial movement of the flow to the boundary layer and thus can not capture this effect. For a given shock speed, this results in a slower flow speed for the one-dimensional simulations that can be seen in Figure 3.32. The flow speed is very similar between the two simulations immediately after the shock arrives (for about 5μs). However, the flow speed rapidly increases on the axisymmetric trace to a value very near that of the shock speed.

As the Pitot pressure is proportional to the velocity squared, a small discrepancy in flow

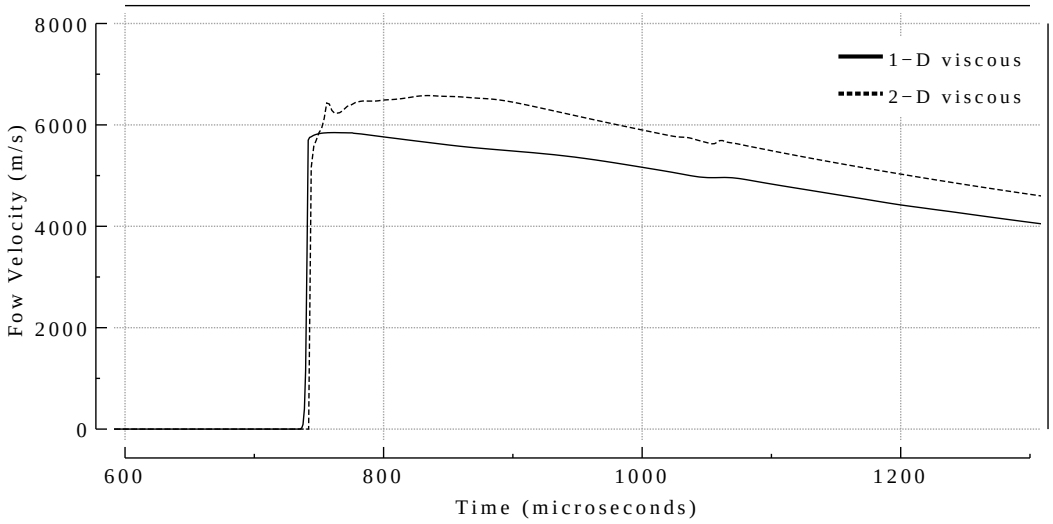

FIGURE 3.32: Flow velocity recorded at the end of the 5.05 m X2 acceleration tube. Comparison of results from one-dimensional (1-D) and axisymmetric (2-D) viscous simulations. (Condition 1)

velocity can lead to a significant difference in the Pitot pressure. The ∼10% slower flow speed for the one-dimensional simulations will result in a ∼21% lower Pitot pressure if the density is assumed the same. Figure 3.33 indicates that the test-flow temperature for the one-dimensional simulation is only slightly lower than that obtained from the axisymmetric simulation (the descrepancy in post-shock accelerator gas temperatures evident in this figure is due to the shear calculations at the wall heavily influencing the 1-D simulation results. This descrepancy is all but eliminated when inviscid flow is assumed as shown in Figure 3.36). As the pressures agreed well between the two techniques, this suggests that there is not much difference in the simulated test flow density. Figure 3.34 is a plot of the Pitot pressure traces obtained from the one-dimensional and axisymmetric simulations compared with that obtained from experiment. This figure shows a decrease of around 20-25% in the one-dimensional Pitot pressure during the nominal test time compared with the axisymmetric Pitot pressure, agreeing well with the 21% less you would expect from the 10% slower flow speed. The one-dimensional simulations utilize a model developed by Doolan and Jacobs [75] to capture the mass-loss to the boundary layer in the region of shock-processed accelerator gas. Figures 3.33 and 3.34 both indicate that the length of shock-processed accelerator gas is in good agreement between the one-dimensional and axisymmetric simulation techniques.

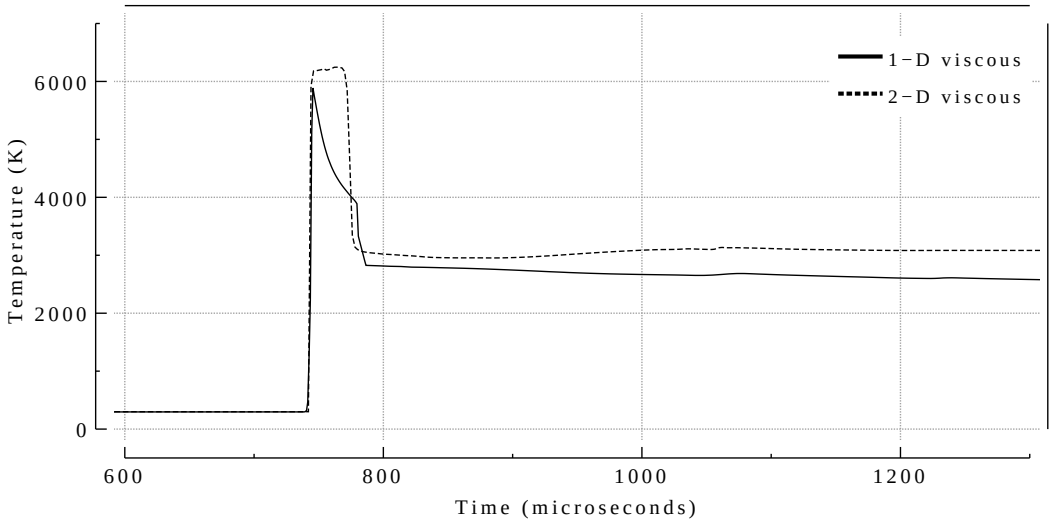

Figure 3.33: Static temperature recorded at the end of the 5.05 m X2 acceleration tube. Comparison of results from one-dimensional (1-D) and axisymmetric (2-D) viscous simulations. (Condition 1).

3.5.2 Inviscid Simulation: Condition 1

The slower flow speed in the the one-dimensional simulations can be avoided by turning the viscous terms off. The inviscid simulation results in a higher shock speed but the flow speed is closer to experimental values. Figure 3.35 shows the excellent agreement between one-dimensional and axisymmetric velocities at the end of the acceleration tube. The time scale has been set in this figure so that the arrival of the interfaces coincide. Because the losses in the shock-processed accelerator gas region are not included in these simulations, the length of the accelerator gas before the arrival of the expanded test gas is noticeably longer than the axisymmetric (2-D) simulations. Also showing excellent agreement between the fully-viscous axisymmetric and inviscid one-dimensional simulations are the temperature traces obtained at the end of the acceleration tube (shown in Figure 3.36). The lack of shear stress at the walls however in the inviscid simulations does result in 6% higher final shock speeds. Coupled to this increase in shock speed is also a higher static pressure that can be seen in Figure 3.37. The inviscid simulations are, however, capable of capturing the drop in static pressure that is seen in the experimental pressure trace. The experimental results showed that there was a drop in static pressure by approximately 1/3rd over the first 100μs

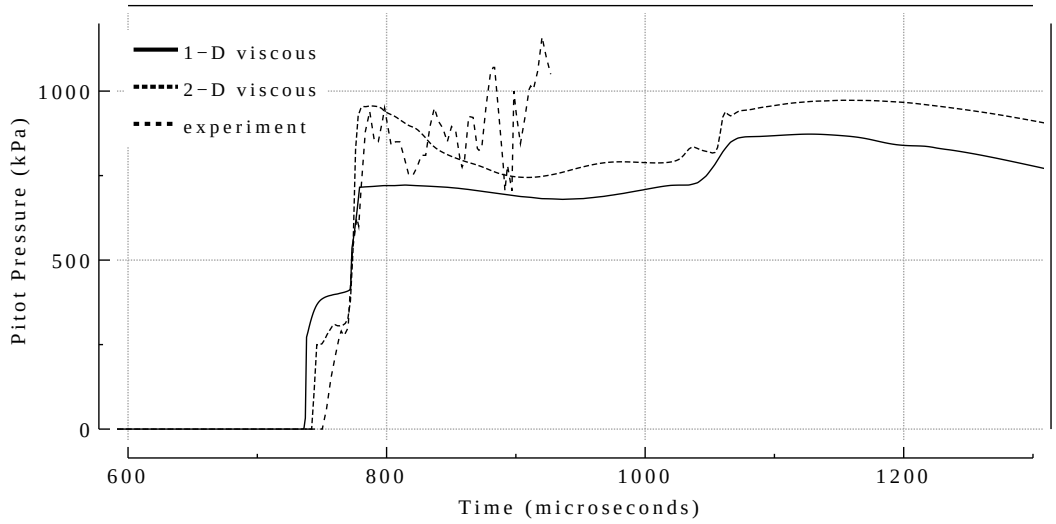

FIGURE 3.34: Pitot pressure history recorded at the exit of the 5.05 m X2 acceleration tube. Comparison of results from one-dimensional (1-D) and axisymmetric (2-D) viscous simulations, and experimental data. (Condition 1)

of test flow. As shown in Figure 3.38, the one-dimensional viscous simulation was not capable of capturing this decrease in static pressure and gave an essentially level static pressure over this period. The reason for this is that in the one-dimensional simulations, the shear stress is applied to a slug of gas which represents the entire diameter of the tube. For a slug of gas to be travelling along the tube at a constant velocity (*i.e.* the expanded test gas) there must be an inherent increasing pressure gradient travelling upstream to compensate for this shear stress that is being applied to the slug of gas.

CPU requirements

The Hybrid simulation of Condition 1 (consisting of both the one-dimensional simulation of the shock tube and the axisymmetric simulation of the acceleration tube) required a total of around 16 hrs of CPU time on an SGI Origin 3000. The axisymmetric component required the majority of this time, with the one-dimensional component requiring only around 30 seconds. The inviscid equilibrium chemistry one-dimensional simulation of both the shock and acceleration tube sections saw a 3 orders of magnitude reduction in the overall CPU time required to only 61 seconds using a 1.8 GHz Athlon processor. The results presented

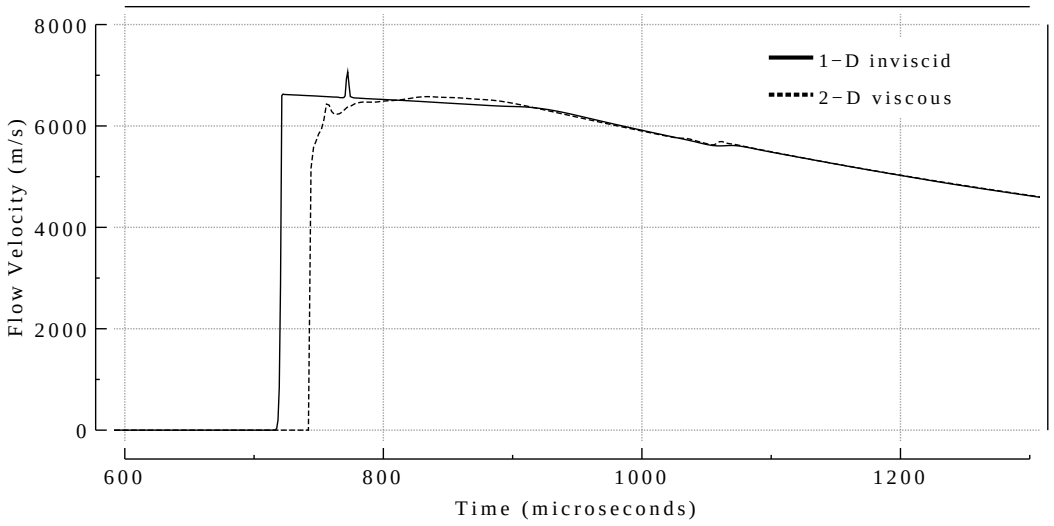

Figure 3.35: Flow velocity history recorded at the end of the 5.05 m X2 acceleration tube. Comparison of results from inviscid one-dimensional (1-D) and viscous axisymmetric (2-D) simulations. (Condition 1)

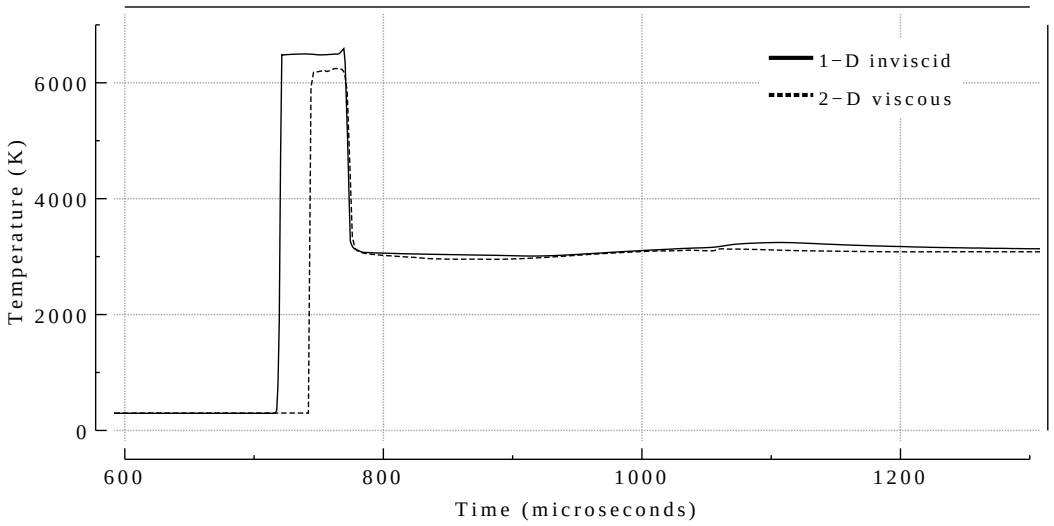

Figure 3.36: Static temperature history recorded at the end of the 5.05 m X2 acceleration tube. Comparison of results from inviscid one-dimensional (1-D) and viscous axisymmetric (2-D) simulations. (Condition 1)

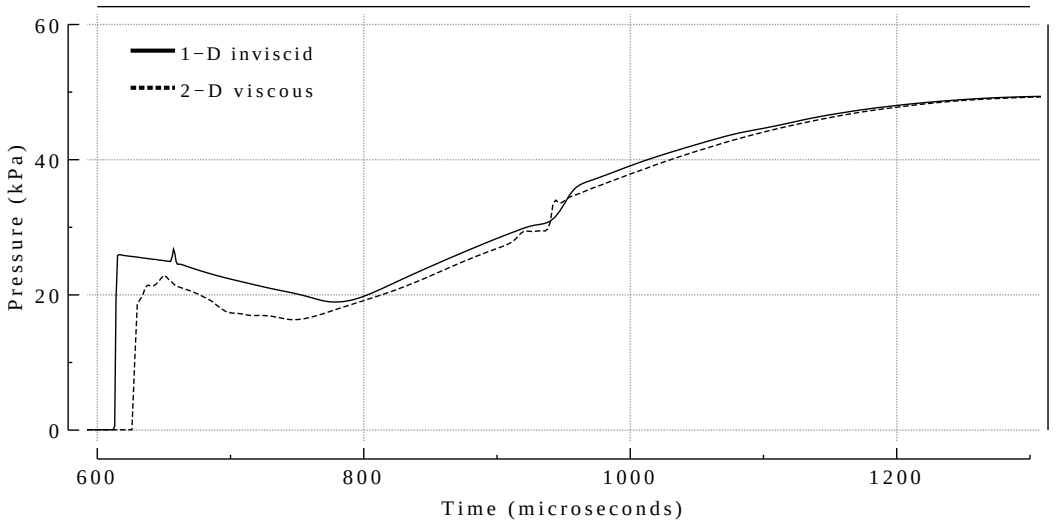

FIGURE 3.37: Static pressure history recorded at the end of the 5.05 m X2 acceleration tube. Comparison of results from inviscid one-dimensional (1-D) and viscous axisymmetric (2-D) simulations. (Condition 1).

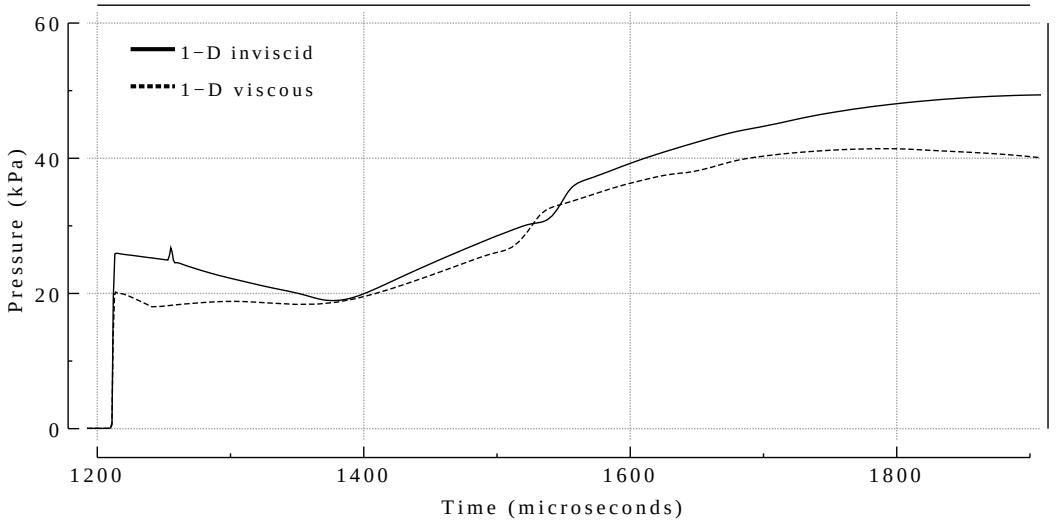

FIGURE 3.38: Static pressure history recorded at the end of the 5.05 m X2 acceleration tube. Comparison of results from inviscid and viscous one-dimensional simulations. (Condition 1)

indicate that the one dimensional technique achieves similar results to the more computationally expensive axisymmetric technique and thus provides a quick and reliable means of simulating these hypersonic flows.

3.6 Summary

The accurate reliable simulation of the flow within an expansion tube is by no means a trivial task. This chapter has investigated the use of various simulation techniques to model the complex flow within the X2 expansion tube. It has been shown that when targeting hypersonic atmospheric flight conditions (*i.e.* static temperatures in the vicinity of 230-270 K) in the proposed RHYFL-X expansion tube, driver sound speeds well below those capable of free-piston drivers are required at the point of diaphragm rupture. For this reason, the accurate simulation of the X2 compression process was deemed unnecessary and the simulations of this expansion tube have modelled from the point of primary diaphragm rupture onwards.

To obtain performance predictions for a proposed large-scale expansion tube, a relatively quick and reliable simulation technique is desired. Initially the one-dimensional flow simulation code *L1D* was used to model the flow up the point of secondary diaphragm rupture. The flow history was recorded at the secondary diaphragm location and then used as the inflow conditions for an axisymmetric simulation of the expansion process down the acceleration tube. All simulations in this chapter has assumed equilibrium chemistry. The results indicated that this simulation technique of combining the one-dimensional and axisymmetric codes adequately modelled the flow characteristics within an expansion tube. Good agreement was seen between simulation and experiment for the lower enthalpy X2 conditions, suggesting that the equilibrium assumption may be valid. For the high enthalpy condition, although the shock speeds and static pressures were in reasonable agreement, the Pitot pressure levels were considerably underestimated. While some error in the acceleration tube fill pressure is believed to exist, this would not account for the large discrepancies in Pitot pressure. For the high enthalpy condition, CPU times were almost 200 hrs and the solutions obtained were still not independent of the grid. For a facility the size of the proposed

RHYFL-X expansion tube (>20 m acceleration tube), these full axisymmetric simulations are not currently a feasible means of establishing a predicted performance envelope. For the same grid resolution as used in the X2 simulations, the ∼10 times greater cross-sectional area combined with having to solve to a simulated time four times as long would result in CPU times in the proximity of 8000 hours using a 600 MHz processor (Origin 3000). Assuming that the simulation can be performed in parallel utilizing 4 processors, CPU speeds of around 7 GHz would be required to enable such a simulation in a practical time frame of 7 days.

In order to be able to predict the overall performance capabilities of a large-scale expansion tube and to investigate the effects of various phenomena on expansion tube flow in a practical time-frame, one-dimensional simulations of the entire expansion tube process are suggested. Both viscous and inviscid one-dimensional simulations were performed of the X2 expansion tube and compared to the results obtained from the axisymmetric simulations. This one-dimensional simulation approach resulted in a 3 orders of magnitude reduction in CPU time and gave results that matched reasonably well with the viscous axisymmetric simulations. The viscous one-dimensional simulations agreed well with static pressure and shock speed but underestimated the flow speed. By turning the viscous terms off, the test flow speed and temperature matched well with the axisymmetric simulations, but the higher shock speed in the inviscid simulations resulted in a higher static pressure. The next chapter uses inviscid one-dimensional simulations to investigate the effect of finite-rate chemistry on expansion tube flow calculations and to determine the validity of using equilibrium chemistry when modelling expansion tube flow.

Chapter 4

Nonequilibrium Chemistry Effects

4.1 Introduction

To obtain an increased knowledge of the test flow properties in a high-enthalpy expansion tube, accurate simulations which include high temperature chemistry effects must be performed of the whole facility. In the early 1990's, Wilson [50] showed that with air as the test gas in the HYPULSE facility, the reflected shock at the secondary diaphragm can lead to significant dissociation of the test gas even after it has been fully expanded. Subsequent axisymmetric simulations by Wilson *et al* [52] of a nitrogen condition in HYPULSE showed that while there was significant finite-rate chemistry effects in the accelerator gas, there was minimal nonequilibrium behaviour in the expanded test gas at speeds of approximately 5 km/s. More recently, studies by Wegener *et al* [61] and Sutcliffe [76] found that nonequilibrium chemical processes were influential in carbon dioxide test flows at speeds between 7 and 9 km/s in the X1 expansion tube, but showed a trend towards equilibrium at higher enthalpies of 11 and 13 km/s.

This chapter aims to quantitatively determine the effects of finite-rate chemistry in two established operating conditions of the X2 expansion tube and in doing so investigate the validity of assuming equilibrium flow in expansion tube calculations and simulations. The first condition examined has an experimental final shock speed of 6.8 km/s (Condition 2 from Chapter 3) while the second condition is a higher enthalpy 9.7 km/s condition (Condition 4).

As the previous chapter demonstrated the suitability of using one-dimensional simulations to model expansion tube flow, the one-dimensional flow simulation code *L1D* was employed for this investigation into finite-rate chemistry phenomena in expansion tube flow. Each condition uses air as both the test and accelerator gas. Therefore the finite-rate chemistry module incorporated into *L1D* uses a 5 species, 17 reaction, model for air (Appendix A). These finite-rate chemistry simulations are compared with equilibrium simulations to determine the effects that finite-rate chemistry has on the flow at various stages during the operational cycle. The simulation results are also compared with experimental data.

4.2 Flow Dissociation in an Expansion Tube

In an expansion tube, an increase in primary shock speed results in an increase in the temperature and velocity of the shock-processed test gas. Hence, the strength of this primary shock determines the magnitude of dissociation in this test gas prior to expansion. Figures 4.1(a) and 4.1(b) show the normalized mass-fraction of O_2 and N_2 in air as a function of the speed of a shock that is passed through it. The normalized mass-fraction is the mass-fraction of each species divided by the mass-fraction of that species in air at standard conditions. The two traces on each plot refer to the initial fill pressure of air in the shock tube. The solid line corresponds to air that had an initial pressure of 10 kPa and the dashed line refers to an initial pressure of 100 kPa. These mass-fractions have been calculated using the EQSTATE [77] routines developed at GASL that utilise the CREK chemistry package of Pratt [78]. While the plot of N_2 mass-fraction (Figure 4.1(b)) indicates that dissociation of N_2 will not be significant until shock speeds of over 5 km/s, Figure 4.1(a) shows that shock speeds in excess of approximately 2.2-2.3 km/s will result in rapidly increasing levels of O_2 dissociation. If primary shock speeds are kept below these speeds corresponding to O_2 dissociation, the issue of recombination and test flow dissociation will be avoided. For primary shock speeds corresponding to noticeable dissociation in the test gas, the level of dissociation in the final test flow will depend on the amount of recombination that occurs during the unsteady expansion centered about the secondary diaphragm. As the X2 facility operates with typical primary shock speeds in the range of 3.8-5 km/s, it is important to

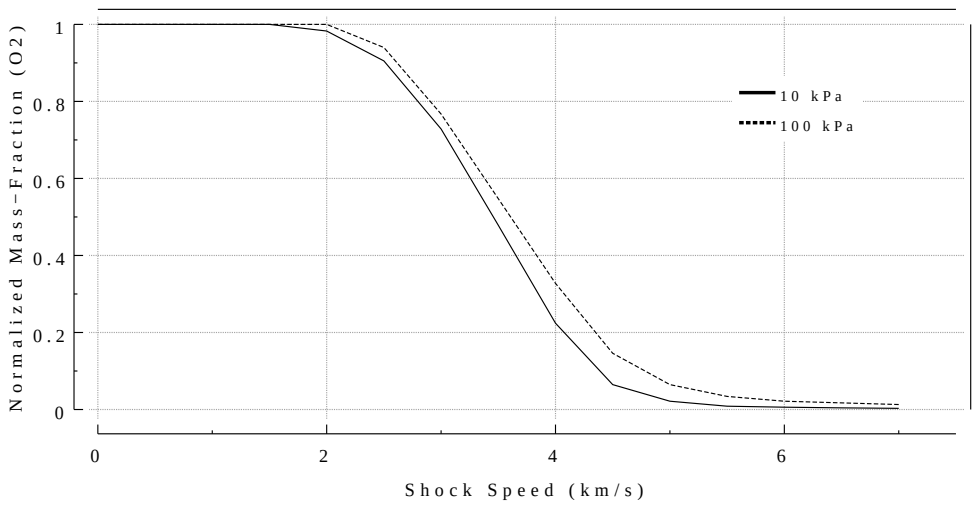

a) O_2 mass-fraction

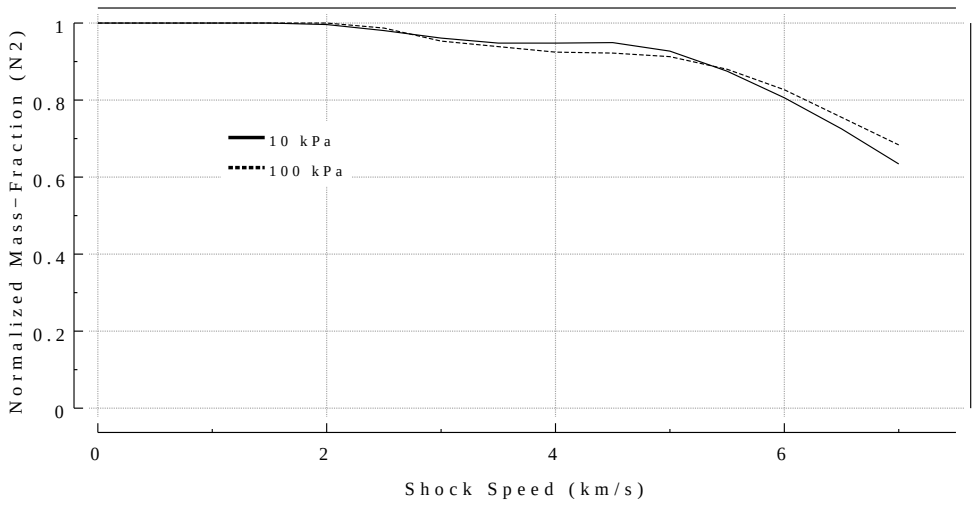

b) N_2 mass-fraction

Figure 4.1: Normalised mass-fraction of O_2 and N_2 in air as a function of shock speed (equilibrium chemistry).

accurately model the chemistry behaviour during this expansion process in order to obtain an accurate description of the test flow properties and composition.

4.2.1 Influence of the Secondary Diaphragm

In the ideal operation of an expansion tube, the secondary diaphragm is assumed to evaporate the instant the primary shock reaches it. In reality, the inertia of the diaphragm material

results in a small reflected shock being formed. This reverse shock would compound the dissociation issue by further increasing the temperature of the test flow prior to expansion. As the test flow originates from test gas that is within a few millimetres of the secondary diaphragm prior to rupture, it is important to model the effects of this reverse shock. All simulations in this work have implemented a 10μs hold-time on the secondary diaphragm to capture the effects of the reverse shock.

4.3 Finite-Rate Chemistry Model

The nonequilibrium chemistry simulations of the X2 expansion tube involved incorporating a finite-rate chemistry package into the Lagrangian one-dimensional code *L1D*. This finite-rate chemistry package utilized a 5 species, 17 reaction model for air. The forward and backward reaction rates are calculated using a modified Arrhenius expression of the form

$$k_f = A_f T^{B_f} \exp(-T_{D_f}/T) \tag{4.1}$$

where A_f and B_f are constants for the reaction and T_{D_f} is the activation energy (For a detailed description of the finite-rate chemistry package, its implementation and associated test cases see Gollan [79]). The values of A_f, B_f and T_{D_f} were obtained from Gupta [80]. The input file `air.chm` lists the reactions and the values of the constants, and is listed in Appendix A. The simulations were also performed using equilibrium chemistry based on 'Equation of State' data produced by the CEA program [60]. This allowed for a direct comparison between the two chemistry models and to determine where in the operational cycle the equilibrium assumption is valid and where finite-rate chemistry phenomena become significant.

4.4 Finite-Rate Chemistry Simulations of X2

4.4.1 Condition 2 (low-enthalpy)

The equilibrium solutions using the axisymmetric code have shown good agreement with the low enthalpy X2 experiments (Section 3.4). This may suggest that the flow chemistry

is approaching an equilibrium state during operation. To investigate finite-rate chemistry phenomena in expansion tube flow, nonequilibrium simulations were performed assuming inviscid flow. While the simulated shock speeds will be higher using the inviscid approximation, the speed of the actual test gas is very close to the shock speed measured experimentally. Due to the Mirels effect, the test flow in the experiments is assumed to be the same as the shock speed. This was shown in Section 3.5 (Figure 3.32) where the axisymmetric simulations result in a test gas velocity that is very similar to the shock speed.

Table 4.1 outlines the initial conditions used in the one-dimensional simulations of this condition. Table 4.2 outlines the geometry and number of cells used in the simulations, with section numbers corresponding to those in Figure 3.30. The cells in the driver gas slug

Table 4.1: Initial conditions for the *L1D* simulations of Condition 2 (low-enthalpy).

Shock Tube Fill, p_1 (air)	7.5 kPa
Accelerator Tube Fill, p_5 (air)	30 Pa
Primary Diaphragm Rupture Pressure, p_4	26 MPa
Driver Gas Rupture Temperature, T_4	2100 K
Secondary Diaphragm Rupture Pressure	45 kPa

Table 4.2: *L1D* simulation geometry of the X2 expansion tube for Condition 2.

Section	1	2	3
Name	Driver	Shock tube	Acceleration tube
Length	115 mm	2.35 m	5.1 m
No of cells	70	500	300

were clustered towards the primary diaphragm (between sections 1 and 2) and the cells in the shock tube were clustered towards the secondary diaphragm (between sections 2 and 3). This clustering aimed to reduce the size of the cells after expansion. This is of particular importance at the secondary diaphragm for the higher enthalpy conditions so that the extreme expansion does not result in very large cells in the expanded test gas. The *L1D* input files for the equilibrium (`s506_10hold.Lp`) and finite-rate chemistry (`s506_10hold_noneq.Lp`) low-enthalpy simulations are included in Appendix B.

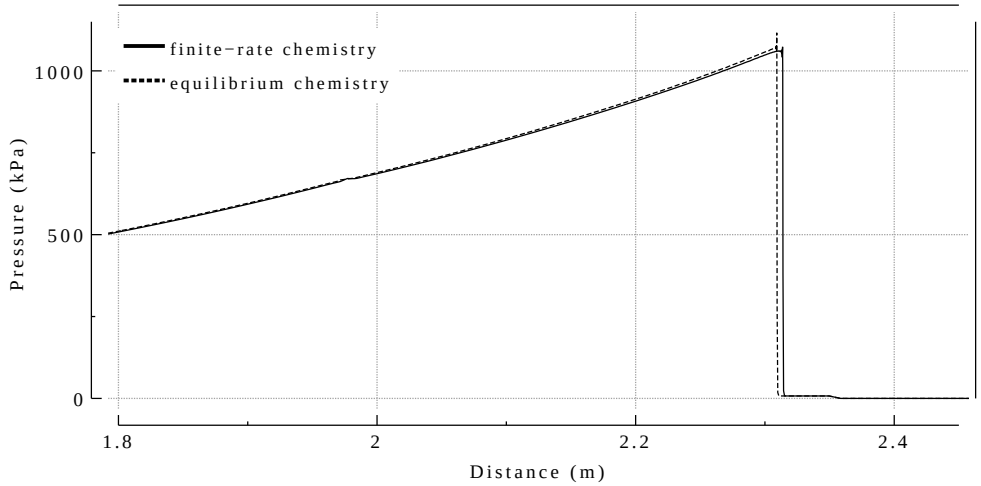

a) Pressure

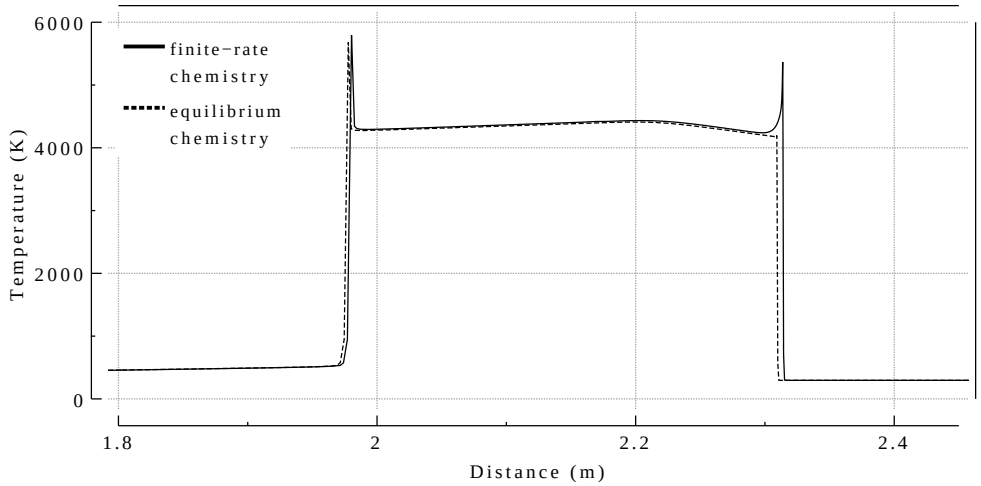

b) Temperature

FIGURE 4.2: Results from equilibrium and nonequilibrium one-dimensional simulations when the shock is at the end of the shock tube for Condition 2 (low-enthalpy).

Figure 4.2 (a) is a plot of the pressure of the shock heated test gas for both the equilibrium and finite-rate chemistry simulations. As can be seen from this figure, there is excellent agreement between these two traces with only a fraction of a percent ($\sim$0.2%) increase in the shock speed for the finite-rate chemistry solution. Figure 4.2 (b) is a plot of the temperature at the same point in time. This figure indicates that while the equilibrium solution jumps straight to the post-shock equilibrium temperature, the non-equilibrium solution has the initial temperature spike following the shock. This corresponds to the small region of gas

just behind the shock where the chemical reactions have not had sufficient time to reach an equilibrium state. Once these reactions have had time to complete, energy is consumed by these dissociation reactions and the temperature returns to the equilibrium level. The spikes that are noticeable on both temperature traces at the interface between the expanded driver gas and the shock processed test gas (x=1.98 m Figure 4.2 (b)) are numerical artifacts associated with the transfer of data between the two gas types at the interface.

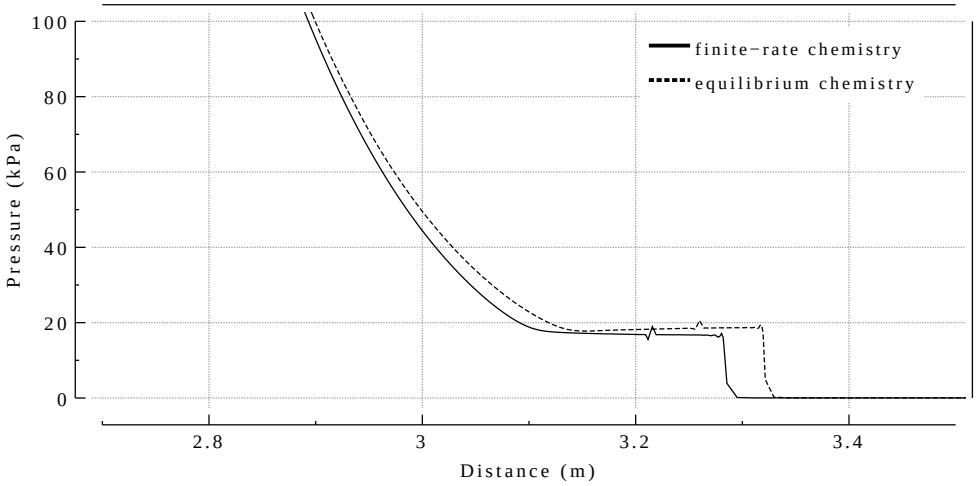

a) Pressure

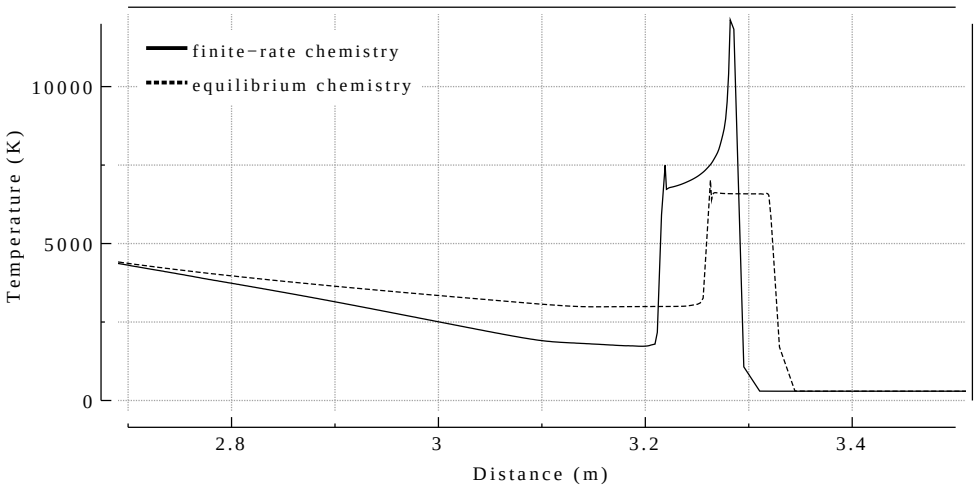

b) Temperature

Figure 4.3: Results from equilibrium and nonequilibrium one-dimensional simulations when the shock is approximately 1 m down the acceleration tube for Condition 2 (low-enthalpy).

Figure 4.3 (a) is a plot of the pressure when the shock is approximately 1 m down the

acceleration tube. Evident in this figure is a ∼4% slower secondary shock speed for the finite-rate chemistry simulation. Linked with this is a 7% reduction in the static pressure level. A plot of the temperature at the same location (Figure 4.3 (b)) shows that the temperature of the expanded test gas in the finite-rate chemistry simulation (1830 K) is only around 60% of that simulated using equilibrium chemistry (2955 K). The energy of formation is "tied-up" in the dissociated molecules resulting in a substantially cooler temperature than if the gas is assumed to reach chemical equilibrium during each time step. By the end of the acceleration tube, the temperature of the expanded test gas slightly increases (5-6%) in the non-equilibrium simulation due to the small amount of recombination that occurs as the flow travels down the tube.

As mentioned previously, the secondary diaphragm is assumed to hold in place for 10μs before being instantaneously removed. This results in a very rapid expansion of the cells near the diaphragm. In reality, the shearing off of the diaphragm would add inertia to the flow and may decrease this rapid rate of expansion [81]. Wheatley [73] performed simulations examining this effect of diaphragm inertia. He found little difference in the final temperature between simulations that modelled the diaphragm as a light piston that travelled a certain distance downstream before being removed and simulations that simply assumed a hold time of 10μs before being instantaneously removed. These simulations however were with a nitrogen test gas which is seen to recombine more rapidly than the oxygen present in the air test gas in the current simulations.

The temperature of the expanded test gas in the equilibrium simulation remains constant at 2955 K as the expanded test gas travels along the acceleration tube. Figure 4.4 (b) is a plot of the temperature at a point in time when the shock has reached the end of the acceleration tube. This plot shows that the non-equilibrium shock speed is still around 4% less than the equilibrium shock speed at the end of the acceleration tube. This is supported by the ∼7% decrease in static pressure for the non-equilibrium simulations evident in Figure 4.4 (a).

With the pressure being in relatively good agreement at the end of the acceleration tube between the two simulations and the temperature being noticeably less for the non-equilibrium simulation, one might expect the density, and hence Pitot pressure to be higher

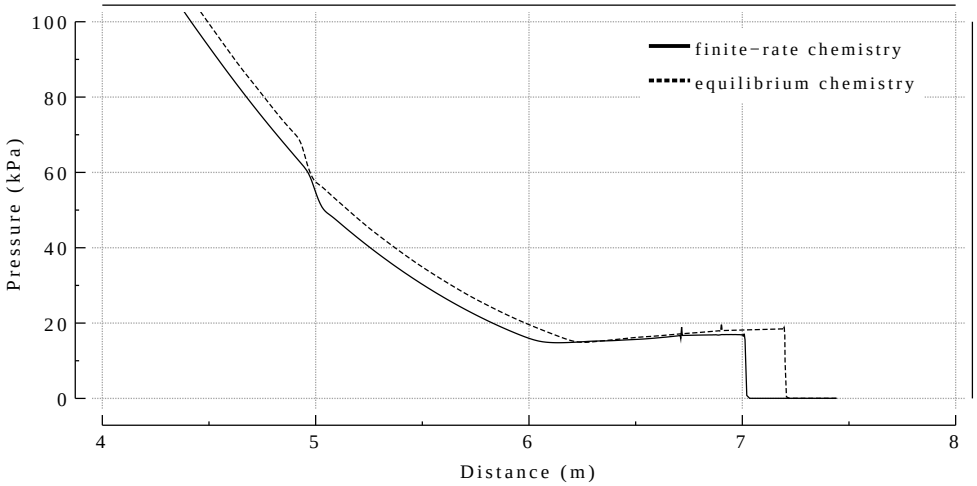

a) Pressure

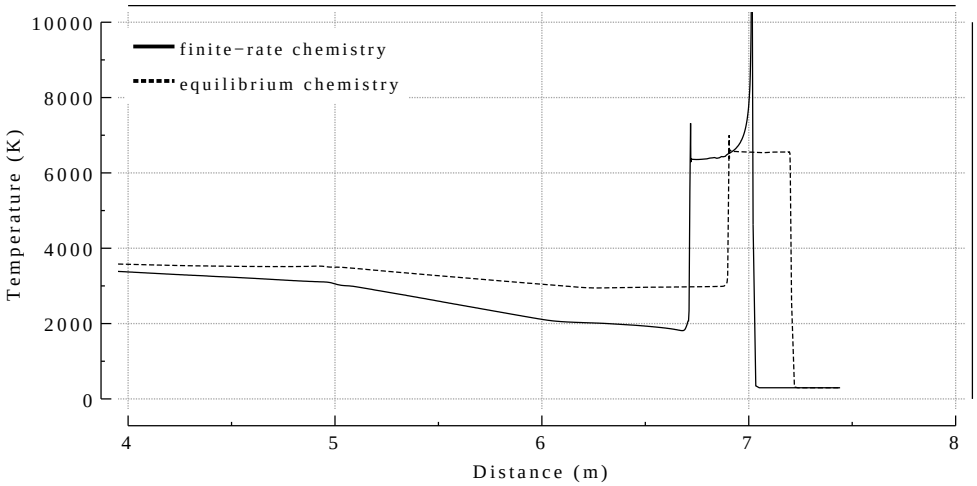

b) Temperature

Figure 4.4: Results from equilibrium and nonequilibrium one-dimensional simulations when the shock has reached the end of the acceleration tube for Condition 2 (low-enthalpy).

for the non-equilibrium simulation. However, the higher dissociation level of the non-equilibrium test gas results in a larger value for the gas constant, R. For this condition, the net result of the nonequilibrium simulation is a slight decrease ($\sim$5%) in the Pitot pressure at the end of the acceleration tube, as can be seen in Figure 4.5 Although there is a significant difference in temperature between the two simulations, Figure 4.6 shows that there is little difference in the Mach number of the test gas as it exits the acceleration

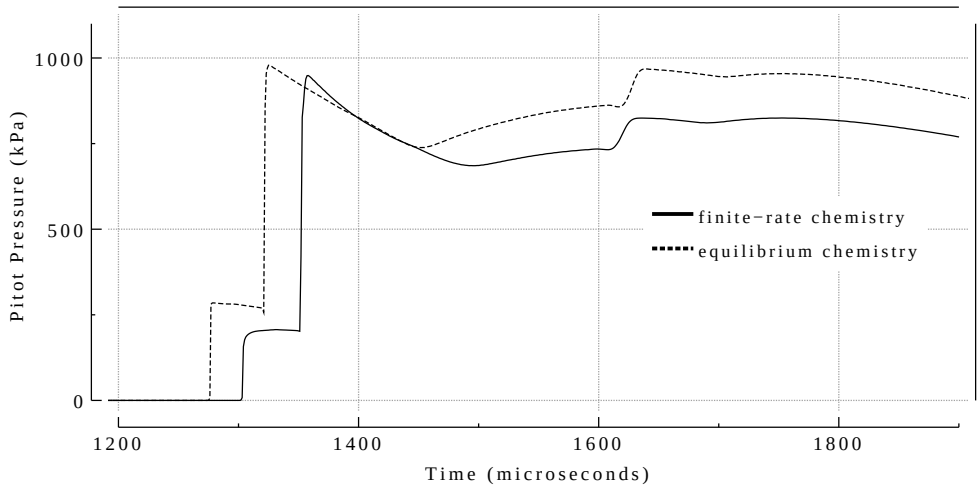

FIGURE 4.5: Pitot pressure history traces taken at the end of the acceleration tube for the finite-rate and equilibrium simulations of Condition 2 (low-enthalpy).

tube. The Mach number of the expanded test gas in the non-equilibrium chemistry simulation begins almost 6% higher ($M_{finite-rate}$=7.24) than that simulated assuming equilibrium chemistry (M_{equil}=6.84) but drops to a value essentially the same as that obtained from the equilibrium chemistry simulation by the end of the $\sim$115μs simulated test time. This drop in Mach number over the test time when using finite-rate chemistry is due to the increasing temperature of the test gas caused by the increasing levels of recombination.

Final Test Flow Properties

The directly comparable finite-rate and equilibrium chemistry one-dimensional simulations allows the decoupling of the effects of the finite-rate chemistry for this condition. Figure 4.7 shows two temperature histories at the exit plane of the acceleration tube. The solid line is using finite-rate chemistry and the dashed line has assumed chemical equilibrium. The test flow temperature assuming chemical equilibrium is around 2955 K whilst the inclusion of finite-rate chemistry reduced this temperature by around 34% to 1945 K. The axisymmetric equilibrium simulation of this conditions from Chapter 3 had a test flow temperature of 2868 K. Multiplying this by the same factor to decouple the effects of finite-rate chemistry gives a temperature of 1887 K. Table 4.3 lists the average test flow properties for both the

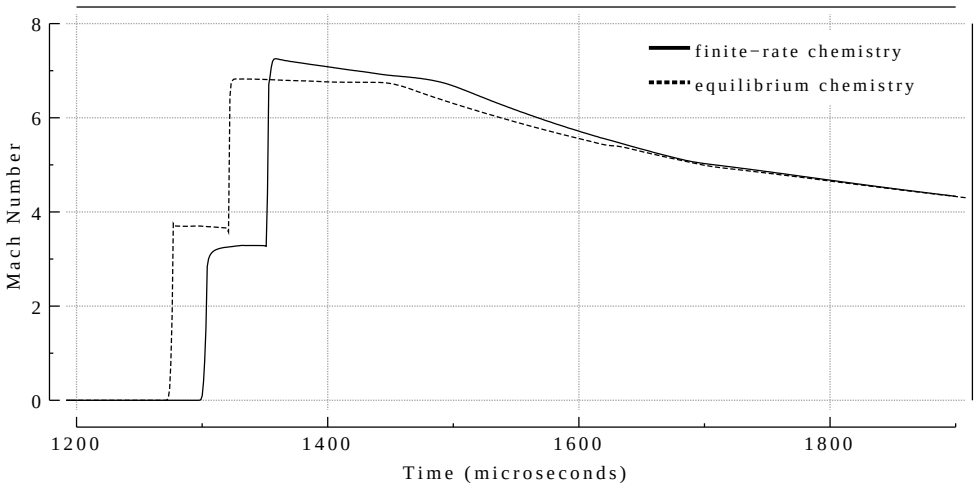

Figure 4.6: Mach number history traces taken at the end of the acceleration tube for the finite-rate and equilibrium simulations of Condition 2 (low-enthalpy).

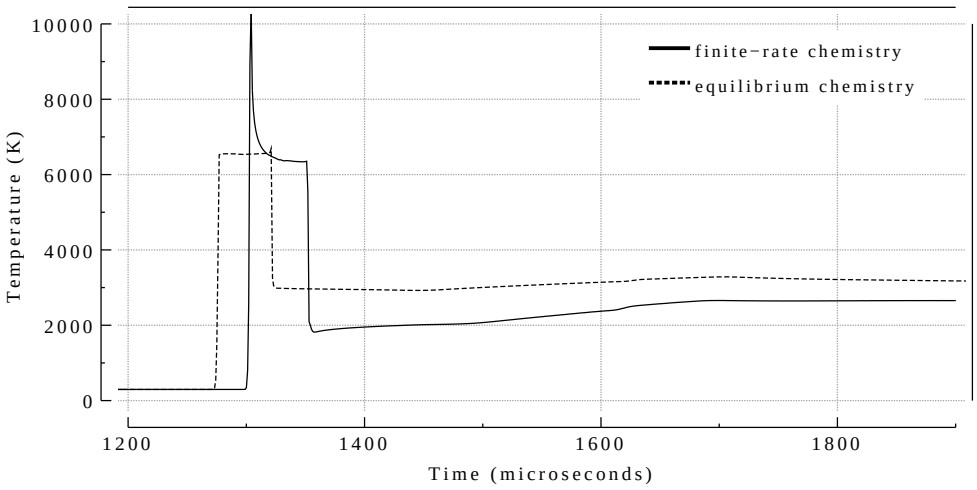

Figure 4.7: Temperature histories at the end of the acceleration tube obtained from inviscid one-dimensional simulations for Condition 2 (low-enthalpy).

finite-rate and equilibrium chemistry inviscid one-dimensional simulations compared with the average experimentally measured values of pressure, flow speed (assumed equal to shock speed) and Pitot pressure. Also in this table is a correction factor which is the quantitative amount that the finite-rate chemistry effects that parameter when compared to the equilibrium results for this particular condition. The correction factor, C_f, is defined by the equation

$$q_{finite-rate} = q_{equil} * C_f \tag{4.2}$$

where q is the quantity of interest. The static pressures in this table correspond to the wall pressures measured 0.72 m upstream from the acceleration tube exit. All other parameters correspond to the flow as it exits the acceleration tube. Recall that the simulations are being run with no viscous effects and are expected to have higher shock speeds and thus pressures than the physical experiment.

Table 4.3: Average test flow properties obtained from inviscid one-dimensional simulations of Condition 2 (equilibrium and finite-rate chemistry) compared with experimental results.

	Experiment	Equilibrium Chemistry	Finite-Rate Chemistry	Correction Factor, C_f
Pressure (kPa)	12.2	15.75	14.7	0.933
Temperature (K)	-	2955	1945	0.658
Density (kg/m^3)	-	0.01775	0.0225	1.268
Shock speed (km/s)	6.8	7.45	7.1	0.953
Flow speed (km/s)	6.8	6.87	6.61	0.962
Sound speed (km/s)	-	1012	932	0.921
Mach number	-	6.8	7.08	1.041
Pitot pressure kPa	680	865	825	0.954
R, $J/(kg.K)$	-	301	331	1.10
γ	-	1.152	1.35	1.172

In chapter 3 it was shown that the axisymmetric simulations assuming equilibrium chemistry agreed well with experimentally measured values of static and Pitot pressure, as well as the shock speed. Table 4.3 indicates that finite-rate chemistry has only a small effect on these parameters for this low enthalpy condition. The inclusion of finite-rate chemistry does

however have a more significant effect on the temperature (decrease by 34%), density (increase by 27%), the specific heats ratio γ (increase by 17%) and the gas constant R (increase by 10%).

Table 4.4 lists the average test flow properties obtained from the axisymmetric simulation of this low enthalpy condition in the previous chapter. Each value is then multiplied by the corresponding correction factor, C_f, from Table 4.3 to obtain the corrected test flow properties for this condition. Note that the static pressure stated in this table is the pressure in the core flow at the exit of the acceleration tube.

Table 4.4: Test flow properties from the axisymmetric equilibrium simulation and the corrected final test flow properties (accounting for finite-rate chemistry effects) for Condition 2 (low-enthalpy).

	Axisymmetric Simulation	Corrected Values
Pressure (kPa)	12.3	11.5
Temperature (K)	2868	1887
Density (kg/m^3)	0.0141	0.0179
Shock speed (km/s)	7.07	6.74
Flow speed (km/s)	7.0	6.73
Mach number	7.0	7.29
Pitot pressure (kPa)	719	686
Total pressure (GPa)	0.57	2.15
Total enthalpy (MJ/kg)	28.4	24.5
R, $J/(kg.K)$	299	329
γ	1.152	1.35

Figure 3.20 (Chapter 3) showed that the static pressure trace from the equilibrium axisymmetric simulation is approximately 6% more than the experimental trace over the first 90 microseconds or so of test flow. The one-dimensional inviscid simulations have demonstrated that the finite-rate chemistry has the effect of reducing the static pressure by ∼6-7% (Table 4.3). Figure 4.8 is a plot of the static pressure obtained from the axisymmetric equilibrium simulation adjusted with this corresponding correction factor. This plot shows excellent agreement between the simulation trace adjusted to account for nonequilibrium chemistry effects and the experimental trace. Also showing good agreement with experimental mea-

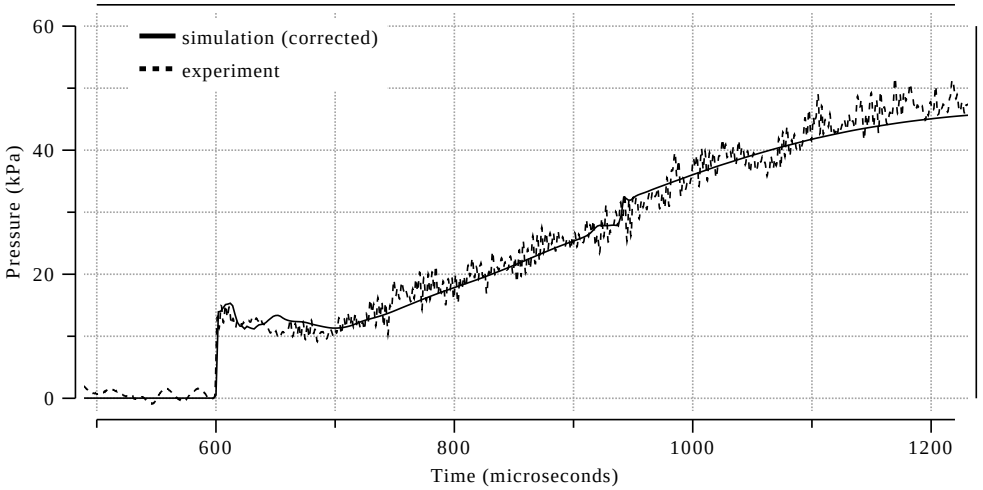

FIGURE 4.8: Plot of the corrected static pressure obtained from axisymmetric simulation compared with experiment for Condition 2 (low enthalpy).

surements is the corrected Pitot pressure trace shown in Figure 4.9. Note that although over 400μs of the experimental Pitot pressure trace is included, the trace is only valid for the first $\sim 80\mu$s due to the bar gauge that was used to measure the Pitot pressure.

To support the predicted final test flow properties for this low enthalpy condition, the temperature and density of the test flow can also be calculated based on the known discrepancies between the inviscid one-dimensional finite-rate chemistry simulations and the experimentally measured properties. Because the nonequilibrium simulations assumed inviscid flow, the simulated shock speeds were higher than that obtained from the experiment. As a result of this, the static pressure was higher than experimentally measured by an average of 20.5% during the test time. Figure 4.10 compares the experimental static pressure trace at a location 0.72 m from the exit of the acceleration tube with that obtained from the inviscid finite-rate chemistry one-dimensional simulation (the experimental trace was plotted so that the test gas/accelerator gas interface coincided with that of the simulation trace). The average simulated Pitot pressure was $\sim$21.3% higher than the experimentally measured level. Taking the Pitot pressure to be proportional to ρu^2 and the fact that the inviscid flow velocity, u, is 2.8% less than experiment, the simulated density, ρ, can be assumed to be 26.8% too high. As the simulated density is $0.0225\,kg/m^3$, the corrected density is $0.0177\,kg/m^3$. This

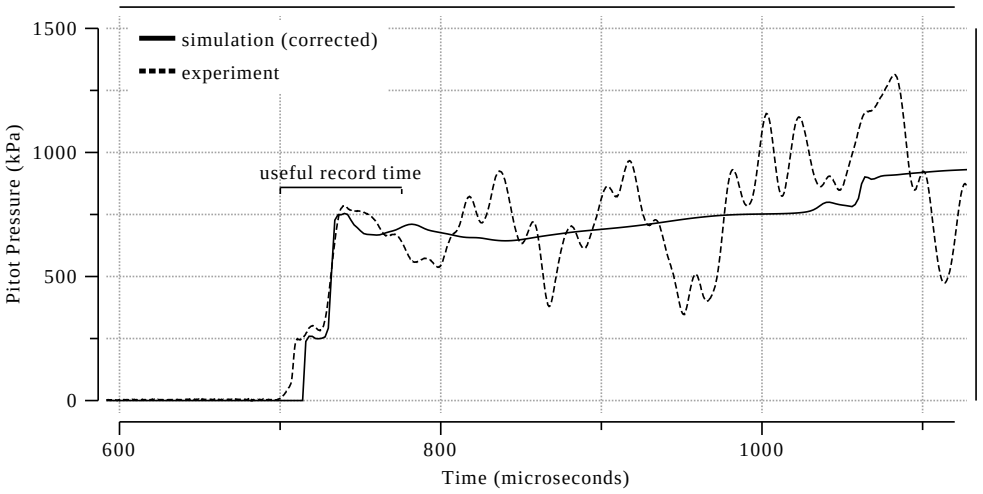

Figure 4.9: Plot of the corrected Pitot pressure obtained from axisymmetric simulation compared with experiment for Condition 2 (low enthalpy).

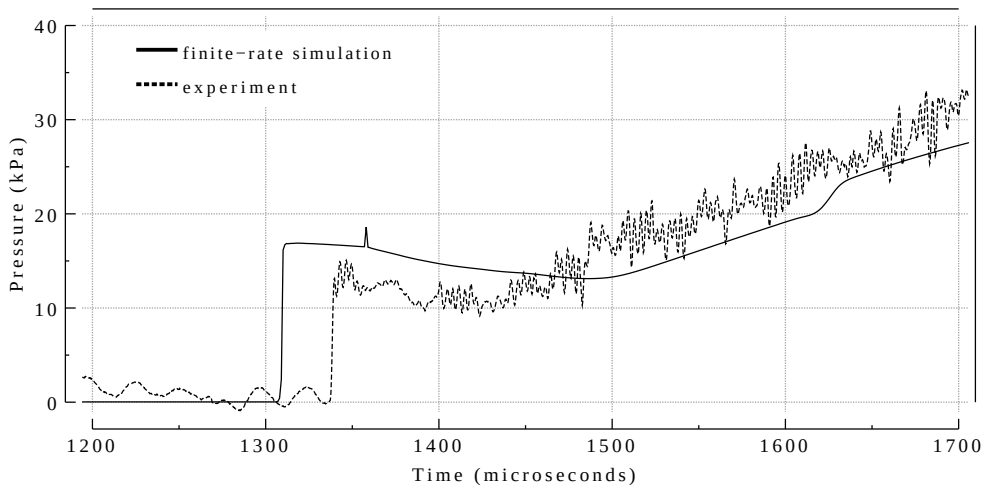

Figure 4.10: Static pressure trace obtained from the inviscid nonequilibrium chemistry one-dimensional simulation compared with experimental data for Condition 2 (low-enthalpy).

agrees very well (within ∼1%) with the density obtained from the axisymmetric simulation adjusted to account for the effects of finite-rate chemistry ($0.0179\,kg/m^3$) listed in Table 4.4. Now assuming that the gas obeys the perfect gas relation $p = \rho/(RT)$ where the simulated pressure is 20.5% too high, the density is 26.8% too high and R remains unchanged for these small perturbations in the test flow properties, the simulated temperature can be considered to be 5% lower than in the experiment. As the simulated test flow temperature from the finite-rate chemistry one-dimensional simulation is 1945 K, the actual experimental temperature can be estimated as being 2047 K. This is around 8% higher than that calculated in Table 4.4.

Test Gas Composition

For the simulations presented, the light secondary diaphragm is assumed to hold in place for 10 microseconds once the shock hits it, representing the inertial characteristics of the diaphragm material. After the 10 microseconds has elapsed, the diaphragm is instantaneously removed. The cells that were originally adjacent to the diaphragm would experience a very sudden and strong expansion. In actual operation, the diaphragm shears off around its periphery once the shock arrives and accelerates downstream in a planar orientation. This would reduce the severity of the reflected shock compared to a model where the diaphragm was held in place for a finite period of time and then suddenly released. For the test gas originally adjacent to the secondary diaphragm, the hold-time model implemented in the simulations is believed to result in a more severe expansion than in practice and may reduce the amount of recombination that occurs in the initial part of the test flow.

Table 4.5 lists the average properties and composition of the test gas both after the primary shock and in the shock-reflected region obtained from the non-equilibrium simulation. As the simulations have shown that the flow in these regions can be assumed to be in chemical equilibrium, the simulated test gas composition using the finite-rate chemsitry package has been compared to the species mass-fractions calculated using equilibrium chemistry curve-fits in the EQSTATE program at the simulated temperature and pressure. The very good agreement between the two techniques suggests that the finite-rate chemistry package

incorporated into L1D is accurately predicting the mass-fractions for the various species in an equilibrium environment. It should be noted that the EQSTATE program assumes that standard air is essentially 76.8% N_2 and 23.2% O_2 by mass (including other trace elements) whereas the finite-rate chemistry model of air used in the simulations assumes mass fractions of 78% N_2 and 22% O_2 for standard air. To compensate for this slight difference in the composition of air, the mass-fractions in the EQSTATE column are determined by obtaining the amount of N, O_2 and NO from EQSTATE and then calculating the amount of N_2 and O from conservation of mass. Also included in Table 4.5 is the percentage of the total enthalpy that is in chemical form, h_{chem}. This percentage of the enthalpy is not acted on by the enthalpy multiplication process of the unsteady expansion.

Table 4.5: Test gas composition behind the primary shock and in the shock reflected region prior to expansion for Condition 2 (low enthalpy).

	1 cm behind primary shock		Shock-reflected region	
	Simulation	EQSTATE	Simulation	EQSTATE
Pressure	1.053 MPa		10.45 MPa	
Temperature	4252 K		7190 K	
N_2	74%	74.1%	70.0%	69.8%
N	$< 0.1\%$	$< 0.1\%$	5.6%	5.5%
O_2	7.3%	7.7%	0.5%	0.5%
O	10.2%	9.9%	18.6%	18.5%
NO	8.4%	8.3%	5.3%	5.7%
h_{chem}	-	4.2%	-	27.2%
R	315	317	355	356
γ	1.31	1.31	1.32	1.34

Figure 4.11 is a history plot of four cells of test gas that are originally in the shock tube at varying distances from the secondary diaphragm. Cell A was cell number 480 in the shock tube (there were 500 cells in the shock tube clustered towards the secondary diaphragm). This cell arrived at the test section around 6μs after the arrival of the accelerator gas /test gas interface (as labelled in Figure 4.11). Cells B, C and D were cells 460, 400 and 300 respectively which arrived at the test section at times corresponding to those labelled in Figure 4.11. This figure illustrates how the cells are first processed by the primary shock to a temperature of

around 4250 K then the reflected shock increases this value to approximately 7200 K. The cells are then processed by the unsteady expansion to the final test flow conditions. The cells which are closer to the secondary diaphragm experience this expansion over a shorter period of time (closer to the focus of the unsteady expansion fan). The cells that are further from the secondary diaphragm pass through the unsteady expansion fan later in time and therefore experience the expansion over a longer period of time.

Cell A which was originally only 20 cells from the secondary diaphragm undergoes a rapid expansion to a certain temperature. After this expansion process, the recombination reactions begin to gradually increase the temperature of the cell as it travels down the acceleration tube. Cell C arrives in the test section approximately half way through the test time. Figure 4.11 shows that this cell expands more gradually but the final temperature is still similar (within approximately 5-6%) to that of the cells A and B. Cell D sees a larger section of the unsteady expansion fan and arrives at the test section after the nominal test time for this condition. All these cells have a final temperature considerably less than the average test gas temperature obtained from equilibrium simulations (marked on Figure 4.11). The fact that the temperature of these cells correspond to levels only approximately two-thirds of the equilibrium temperature indicates that the process is not in chemical equilibrium. The higher temperature of cell D is due to a combination of reasons: 1) it corresponds to flow outside of the test flow and is thus not fully expanded and 2) the fact that it has passed through a larger portion of the unsteady expansion means that it has had more time for the recombination reactions to take place and in doing so increase the static temperature of the flow.

Figure 4.12 shows the mass-fraction of N2 of the same 4 cells as in Figure 4.11. This figure shows that the mass-fraction of N2 rapidly returns to equilibrium values through the unsteady expansion. Even the cell closest to the secondary diaphragm (Cell A) goes straight to the equilibrium N2 concentration. The final N2 mass-fractions at the test section for all four cells are between 77-78%.

Figure 4.13 is a plot of the O_2 mass-fractions for these 4 cells. Cells A and B which represent the start of the final test flow undergo a rapid expansion through which the O_2

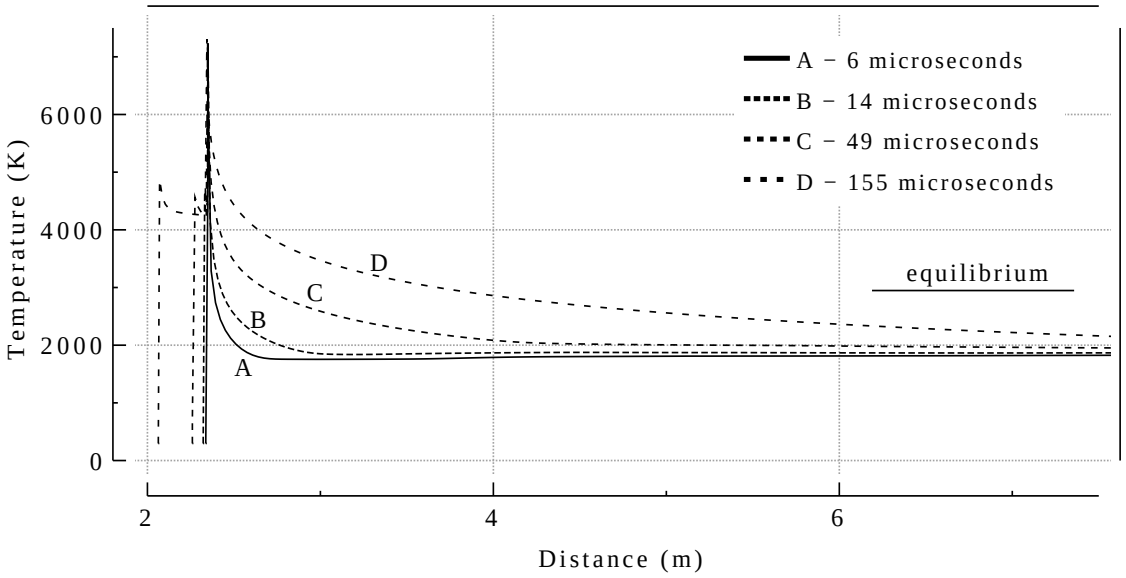

Figure 4.11: The temperature history of four elements of test gas for Condition 2 (low enthalpy) as they undergo the expansion and travel down the acceleration tube (times correspond to the arrival time at the test section after the start of the test flow).

levels are essentially frozen at the levels obtained in the reflected shock region. As these cells travel down the acceleration tube however, the amount of O_2 slowly increases as the recombination reactions begin to take place. The mass-fraction of O_2 in these cells at the test section is still only 1 or 2% higher than the levels in the reflected shock region. Cells C and D pass through the unsteady expansion fan at a later time, hence experiencing a more gradual expansion and achieving more recombination of O_2. These cells still only reach O_2 mass-fractions of around 5-6% at the end of the acceleration tube which is well below the 15-16% expected if equilibrium chemistry was assumed.

These figures show that the mass-fraction of N_2 quickly achieves equilibrium levels through the unsteady expansion for both the cells near to the secondary diaphragm as well as the cells that pass through the unsteady expansion fan at a later time. However, the recombination rate of O_2 is seen to be considerably less than that of N_2. While the levels of O_2 begin to increase, the O_2 mass-fraction at the end of the acceleration tube in the test section is well below that expected from equilibrium simulations. Figure 4.13 shows that the gas that arrives early on in the test flow has a higher level of dissociated oxygen than flow

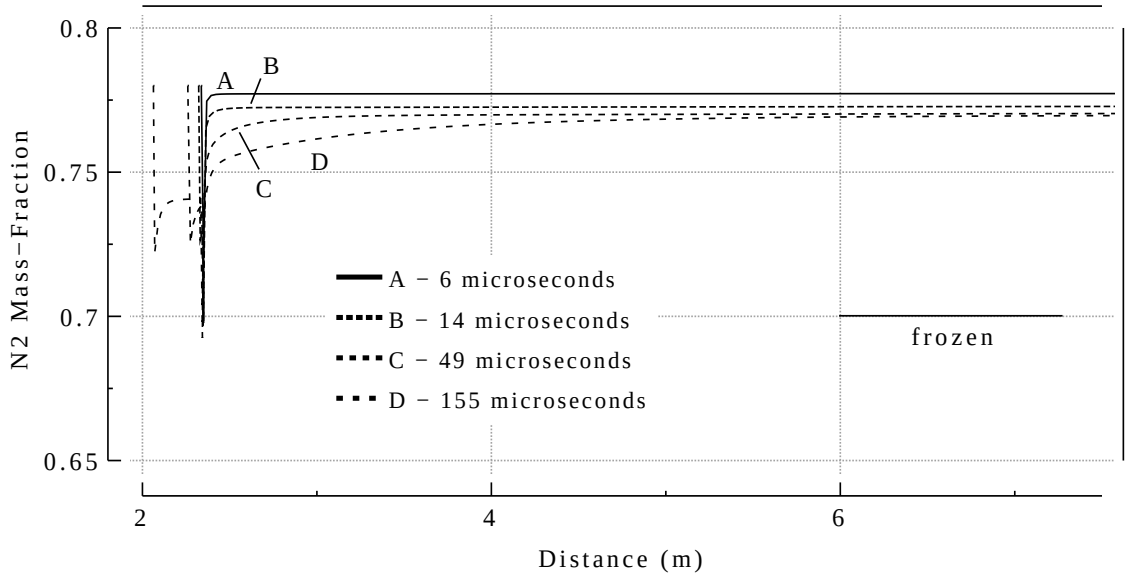

FIGURE 4.12: The N_2 mass-fraction history of 4 elements of test gas for the low enthalpy X2 condition s506 as they undergo the expansion and travel down the acceleration tube (times correspond to the arrival time at the test section after the start of the test flow).

arriving later on. Average test flow conditions will be taken around 50μs after the arrival of the test flow for two main reasons. Firstly, the dissociation of the gas in the first portion of the simulated test flow is believed to have a higher level of dissociation than in practice due to the rapid expansion caused by the diaphragm model outlined previously. Secondly, a portion of the leading test gas would be lost to the boundary layer by the time the flow arrived at the end of the acceleration tube.

Figures 4.14 and 4.15 show the history of the mass-fractions of the 5 different species at the exit plane of the acceleration tube. In Figure 4.14, the mass-fractions of N_2 and N begin at the predefined 78% and 0% respectively. When the shock reaches the test section at t=1300μs, these values jump to the dissociated levels of the shock-processed accelerator gas. Then there is another jump at t=1350μs when the test flow arrives. The mass-fraction of N_2 is around 77% and remains essentially constant. Calculations using EQSTATE show that only around 0.3% of the N_2 dissociates at these final test flow conditions. This small amount of dissociated nitrogen is used in creating NO, leaving no monotomic nitrogen (N) in the test flow. This indicates that the final values of the N_2 and N mass-fractions for the

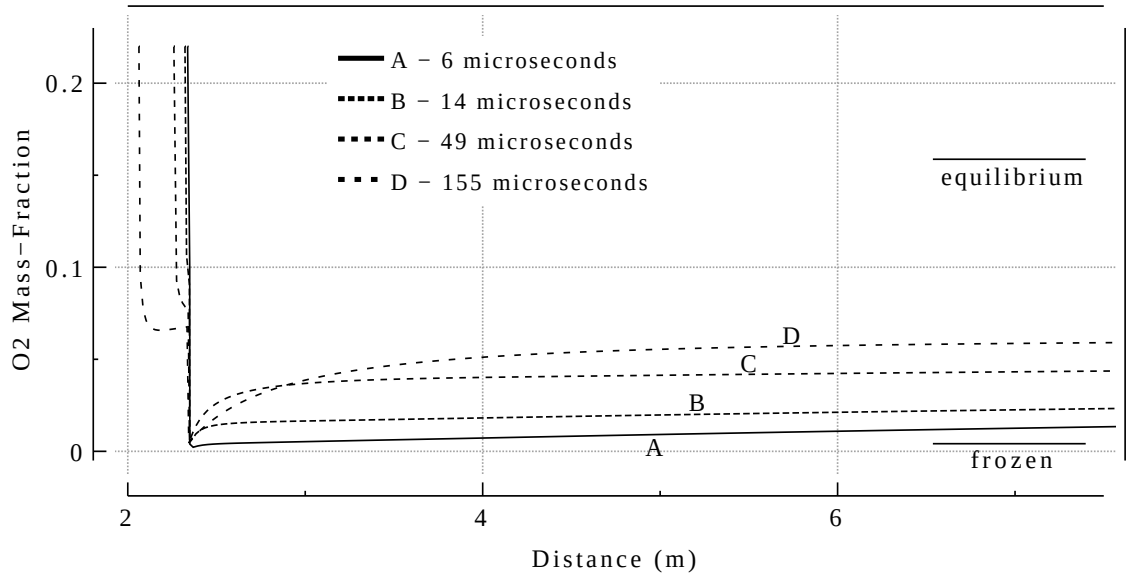

Figure 4.13: The O_2 mass-fraction history of 5 elements of test gas for condition s454 as they undergo the expansion and travel down the acceleration tube.

finite-rate chemistry simulations quickly reach equilibrium values.

Figure 4.15 shows more recombination of the oxygen later in the test flow. This is consistent with earlier statements that the initial test gas will have higher levels of dissociation due to the rapid expansion at the secondary diaphragm. As the oxygen starts to recombine (O_2 increases), the amount of monotomic oxygen (O) decreases to compensate. At a time 50μs after the test flow arrives, the mass-fractions of O_2 and O are 4.6% and 16.3% respectively, while 200-300μs after the test flow arrives, their respective mass-fractions are around 6% and 15%. The NO mass-fraction rapidly reaches around 2% and remains essentially constant over the next 200-300μs. EQSTATE calculations show that there is very little dissociation for air with the the pressure and temperature of the test gas obtained from the equilibrium simulation for this condition (primarily N_2 and O_2 with around 0.7% NO). These numbers indicate that, while the oxygen experiences a certain level of recombination as it passes through the unsteady expansion fan and continues down the acceleration tube, it is far from an equilibrium process.

Table 4.6 lists the average chemical composition of the test flow based on 1) a frozen

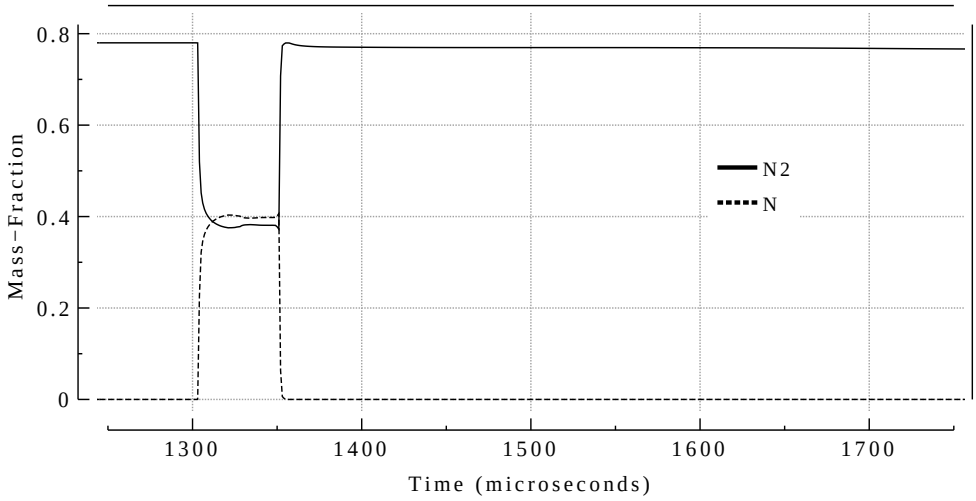

FIGURE 4.14: Mass-fractions of N_2 and N at the exit plane of the acceleration tube for the low enthalpy X2 condition s506.

Table 4.6: Final test flow composition for Condition 2 (low-enthalpy) assuming (a) frozen chemistry, (b) finite-rate chemistry and (c) equilibrium chemistry through the unsteady expansion.

	Frozen Expansion	Finite-rate Expansion	Equilibrium Expansion
N_2	70%	77.0%	76.0 %
N	5.5%	0%	0 %
O_2	0.5%	5%	15.0 %
O	18.5%	16.0%	5.0 %
NO	5.5%	2%	4.0 %
R	355	331	301
γ	1.32	1.31	1.15

expansion from equilibrium conditions behind the secondary diaphragm, 2) equilibrium flow throughout the entire process, and 3) using the finite-rate chemistry package incorporated into *L1D*. This table shows that while the mass-fractions of monotomic and diatomic nitrogen agree well with equilibrium assumptions, the oxygen species (O_2 and O) undergo a more frozen expansion process. The N_2 mass-fraction for the finite-rate chemistry simulation is slightly larger than that obtained for the equilibrium simulation due to the considerably

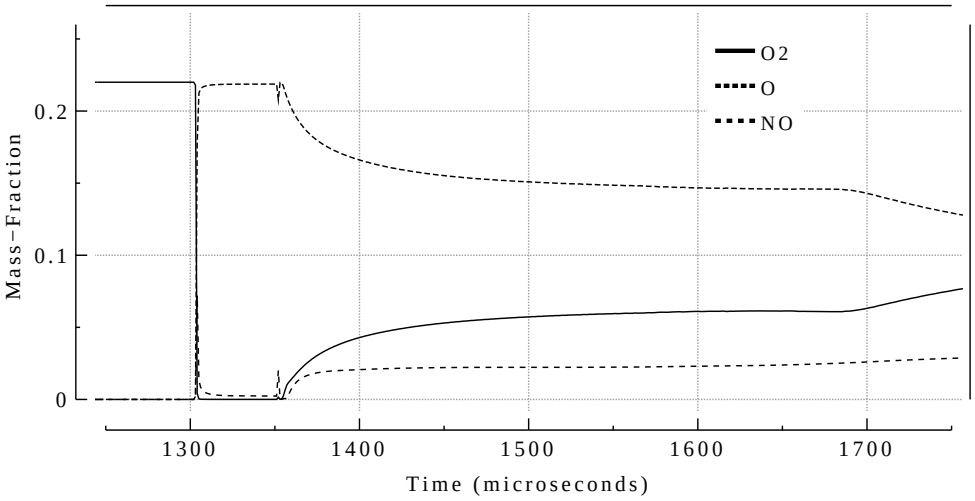

Figure 4.15: Mass-fractions of O_2, O and NO at the exit plane of the acceleration tube for condition s454.

higher temperature obtained in the equilibrium chemistry simulation.

4.4.2 Condition 4 (high-enthalpy)

As with the low enthalpy condition (Condition 2), one-dimensional simulations of the high enthalpy X2 operating condition were performed using equilibrium and non-equilibrium chemistry. This condition has a significantly faster flow speed than the conditions of interest for the proposed RHYFL-X facility, but will be examined to investigate non-equilibrium effects in higher enthalpy expansion tube flow. Table 4.7 lists the initial conditions used in the simulations. Table 4.8 shows that there was a slight increase (5%) in the length of the driver

Table 4.7: Initial conditions for the *L1D* simulations of Condition 4 (high-enthalpy).

Shock Tube Fill, p_1 (air)	2.4 kPa
Accelerator Tube Fill, p_5 (air)	0.933 Pa
Primary Diaphragm Rupture Pressure, p_4	26 MPa
Driver Gas Rupture Temperature, T_4	2100 K
Secondary Diaphragm Rupture Pressure	45 kPa

for this condition because of slightly different driver conditions. There were also more cells

used in the driver and shock-tube due to the larger pressure ratios and more severe expansions. The *L1D* input files for the equilibrium (`s833_10hold.Lp`) and finite-rate chemistry

Table 4.8: *L1D* simulation geometry of X2 expansion tube for Condition 4 (high-enthalpy).

Section	1	2	3
Name	Driver	Shock tube	Acceleration tube
Length	121 mm	2.35 m	5.1 m
No of cells	100	600	300

(`s833_10hold_noneq.Lp`) high-enthalpy simulations are also included in Appendix B.

At the end of the lower speed shock tube segment, the pressure levels between the nonequilibrium and equilibrium simulations show similar levels of agreement as the previous low enthalpy condition. Figure 4.16(a) shows the very good agreement in pressure between the two simulations. Again, the small glitch that can be seen in this figure at around 2.05 m is a numerical artifact at the interface between the driver gas and test gas. Figure 4.16(b) is a plot of the temperature of the gas in the shock tube. The relaxation zone is still seen behind the shock, with the temperature returning to the equilibrium value once the reactions have had time to reach an equilibrium state.

Figure 4.17(a) shows the pressure traces for the two simulations when the shock has travelled approximately 1 m down the acceleration tube (0.8 ms after the rupture of the secondary diaphragm). The nonequilibrium shock speed is 11-12% less than that obtained from the equilibrium simulation with a corresponding decrease in the static pressure of the gas behind shock of around 17%. The glitch at the interface is more pronounced in these simulations due to the increase in the extreme pressure ratio across the secondary diaphragm coupled with the larger cell sizes after expansion ($\sim$45 mm). Figure 4.17(b) shows the significant difference in the expanded test gas temperature immediately after expansion. The equilibrium-chemistry assumption results in a temperature of 3160 K while the non-equilibrium simulation gives a temperature of around 1210 K, only 38% of the equilibrium temperature. Also seen from this figure is the hotter shock-processed accelerator gas in the non-equilibrium simulation because of the insufficient time for the chemical reactions in this

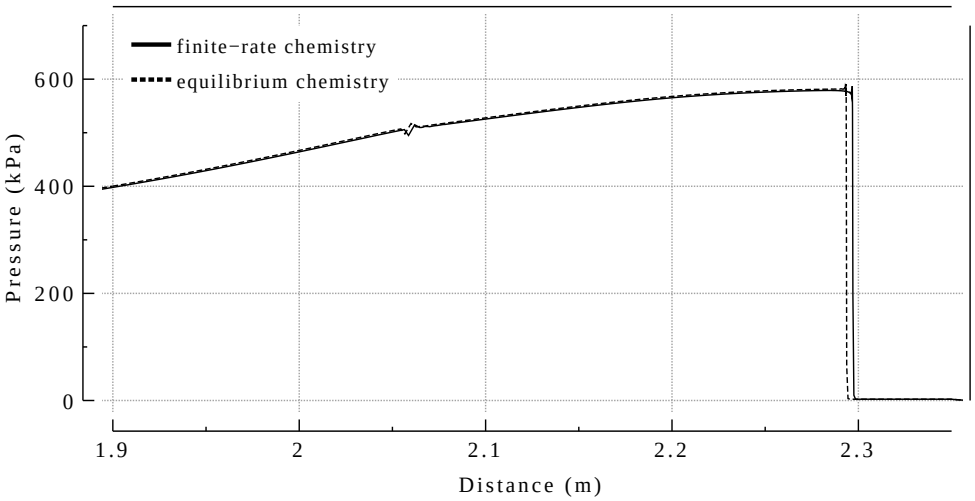

a) Pressure

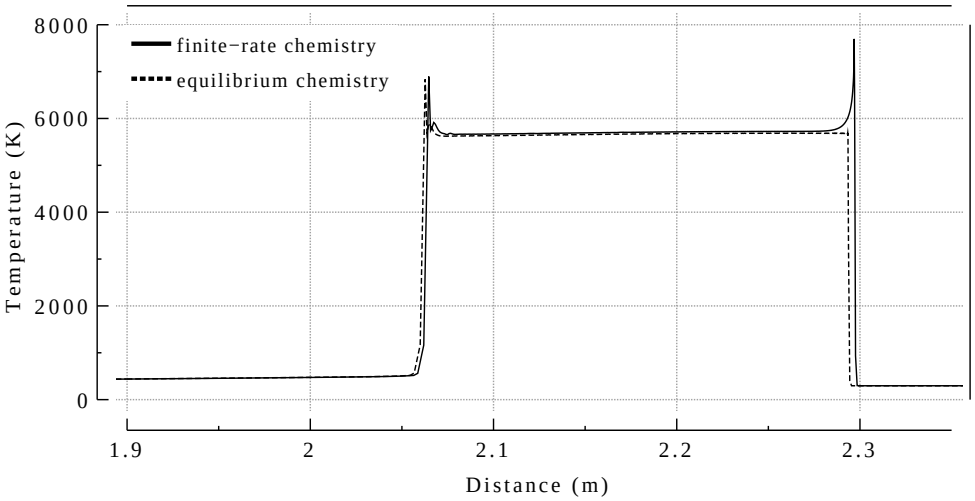

b) Temperature

Figure 4.16: Results from equilibrium and nonequilibrium simulations when the shock is at the end of the shock tube for Condition 4 (high-enthalpy).

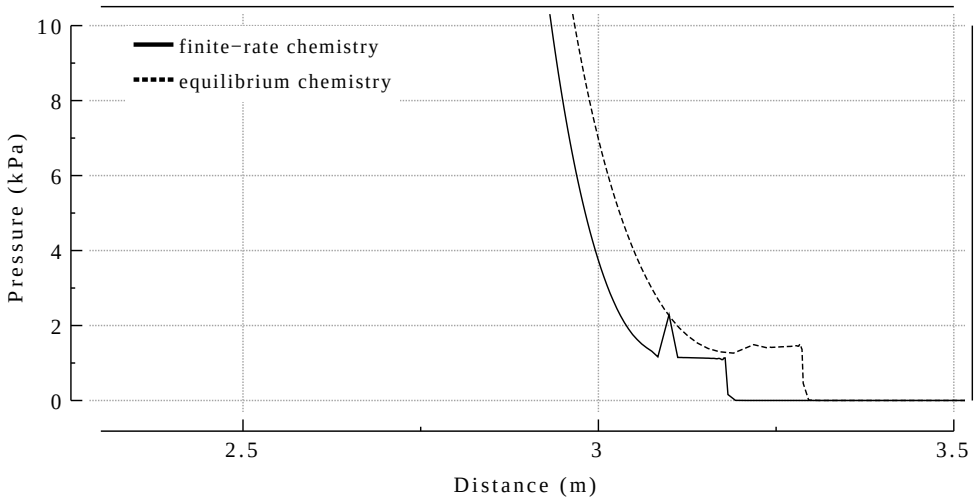

a) Pressure

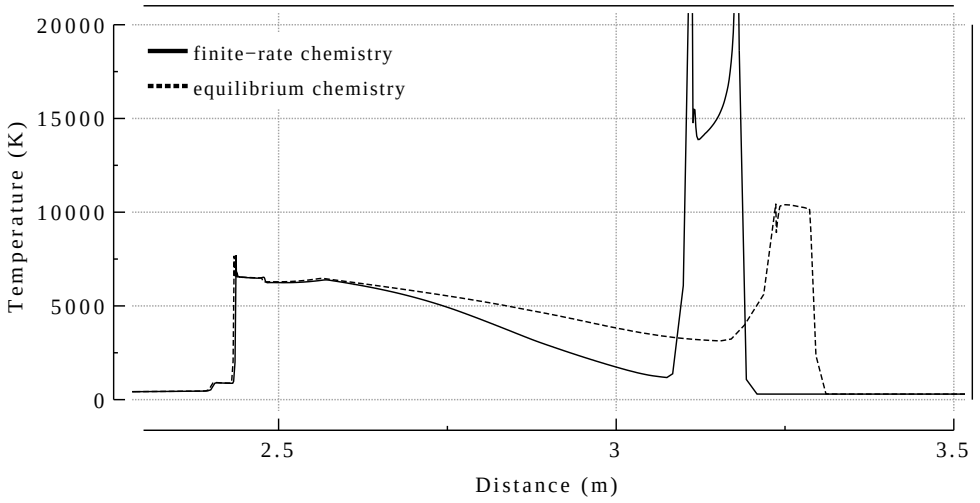

b) Temperature

FIGURE 4.17: Results from equilibrium and nonequilibrium simulations when the shock is approximately 1 m down the acceleration tube for Condition 4 (high-enthalpy).

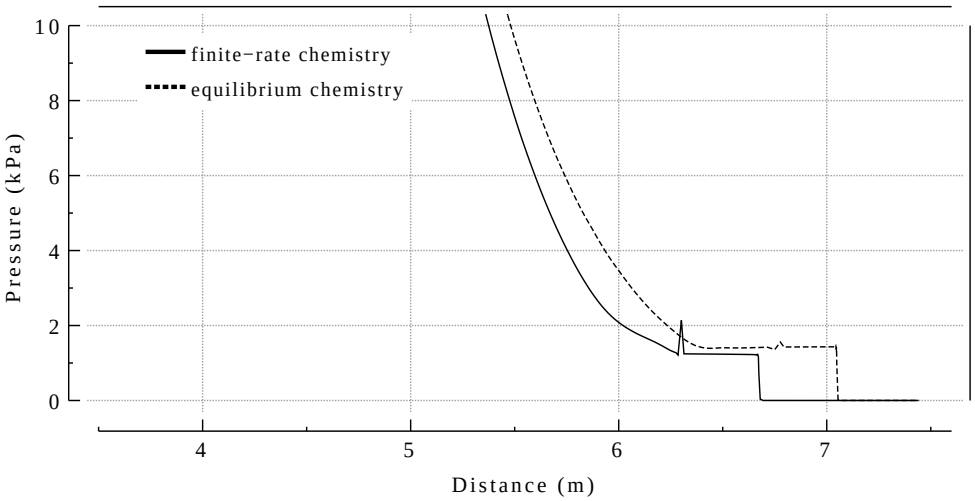

a) Pressure

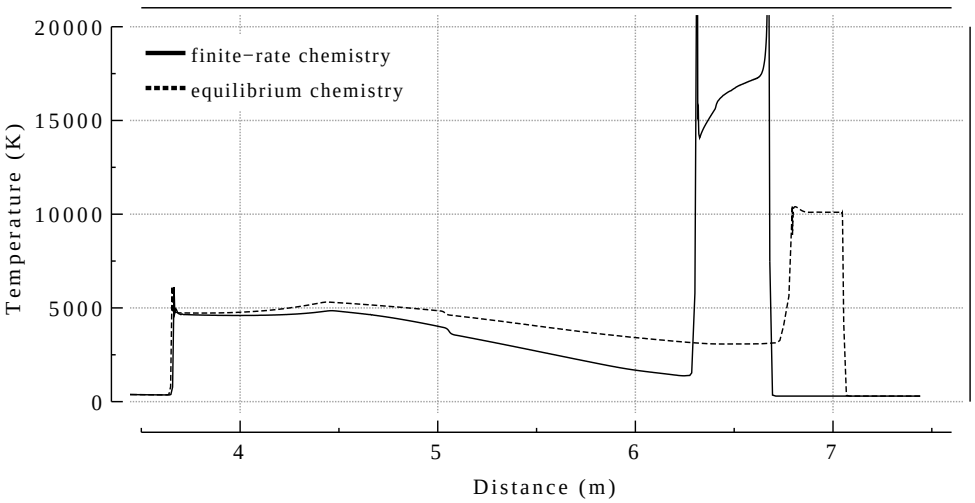

b) Temperature

Figure 4.18: Results from equilibrium and nonequilibrium simulations when the shock has reached the end of acceleration tube for Condition 4 (high-enthalpy).

region to reach an equilibrium state.

Figure 4.18(a) shows that there is approximately 0.35 ms of steady test gas pressure after the small glitch at the interface on the equilibrium trace. This is not seen in the finite-rate chemistry trace but rather a noticeable increase in pressure is observed in the expanded test gas. This is thought to be coupled to the rapid rise in temperature of the test gas in this region due to the greater amount of recombination in the gas that has passed through the unsteady expansion at a later time. The temperature traces plotted in Figure 4.18(b) indicate that the temperature of the expanded test gas in the finite-rate chemistry simulation (1390 K) is about 45% of that obtained from the simulation assuming equilibrium chemistry (3080 K).

Final Test Flow Properties

While the test time for the inviscid equilibrium simulation is evident by the period of steady pressure, as mentioned previously the finite-rate chemistry simulation results did not have this period of steady pressure. The average test flow properties for the finite-rate chemistry simulation will be the average of the first 30μs of test gas after the arrival of the interface as that was the period of steady flow seen in the equilibrium simulation. This will result in a higher pressure for the finite-rate chemistry simulation compared to the equilibrium simulation even though the shock speed was less. This can be seen in Figure 4.19 which is a plot of the static pressure time history taken at the end of the acceleration tube for the equilibrium and finite-rate chemistry simulations. Note that the time scale for the equilibrium trace has been shifted so that the interface arrival times coincide allowing the pressure levels to be directly compared.

Figure 4.20 indicates that the finite-rate chemistry has the effect of increasing the Pitot pressure of the test flow. Again the time-scale has been adjusted to allow a direct comparison of the two traces. The inviscid one-dimensional simulations show that the nonequilibrium chemistry increases the Pitot pressure by up to 28% during the test time compared to when equilibrium chemistry is assumed. The results of Section 3.4.4 showed that the axisymmetric equilibrium chemistry simulations were significantly underestimating the Pitot

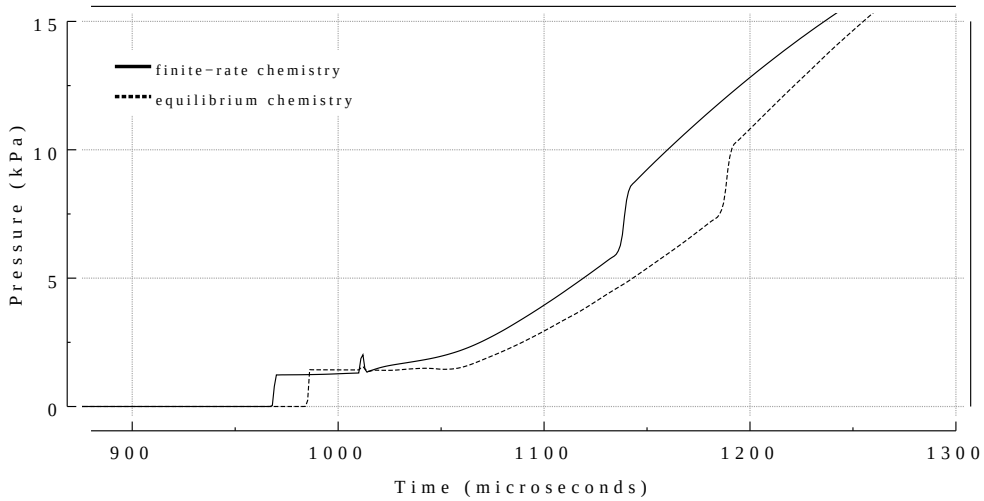

Figure 4.19: Static pressure history traces from equilibrium and non-equilibrium chemistry simulations recorded at the end of the acceleration tube for Condition 4 (high-enthalpy).

pressure levels at the end of the acceleration tube for this high enthalpy condition. These nonequilibrium results therefore suggest that the discrepancies in Pitot pressure seen between equilibrium simulations and experimental results can, to some degree, be attributed to the non-equilibrium phenomena of the flow.

Section 3.4.4 showed that the axisymmetric equilibrium chemistry simulation underestimated the static pressure on the wall towards the end of the acceleration tube by ∼38% when compared to experimental results. Although resulting in a lower static pressure, the simulations gave a final shock speed that was around 6-7% more than that measured experimentally. Mesh refinements were seen to have negligible effect on the static pressure and the shock speed obtained in these axisymmetric simulations. The higher shock speed but lower static pressure obtained from the simulations suggests that the actual fill pressure of the acceleration tube during the experiment was slightly more than that stated as the fill pressure for this condition. As the stated fill pressure for this conditions is only 0.933 Pa, a slight leak could easily result in an increase in pressure that would take a finite time to spread out over the length of the tube. One-dimensional inviscid simulations assuming equilibrium chemistry show that increasing this fill pressure by 54%, or around half a pascal, to 1.5 Pa has the effect of increasing the test flow static pressure by around 50% while only

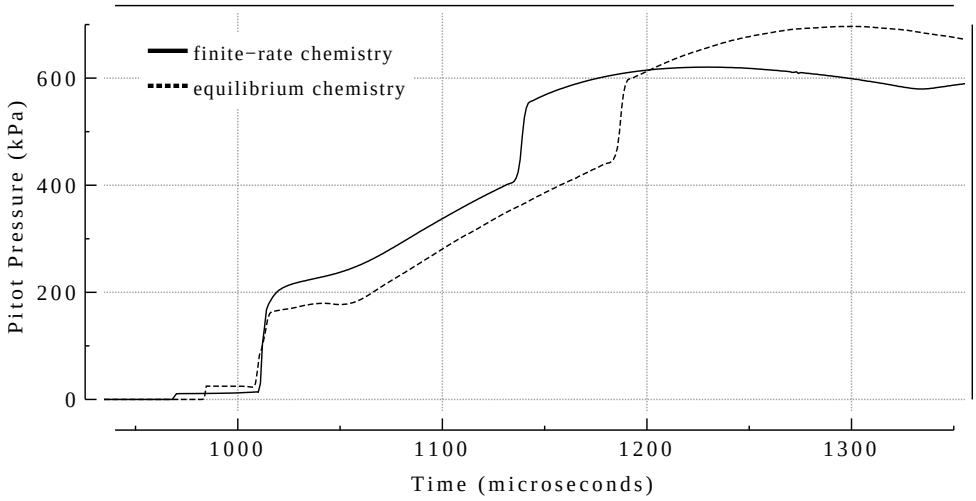

FIGURE 4.20: Pitot pressure history traces from equilibrium and non-equilibrium chemistry simulations recorded at the end of the acceleration tube for Condition 4 (high-enthalpy).

reducing the shock speed by around 3%. This demonstrates that while the final shock speed is relatively insensitive to the acceleration tube fill pressure for this condition, the static pressure of the test flow is more heavily influenced by changes in the fill pressure.

The axisymmetric equilibrium chemistry simulation gave a Pitot pressure only 37% of that measured in experiment, although further mesh refinement was seen to increase the simulated level of test flow Pitot pressure. The one-dimensional inviscid equilibrium simulation with the higher acceleration tube fill pressure (1.5 Pa) resulted in an increase in Pitot pressure by around 50%. So while more than compensating for the lower pressure levels seen in the axisymmetric simulation as well as reducing the shock speed towards that measured in experiment, the increase in fill pressure would still result in the simulated Pitot pressure being only ∼56% of that measured experimentally (based on the axisymmetric simulation of this condition).

Table 4.9 lists the final test flow properties for both the finite-rate and equilibrium chemistry simulations compared with the experimentally measured values. This table also includes the correction factor, C_f, defined by equation 4.2, to quantitatively ascertain the effects of finite-rate chemistry for this high enthalpy condition. As anticipated, the inviscid assumptions for this higher enthalpy condition resulted in shock speeds, and hence pressures, higher

Table 4.9: Average test flow properties obtained from inviscid one-dimensional simulations of Condition 4 (equilibrium and finite-rate chemistry) compared with experimental results.

	Experiment	Equilibrium Chemistry	Finite-Rate Chemistry	Correction Factor, C_f
Pressure (kPa	0.93	1.42	1.63	1.15
Temperature (K	-	3100	1575	0.51
Density (kg/m^3)	-	0.00139	0.00275	1.98
Shock speed (km/s)	9.7	11.8	11.1	0.94
Flow speed (km/s)	9.7	11.15	10.22	0.92
Sound speed (m/s)	-	1086	925	0.85
Mach number	-	10.3	11.05	1.07
Pitot pressure (kPa)	190	173	221	1.28
R, $J/(kg.K)$	-	330	376	1.14
γ	-	1.15	1.43	1.24

than measured in experiment, however the effects of finite-rate chemistry can be clearly identified for this high-enthalpy X2 operating condition. The shock speed is seen to decrease by 6% when nonequilibrium effects are included, correlating well with the fact that axisymmetric simulations overestimated the shock speed by around 6-7%. Of noticeable interest in this table is the increase in Pitot pressure by almost 30% for the finite-rate chemistry simulation.

Though the inviscid one-dimensional simulations significantly over-predicted the shock speed (14-15%) and pressure (75%), the results can be used to estimate the actual experimental test flow properties. Firstly, Table 4.9 shows that finite-rate chemistry simulation resulted in a Pitot pressure ∼16.3% higher than experimentally measured. The flow velocity, u was also over-predicted by ∼5.4%. Now, assuming the Pitot pressure to be proportional to ρu^2, it can be calculated that the simulated density ($0.00275\,\mathrm{kg}/m^3$) is ∼4.5% too high. Thus the corrected density would be $0.00262\,\mathrm{kg}/m^3$. From the perfect gas relationship, $T \propto P/\rho$, the simulated temperature (1575 K) can be approximated as being 67.4% higher than that obtained in experiment. This leads to a corrected temperature of the expanded test flow of 941 K. From the perfect gas law, $R = P/(\rho T)$, the gas constant, R, can be calculated as being $377\,J/(kg.K)$. Table 4.10 tabulates these corrected estimates of the final test flow

conditions for this high enthalpy X2 operating condition.

Table 4.10: Corrected estimates of the final test flow properties for X2 Condition 4 (high-enthalpy).

Pressure (kPa)	0.93
Temperature (K)	941
Density (kg/m^3)	0.00262
Flow speed (km/s)	9.7
Mach Number	13.6
Total pressure (GPa)	128
Total enthalpy (MJ/kg)	47
R ($J/(kg.K)$)	376

Gas Composition and Chemical Freezing

Table 4.11 lists the average dissociation levels of the air test gas after the primary shock and in the reflected shock region. Also in the table are the values of γ and R in these two regions. The gas composition from the finite-rate chemistry simulation was compared to that obtained from the EQSTATE program which assumes the gas is at chemical equilibrium. To compensate for the slight difference in the composition in air between EQSTATE and the simulation, the amount of N, O_2 and NO in the flow is obtained from EQSTATE and the amount of N_2 and O is calculated from conservation of mass. The close agreement in the mass-fraction of each species seen in Table 4.11 verifies both the finite-rate chemistry package used in the simulations as well as the equilibrium nature of the flow in both of these regions. Almost 50% of the enthalpy of the flow in the shock reflected region is now in chemical form (h_{chem}).

Figure 4.21 shows the N_2 mass-fraction of three particles of test gas as they traverse the acceleration tube. Cell A represents an element of gas that arrives approximately 13μs after the arrival of the accelerator gas/test gas interface (A/T interface) at the exit of the acceleration tube. Cells B and C arrive 30μs and 50μs respectively after this interface, with the nominal test time for this condition being around 50μs. Again, it can be seen that cell A, which experiences the expansion over a shorter section of the expansion fan, freezes at a lower

Table 4.11: Test gas composition behind the primary shock and in the shock reflected region prior to expansion for X2 Condition 4 (high-enthalpy).

	1 cm behind primary shock		Shock-reflected region	
	Sim	EQSTATE	Sim	EQSTATE
Pressure	580 kPa		6.83 MPa	
Temperature	5700 K		8600 K	
N_2	73.7%	73.8%	51.5%	51.4%
N	2.8%	2.7%	25.5%	25.4%
O_2	0.3%	0.3%	$< 0.1\%$	$< 0.1\%$
O	20.1%	20.0%	20.7%	20.6%
NO	3.1%	3.2%	2.2%	2.5%
h_{chem}	-	13.0%	-	48.3%
R	353	351	419	420
γ	1.33	1.34	1.34	1.36

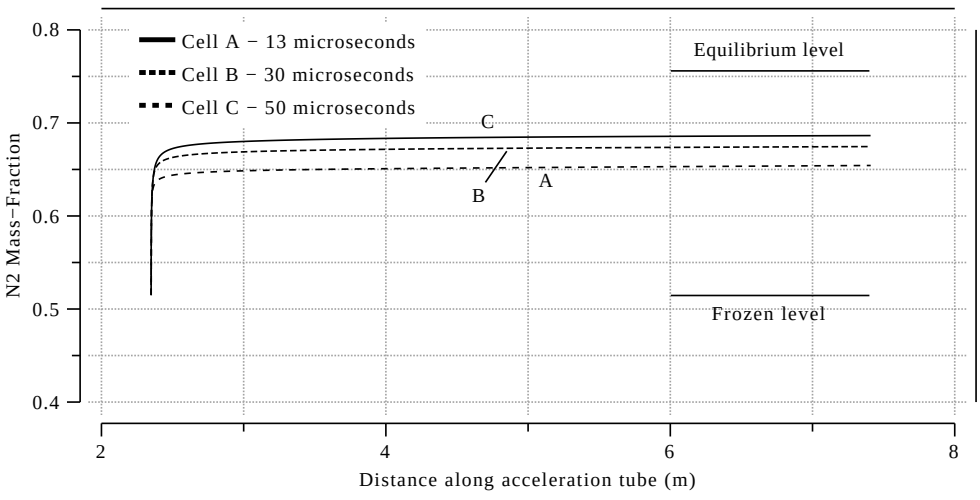

Figure 4.21: The N2 mass-fraction history of three elements of test gas for the high-enthalpy condition. Times correspond to the arrival time at the test section after the start of the test flow.

N_2 mass-fraction than cells B and C which pass through progressively larger portions of the unsteady expansion. This figure shows that although the cells which pass through the larger section of the unsteady expansion experience more recombination, they still do not reach the equilibrium level.

The previous table (Table 4.11) has shown that the amount of diatomic oxygen, O_2, prior to expansion is negligible. Table 4.12 lists the average dissociation levels in a 40μs window that starts 10μs after the accelerator-gas/test-gas interface for the finite-rate chemistry simulation. Compared with this is the average test flow composition of the test flow calculated based on an equilibrium expansion of the test gas as well as a completely frozen expansion of the test gas. This table shows that the test gas expansion incorporating finite-rate chemistry results in essentially no O_2 in the final test flow. This agrees very well with that predicted using a pure frozen expansion from the shock-processed conditions, indicating that the oxygen undergoes an essentially frozen expansion process for this high enthalpy condition. The amount of N_2 in the final test flow in the finite-rate chemistry simulation (66.5%) is somewhere between the frozen and equilibrium assumptions. This table also shows that the finite-rate chemistry simulation resulted in negligible NO in the final test flow, meaning that all oxygen is in monotomic form (O).

Table 4.12: Final test flow composition for Condition 4 (high-enthalpy) assuming (a) frozen chemistry, (b) finite-rate chemistry and (c) equilibrium chemistry through the unsteady expansion.

	Frozen Expansion	Finite-rate Expansion	Equilibrium Expansion
N_2	51.5%	66.5%	75.6%
N	25.5%	11.5%	$< 0.1\%$
O_2	$< 0.1\%$	<0.1%	5.0%
O	20.7%	22.0%	16.7%
NO	2.2%	<0.1%	2.7%
R	418	380	332
γ	1.341	1.42	1.34

4.4.3 CPU requirements and predictions

The inviscid one-dimensional simulations of the low enthalpy condition s506 assuming chemical equilibrium required 193 seconds to solve to a simulation time of t=1.9e-3 s using a 2 GHz Xeon processor (Gemini). This CPU time increased by a factor of 70 to a time of 3.8 hrs for the simulation incorporating finite-rate chemistry. The time required to solve the high-enthalpy equilibrium chemistry one-dimensional simulation was 740 seconds. This increased by a factor of 40 to 8.1 hrs for the finite-rate chemistry simulation.

The axisymmetric viscous simulation of just the acceleration tube section for the low enthalpy condition assuming equilibrium chemistry required 11.3 hrs on the APAC National Facility. Using the axisymmetric code to solve a full viscous non-equilibrium simulation of just the acceleration tube is predicted to take around 1100 hrs (or 46 days) of CPU time utilizing this finite-rate chemistry package. If this approach was to be used to model the acceleration tube on a much larger facility such as the proposed RHYFL-X facility with cross-sectional areas around 10 times that of X2, the CPU requirements would be extreme at approximately 11,000 hrs or 468 days.

4.5 Summary

This chapter has presented the results of one-dimensional finite-rate chemistry simulations of two operating conditions of the X2 expansion tube. The aim of the work was to investigate the validity of assuming equilibrium flow during the cycle of both a low and a high enthalpy operating condition. The inviscid simulations started at the point of primary diaphragm rupture and modelled the entire expansion tube with a 5 species finite-rate chemistry model of air. The simulations incorporated a 10μs hold time for the secondary diaphragm.

Excellent agreement was seen between the two simulations up to the point of secondary diaphragm rupture indicating that an equilibrium assumption is valid up to this point. The sudden expansion experienced by the gas upon rupture of the secondary diaphragm however resulted in a noticeable difference between the equilibrium and finite-rate chemistry simulations, with these discrepancies increasing for the higher enthalpy condition. The

insufficient time for the recombination reactions to establish equilibrium levels means that energy consumed in the dissociation reactions is not returned to the flow to the extent that equilibrium assumptions predict. This results in a slight reduction in the computed shock speeds (∼5-6%) and pressure levels as well as significant reductions (∼35-50%) in the static temperature of the test flow in the finite-rate chemistry simulations.

For the lower-enthalpy condition, the small amount of dissociated N_2 in the shock-processed test gas was seen to recombine rapidly through the unsteady expansion and approached equilibrium levels. The O_2 however did not recombine as quickly and did not agree with the equilibrium calculations. For the higher enthalpy condition, the higher levels of dissociation of the test gas prior to the more severe unsteady expansion process meant larger differences were seen between the equilibrium and finite-rate chemistry simulations. As the test flow originates from a small region of test gas adjacent to the secondary diaphragm (∼1-2 mm for the high-enthalpy condition) the *hold-time* approximation for the inertial effects of the secondary diaphragm may have resulted in dissociation levels somewhat higher than would be attained if the inertial effects of the diaphragm were taken into account. This would, however, be mitigated by the loss of early test gas into the boundary layer if viscous effects were present. Even so, these results have shown that the unsteady expansion of the air test gas, especially for the higher enthalpy condition, is a non-equilibrium process and can not be accurately calculated using equilibrium assumptions. Finite-rate chemistry should be incorporated into expansion tube simulations to obtain an accurate description of the final test flow properties and composition in conditions where higher primary shock speeds lead to dissociation of the air test gas prior to expansion. The initial acceleration and planar movement of the secondary diaphragm following its peripheral rupturing caused by the primary shock should be modelled in the future to attain an increased knowledge of the effects that the inertial characteristics of this diaphragm has on recombination rates. For conditions where dissociation of the test gas caused by the primary shock is negligible, the added complexity of modelling finite-rate chemistry is superfluous. For these conditions (which are relevant to scramjet testing in RHYFL-X), the equilibrium assumption is not only valid, but preferred due to the marked decrease in both computational and coding

requirements.

Chapter 5

Performance Predictions for RHYFL-X

5.1 Introduction

This chapter uses the simulation techniques verified in the previous chapters to obtain performance estimates of the proposed RHYFL-X expansion tube. One-dimensional simulations assuming equilibrium chemistry are performed of 3 proposed RHYFL-X operating conditions. Axisymmetric simulations of the acceleration tube were also performed for the Mach 10 condition (RX-1) to check the agreement between the one-dimensional and axisymmetric simulation techniques. The axisymmetric simulation also provides an indication as to the size of the uniform core flow that could be expected from this proposed facility. Table 5.4 outlines the target test flow properties of the 3 operating conditions called RX-1, RX-2 and RX-3 which are based on flight parameters obtained by sampling an anticipated flight trajectory of a scramjet powered vehicle [2]. The velocities associated with these target test flow conditions (especially RX-1 and RX-2) are below the typical operating enthalpies of free-piston driven expansion tubes. The aim of these conditions is to generate true Mach number test flows with the total pressures associated with anticipated scramjet flight in our atmosphere without test flow dissociation.

Table 5.1: Target test conditions for the RHYFL-X Expansion Tube.

	RX-1	RX-2	RX-3
Mach number	10	15	20
Altitude (km)	30	35	42
Sound Speed (m/s)	300	308	320
Flow Speed (m/s)	3000	4620	6400
Temperature (K)	224	236	255
Total Temperature (K)	3643	7382	12546
Total Enthalpy (MJ/kg)	4.4	10.6	20.4
Pressure (kPa)	1.2	0.7	0.25
Total Pressure (GPa)	0.11	2.94	21.86

All assumptions, calculations and simulations in this chapter assume a standard free-piston, single-driver expansion tube with the dimensions of the RHYFL-X hardware. Optimum lengths of the shock tube and acceleration tube sections are estimated using perfect gas relations and then refined using the one-dimensional simulations.

5.2 RHYFL-X Predictions

5.2.1 Condition RX-1

The first proposed operating condition for the RHYFL-X expansion tube, RX-1, is aimed at producing test flow corresponding to atmospheric flight at Mach 10 at an altitude of 30 km. As seen in Chapter 3, there is a theoretically infinite number of primary shock speeds that can be used to obtain a particular final shock speed. As the primary shock speed changes so too do the properties of the final expanded test flow. For a set final flow speed, the temperature of the expanded test flow is independent of the driver conditions at rupture and depends only on the primary shock speed. For this condition, the primary shock speed must be set such that, after expansion, the test flow temperature corresponds to the atmospheric temperature at 30 km (∼224 K). Assuming perfect-gas properties for air (γ=1.4), the graph in Figure 5.1 shows how, for a set final flow speed of 3 km/s, the final test flow temperature varies with the primary shock speed. In the perfect-gas calculations, the final test gas velocity has been

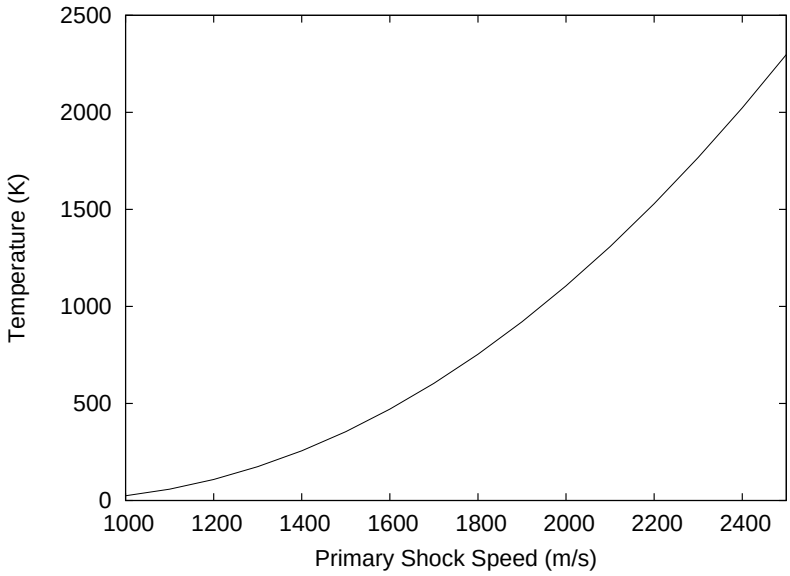

Figure 5.1: Temperature of final test flow as a function of the primary shock speed for a final flow speed of 3 km/s (perfect-gas).

set to 3 km/s rather than the final shock speed. As these calculations do not account for the mass-loss to the boundary layer, the shock speed will be noticeably higher (∼3600m/s). Closer inspection of Figure 5.1 reveals that a primary shock speed of around 1363 m/s will result in an ideal final test flow temperature of 224 K. This primary shock speed now sets the temperature of the shocked air test gas at 1176 K with a corresponding sound speed of 687 m/s. In order to satisfy Paull's [46] sound speed buffer requirement of a ratio no less than 1.25 across the expanded-driver-gas / shocked-test-gas interface, the expanded driver gas must have a sound speed of no more than 550 m/s. With helium as the driver gas and still assuming perfect gas properties, this relates to a sound speed of the driver gas prior to rupture of no more than 783 m/s. This sound speed in helium corresponds to an impractical temperature of only 177 K. A major advantage of the free-piston driver concept is the ability to use a combination of gases as the driver gas. The use of a suitable gas or mixture of gases to obtain these low driver sound speeds at rupture is discussed later in the chapter. All calculations and simulations used to determine operating conditions of the proposed RHYFL-X facility assume helium as the driver gas with the maximum design rupture pressure of 250 MPa.

Now that the driver conditions at rupture are estimated and the speeds of the primary and secondary shocks are known, the fill pressure for both the shock and acceleration tubes can be calculated as being around 2.35 MPa and 992 Pa respectively. Due to the large area ratio between the driver and shock tube sections, Mach 1 conditions are assumed at the throat in the calculations. Table 5.2 outlines the initial conditions as well as expanded test gas conditions for RHYFL-X condition RX-1 based on perfect-gas calculations. All initial temperatures are assumed to be 296 K.

Table 5.2: Initial conditions for RX-1 based on perfect-gas analytical calculations with Mach 1 conditions at the throat.

Primary Diaph. Burst	250 MPa
Driver Temp (He)	177 K
Driver Sound Speed	784 m/s
Shock Tube Fill (air)	2.35 MPa
Acceleration Tube Fill (air)	992 Pa
Test Flow Velocity	3000 m/s
Test Flow Pressure	128 kPa
Test Flow Temperature	224 K

One-Dimensional Simulations

The initial conditions in the previous section (Table 5.2) were based on perfect-gas assumptions for the flow within the expansion tube. The one-dimensional flow simulation code L1D was then used to refine these fill conditions and determine appropriate shock tube and acceleration tube lengths. As the piston compression is not modelled, a driver gas slug length of 2 m is assumed at the point of primary diaphragm rupture to prevent driver related disturbances in the test flow. Provided the driver is operated with piston speed matched to that required to maintain the pressure after rupture (tuned operation), the choice of driver gas length in the simulations should not effect results downstream. As previous simulations of the X2 expansion tube have shown that the influence of the secondary diaphragm has a significant effect on the final flow properties, and that the diaphragm thickness will scale with the pressure ratio across the secondary diaphragm, all simulations of the RHYFL-X

facility also assume a 10μs hold time for the secondary diaphragm. These simulations also assume equilibrium chemistry.

The nature of the one-dimensional code means that the gas properties within a cell are an average of the flow over the diameter of the tube. This has little effect on the pressure but can significantly influence properties, such as temperature, where there are large differences between the boundary layer and the core flow. To account for this attribute of one-dimensional modelling, both viscous and inviscid one-dimensional simulations of this condition were performed. The viscous simulations of the RHYFL-X facility also included the mass-loss model in the shock-processed accelerator gas.

Table 5.3 outlines the initial conditions for the L1D simulations along with the segment lengths and the number of computational cells used in each section. The cells in the shock

Table 5.3: L1D simulation details of RHYFL-X condition RX-1.

Section	1	2	3
Name	Driver	Shock tube	Acceleration tube
Length	2 m	10 m	20 m
gas	helium	air	air
Pressure	250 MPa	1.86 MPa	700 Pa
Temperature	150 K	296 K	296 K
No. of cells	400	3000	1667

tube (Section 2) were heavily clustered towards the secondary diaphragm to prevent excessively large cells after expansion. The cells in the driver were also clustered, but not as heavily, towards the primary diaphragm for the same reason. Cell-fusing was used on the cells in the acceleration tube to prevent the shock processed cells from becoming too small. Once the cells became a certain size they would fuse together to make one larger cell and hence avoid the very small time steps associated with tiny cells containing hot gas. The L1D input files for these inviscid and viscous one-dimensional simulations are included in Appendix B. This Appendix also includes the input files for the one-dimensional simulations of RX-2 and RX-3. Due to the minimal difference (specifically, turning on a viscous flag) between the inviscid and viscous input files, only the inviscid simulation input files are

included for the latter simulations.

Figure 5.2 is an xt-diagram obtained from the inviscid L1D simulation of this condition. The boundaries between the different slugs are included in this plot. The D/T interface intercepts the upstream edge of the unsteady expansion fan centered about the secondary diaphragm at $t\sim$10 ms (point A, Figure 5.2). The disturbance wave travelling downstream from the driver arrives at this unsteady expansion at approximately t=15 ms (point B). This implies that the shock tube could be made longer than 10 m before the test gas is disrupted by driver disturbances. The conservative length of 10 m for the shock tube was used because the precise length of the driver gas slug at rupture is unknown, and will lead to a conservative test time prediction. Also evident from this figure is the fact that the $u + a$ wave (shown

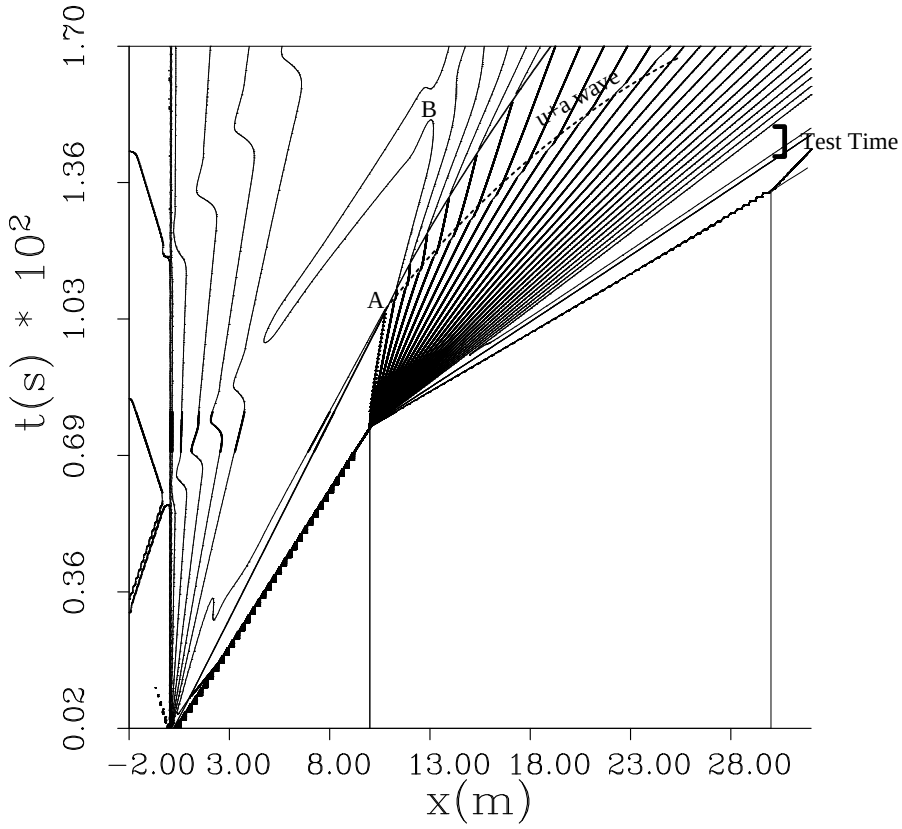

FIGURE 5.2: An xt-diagram from the one-dimensional simulation of RHYFL-X condition RX-1. Contours are of pressure on a logarithmic scale.

dashed in Figure 5.2) generated by the intersection of the D/T interface and the upstream edge of the unsteady expansion fan reaches the test section approximately 2.5 ms after the steady test flow terminates. This means that the acceleration tube could also be made longer, resulting in an increase in test time which which has a linear relationship with the increase in acceleration tube length.

Figure 5.3 is a plot of the flow velocity obtained at a point 10 m down the acceleration tube from the inviscid and viscous one-dimensional simulations. Though the simulation included a 20 m acceleration tube, the properties have been plotted at the 10 m point to be able to compare with an axisymmetric simulation of a 10 m acceleration tube for this condition discussed later (Except for test gas duration, all test flow properties should remain the same). This figure shows that the relatively high densities and low speeds associated

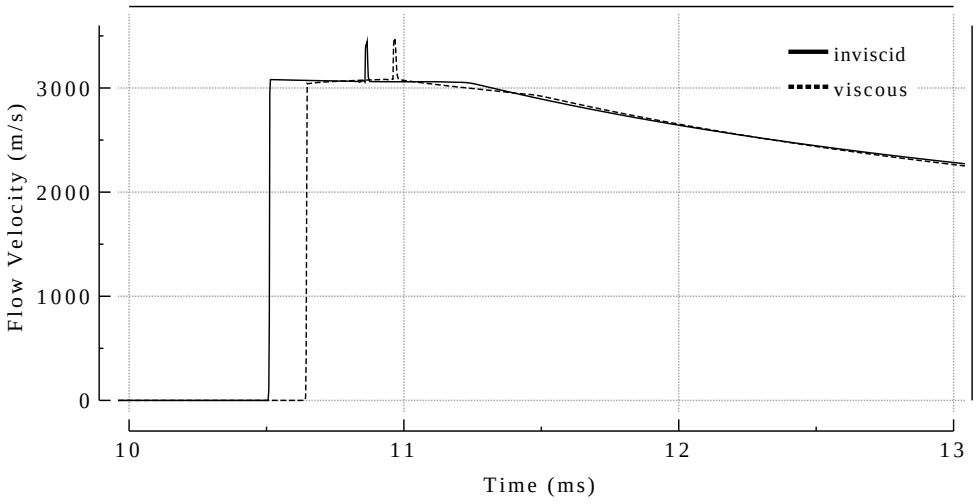

Figure 5.3: Flow velocity history at a point 10 m down the acceleration tube. Results from the inviscid and viscous one-dimensional simulations of RHYFL-X condition RX-1.

with this condition result in little difference (no more than 2%) between the flow velocities obtained from these 2 simulations. There is also little difference in the length of shock-processed accelerator gas indicating that the mass-loss to the boundary layer may not be significant in this high density, low speed condition. The small effect of viscous interactions for this condition suggests that the shock speed should also be in close agreement. By measuring the time taken for the shock to traverse history points along the acceleration

tube, the shock velocity can be determined. The shock velocity for the viscous simulation was 3397 m/s. The inviscid simulation had a shock velocity less than 1% faster than this at 3412 m/s. Figure 5.4 supports this closeness in shock speed, showing the good agreement in the static pressure traces . The viscous trace has been slightly shifted in this figure so that

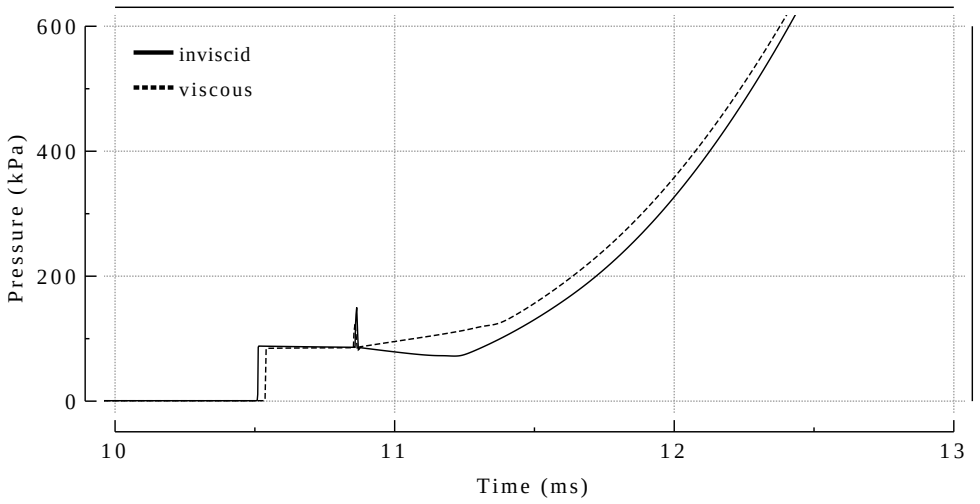

FIGURE 5.4: Static pressure history at a point 10 m down the acceleration tube. Results from the inviscid and viscous one-dimensional simulations of RHYFL-X condition RX-1. Note that the accelerator-gas/test-gas interfaces for the two simulation traces have been aligned.

the arrival of the interface coincides with that of the inviscid simulation so that the traces can be directly compared. The viscous simulation has an increasing pressure over the test time where the inviscid simulation has a slightly decreasing pressure over this time. The decrease in static pressure in the inviscid simulation is directly related to the 10μs hold time imposed on the secondary diaphragm. The exact same inviscid simulation was performed but without the hold-time imposed on the secondary diaphragm and the static pressure was flat over this test time period (as seen in Figure 5.5). The increasing pressure gradient balances the wall shear stress applied to the moving gas cells.

Figure 5.6 is a plot of the temperature attained at the end of the 10 m acceleration tube for the viscous and inviscid simulations. There is good agreement in the temperature in the shock processed accelerator gas region, but there is a significant discrepancy in the temperature of the expanded test gas (though difficult to see due to the temperature scale used on the

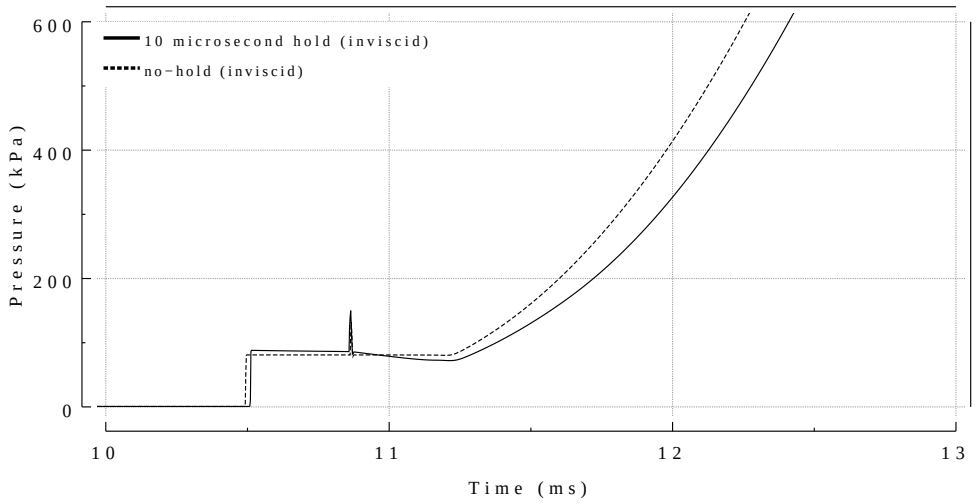

Figure 5.5: Static pressure history at a point 10 m down the acceleration tube. Results from inviscid simulations with and without hold-times for the secondary diaphragm.

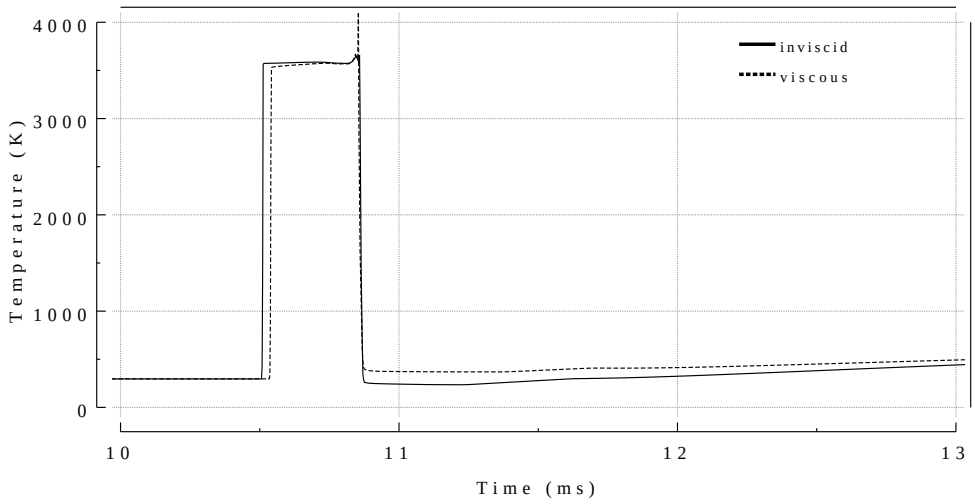

Figure 5.6: Temperature history at a point 10 m down the acceleration tube. Results from the inviscid and viscous one-dimensional simulations of RHYFL-X condition RX-1.

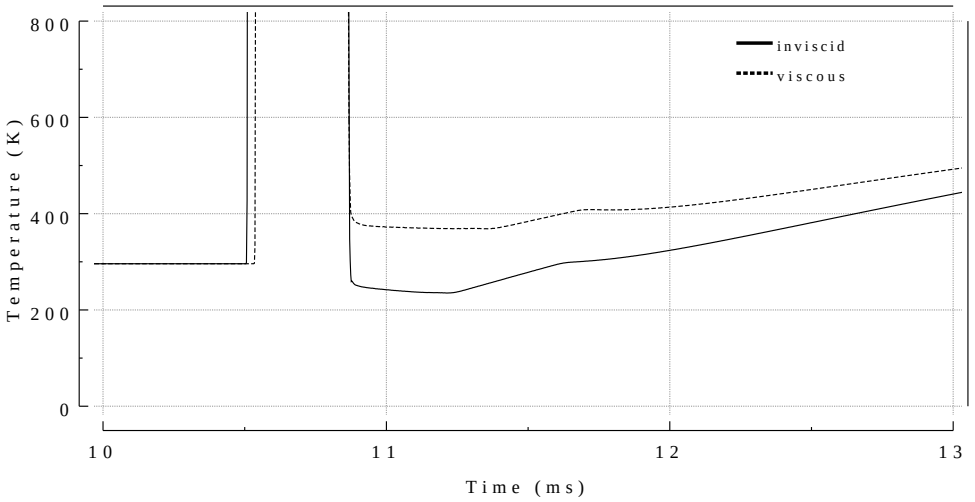

FIGURE 5.7: Temperature history traces from the inviscid and viscous one-dimensional simulations of RHYFL-X condition RX-1. Same results as in Figure 5.6 but with reduced temperature scale on vertical axis.

vertical axis). Figure 5.7 has zoomed into the test gas region of Figure 5.6. On this figure it can be seen that the temperature of the expanded test gas in the inviscid simulation is around 243 K. The viscous simulation has a temperature over 50% higher than this at 370 K. This increase in temperature in the viscous simulation is due to the cell properties in the one-dimensional simulation containing a blend of the boundary layer and the core flow properties. The higher temperature in the boundary layer increases the average temperature across the diameter of the acceleration tube and hence results in a higher temperature in the viscous simulations. For this reason, the inviscid results provide a more accurate estimate of the temperature of the core flow. Because this condition does not suffer from substantial viscous interaction, the inviscid one-dimensional technique will provide a more accurate estimate of the temperature of the core flow and so, will be used as the basis for predicting the test flow properties for this condition.

Axisymmetric simulations

To validate the inviscid one-dimensional simulation technique, full axisymmetric simulations utilizing the Baldwin-Lomax algebraic turbulence model were performed of the acceleration tube section using the Navier-Stokes solver MB-CNS. Due to the significant computational requirements, the axisymmetric simulations will be of a 10 m section of acceleration tube rather than the 20 m acceleration tube modelled in the one-dimensional simulations. The one-dimensional and axisymmetric simulations will be compared at the 10 m point with the level of agreement being considered indicative of the agreement between the two simulation techniques at the end of a 20 m acceleration tube section.

As the simulation was to be solved in parallel on 4 processors, the 10 m acceleration tube was divided into 4 equal blocks of 2.5 m in length with a radius 0.1 m. Each block had 1000 cells in the axial direction and 30 cells across the radius clustered towards the wall, for a total of 120000 cells. The simulation was also solved with approximately twice the total number of cells (1414 x 42 cells x 4 blocks, total of 237552 cells) in order to investigate grid independency. The inflow condition for these simulations used the *transient uniform* boundary condition which enabled the use of a time-varying input obtained at the secondary

diaphragm station of the one-dimensional simulation. Figure 5.8 shows the pressure history at a point slightly off the centre-line at the exit of the 10 m acceleration tube from the simulations at both resolutions. This shows that while the finer characteristics of the trace

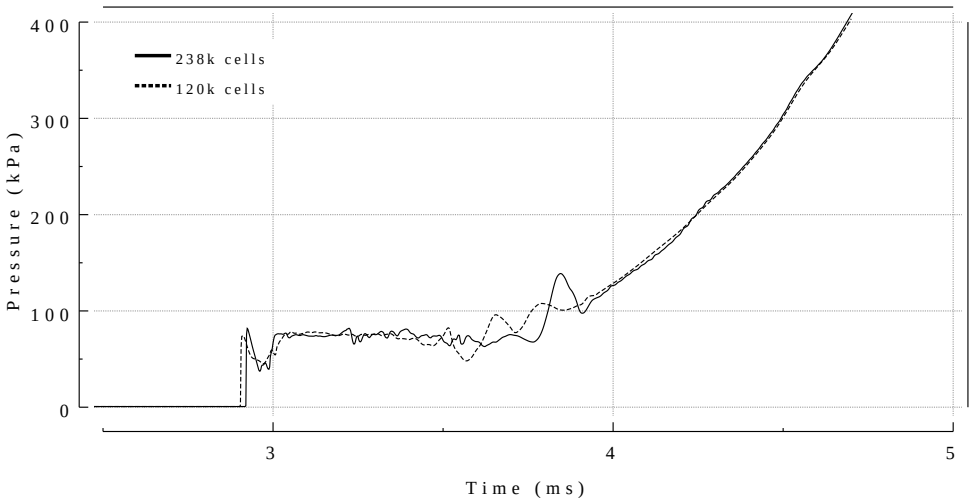

FIGURE 5.8: Pressure history recorded at end of the 10 m acceleration tube from the low (120k cells) and higher (238k cells) resolution axisymmetric simulations of RHYFL-X condition RX-1.

vary between the two simulations, the overall values are within approximately 2%. The more coarse of the two simulations required 53 hours of CPU time to solve on the APAC National Facility, while the simulation with double the total number of cells required around 140 hours. To double the total number of cells again would require CPU times in the vicinity of 370 hours and was not warranted for this study.

Figure 5.9 shows the last 5 m of the 10 m acceleration tube when the shock has reached $x = 9.8$ m ($t = 3$ ms) from the highest resolution simulation. Note the difference in scales between the x and y axes on this figure. The temperature contours clearly indicate the shock front as well as the interface between the test gas and accelerator gas. Also evident in this figure are the boundary layers and the resulting core flow. Figure 5.10 shows the temperature and velocity profiles of the test gas taken at $x = 8.5$ m in Figure 5.9. This figure includes results from both the lower (120k cells) and higher (238k cells) resolution simulations. The increase in resolution resulted in a more accurately resolved boundary layer and a larger

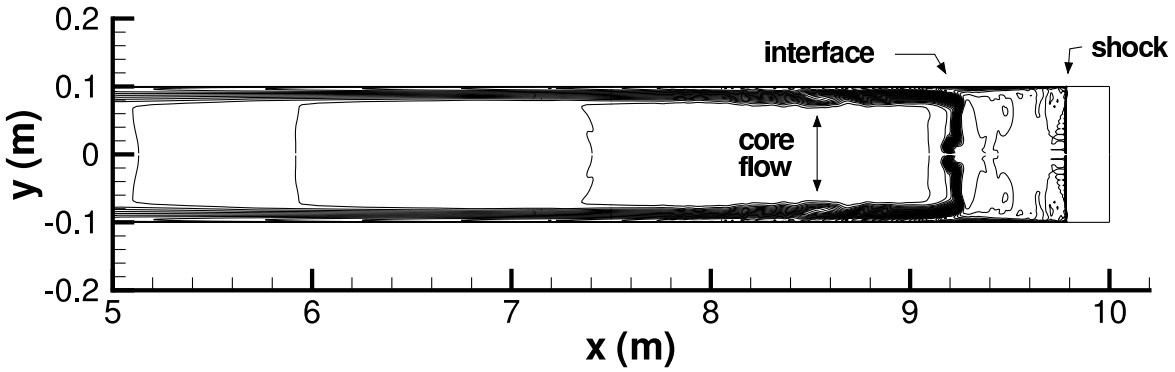

Figure 5.9: Contour plot of the last 5 m of the 10 m acceleration tube for RHYFL-X condition RX-1 when $t = 3$ ms. Contours are of temperature.

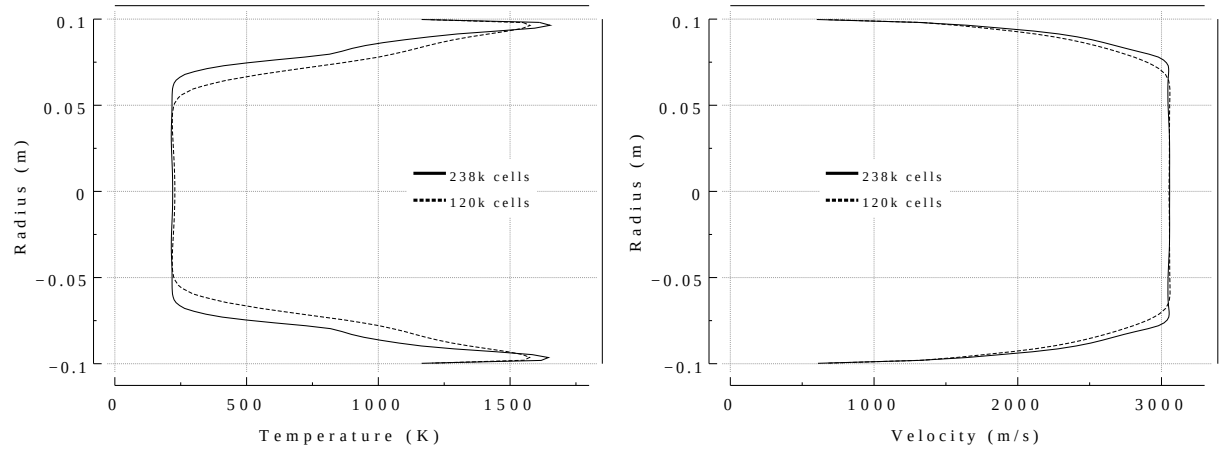

Figure 5.10: Temperature and velocity profiles of the test gas taken from the axisymmetric simulations at x=8.5 m when t=3 ms of RHYFL-X condition RX-1.

core flow. This effect is more prominent in the temperature profiles where the diameter of uniform core flow increased from 100 mm for the lower resolution simulation, to 124 mm for the higher resolution simulation. The velocity profile shows that the increase in resolution increased the diameter of uniform velocity from 134 mm to 148 mm. Though these results suggest that a further increase in resolution is required to obtain a more accurate description of the boundary layer, they also suggest that minimum uniform core flows of approximately 125-150 mm in diameter could be expected for this condition.

One-Dimensional Versus Axisymmetric Simulations

To validate the use of the one-dimensional simulation technique for the large RHYFL-X facility, the L1D results at a point 10 m down the acceleration tube are compared to those taken at the exit of the 10 m acceleration tube from the axisymmetric simulation. Figures 5.11 and 5.12 are history traces of the pressure and temperature obtained after 10 m of acceleration tube from the viscous and inviscid one-dimensional simulations compared to the finest-resolution axisymmetric simulation. On these graphs, the interface arrival times have

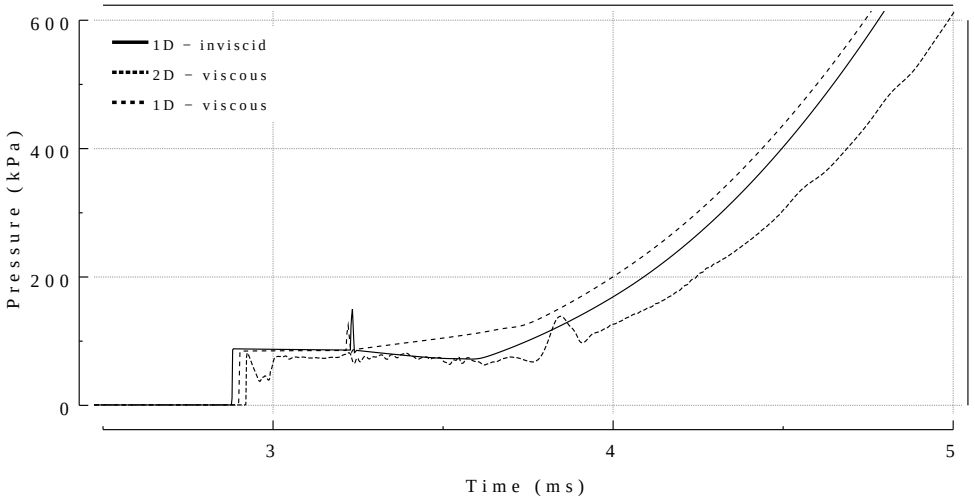

FIGURE 5.11: Pressure history comparison between one-dimensional and axisymmetric simulations of RHYFL-X condition RX-1 at a point 10 m along the acceleration tube.

been set to coincide with that of the axisymmetric simulation. It is evident that the test gas properties, especially the temperature, obtained from the inviscid one-dimensional simulation agree significantly better with the axisymmetric simulation results than results from the viscous one-dimensional simulation. This is because the inviscid simulations do not include the boundary layer effects which alter the overall average of the cell properties in the one-dimensional simulations. For highly viscous flows, the inviscid simulations would result in considerably higher shock speeds, and hence pressures, than what would be obtained from the viscous simulations. For these highly viscous conditions, the viscous one-dimensional simulations would suffer more from this effect of combining the boundary layer properties with the core flow. This suggests that the one-dimensional simulations are more suited to

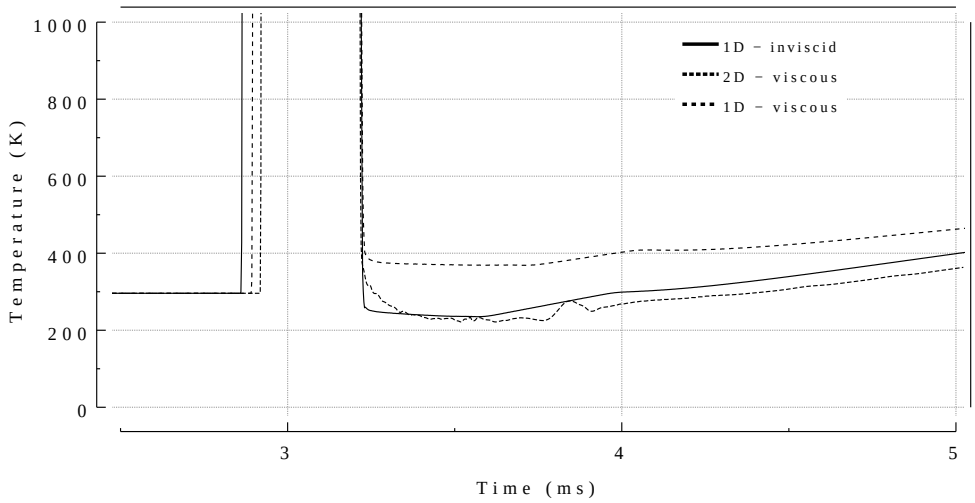

Figure 5.12: Temperature history comparison between one-dimensional and axisymmetric simulations of RHYFL-X condition RX-1 at a point 10 m down along the acceleration tube.

simulating the high density, lower speed conditions associated with the proposed RHYFL-X facility and scramjet testing.

The L1D simulations of this RHYFL-X condition required significant computer resources considering they were one-dimensional computations. The complete inviscid simulation from the point of primary diaphragm rupture required 2.5 hours of CPU time on a 2.0 GHz Xeon processor. This increased to approximately 4 hrs for the viscous simulation. This is still well over an order of magnitude decrease in CPU time compared to the 53 hours (120k cells) and 140 hours (238k cells) required for the axisymmetric simulations.

As L1D is a Lagrangian code, each cell retains the original mass. This therefore requires that the cells adjacent to the secondary diaphragm be very small in order to avoid overly large cells after the sudden expansion when the diaphragm ruptures. The cells in the shock tube are therefore clustered quite strongly towards the secondary diaphragm. When shock processed by the primary shock, these cells become even smaller resulting in very small time steps. Shock-reflection at the secondary diaphragm results in smaller cells still (fractions of a mm) and the high temperatures in this region result in time-steps of around 10 nanoseconds (10e-9s̈ec). The CFL (Courant-Friedrichs-Levy) number, which is a number corresponding to the fraction of the time taken for a wave to travel the length of a cell, was kept relatively small (0.35) to enhance stability of the calculation immediately following the rupture of the secondary diaphragm. The number of Newtonian-iterations between each time step was also increased to aid the calculations at this computationally difficult point. At this instant, the pressure and temperature behind the reflected shock are 185 MPa and 1840 K respectively. The cell size here is approximately 1/40th of a mm. The cell adjacent to this in the test gas is at 700 Pa and room temperature corresponding to a pressure ratio of around 265000. This extreme expansion causes difficulties in calculating the properties of the cell closest to the diaphragm once it ruptures and results in a numerical glitch that can be seen in the simulation traces at the interface. The smaller the expanded test gas cells can be kept, the smaller the cell that has the ill-calculated properties. After expansion for this condition, the test-gas cell adjacent to the interface is 20 mm long while the other expanded test gas cells are 10 mm in length. It is evident though that the error in calculating the properties of this

one cell has an insignificant effect on the properties of neighbouring cells.

Test conditions for RX-1

As mentioned earlier in the chapter, condition RX-1 is aimed at producing test flow conditions corresponding to Mach 10 flight at an altitude of 30 km. Figure 5.13 shows the time-histories of pressure, temperature, flow velocity and Mach number as recorded at the end of the 20 m acceleration tube from the one-dimensional simulation for this condition. The test time period is marked on each graph with the average flow properties during this period tabulated in Table 5.4. This table also compares these simulated values with the desired test flow properties for Mach 10 flight an altitude of 30 km. It is evident from Table 5.4 that the

Table 5.4: Predicted test flow properties for condition RX-1 compared to corresponding flight conditions.

	RX-1 Test Conditions	Target Flight Conditions
Mach number	9.9	10
Sound Speed (m/s)	305	300
Flow Speed (m/s)	3030	3000
Temperature (K)	232	224
Total Temperature (K)	3750	3643
Total Enthalpy (MJ/kg)	4.5	4.4
Pressure (kPa)	75	1.2
Total Pressure (GPa)	6.7	0.11
Test Time (μs)	>750	n/a

predicted RHYFL-X test flow conditions for RX-1 closely match conditions associated with atmospheric flight. As the initial fill conditions of the expansion tube can be changed to tune test flow parameters such as temperature and velocity, the static pressure of the test flow is a primary indicator of the facilities ability to generate certain flow conditions. For example, if targeting a specific test flow temperature and velocity in a lower performance expansion tube, the fill pressures can be reduced until the desired shock speed and flow temperature is attained. In this case however, the static pressure will be less due to the reduction in the fill pressure. Of noticeable interest in Table 5.4 is the significantly higher static pressure

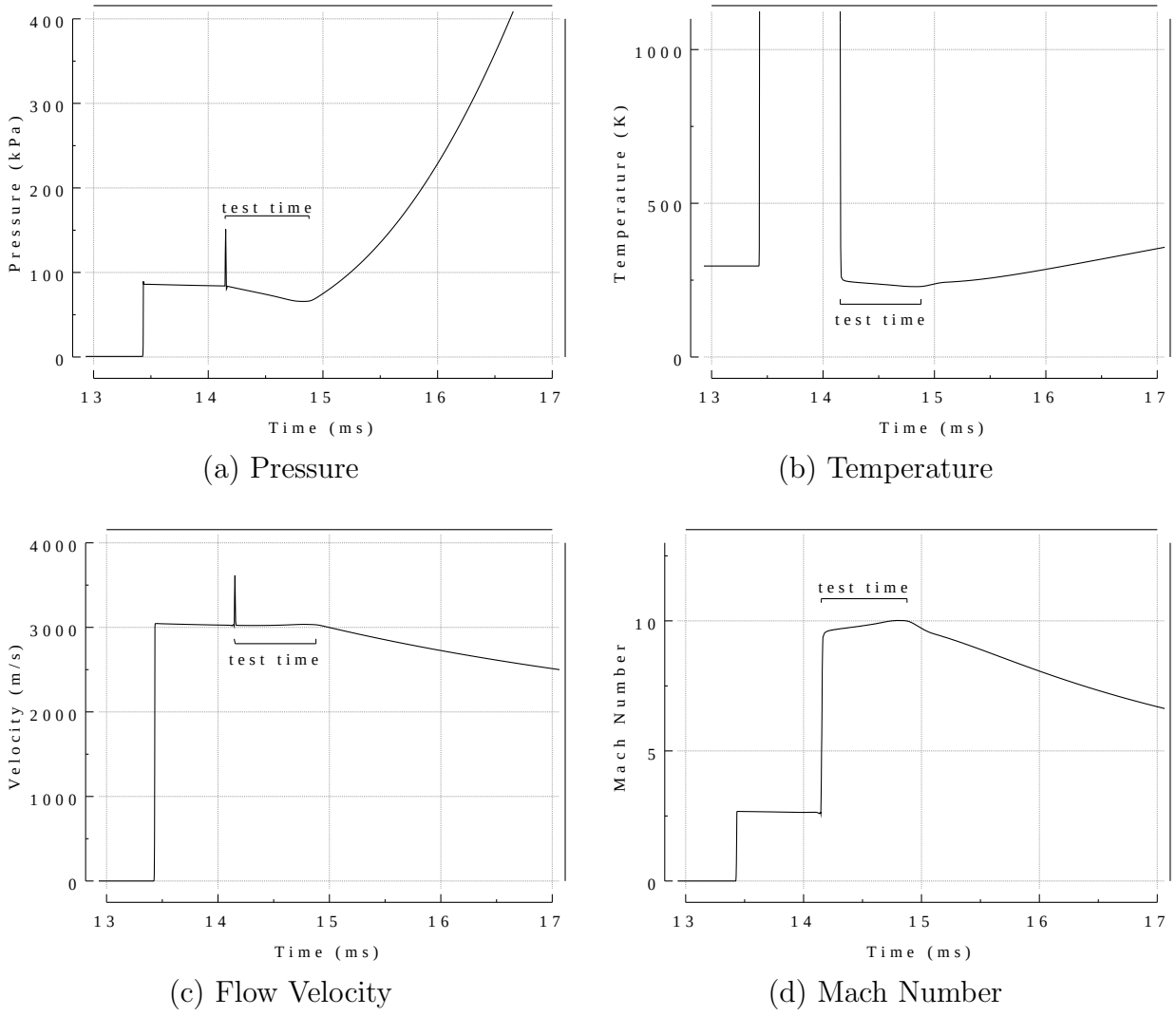

(a) Pressure (b) Temperature

(c) Flow Velocity (d) Mach Number

FIGURE 5.13: Time-histories of (a) pressure, (b) temperature, (c) flow velocity and (d) Mach number as recorded at the end of the 20 m acceleration tube for the inviscid one-dimensional simulation of RHYFL-X condition RX-1.

obtainable by the RHYFL-X expansion tube compared to what would be experienced during flight. This is beneficial for a number of reasons. Firstly, all simulations and predictions have been made assuming the maximum design rupture pressure of 250 MPa. The static pressure is linearly variable throughout the expansion tube process, meaning that if the primary diaphragm rupture pressure is halved, the final flow pressure will be halved with all other properties remaining the same (This is based on inviscid, perfect-gas calculations. In a

real, viscous flow, changing the pressure would alter the viscous interactions of the flow and may therefore effect other parameters). The facility could afford to not operate at maximum design rupture pressure and still readily achieve in excess of the required static pressure. Secondly, the higher static pressure also means a higher density which is useful for experiments involving binary scaling, where subscale models can be tested whilst still matching the ρl product. In addition to these factors, the fact that the predictions for RX-1 indicate a pressure over 60 times that required to duplicate atmospheric conditions provides room for error between the predictions and actual facility performance. In order to illustrate these points further, assume that instead of having the maximum primary diaphragm rupture pressure of 250 MPa, actual operation saw a rupture pressure of only 100 MPa. Also assume that the simulations over-predicted the pressure by 500%. This would mean that instead of a static pressure of 75 kPa in the test flow, a pressure of approximately 6 kPa would be realized. This is still 5 times the pressure required to match atmospheric flight conditions associated with RX-1.

Test Flow Dissociation

The expansion tube concept provides the opportunity to produce test flows corresponding to hypersonic flight conditions with no, or very little, dissociation. It was shown in previous chapters however that, with air as the test gas, typical operating conditions for current expansion tubes are such that test flow dissociation does occur. Due to the chemical freezing through the unsteady expansion at the secondary diaphragm, the dissociation of the test gas caused by the primary and reflected shocks may remain until the test section. It is important to evaluate the dissociation levels, if any, of the test gas in the RHYFL-X test flows when targeting scramjet flight conditions.

During the operation of an expansion tube, any dissociation of the test gas is caused by the primary shock wave. Further dissociation occurs in the small region of the reflected shock caused by the secondary diaphragm. For the current condition (RX-1), the temperature and pressure of the test gas behind the primary shock are 1050 K and 31 MPa respectively. The O_2 in air at 1 atm begins to dissociate at around 2500 K and the N_2 at around 4000 K. The

high pressure in this region would also act to raise these temperatures corresponding to the onset of significant dissociation. This indicates that there will be no dissociation of the air test gas after being processed by the primary shock. The shock reflection at the secondary diaphragm increases the temperature and pressure of this test gas to 1840 K and 185 MPa. This is still below the ~2500 K onset for dissociation of O_2. Table 5.5 lists the equilibrium mass-fractions of N_2, O_2, N, O and NO in the test gas after the primary shock and in the shock reflected region obtained from the EQSTATE program. Also included in this table are the mass-fractions for air at 100 kPa and 300 K. The worst case scenario with regards

Table 5.5: Mass-fractions for the air test gas after the primary shock and in the shock reflected region compared with that at 100 kPa and 300 K for RHYFL-X condition RX-1.

	Standard Air (100 kPa, 300 K)	After Primary Shock (31 MPa, 1050 K)	Shock Reflected Region (185 MPa, 1840 K)
N_2	0.768	0.768	0.766
O_2	0.232	0.232	0.229
N	neg (e^{-19})	neg (e^{-19})	neg (e^{-13})
O	neg (e^{-19})	neg (e^{-11})	neg (e^{-6})
NO	neg (e^{-16})	$6e^{-5}$	0.005

to test flow dissociation is a completely frozen expansion process from the shock reflected region and for the flow to remain frozen as it travels down the acceleration tube. Assuming this to be the case, Table 5.5 shows that the final test flow will be essentially dissociation free ($\approx 0.5\%$ by mass of NO) for this Mach 10 condition.

Test Time

Assuming that no disturbance waves travel forward and disrupt the flow, the test time can be analytically calculated by determining the difference in the time required for the downstream edge of the unsteady expansion fan ($u-a$ wave) and the accelerator gas/test gas interface to travel the length of the acceleration tube. Based on simulated values of the flow speed and the expanded test gas sound speed from the one-dimensional simulations, a 370μs period of steady test flow is calculated at a point 10 m down the acceleration tube. This corresponds very well with the periods of steady flow from the inviscid simulation in Figures 5.3, 5.4 and

5.7 of around 380μs. The axisymmetric simulations however show an approximately 30-35% larger period of steady flow at the same point of around 500μs (Figure 5.11).

Again assuming that no disturbance waves travel forward into the test flow, doubling the length of acceleration tube would double the amount of steady flow. The one-dimensional simulation that included the 20 m acceleration tube indicates a test time of around 750μs, which is approximately double the 380μs seen at 10 m. As the axisymmetric simulation of the 10 m acceleration tube gave a test time of $\sim$500μs, it is reasonable to expect that an axisymmetric simulation of the full 20 m acceleration tube would result in a steady test flow period of around 1 ms. These results therefore suggest that the proposed RHYFL-X expansion tube would be capable of producing steady true flight conditions at Mach 10 for periods of up to around 1 ms.

5.2.2 Condition RX-2

The RX-2 condition for the RHYFL-X expansion tube is aimed at producing a test flow which corresponds to Mach 15 flight at an altitude of 35 km. The same techniques and principles that were employed for condition RX-1 were used to determine the fill conditions for the RX-2 operating condition. Table 5.6 summarizes the initial conditions used in the one-dimensional simulations of condition RX-2. Again the cells were clustered towards the

Table 5.6: L1D simulation details of RHYFL-X condition RX-2.

Section	1	2	3
Name	Driver	Shock tube	Acceleration tube
Length	2 m	12 m	20 m
gas	helium	air	air
Pressure	250 MPa	1.05 MPa	30 Pa
Temperature	270 K	296 K	296 K
No. of cells	400	2900	1667

primary and secondary diaphragms to reduce the size of the expanded cells.

As with RX-1, both inviscid and viscous one-dimensional simulations were performed to determine the extent of viscous interactions for this condition and the applicability of using

this one-dimensional technique at a higher enthalpy. Figure 5.14 is a plot of the flow velocity at the end of the 20 m acceleration tube for these inviscid and viscous simulations. The shock

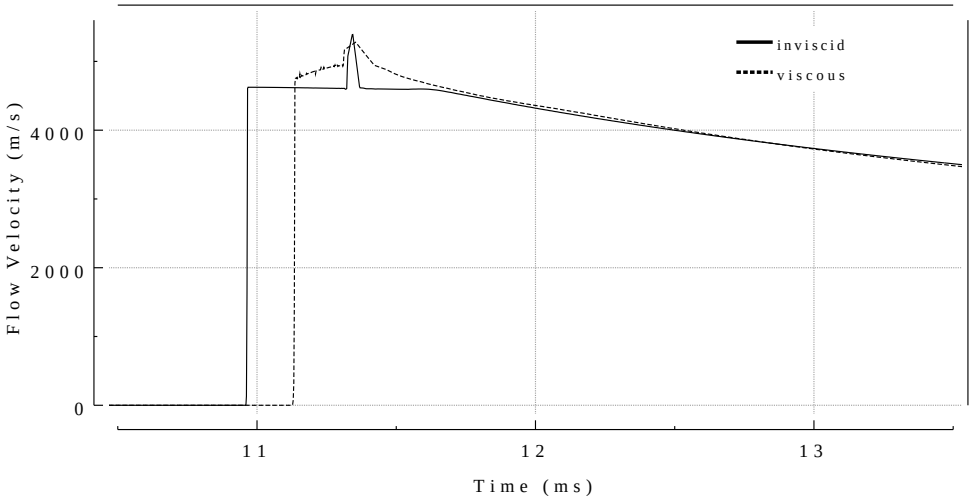

FIGURE 5.14: Flow velocity obtained at the exit of the acceleration tube for the inviscid and viscous one-dimensional simulations of RHYFL-X condition RX-2.

speed obtained from the inviscid simulation was approximately 4% more than that obtained from the viscous simulation. The inclusion of the mass-loss to the boundary layer however in the viscous simulation results in a slightly faster flow speed around the T/A interface even though the shock speed is less. The test flow speed in the viscous simulation is around 4-5% more than in the inviscid simulation due to this Mirels' effect. The increase in viscous interactions in this condition results in an increased difference in the test flow temperatures between the inviscid and viscous simulations. Figure 5.15 is a plot of the temperature history recorded at the exit of the acceleration tube for both the inviscid and viscous one-dimensional simulations. The temperature of the test flow in the inviscid simulation is around 210 K. The viscous simulation, which combines the temperatures in the boundary layer with that of the core flow, produces a significantly higher test flow temperature of around 880 K. This substantially higher temperature in viscous simulation results in twice the sound speed in the test gas and hence half the Mach number than that obtained in the inviscid simulations. This further supports the view that the viscous simulations should not be used to obtain estimates of the test flow temperature in flows where viscous interactions become more significant. A

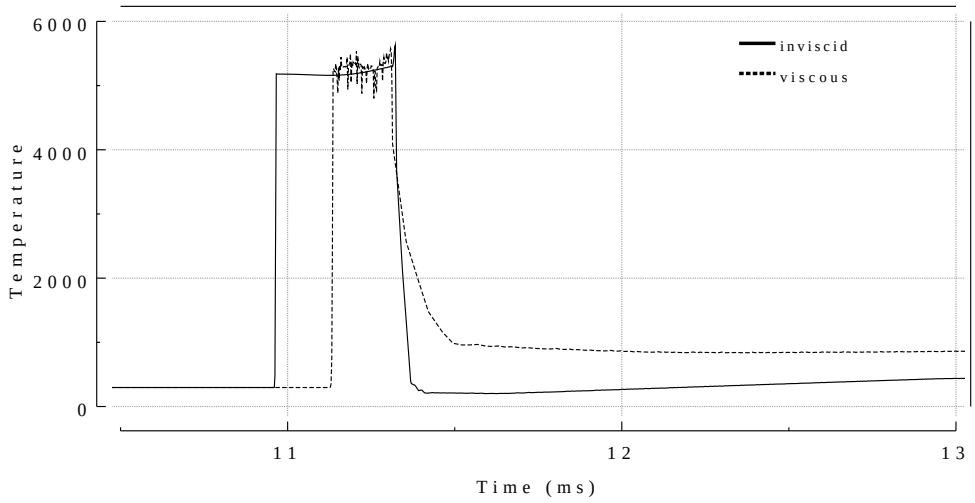

Figure 5.15: Temperature history recorded at the exit of the acceleration tube for the inviscid and viscous one-dimensional simulations of condition RX-2.

miss-calculation of the temperature results in errors in the Mach number which leads to significant changes in the total pressure due to its Mach-number squared dependency.

In the simulations of condition RX-2, the pressure behind the reflected shock at the secondary diaphragm just prior to rupture is 205 MPa. The fill pressure in the acceleration tube is 30 Pa, corresponding to a pressure ratio of around 6.8 million. This extreme pressure ratio between two adjacent cells leads to greater difficulties in calculating the properties of the first test gas cell to undergo expansion, as seen for condition RX-1. The more severe expansion results in longer expanded test gas cells, exaggerating the presence of this problem cell. The size of this cell at the point of secondary diaphragm rupture is $1/55^{th}$ of a millimeter ($1.8{*}10^{-5}$ m) and experiences an increase in volume by over 9500 times to 173 mm during the unsteady expansion. This also illustrates how the test flow originates from very close to the secondary diaphragm where the reflected shock is strong. The static pressure trace plotted in Figure 5.16 clearly identifies the cell with the ill-calculated properties at $t \approx 11.3$ ms.

The test time marked on Figure 5.16 corresponds to around 330μs of steady flow. The average static pressure during this time is around 7.5 kPa plus/minus 7%. All test flow properties during this test period are listed in Table 5.7 and are compared to what would be expected during atmospheric flight. As the axisymmetric simulations of condition RX-1

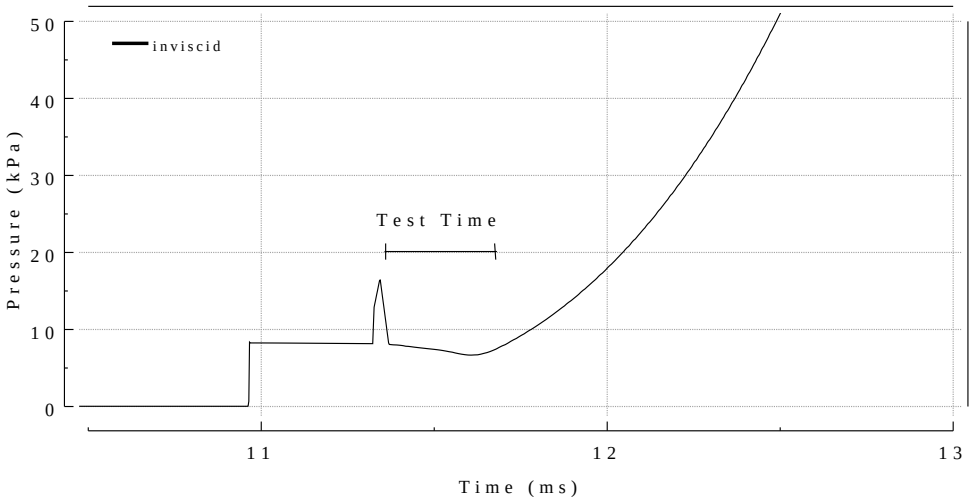

FIGURE 5.16: Static pressure history recorded at the exit of the acceleration tube for the inviscid one-dimensional simulation of condition RX-2.

(Section 5.2.1) gave test times ∼33% larger than the one-dimensional simulation, the 330μs test time obtained from the one-dimensional simulation is believed to be a conservative estimate. The results in Table 5.7 indicate that while the proposed RHYFL-X expansion tube could readily generate the scramjet flight enthalpies for this condition, it is also capable of generating a total pressure over 14 times greater than that required to duplicate free-stream conditions.

Table 5.7: Predicted test flow properties for condition RX-2 compared with to corresponding flight conditions.

	RX-2 Test Conditions	Target Flight Conditions
Mach number	15.9	15
Sound Speed (m/s)	290	308
Flow Speed (m/s)	4600	4620
Temperature (K)	210	236
Total Temperature (K)	7649	7382
Total Enthalpy (MJ/kg)	10.5	10.6
Pressure (kPa)	7.5	0.7
Total Pressure (GPa)	41.9	2.94
Test Time (μs)	>330	n/a

Test Flow Dissociation

After being processed by the primary shock, the air test gas has a pressure of 30 MPa and a temperature of 1535 K. The reflected shock at the secondary diaphragm increases this values to 205 MPa and 2750 K respectively. Table 5.8 shows the equilibrium dissociation levels calculated for these two regions. The species mass-fractions of air at 100 kPa and 300 K are also included for comparison. Assuming that the test flow experiences no recombination

Table 5.8: Mass-fractions for the air test gas after the primary shock and in the shock reflected region compared with that at 100 kPa and 300 K for RHYFL-X condition RX-2.

	Standard Air (100 kPa, 300 K)	After Primary Shock (30 MPa, 1535 K)	Shock Reflected Region (205 MPa, 2750 K)
N_2	0.768	0.7676	0.752
O_2	0.232	0.231	0.213
N	neg (e^{-19})	neg (e^{-15})	neg (e^{-8})
O	neg (e^{-19})	neg (e^{-7})	$2.4e^{-4}$
NO	neg (e^{-16})	$1.6e^{-3}$	$3.5e^{-2}$

from the shock reflected region to the test section, Table 5.8 indicates that the test flow will contain around 3.5% NO (by mass) and an insignificant amount (0.024% by mass) of monotomic oxygen, O. This complete chemical freezing is however quite a severe assumption and any recombination that does take place during the expansion will essentially eliminate the insignificant dissociation for this Mach 15 condition.

5.2.3 Condition RX-3

Condition RX-3 represents the upper portion of potential atmospheric scramjet flight. It aims at producing a test flow corresponding to flight at Mach 20 at an altitude of around 42 km. Table 5.9 summarizes the geometry and fill conditions for the RX-3 simulations. As with the other simulations, the cells were clustered towards the primary and secondary diaphragms in an attempt to minimize the size of the cells after expansion. At the point of rupture of the secondary diaphragm, the size of the constant-mass cells in the reflected shock region are $1/50^{th}$ of a mm ($2 * 10^{-5}$ m) long. The pressure and temperature in this region

Table 5.9: L1D simulation details of RHYFL-X condition RX-3.

Section	1	2	3
Name	Driver	Shock tube	Acceleration tube
Length	2 m	12 m	20 m
gas	helium	air	air
Pressure	250 MPa	612 kPa	1.4 Pa
Temperature	400 K	296 K	296 K
No. of cells	400	3200	1667

are 200 MPa and 3100 K respectively. The cell of accelerator gas adjacent to the secondary diaphragm at this instant is 12 mm long with a pressure of 1.4 Pa and a temperature of 296 K. This relates to a pressure ratio of 150 million. This immense pressure ratio causes serious difficulties when calculating the gas properties of the first test gas cell to expand and worsens the numerical glitch seen in previous simulations. This numerical artifact can be seen in Figure 5.17 which is a plot of the flow velocity at the end of the 20 m acceleration tube for both an inviscid and viscous simulation of this highest enthalpy RHYFL-X condition. The viscous simulation trace has been slightly shifted so that the arrival of the interface

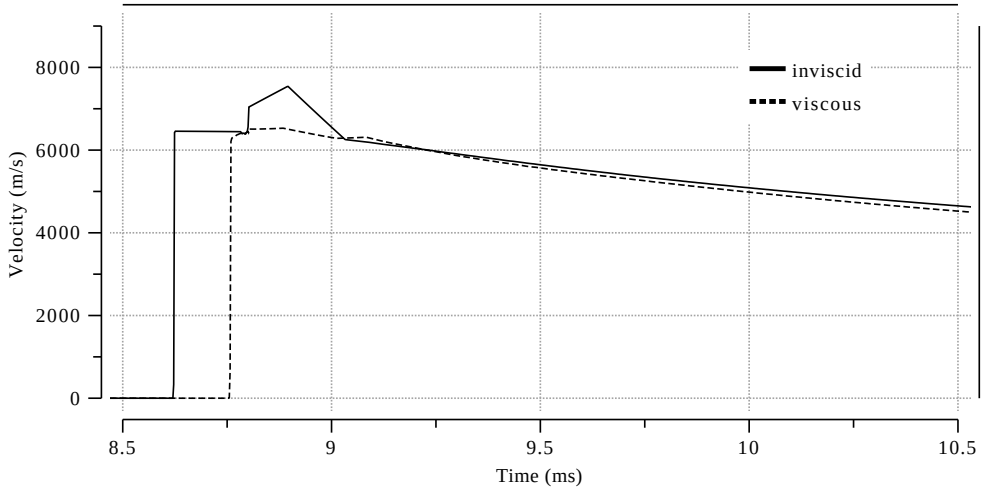

FIGURE 5.17: Flow velocity history recorded at the exit of the acceleration tube for the inviscid and viscous one-dimensional simulations of RHYFL-X condition RX-3.

coincides with that of the inviscid trace. The viscous simulation seems to dissipate the

numerical anomaly at the interface which is quite noticeable in the inviscid simulation. As with previous simulations, the ill-calculated properties exist in only the one test gas cell adjacent to the interface and does not spread into neighboring cells. The exact reason for this lack of dissipation into nearby cells is unclear.

The inviscid simulation results in a shock speed that is 3-5% faster than obtained in the viscous simulation. The modelling of the mass-loss to the boundary layer in the viscous simulation however acts to increase the flow velocity around the interface and results in very good agreement in flow velocity between the two simulations of 6440 m/s

Figure 5.18 is a plot of the static pressure recorded at the exit of the acceleration tube for RX-3. The increasing viscous interactions for this condition results in larger differences between the inviscid and viscous simulation results. The rapidly rising static pressure trace from the viscous simulation is coupled with the excessively high temperature of the test gas calculated in the viscous simulation (Figure 5.19). These simulation results demonstrate

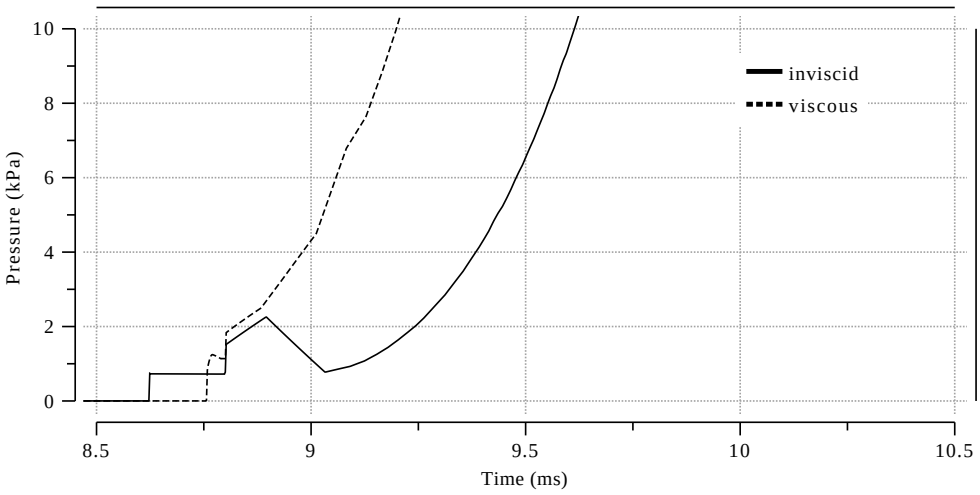

Figure 5.18: Static pressure history recorded at the exit of the acceleration tube for the inviscid and viscous one-dimensional simulations of RHYFL-X condition RX-3.

the limitations of using the viscous one-dimensional modelling technique when simulating conditions where viscous effects begin to play a more significant role. The large errors encountered when using it for these types of conditions highlights the need to use the inviscid simulation results to obtain the final test flow properties. The lack of shear stress however in

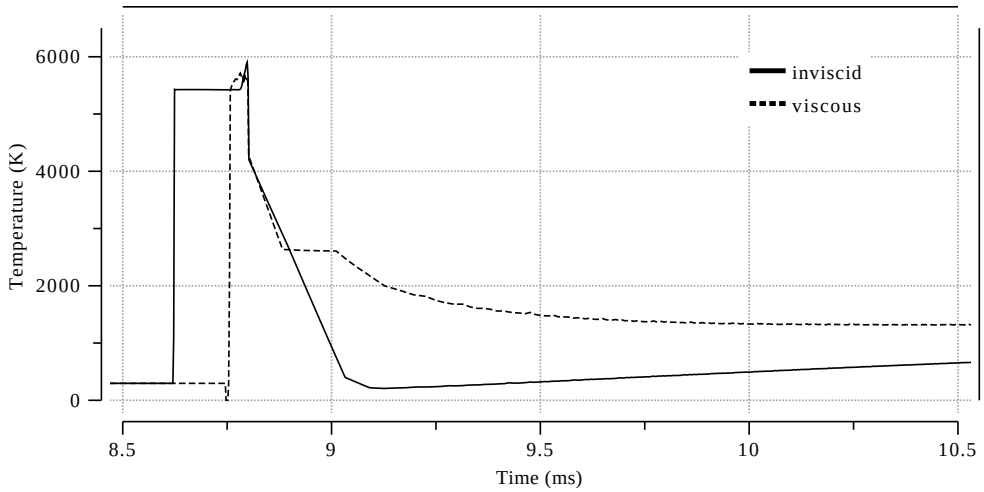

FIGURE 5.19: Static pressure history recorded at the exit of the acceleration tube for the inviscid and viscous one-dimensional simulations for RHYFL-X condition RX-3.

the inviscid simulations can lead to significantly higher shock speeds, and hence pressures, than would be physically realized in conditions with substantial viscous interaction.

The large (1.18 m long), miss-calculated cell in the inviscid results occupies the majority of the $\sim 230 \mu$s of test time. The test flow properties will therefore be taken as those of the test gas cell adjacent to the cell suffering from numerical difficulties. Table 5.10 outlines these final test flow properties that could be expected from the RHYFL-X expansion tube for condition RX-3. These predicted test conditions indicate that the RHYFL-X expansion tube would be capable of matching free-stream flight conditions associated with the higher enthalpy end of a scramjet-powered vehicle's flight trajectory, with a simulated total pressure over 6 times that experienced by a vehicle at these flight conditions. Table 5.11 lists the mass-fractions of the air test gas behind the primary shock and in the shock reflected region. The faster shock speeds for this condition results in higher temperatures both after the primary shock and in the shock reflected region at the secondary diaphragm. As a result, the level of dissociation is slightly greater with 5.3% by mass of NO and still less than 0.1% monotomic oxygen (O) in the test gas prior to expansion. If, once again, the flow is assumed to experience a chemically frozen expansion from behind the reflected shock to the test section, these minimal dissociation levels correspond to the final test flow dissociation

Table 5.10: Predicted Test Flow Properties for condition RX-3 compared to corresponding flight conditions.

	RX-3 Test Conditions	Target Flight Conditions
Mach number	22.7	20
Sound Speed (m/s)	284	320
Flow Speed (m/s)	6440	6400
Temperature (K)	200	255
Total Temperature (K)	13372	12546
Total Enthalpy (MJ/kg)	20.6	20.4
Pressure (Pa)	760	250
Total Pressure (GPa)	143	21.9
Test Time (μs	>230	n/a

Table 5.11: Mass-fractions for the air test gas after the primary shock and in the shock reflected region compared with that at 100 kPa and 300 K for RHYFL-X condition RX-3.

	Standard Air (100 kPa, 300 K)	After Primary Shock (27 MPa, 1888 K)	Shock Reflected Region (200 MPa, 3100 K)
N_2	0.768	0.766	0.743
O_2	0.232	0.229	0.203
N	neg (e^{-19})	neg (e^{-11})	neg (e^{-6})
O	neg (e^{-19})	neg (e^{-6})	$8e^{-4}$
NO	neg (e^{-16})	$6e^{-3}$	$5.3e^{-2}$

for this condition. However with the high pressures and large length scales, recombination to some degree would be expected, reducing these already insignificant dissociation levels.

Computer Resources

The equilibrium inviscid L1D simulation required around 1.8hrs of CPU time to solve using one 2.0 GHz Xeon processor of the Gemini server. This increased to approximately 8 hrs for the viscous simulation. These relatively large CPU times required for the one-dimensional problems is due to the very small computational cells that are created throughout the simulation, especially when the primary shock has reflected off of the secondary diaphragm. The simulation time step is related, through the CFL number (a fraction typically between 0 and

1), to the time taken for a wave to travel the length of a cell and is given by the following equation:

$$t = \text{CFL number} \times \frac{\text{cell size}}{a} \tag{5.1}$$

where t is the time step and a is the sound speed within the cell. As the smallest time step calculated over the computational domain is used, the small cells ($2 * 10^{-5}$ m) in the shock reflected region, coupled with the high temperature in this region, results in time steps as small as $5 * 10^{-9}$ s in the RX-3 simulations.

5.3 Performance Overview

Figure 5.20 is a plot of the stagnation pressure experienced during various atmospheric flight trajectories which was initially introduced in Chapter 1 (Figure 1.5). Included in Figure 5.20 is the approximate upper limit for total pressure generation of reflected shock tunnels. It can be seen that while these facilities offer a convenient means of generating total pressures corresponding to the lower enthalpy end of anticipated scramjet flight (and orbital reentry) they cannot generate the large total pressures required for full duplication of scramjet flight parameters at higher enthalpies. The results from the RHYFL-X simulations (RX-1, RX-2 and RX-3) have been plotted on this graph to obtain an upper limit of the performance capabilities of the proposed RHYFL-X expansion tube operating at the maximum primary diaphragm burst pressure of 250 MPa. These results indicate that this facility would be capable of generating total pressures well in excess of that required for full reproduction of free-stream parameters over the intended scramjet flight trajectory. As a free-piston driven expansion tube, the RHYFL-X facility would offer test flow total pressures well above that capable of any other facility in operation today. The fact that simulations indicate that the proposed RHYFL-X facility is capable of generating total pressures significantly higher than required to match free-stream flight parameters means that the facility can afford to operate well below design limits and still generate the required pressures. The inherently smaller test section size of an expansion tube means that the higher pressures would also be advantageous for binary (ρl) scaling requirements when testing sub-scale models.

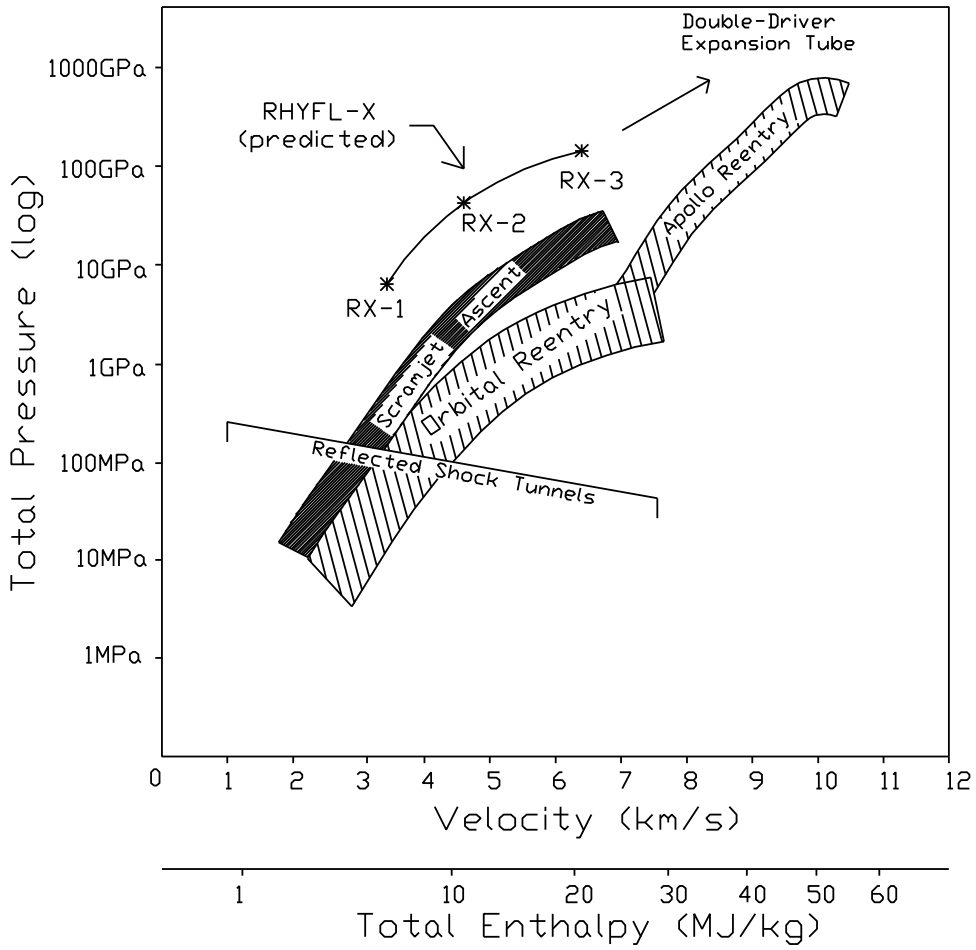

Figure 5.20: The predicted maximum total pressure capabilities of the RHYFL-X expansion tube compared with various atmospheric trajectories as well as the approximate upper limit of reflected shock tunnels.

The price that must be paid for the dramatic increase in simulation capabilities of an expansion tube is a marked decrease in the period of steady flow available for testing. The lower enthalpy end of the proposed operating envelope of the RHYFL-X expansion tube is predicted to have test periods in the vicinity of one millisecond. The one-dimensional simulation of the RHYFL-X condition with test flows corresponding to the upper end of anticipated scramjet flight (RX-3) suggests test times of around 230μ s.

5.4 Driver Conditions

As noted previously, the driver sound-speeds for the RHYFL-X conditions presented in this chapter are well below what free-piston drivers are capable of generating. Helium has been assumed to be the driver gas in all the predictions and simulations associated with the predicted RHYFL-X operating conditions. With helium as the driver gas, driver temperatures at rupture when targeting atmospheric flight conditions have been calculated as being between 150 and 400 K. These driver temperatures are not feasible due to the compression ratios associated with free piston drivers. A major benefit of the free-piston driver however is the ability to use various gases or mixtures of gases. A suitable driver gas would be one that would start at around room temperature prior to compression and would have a temperature corresponding to the required sound-speed at the point of primary diaphragm rupture after a suitable compression ratio. This section investigates the use of air and helium to generate suitable driver gas mixtures for the three RHYFL-X operating conditions presented previously.

5.4.1 Suitable Gas Mixtures

The molecular weight, MW, of an air/helium gas mixture is the weighted average of the molecular weight of each gas and is given by

$$MW = m_{air}\, MW_{air} + m_{He}\, MW_{He}$$

where m_{air} and m_{He} are the mole-fraction of air and helium respectively. The gas constant, R, for the gas mixture is calculated by dividing the universal gas constant, R_u, by the molecular weight of the gas mixture,

$$R = \frac{R_u}{MW}$$

The specific heat at constant pressure, C_p, is then calculated as follows

$$C_p = \frac{m_{air}\, MW_{air}\, C_{p\,air} + m_{He}\, MW_{He}\, C_{p\,He}}{MW}$$

The ratio of specific heats, γ, for the gas mixture can then be obtained from the following relation

$$\gamma = \frac{C_p}{(C_p - R)}$$

Knowing that $MW_{air} = 28.97$, $MW_{He} = 4$, $C_{p\,air} = 1003\,\mathrm{J/kg/K}$, $C_{p\,He} = 5192.6\,\mathrm{J/kg/K}$ and $R_u = 8314\,\mathrm{J/kg/K}$ the gas properties of any air/helium gas mixture can be calculated. Also knowing that for an isentropic process

$$\lambda = \frac{V_1}{V_2} = \left[\frac{T_2}{T_1}\right]^{\frac{1}{\gamma-1}}$$

the final temperature, and hence sound speed, after an ideal compression ratio, λ, can be calculated. Figure 5.21 is a graph showing the compressed driver gas sound speed (y axis) as a function of the isentropic compression ratio (x axis) assuming that the initial temperature of the gas is 296 K. The contours on the graph indicate various driver gas mixtures (air/helium) ranging from pure air to pure helium and have been calculated assuming constant gas properties. The shaded region indicates a range of suitable compression ratios between 40 and 60.

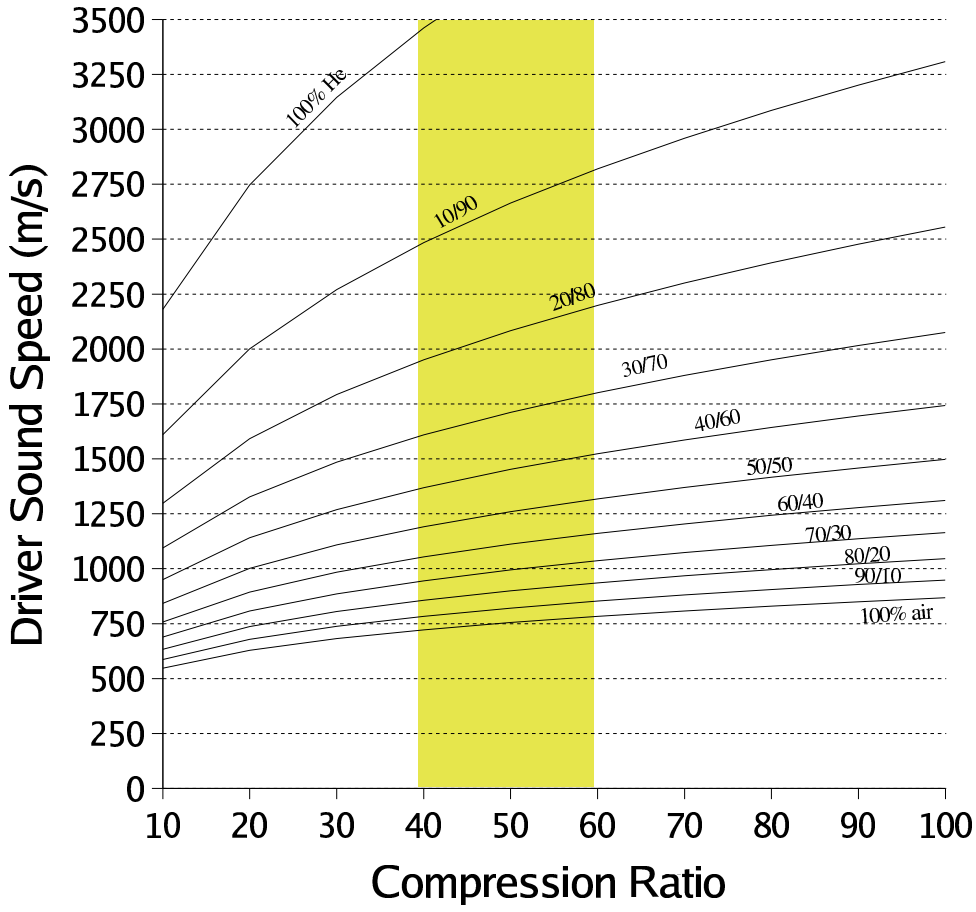

FIGURE 5.21: Compressed driver gas sound speed verse compression ratio for various air/helium mixture ratios (mole-fraction) ranging from 100% air to 100% helium.

RX-1

The proposed RHYFL-X operating condition RX-1 requires a driver sound speed at rupture of around 721 m/s. Figure 5.21 indicates that pure air could be used as the driver gas for this condition with a compression ratio of approximately 40 and a rupture temperature of 1294 K. The use of air would reduce the operating costs compared to having to evacuate and then fill a 50 m compression tube with another type of gas, but has the additional safety and operational concerns associated with the oxygen present (burning oil, O-rings, etc). Nitrogen is a possible (though somewhat more expensive) alternative to air as it has very similar gas properties but avoids the oxygen-related issues.

RX-2

A driver-sound speed of 967 m/s is required for the RX-2 operating condition. If air was used as the driver gas for this condition, a temperature of over 2300 K would be needed at rupture with a compression ratio of over 170. A gas mixture consisting of around 70% air and 30% helium would significantly reduce this compression ratio to approximately 44 (Figure 5.21) and the temperature to 1673 K. Table 5.12 lists the properties of such a gas-mixture.

Table 5.12: Gas-mixture properties for 70% air / 30% He for the driver gas for condition RX-2.

Molecular Weight	21.5
Gas Constant, R	386.7
Specific Heat, C_p	1237.3
Specific Heat Ratio, γ	1.455

RX-3

The required driver sound speed at rupture for condition RX-3 is 1177 m/s. Figure 5.21 shows that gas mixtures of between 50/50 and 60/40 (air/helium) would result in suitable compression ratios for this condition. Table 5.13 lists the properties of a gas mixture consisting of 55% air and 45% helium. The required driver temperature of 2032 K (giving a sound

Table 5.13: Gas-mixture properties for 55% air / 45% He for the driver gas for condition RX-3.

Molecular Weight	18.15
Gas Constant, R	458.1
Specific Heat, C_p	1396.8
Specific Heat Ratio, γ	1.488

speed of 1177 m/s) corresponds to a temperature ratio of 6.87 and a compression ratio of 52. Though dissociation of air will not be an issue at this temperature, the specific heat C_p of air does increase with temperature. Though neglected in these approximations, the

increasing values of C_p would have the effect of reducing the value of γ and increasing the required compression ratio for a given driver sound speed.

This analysis shows that the low driver sound speeds required when targeting atmospheric flight conditions in a free-piston driven expansion tube can be readily attained through the adjustment of an air/helium gas mixture. While pure air can be utilized for the lower enthalpy conditions, the addition of helium creates a gas-mixture suitable for generating the driver sound-speeds associated with the higher enthalpy conditions with suitable compression ratio's. An additional benefit of utilizing air in the driver gas is a reduction in the pressure drop across the expansion for a particular expanded flow velocity. Figure 5.22 is a plot of the driver gas pressure ratio across the expansion (P_3/P_4) as a function of the driver equivalent flow Mach number (M_*) for gases with varying specific heat ratio's (γ). The RHYFL-

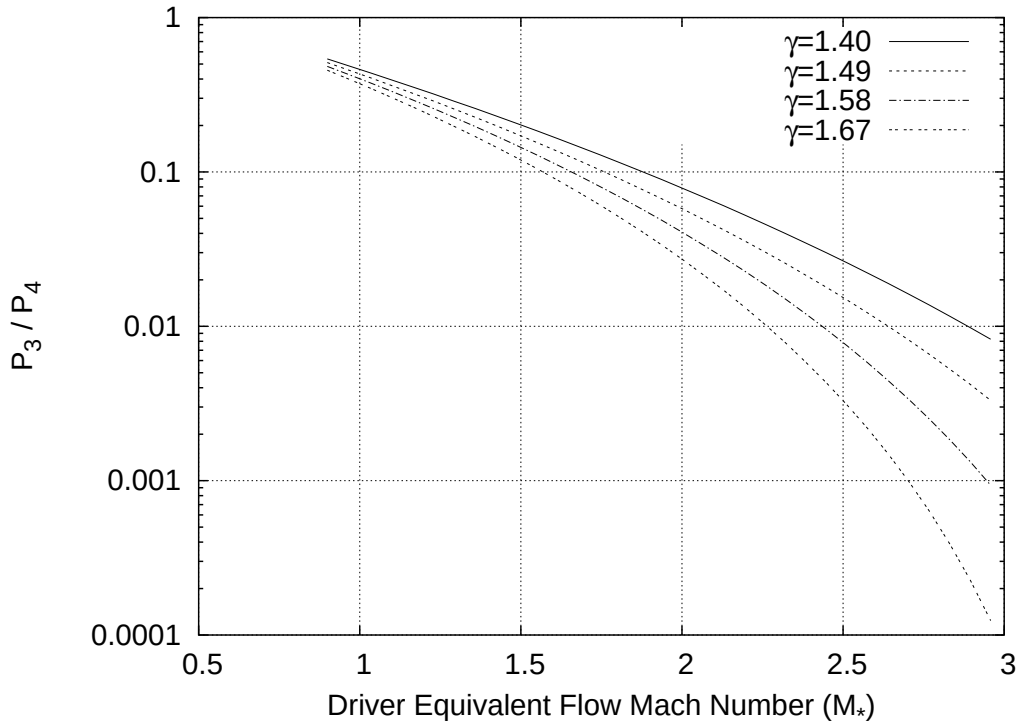

FIGURE 5.22: Driver gas pressure ratio across the expansion (P_3/P_4) as a function of the driver equivalent flow Mach number (M_*) for gases with varying specific heat ratio's (γ).

X scramjet testing conditions presented in this chapter have an M_* of approximately 1.5. Figure 5.22 suggests that a pressure increase of $\sim$60% could be expected if a gas with γ=1.4

was used as the driver gas, instead of one with γ=1.67, for a given driver sound speed. However, this analysis is neglecting the sound speed buffer requirements across the driver-gas/test-gas interface. The lower value of γ results in a smaller drop in temperature across the expansion and thus requires a lower driver sound speed at rupture in order to maintain the sound speed buffer at the interface for a particular shock speed. Figure 5.23 is similar to Figure 5.22 but the perfect gas calculations now maintain a sound speed buffer of a_3/a_2=0.8 across the driver-gas/test-gas interface. Also included on this graph are constant shock speed (and hence expanded driver gas velocity) lines between the four varying values of γ. The lines

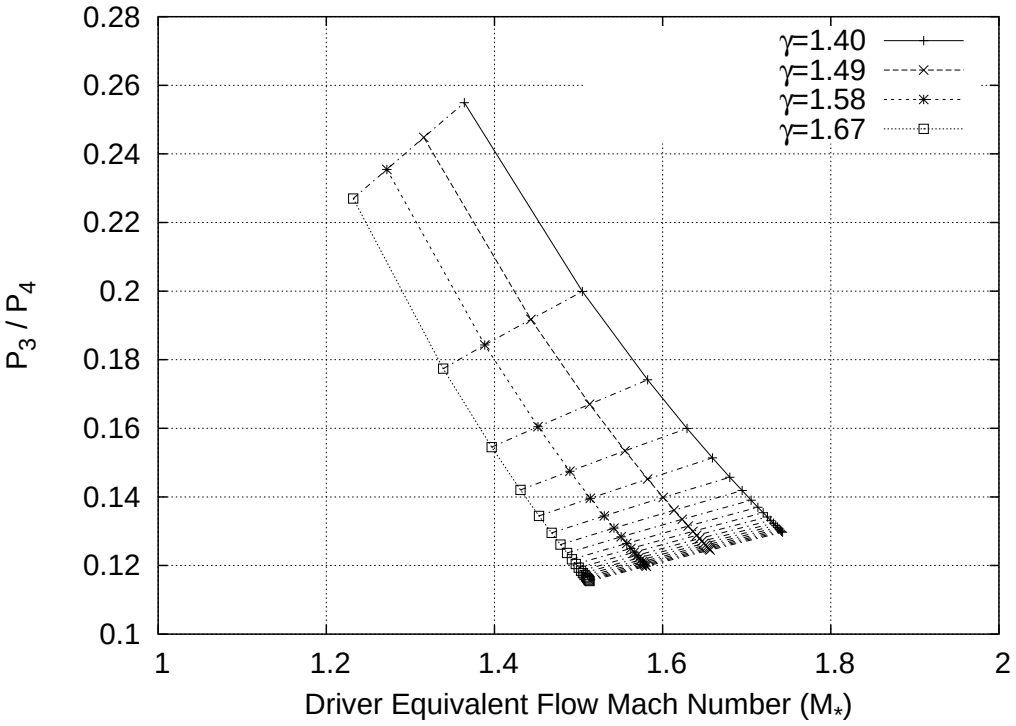

Figure 5.23: Driver gas pressure ratio across the expansion (P_3/P_4) as a function of the driver equivalent flow Mach number (M_*). Calculations maintain a sound speed buffer of a_3/a_2=0.8 across the driver-gas/test-gas interface for driver gases with varying specific heat ratio's (γ). Also included are lines of constant expanded driver gas (and hence test gas) velocity linking the four lines of constant γ. The test gas is air initially at room temperature.

of constant velocity approach a limit for each value of γ as the value of M_2 approaches the strong shock approximation given by Equation 2.3 (Chapter 2). For a fixed primary shock speed, the ideal pressure ratio that could expected for driver gases with varying values of γ

can be obtained from Figure 5.23 by following the lines of constant velocity to the required value of γ. RHYFL-X condition RX-1 utilized helium as the driver gas (γ=1.67) and had an $M_*\approx$1.5, corresponding to an ideal pressure ratio (P_3/P_4) of 0.1194. By using air (γ=1.4) as the driver gas results in an ideal pressure ratio of 0.134 across the expansion for the same primary shock speed. This indicates that the static pressure obtained from the simulations of this condition could be increased by around 12% by using air as the driver gas while still complying with the sound speed requirement across the driver-gas/test-gas interface. This potential pressure benefit diminishes for conditions RX-2 and RX-3 to around 8-9% as they require driver gas mixtures with higher values of γ.

5.5 Conclusion

This chapter has utilized both one-dimensional and axisymmetric simulation techniques to simulate the flow in the proposed RHYFL-X expansion tube. There were three target test conditions associated with atmospheric scramjet flight. The first condition, RX-1, aimed at producing testing conditions corresponding to Mach 10 flight at an altitude of 30 km. The second condition, RX-2, targeted Mach 15 flight at an altitude of 35 km and the third condition, RX-3, targeted test conditions matching those of Mach 20 flight at an altitude of 42 km.

Perfect gas calculations were used to estimate driver conditions at rupture and fill pressure of the shock and acceleration tube sections. To ensure that static temperatures of the test flow correspond to atmospheric conditions, it was found that low primary shock speeds are required. In order to maintain Paull's sound speed buffer requirements across the driver gas/test gas interface, the low primary shock speed meant that driver sounds speed well below those capable of free-piston drivers are required at the point of primary diaphragm rupture. Driver gas mixtures were calculated for each proposed operating condition that gave the desired sound speed at rupture after a suitable compression ratio. Both viscous and inviscid one-dimensional simulations were used to refine the fill conditions and obtain final test flow properties. While the inviscid one-dimensional simulation of RX-1 agreed well with results from a viscous axisymmetric Navier-Stokes simulation of the acceleration tube, the

viscous one-dimensional simulation resulted in a significantly higher test flow temperature. This higher test flow temperature in the viscous one-dimensional simulations is due to the fact that the cell properties are an average of the core flow and boundary layer properties. This phenomenon was seen to worsen rapidly as the viscous effects became more substantial in the higher enthalpy conditions. Also identified in the simulations was the difficulty encountered when calculating the properties of the first test gas cell to undergo the severe expansion once the secondary diaphragm ruptures in the inviscid simulations. The ill-calculated properties were confined to this one cell which, in the higher enthalpy conditions with more severe expansions, was quite pronounced in the final test flow.

The simulation results indicate that the proposed RHYFL-X expansion tube would be capable of generating test flows duplicating those that would be experienced over the full range of anticipated scramjet flight with negligible, if any, dissociation. For the low to mid scramjet flight enthalpies it was seen that static pressures over an order of magnitude greater than would be experienced during flight were possible using the maximum design rupture pressure of the primary diaphragm of 250 MPa. For the higher enthalpy regions of the proposed scramjet flight trajectory (Mach 20), simulations indicated that the RHYFL-X expansion tube would be able to match all flight parameters corresponding to atmospheric flight at Mach 20 at an altitude of 42 km, with a test flow static pressure around 3 times greater than the atmospheric static pressure at that altitude. The penalties to be paid for the superior flow generation capabilities of the RHYFL-X expansion tube are the very short test times and generically small test sections. The conservative shock and acceleration tube lengths used in the RHYFL-X simulations gave test times ranging from around 1 ms for the lower enthalpy condition down to a few hundred microseconds for the highest enthalpy condition. The axisymmetric simulations showed that core flow diameters in the range of 125-150 mm could be expected in the standard expansion tube configuration. The following chapter examines the use of a hypersonic nozzle placed at the end of the expansion tube to increase the size of this uniform core flow available for testing.

Chapter 6

Hypersonic Nozzles

6.1 Introduction

Test sections for standard expansion tubes are limited to the inside diameter of the tube and are typically quite small when compared to other types of facilities of similar overall size. This fact is aggravated by the large boundary layers at high Mach numbers. A method of increasing the diameter of core flow suitable for testing is to place a nozzle at the end of the acceleration tube to expand the flow out to a larger area. This chapter investigates the principles and concerns regarding the use of a full-capture contoured hypersonic nozzle placed at the end of the RHYFL-X expansion tube. Inviscid axisymmetric simulations are performed to validate a nozzle design based on the Method of Characteristics procedure. Viscous axisymmetric simulations of the acceleration tube and nozzle were also performed to determine the size of the expanded test gas, the available test-time and test flow properties that could be expected for a particular proposed RHYFL-X operating condition.

6.2 Hypersonic Nozzles

Most wind-tunnel concepts utilize a nozzle of some description to expand a stagnated supply region of test gas out to the desired conditions. As the flow is being expanded from stagnated conditions, the nozzles typically have large area ratios and can result in test section diameters of the order of 1 m for large shock-tunnel facilities. As an expansion tube benefits from the

unsteady expansion process to add energy to the expanding test flow, it does not require a nozzle and hence test section sizes are that of the inside diameter of the acceleration tube. Because the cost of manufacturing an expansion tube increases rapidly as the tube diameters are increased, expansion tube test sections are typically quite small. The X3 free-piston driven expansion tube [47] is the largest facility of its kind and has an inside diameter of 183 mm. Boundary layers reduce the diameter of the usable core flow to even less (typically around 150 mm for the X3 facility). As mentioned in Chapter 2, a possibility to increase the test section size in an expansion tube is to place a nozzle at the end of the acceleration tube. Figure 6.1 (from Chapter 2) depicts the proposed RHYFL-X expansion tube with such a nozzle arrangement.

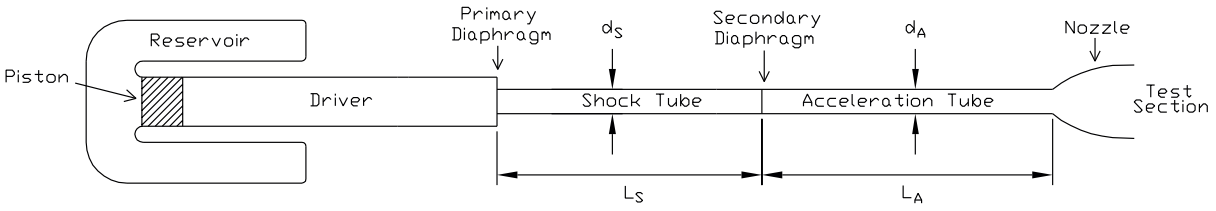

FIGURE 6.1: Schematic diagram of the expansion tube/nozzle arrangement as used in the simulations.

The high Mach number flows associated with this type of nozzle makes them highly susceptible to strong shock waves and pressure waves which disrupt the core test flow. Inviscid simulations by Chue *et al* [82] of a contoured nozzle found that shocks of significant magnitude were created by the inflection point of the nozzle contour, destroying the flow uniformity. The high Mach numbers combined with the decreasing axial pressure gradient also leads to rapid boundary layer growth along the nozzle wall, considerably reducing the effective exit area of the nozzle [83]. In addition to these challenges there are concerns regarding the start-up time of such nozzles in the short test times inherent in expansion tube flow. Because the shock must slow down when it enters the diverging nozzle, but the test flow velocity slightly increases, a reverse shock structure is established which consumes part of the test gas [84] [32]. It is therefore important to ascertain the impact that the nozzle

start-up process has on the duration of available test time.

6.3 Nozzle Design

The chapter investigates the design of a nozzle for one particular operating condition of the proposed RHYFL-X expansion tube. The nozzle is designed using an Interactive implementation of the Method Of Characteristics for supersonic irrotational flow in a two-dimensional geometry (*IMOC*[85, 86]). In this design method, the inflow Mach number is specified as well as the Mach number after the sudden turn at the start of the nozzle. The contour of the nozzle is then calculated using the Method of Characteristics technique to reach a fully expanded parallel inviscid flow.

One-dimensional simulations were performed to establish a proposed RHYFL-X operating condition that could utilize a nozzle to expand the test flow to atmospheric scramjet flight conditions. Viscous axisymmetric simulations of the acceleration tube were conducted to obtain the Mach number of the core flow prior to expansion through the nozzle. As shown later, the average Mach number of the test flow at the end of the acceleration tube for this operating ocndition is 8.75. A Mach number of 8.75 was therefore used as an inflow design constraint for the nozzle. The method of characteristics procedure can result in very long nozzles as the Mach numbers become large. The final expanded Mach number was chosen such that the overall length of the nozzle remained at a practical length. The length of the full inviscid nozzle design was initially set to 5 m and resulted in a final Mach number of 13.1 at the exit. Figure 6.2 shows the profile of the nozzle designed using the IMOC program with the corresponding nodes and characteristics. The initial diameter of the nozzle is 200 mm (RHYFL inside diameter) and the exit diameter is 524 mm, corresponding to an area ratio of 6.86.

In Figure 6.2, the last characteristic is reflected from the centre-line at $x \approx 1.54$ m, indicating that the ideal flow along the centre-line is completely expanded by this point. From this point to the exit plane of the nozzle, the diameter of the fully expanded core flow is linearly dependent on the axial distance towards the end of the nozzle. At the exit plane,

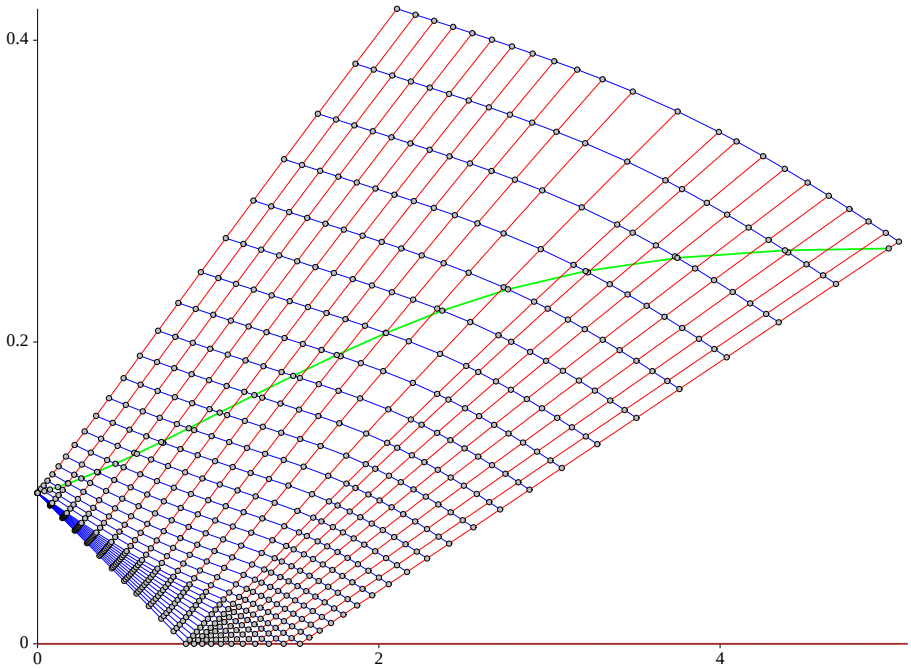

FIGURE 6.2: Mach 8.75 – 13.1 nozzle designed using the IMOC program. Note the difference in scale for the x and y axes.

the entire diameter of the flow in the inviscid calculation is at the final Mach number. In a viscous flow however with high Reynolds numbers and Mach numbers, the boundary layer size will occupy a significant portion ($\sim$50%) of the overall diameter. It is therefore needless to have the full 5 m nozzle as the last section would only be trying to expand flow which would be in the boundary layer. By truncating the nozzle, the correct wave-cancelling profile is maintained whilst shortening the overall nozzle length. As well as reducing the effects of any waves and/or shocks generated by the nozzle contour, the shorter nozzle would also reduce the nozzle start-up time. It was decided that the nozzle be truncated at 3.75 m. Much shorter than this and the smaller expanded core flow approaches a point where the added complexity and cost of a nozzle becomes unwarranted. Table 6.1 lists the coordinates defining the contour of the truncated nozzle used in the following simulations, with $y = 0$ being the centre line of the nozzle.

Table 6.1: Coordinates (in metres) defining the contour of the Mach 8.75 – 13.1 nozzle.

Mach 8.75–13.1 Nozzle			
x	y	x	y
0.000000	0.100000	0.88610	0.142837
0.039902	0.101179	1.06744	0.153206
0.072391	0.102219	1.27054	0.164814
0.118567	0.103872	1.49799	0.177588
0.179594	0.106287	1.75342	0.191392
0.256234	0.109602	2.04216	0.205974
0.348202	0.113901	2.37172	0.220782
0.456750	0.119318	2.75669	0.234929
0.581850	0.125904	3.21166	0.246975
0.724629	0.133733	3.74964	0.255766

6.4 Inviscid Simulations

To verify the method of characteristics procedure employed to design the nozzle, an axisymmetric simulation of the 3.75 m truncated nozzle was performed using the MB-CNS flow solver. The inflow conditions were set to approximate the properties of the core flow at the exit of the acceleration tube in the full viscous simulations of the acceleration tube. The velocity and temperature were adjusted slightly to provide a constant inflow Mach number of 8.75. The nozzle fill conditions were set the same as the acceleration tube fill conditions used in the full viscous simulations. Table 6.2 outlines the inflow and fill conditions for the inviscid simulation of the nozzle.

Table 6.2: Inflow and fill conditions for the inviscid axisymmetric simulation of the nozzle.

Inflow Conditions	
Mach number	8.75
Temperature (K)	560
Pressure (kPa)	120

Fill Conditions	
Pressure (Pa)	662
Temperature (K)	296

The computational domain consisted of 1800 cells spaced evenly along the axial direction with 42 cells across the radius clustered towards the wall. The MB-CNS input file `nozzle_inviscid.sit` is included in Appendix C.1. This simulation required approximately 15 hrs of CPU time using a 2.0 GHz Xeon processor (Gemini).

Figures 6.3 and 6.4 illustrate the Mach number and density contours of the nozzle starting process obtained from the inviscid perfect-gas simulation. The nozzle is seen to successfully expand an inviscid perfect-gas without the generation of shocks or compression waves by the wall contour. This procedure for designing hypersonic nozzles was also shown to be successful for other nozzle area ratios and lengths [87].

The sequence of contour plots illustrates the reverse shock structure that is formed due to the deceleration of the shock processed gas following its acceleration in the early part of

the nozzle. This reverse shock and associated flow structure is flushed out of the nozzle after 1.2 ms. Figure 6.5 is a plot of density contours at 0.8 ms and identifies the flow structure in the nozzle at this point.

Figure 6.6 shows the profiles of pressure, temperature, Mach number and velocity across the exit plane of the nozzle at $t = 1.2$ ms from the inviscid axisymmetric simulation. As the nozzle has been truncated from the full-size design, the flow near the nozzle wall has not been expanded to the same extent as the rest of the flow. These profiles show that the nozzle has increased the diameter of uniform flow from 200 mm to around 310 mm. This represents an area ratio of around 2.4. The effective area ratio is believed to increase for viscous conditions where the boundary layer significantly reduces the size of the core flow prior to expansion.

6.5 Viscous Simulations

In order to investigate the starting characteristics of a hypersonic nozzle, full axisymmetric viscous simulations of the acceleration tube as well as the nozzle must be performed so that the flow development of the incoming nozzle flow is captured. Due to the magnitude of the computational expense, an acceleration tube of 11 m in length was used. This would result in a shorter period of steady test time at the end of the acceleration tube than would be achieved if the full ∼20 m acceleration tube was simulated. It does, however, demonstrate the flow structure and characteristics associated with the use of a hypersonic nozzle in the short test times inherent with expansion tubes.

6.5.1 One-dimensional Simulation

One-dimensional simulations were initially performed to obtain the transient inflow conditions for the axisymmetric simulations of the acceleration tube. As with the other simulations of the RHYFL-X facility, the driver temperature was chosen to meet the sound speed buffer requirements across the driver gas/test gas interface. The 10 μs hold time was also imposed

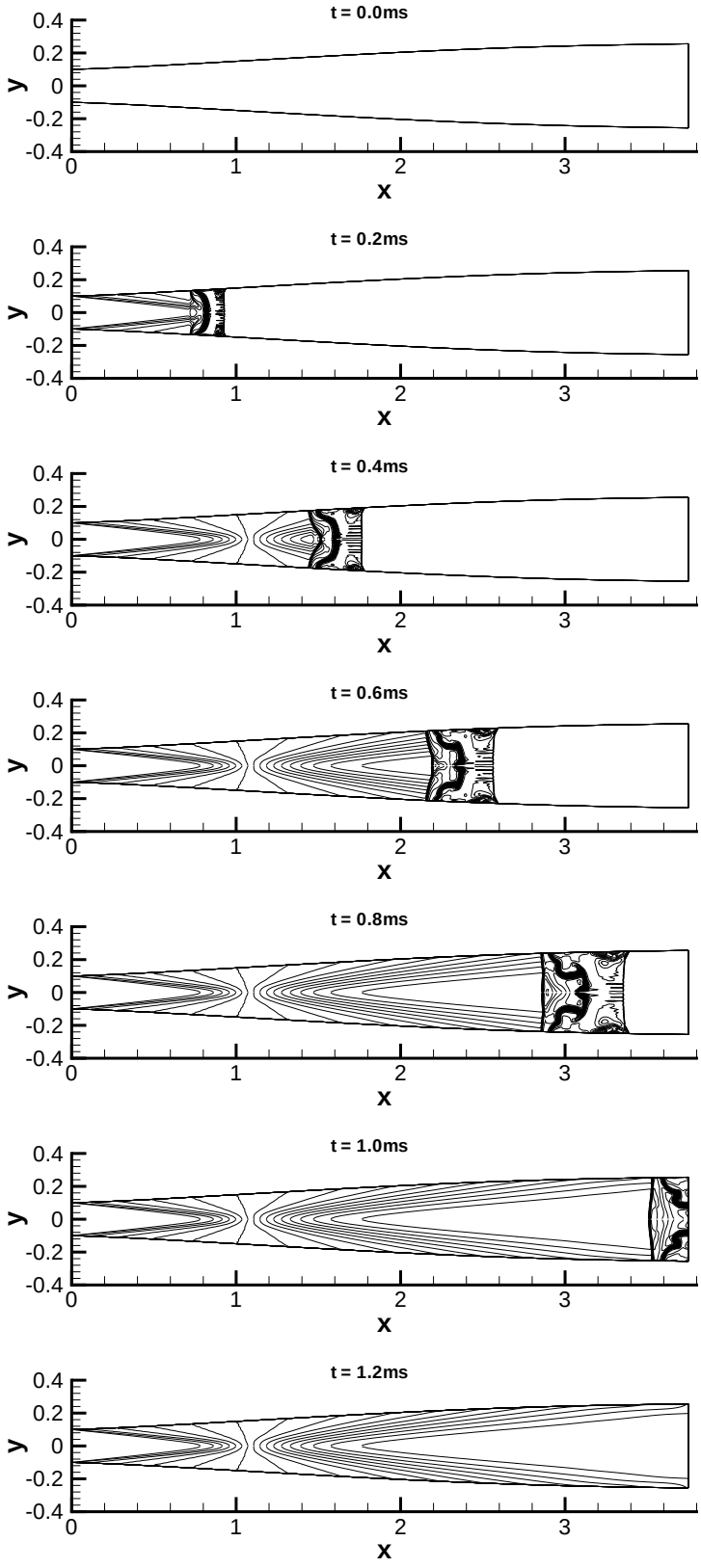

FIGURE 6.3: Mach number contours of the starting process of the Mach 8.75 – 13.1 nozzle from the inviscid axisymmetric simulation. Lengths are in metres.

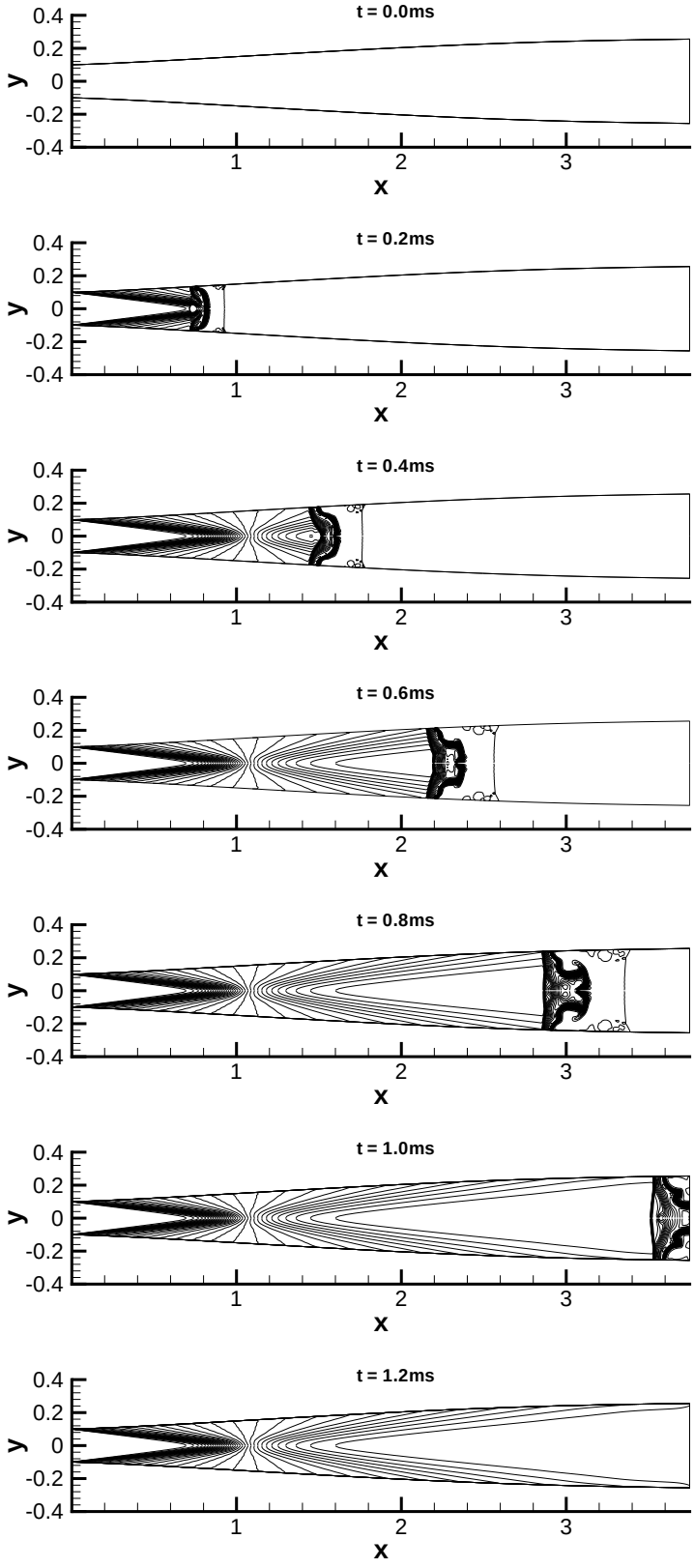

Figure 6.4: Density contours of the starting process of the Mach 8.75 – 13.1 nozzle from the inviscid axisymmetric simulation. Lengths are in metres.

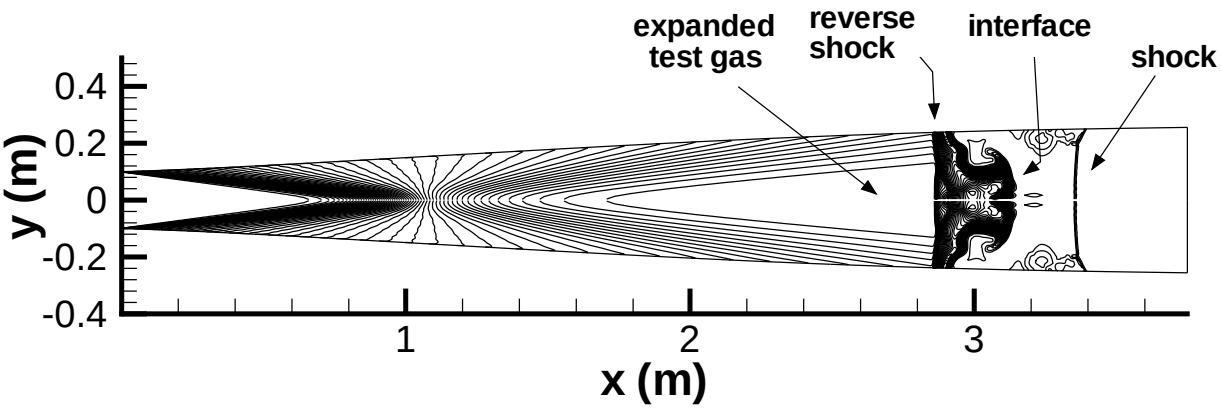

FIGURE 6.5: Flow structure in the nozzle at $t = 0.8\,\text{ms}$. Contours indicate density variation.

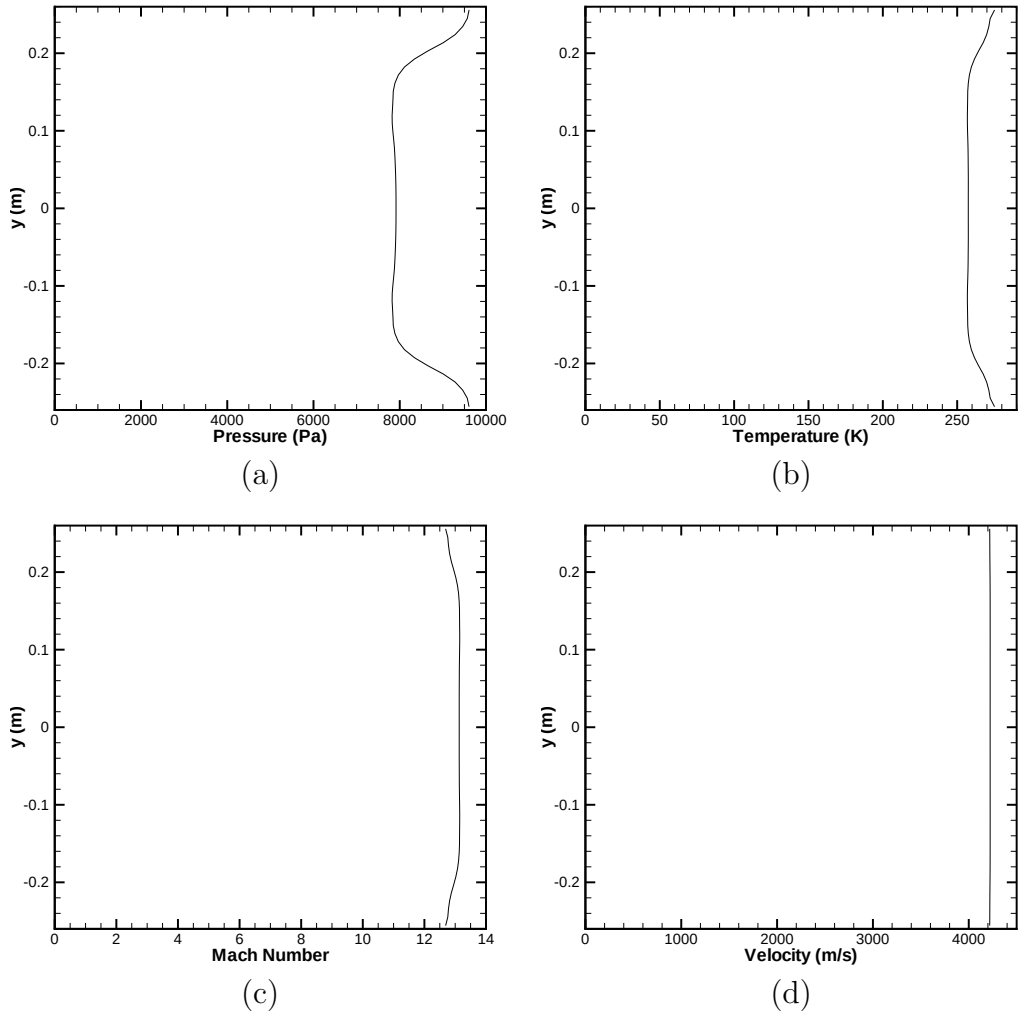

Figure 6.6: Profiles of (a) Pressure, (b) Temperature, (c) Mach number and (d) Velocity across the exit plane of the truncated Mach 8.75 – 13.1 nozzle from the inviscid axisymmetric simulation at $t = 1.2\,\text{ms}$. Nozzle centre-line at y=0.

on the secondary diaphragm. Table 6.3 outlines the initial conditions used in the L1D simulations of the RHYFL-X nozzle condition. The cells initially in the acceleration tube are set to fuse together once they reach a certain minimum size to avoid excessively small cells caused by the strong secondary shock. The input file (`RHYFLX_nozzle_inv.Lp`) for this L1D simulation is contained in Appendix B.

Table 6.3: Initial conditions for the L1D simulation of the RHYFL-X nozzle condition.

	Driver	Shock Tube	Accel. Tube
Fill Pressure	250 MPa	784 kPa	662 Pa
Fill Temperature	320 K	296 K	296 K
Length	2 m	12 m	20 m
Diameter	600 mm	200 mm	200 mm
No. of Cells	400	3000	1667

6.5.2 Axisymmetric Simulation

Due to the high unit Reynolds number (∼100 million per metre) and high Mach number, the simulation of the nozzle and acceleration tube is assumed to have turbulent boundary layers throughout (Baldwin-Lomax turbulence model). To reduce the overall CPU time, the simulation of the acceleration tube and nozzle was performed in 2 stages. The first stage was a simulation of just the 11 m acceleration tube. This was solved until the shock reached the end of the acceleration tube. The solution was saved at this point and then used as initial conditions in the second simulation which included the nozzle on the end of the acceleration tube.

The simulation of just the acceleration tube involved dividing the 11 m acceleration tube into 4 sections (blocks) so it could be solved in parallel on 4 processors (Figure 6.7(a)). For the second stage of the simulation when the nozzle was placed on the end of the acceleration tube (Figure 6.7(b)), the first block of the acceleration tube, Block 0, was removed so that the number of blocks, and hence processors, remained at 4. The fill conditions for the acceleration tube were the same as for the one-dimensional simulation described in Table 6.3. The nozzle contour was as described in the inviscid simulation. Because Block 0, along with its data,

is removed for the second part of the simulation, it was made smaller than Blocks 1, 2 and 3. This was firstly to ensure that its removal did not affect the final test flow when solving the rest of the acceleration tube and nozzle. Also, the larger blocks in the acceleration tube meant that they were of similar size to the nozzle block, Block 4, resulting in more efficient parallel computations. The high Reynolds numbers and Mach numbers associated with the flow meant that the flow was assumed turbulent in all blocks.

This simulation was solved on both the Origin 3000 and the National APAC Facility. On the APAC machine, the simulation required 103 hrs of CPU time to solve up to the point at which the shock reaches the end of the tube (2.55e-3 s). The second stage of the simulation including the nozzle required an additional 67 hours to solve to a total simulated time of 6.0e-3 s. This is a total CPU time of 170 hrs required for the viscous axisymmetric simulation of the 11 m acceleration tube and 3.7 m nozzle. This CPU time was increased by over a factor of 2 to a total of 360 hrs (219 hrs for the just acceleration tube plus 141 hrs for the acceleration tube and nozzle) when solved on UQ's Origin 3000.

6.5.3 Results

Figure 6.8 is a plot of the static pressure obtained at two locations on the exit plane of the acceleration tube for the viscous axisymmetric simulation. One point is at a distance of 12 mm from the centre line (r=12 mm) and the other a distance of 42 mm from the centre-line (r=42 mm). This figure indicates that, after the $\sim$115μs of accelerator gas, there is approximately 340μs of steady test gas pressure. This agrees well with 350μs calculated analytically from the simulated interface speed (assumed equal to shock speed) and simulated expanded test gas sound speed. The Mach number history at the same two locations is shown in Figure 6.9. This graph indicates the average Mach number (M =8.75) over the test time used to design the nozzle.

Figures 6.10 and 6.11 show the static pressure and Mach number history recorded 30 mm and 107 mm from the axis of symmetry at the exit plane of the nozzle. Evident in these figures is the first $\sim$500μs of flow associated with the nozzle start-up process followed by around 535μs of steady flow. The good agreement between the pressure and Mach number

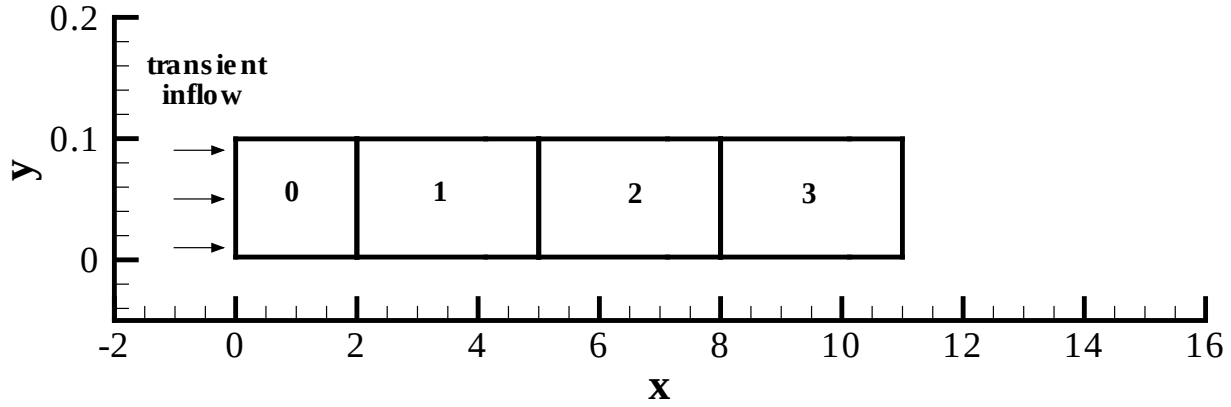

(a)

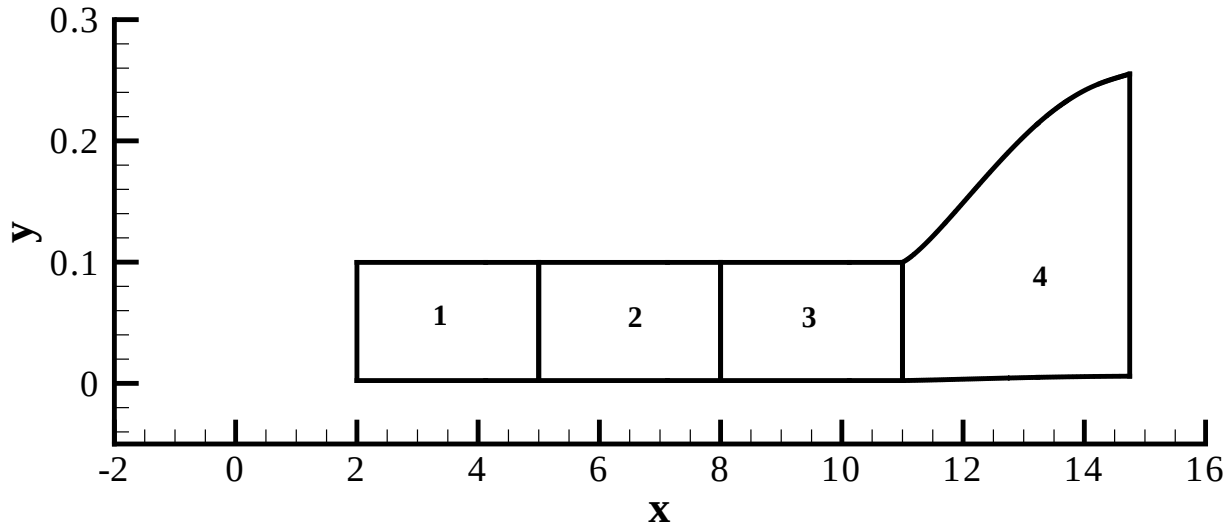

(b)

Block	0	1	2	3	4
Number of cells	1131 x 42	1697 x 42	1697 x 42	1697 x 42	2018 x 42

FIGURE 6.7: Computational domains for the two parts of the viscous axisymmetric simulation - (a) just acceleration tube, (b) acceleration tube and nozzle. Axis of symmetry is along y=0.0. Note difference in scale on the x and y axes.

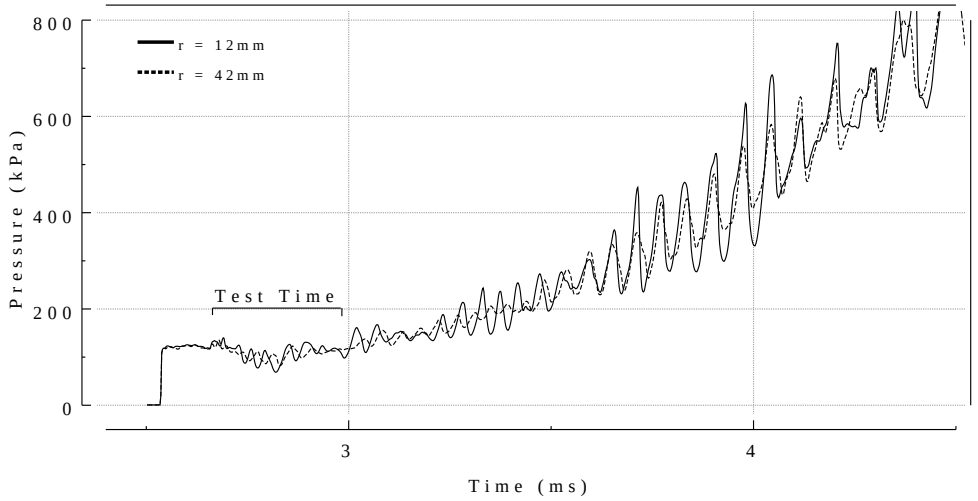

Figure 6.8: Static pressure history recorded at distances of 12 mm and 42 mm from the centreline at the exit plane of the acceleration tube. Results from the viscous axisymmetric simulation of the RHYFL-X nozzle condition.

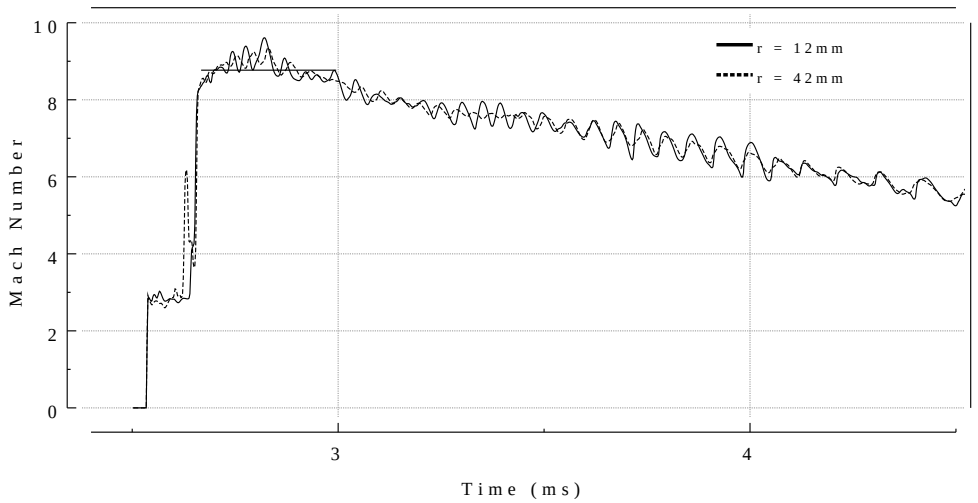

Figure 6.9: Mach number history recorded at distances of 12 mm and 42 mm from the centreline at the exit plane of the acceleration tube. Results from the viscous axisymmetric simulation of the RHYFL-X nozzle condition.

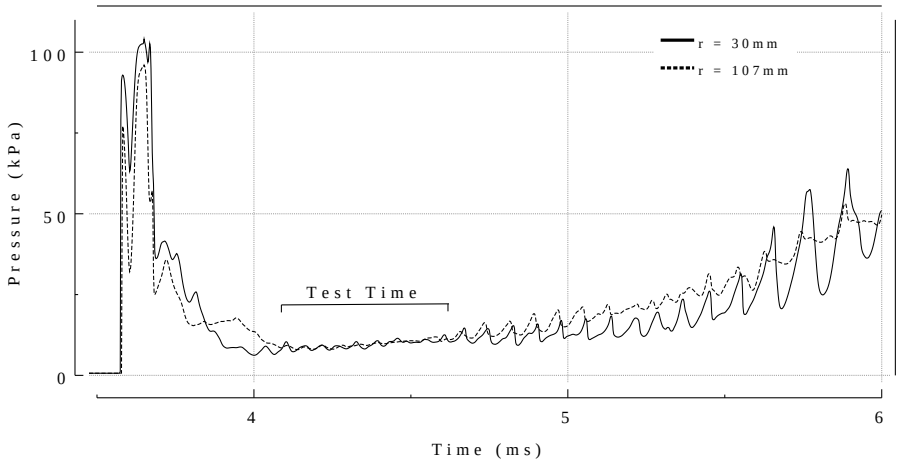

FIGURE 6.10: Static pressure history recorded at distances of 30 mm and 107 mm from the centre-line at the exit plane of the nozzle. Results from the viscous axisymmetric simulation of the RHYFL-X nozzle condition.

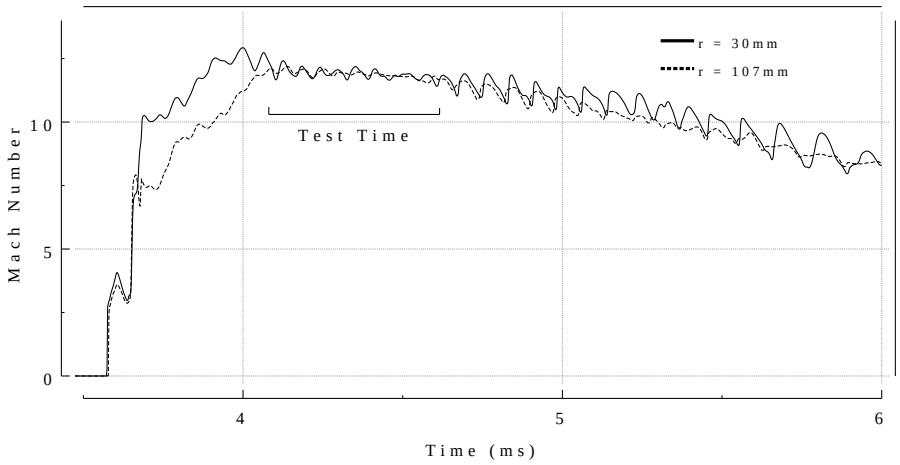

FIGURE 6.11: Mach number history recorded at distances of 30 mm and 107 mm from the centre-line at the exit plane of the nozzle. Results from the viscous axisymmetric simulation of the RHYFL-X nozzle condition.

traces at the two different locations across the exit plane ($r = 30\,\text{mm}$ and $r = 107\,\text{mm}$) suggests a uniform core flow of at least 214 mm in diameter for the duration of the 535μs test time. The final expanded Mach number for the viscous axisymmetric simulation is around 12.2 compared to the inviscid simulation which expanded the flow to approximately 13.

The 535μs of steady flow at the nozzle exit represents an almost 60% increase in the duration of steady flow available prior to expansion through the nozzle. Stewart *et al* [87] demonstrated this increase in test time for other hypersonic nozzle designs using the same viscous simulation technique. Such a test time increase was originally suggested by Trimpi and Callis [88] in 1965 based on a perfect-gas one-dimensional flow analysis. There has been a number of examples of nozzle implementation on expansion tubes [49, 89] though no concise experimental demonstration of increased test time has been found in the literature.

The starting process of the nozzle is depicted in Figures 6.12 and 6.13 via contour plots of the Mach number (Figure 6.12) and density on a logarithmic scale (Figure 6.13). The times indicated on these figures are from the point of secondary diaphragm rupture, and the x-coordinates originate ($x = 0.0$) at the secondary diaphragm location. This figures show that even though the inviscid nozzle design has not accounted for the substantial boundary layers present in the viscous simulations, it can successfully expand the hypersonic flow exiting the acceleration tube. The start-up shock structure does however take longer to flush out of the nozzle than seen in the inviscid simulations. The inviscid simulations indicated that this start-up shock structure is cleared from the nozzle 1.2 milliseconds after the flow enters the nozzle, leaving a clean shock-free nozzle. The viscous simulation of the nozzle indicates that it requires 400μs longer (1.6 ms) to flush the shock structure associated with the start-up process out of the nozzle. The red contours in the Mach number plots indicate test flow with a Mach number of $12.2 \pm 3\%$.

Figure 6.14 shows the velocity and Mach number profiles across (a) the exit of the acceleration tube at $t = 2.9\,\text{ms}$ and (b) across the nozzle exit at $t = 4.5\,\text{ms}$. The Mach number is seen to be uniform over a diameter of around 280 mm at the exit of the nozzle. This is an increase in area by a factor of 7 over the 106 mm diameter core flow available at the end of

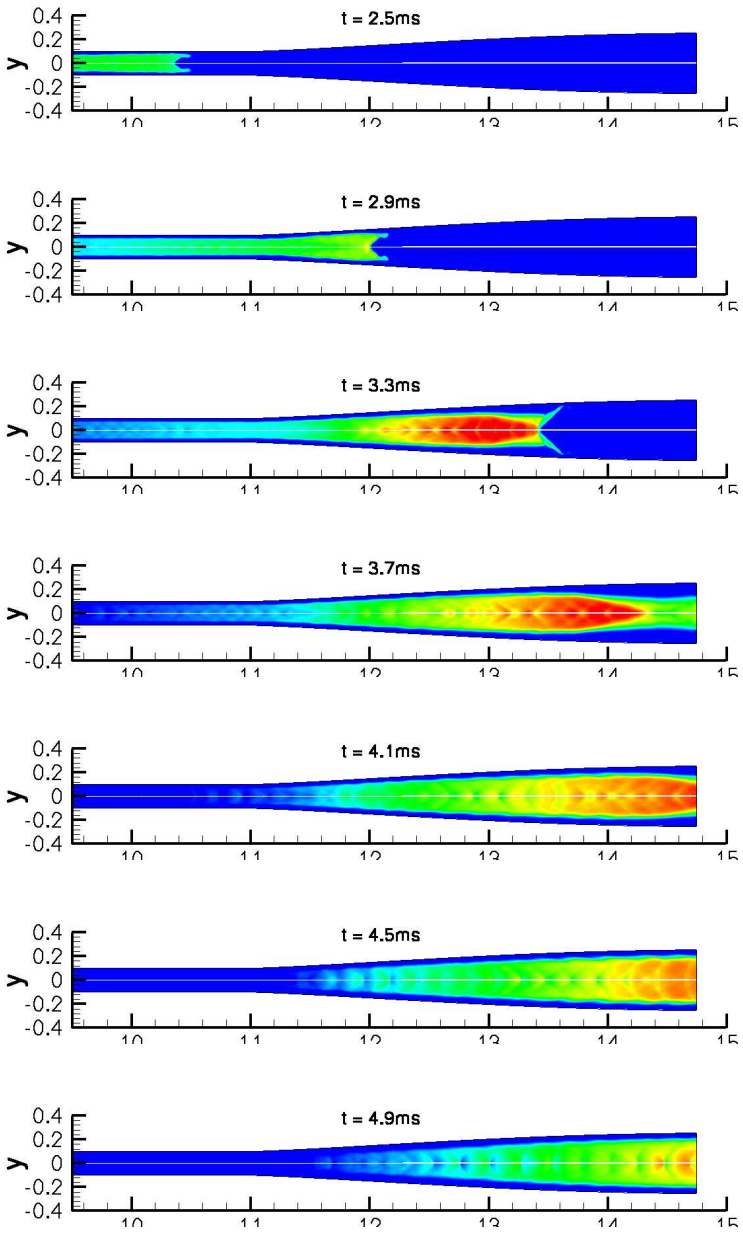

FIGURE 6.12: Results from the viscous axisymmetric RHYFL-X simulation of the acceleration tube and contoured nozzle. Contours are of Mach number and lengths are in metres. Red contours indicate test flow with a Mach number of $12.2 \pm 3\%$..

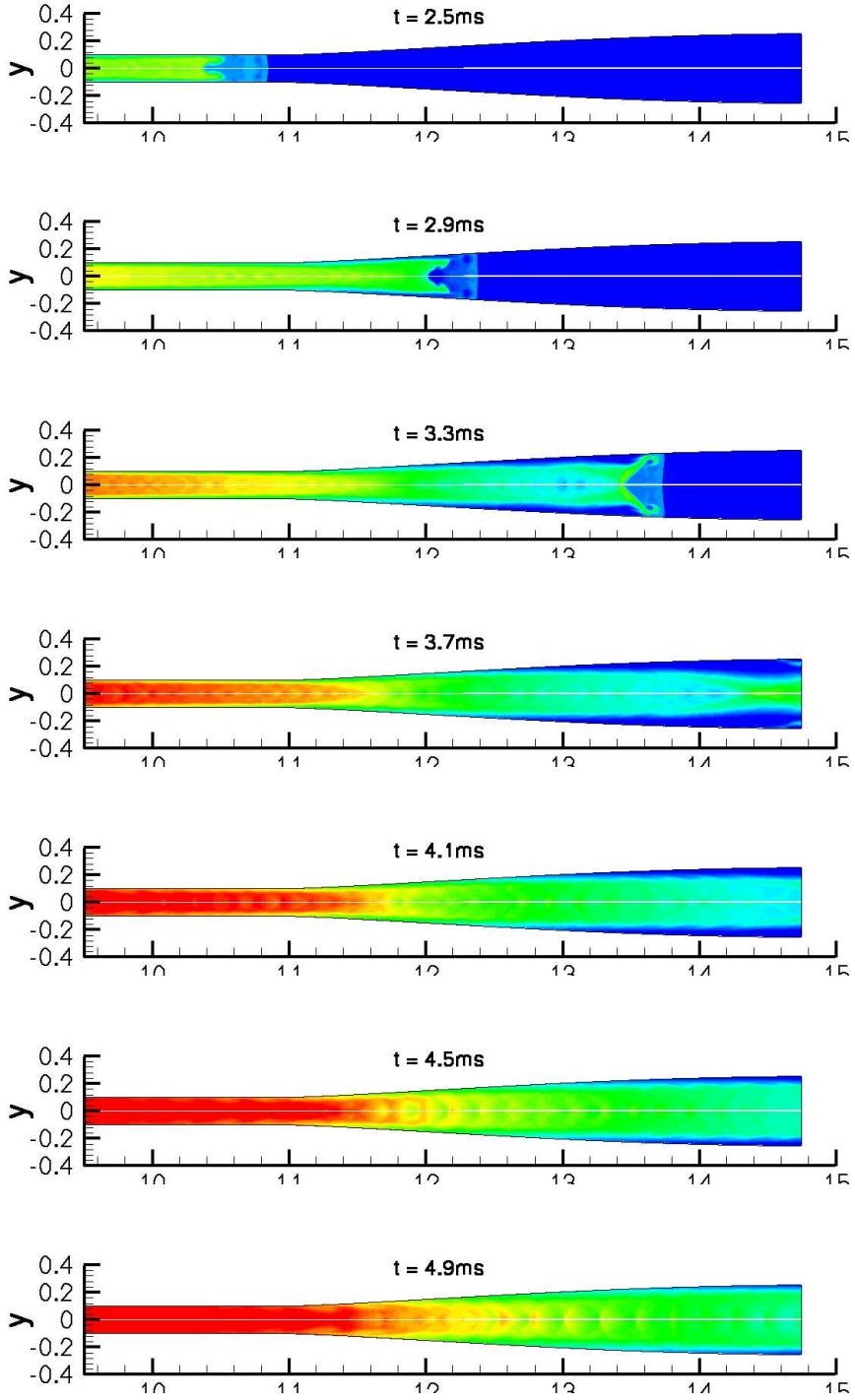

Figure 6.13: Results from the viscous axisymmetric RHYFL-X simulation of the acceleration tube and contoured nozzle. Contours are of density (logarithmic scale) and lengths are in metres.

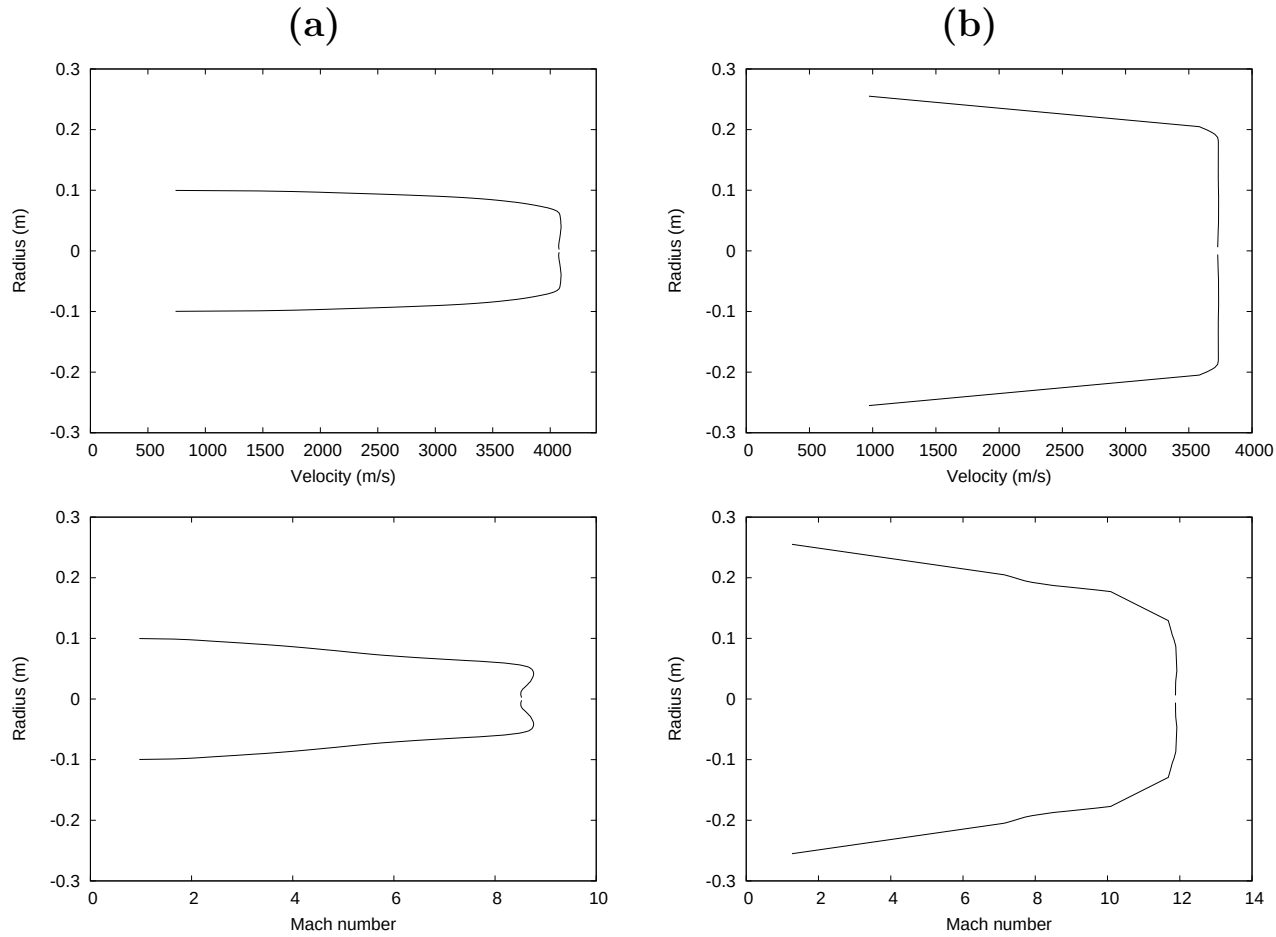

FIGURE 6.14: Profiles of velocity and Mach number obtained from viscous axisymmetric RHYFL-X simulations of the acceleration tube and nozzle. (a) Acceleration tube exit ($t = 2.9$ms), (b) nozzle exit ($t = 4.5$ms).

the acceleration tube. The diameter of uniform velocity increases from 130 mm at the exit of the acceleration tube to 380 mm at the exit of the nozzle. This corresponds to an area ratio of 8.5.

6.5.4 Nozzle Test Flow Conditions

Assuming that the test flow is not disrupted by disturbances propagating downstream, the test time for a standard length of acceleration tube is the difference in arrival time between the T/A interface and the most downstream $u - a$ wave of the unsteady expansion. This test time can be calculated analytically from the equation:

$$t = \frac{l_A}{u_{int} - a_6} - \frac{l_A}{u_{int}} \tag{6.1}$$

where l_A is the length of acceleration tube, u_{int} is the velocity of the interface and a_6 is the sound speed of the expanded test gas. Equation 6.1 can be rewritten as

$$t = \frac{a_6\, l_A}{u_{int}(u_{int} - a_6)} \tag{6.2}$$

which shows that, assuming that the interface velocity (assumed equal to shock velocity) and expanded test gas sound speed remain essentially unchanged, the test time is directly proportional to the length of the acceleration tube. The simulations indicated a test time of approximately 340μs was available at the end of the 11 m acceleration tube. The simulation shows that an increase in this test time of around 200μs, or almost 60%, is achieved by placing the nozzle on the end of the acceleration tube. If a 20 m acceleration tube was used, the test time at the end of the acceleration tube would be around 620μs. This indicates that approximately 820–1000μs of steady test flow could be expected at the exit of a nozzle placed at the end of a 20 m acceleration tube.

Table 6.4 outlines the predicted testing conditions available from this proposed RHYFL-X operating condition obtained from viscous axisymmetric simulations. Included in this table is the diameter of uniform core flow in the test section as well as the predicted test time that would be available assuming a 20 m acceleration tube. These test flow properties are compared with what would be required to exactly reproduce free-stream conditions at the

Table 6.4: RHYFL-X nozzle testing conditions compared with atmospheric scramjet flight.

	RHYFL-X (nozzle)	Flight
Mach number	12.1	12.0
Altitude (km)	n/a	31.5
Sound Speed (m/s)	328	303
Flow Speed (m/s)	3970	3640
Temperature (K)	269	228
Total Temperature (K)	5852	4929
Total Enthalpy (MJ/kg)	7.9	6.6
Pressure (kPa)	8.0	0.935
Total Pressure (GPa)	4.9	0.46
Test time (μs)	∼820–1000	n/a
Core flow diameter (mm)	∼280	n/a

corresponding Mach number during a typical scramjet flight path (Figure 1.4). The core flow diameter is based on the Mach number because that has the smallest diameter of uniform flow at the exit of the nozzle. These results indicate that the use of a nozzle attached at the end of the acceleration tube would allow the RHYFl-X facility to generate free-stream conditions associated with scramjet flight at Mach 12 with uniform core flow diameters of around 250-300 mm.

6.6 Conclusion

The chapter has utilized an Interactive Method of Characteristics program to design a contoured nozzle to be placed on the end of the RHYFL-X expansion tube with the intent of increasing the uniform core flow suitable for testing. The nozzle design was truncated to reduce its overall length and to reduce the start-up time required. The truncated nozzle design was validated via an inviscid axisymmetric simulation with a uniform inflow. The shock structure associated with the starting process of such a nozzle was clearly identified in the inviscid simulation results. The nozzle contour did not generate any shocks or strong compression waves at the inflection point and successfully expanded a uniform hypersonic flow from a Mach number of 8.75 to 13.

The viscous simulations consisted of 11 m of acceleration tube with the 3.75 m nozzle placed at the end. Although based on inviscid flow principles with no allowance for the large boundary layers, the nozzle successfully expanded the flow to around Mach 12.1. No flow-altering pressure waves or shock waves were generated by the nozzle and the uniform core flow was expanded from around 106 mm to 280 mm - an area ratio of approximately 7. Simulation results showed that around 340μs of steady flow was available at the end of the acceleration tube. After the subsequent expansion through the nozzle, this period of steady flow increased to around 535μs. This means that the implementation of a contoured hypersonic nozzle on the proposed RHYFL-X expansion could offer the benefits of not only increasing the diameter of the core test flow but also increasing the available test time.

Chapter 7

Conclusions

The general aim of this thesis was to investigate the performance potential of a large scale free-piston driven expansion tube for the purpose of sub-orbital scramjet testing. The proposed expansion tube was based on the RHYFL shock tunnel project of the late 1980's and was dubbed RHYFL-X. In order to refine and validate the simulation techniques employed for obtaining performance predictions of the proposed facility, simulations were first conducted of several operating conditions of a currently operational expansion tube X2. This final chapter of the thesis provides a summary of the expansion tube concept, simulation techniques and nonequilibrium chemistry concerns, as well as the general capabilities of the proposed RHYFL-X expansion tube to generate flows suitable for scramjet testing. Some comments regarding the research as well as recommendations for further research into this area are also included

7.0.1 The Expansion Tube Concept

The unsteady flow processes of an expansion tube were presented and compared with other ground-based hypersonic testing facilities. It was shown that based on currently available technologies, the expansion tube concept is the only facility that can generate the flow fields associated with the anticipated atmospheric flight of a scramjet powered vehicle up to orbital speeds. Due to the nature by which the expansion tube generates the final test flow, these high energy flows are possible with negligible, if any, dissociation. Based on these facts, it

is of significant interest to determine the performance potential of a large-scale expansion tube based on the RHYFL shock tunnel design.

7.0.2 Simulations of the X2 Expansion Tube

The numerical simulation techniques employed to simulate the flow processes within the proposed RHYFL-X facility were validated and verified on a currently operating expansion tube, X2. Though one-dimensional simulations of the two-stage compression process were performed which incorporated a transient heat-transfer model to capture heat-loss in the piston transition process, the rupture pressure and driver gas slug length used in the simulations were obtained from experiment. The driver temperature was chosen such that the simulated primary shock speed matched that measured from experiment. The higher density, lower speed section of the expansion tube from the point of primary diaphragm rupture to the point of secondary diaphragm rupture was simulated using the Lagrangian one-dimensional flow simulation code L1D assuming equilibrium chemistry. The flow history at the secondary diaphragm location was recorded and then used as a time-varying input to an axisymmetric simulation of the acceleration tube using the Multi-Block, Compressible Navier-Stokes solver MB-CNS also assuming equilibrium chemistry. As driver-related attenuation was seen to have a significant effect on the final test flow properties in certain X2 operating conditions, this method enabled any noise and/or disturbances propagating downstream from the driver to be captured. Good agreement of simulation results with experimental data indicates that this technique of combining one-dimensional and axisymmetric simulations adequately describes the flow processes in an expansion tube at sub-orbital scramjet enthalpies. The inclusion of a $10\,\mu$s hold-time imposed on the secondary diaphragm as a simplistic model of the diaphragm inertial characteristics resulted in closer agreement with experimentally measured data.

The computational expense of the axisymmetric technique is justified when investigating established flow phenomena in a smaller facility such as X2, but for determining an envelope of proposed operating conditions for a large-scale facility such as the RHYFL-X expansion

tube, CPU requirements become impractically large. For this reason, one-dimensional simulations of the entire X2 expansion tube were also performed. Though these simulations were performed on different machines therefore not allowing a direct comparison of CPU requirements, an approximate three orders of magnitude reduction in CPU time was seen between the axisymmetric and one-dimensional simulations. While the viscous one-dimensional simulations were found to agree well with experimental shock speeds, they significantly overestimated the temperature of the expanded test flow. This is because the one-dimensional nature of the code models the diameter of the tube as one cell with flow properties that are an average of boundary layer and core flow properties. Hence this effect of over-predicting the test flow temperature was seen to worsen as the viscous interactions became more significant with the higher shock speeds and lower densities. Inviscid simulations were also performed to eliminate this phenomenon inherent in the viscous one-dimensional simulations. The flow velocity and temperature were seen to agree very well with the more computationally expensive viscous axisymmetric simulations. The lack of viscous interaction however did result in an approximately 6% higher final shock speed and hence a slightly higher static pressure. Results showed that the inviscid one-dimensional simulation technique offered a convenient, computationally efficient method of adequately modelling the flow within an expansion tube operating at scramjet flight enthalpies and relatively high densities. For higher enthalpy, lower density conditions however, the significant viscous effects makes both the viscous and inviscid one-dimensional simulation techniques less reliable.

One-dimensional simulations incorporating finite-rate chemistry were also performed for two X2 operating conditions to examine the validity of assuming equilibrium chemistry for air test gases in expansion tube operation. Though expansion tubes have the potential to produce clean, dissociation free test flow, it was shown that current moderate to high enthalpy operating conditions of the X2 facility are such that dissociation of the final test flow can be substantial. The relatively high primary shock speeds, coupled with the reflected shock region caused by the secondary diaphragm, results in significant dissociation of the test gas prior to the unsteady expansion. The extent to which recombination occurs during the expansion process depends on the operating condition. For the lower enthalpy, 6.8 km/s

final shock speed condition (Condition 2), the nitrogen in the air was seen to recombine rapidly and levels of dissociation agreed well with the equilibrium simulation. The dissociated oxygen however did not recombine as rapidly as the equilibrium calculations predicted and experienced a more frozen expansion process. This chemical freezing resulted in a slightly slower final shock speed and a lower test flow temperature than seen in the equilibrium simulation. For the higher enthalpy, 9.7 km/s final shock speed condition (Condition 4), the oxygen experienced essentially no recombination during the expansion from the highly dissociated state in the reflected shock region. The dissociated nitrogen in the test flow did experience a certain level of recombination during the unsteady expansion, but did not reach levels predicted by the equilibrium simulation. This resulted in a test flow temperature only half of that obtained from the equilibrium simulation and suggests that nonequilibrium effects are more influential in this higher enthalpy condition.

7.0.3 Proposed RHYFL-X Expansion Tube

All calculations and simulations performed for the predicted RHYFL-X expansion tube assumed a maximum primary diaphragm burst pressure of 250 MPa, an inside diameter of the shock tube and acceleration tube of 200 mm, and a 9:1 area ratio between the driver and shock tube. The simulations also included the 10 μs hold time imposed on the secondary diaphragm. The final compressed driver length was set at 2 m, with the shock tube and acceleration tube lengths then determined such that the final test flow for each condition was not affected by driver-related disturbances. The compression process was not modeled because the driver sound speeds required when targeting static atmospheric temperatures in the test flow were seen to be well below what free-piston drivers are capable of generating in practice. A major operational design constraint imposed on the proposed operating conditions is the requirement of a sound speed buffer across the expanded-driver-gas/shock-processed-test-gas interface. An increase in sound speed of at least 20% across this interface acts as a buffer against noise generated in the driver and helps produce a cleaner final test flow. The low primary shock speeds required when targeting test flow temperatures in the vicinity of 250–270 K means that this sound speed buffer severely limits the driver sound

speeds at rupture and causes a significant reduction in the final realisable test flow pressures than what would be otherwise obtainable.

The three specific flight conditions targeted were at Mach 10 (RX-1), Mach 15 (RX-2) and Mach 20 (RX-3) at altitudes corresponding to the anticipated scramjet flight trajectory shown in Figure 1.4 (Chapter 1). A viscous axisymmetric simulation of the acceleration tube section was performed for condition RX-1 to compare with the viscous and inviscid one-dimensional simulations of this condition. The good agreement between these two simulation techniques further emphasizes the benefits of utilizing the significantly more computationally efficient one-dimensional approach for simulating high-density expansion tube flow. All simulations of the RHYFL-X facility assumed equilibrium chemistry because test gas dissociation was shown to be negligible for these conditions with low primary shock speeds (Tables 5.5, 5.8 and 5.11). For the lowest enthalpy RHYFL-X operating condition, RX-1, the simulations indicate that all flight parameters can be matched in the test flow with a pressure over 60 times greater than what would be expected during flight. Simulations of conditions RX-2 and RX-3 also indicate that the proposed RHYFL-X expansion tube would be capable of generating test flows that duplicate free-stream conditions over the full range of anticipated atmospheric scramjet flight with static pressures significantly greater that the atmospheric static pressure at the corresponding altitudes. The excess pressure predicted by the simulations allows for binary scaling for testing of sub-scale models, as well as for any errors between simulation and actual facility performance. A relaxation in the sound speed buffer requirement across the driver gas/test gas interface during actual operation would result in higher pressures than seen in the current simulations.

The inevitable price to be paid for the superior flow generation capabilities of an expansion tube is a severe reduction in the available test time and core flow diameter. The available test times for the three RHYFL-X operating conditions studied range from around one millisecond for the lower enthalpy condition to around 230 μs for the Mach 20 condition. The diameter of the uniform core flow available in the standard configuration expansion tube would be approximately 125-150 mm. The use of a hypersonic nozzle to increase the diameter of this test flow was also examined. The nozzle was designed utilizing an inviscid method

of characteristics procedure, and was seen to successfully expand an inviscid hypersonic flow in an axisymmetric simulation. Viscous axisymmetric simulations of the acceleration tube with the truncated nozzle attached indicated that the nozzle not only successfully expanded the flow out to a larger area but had the unexpected, though desirable, effect of increasing the duration of steady flow.

7.0.4 Comments & Recommendations

Driver

In a free piston driven expansion tube, the length of compressed driver gas at the point of primary diaphragm rupture determines the lengths of the shock and acceleration tubes which ultimately determine the final test time duration. Tuned operation of the piston in a facility with a large area ratio between the driver and shock tube means that the rupture pressure is maintained for a longer period after diaphragm rupture and allows for a longer shock tube. A 2 m static driver gas slug was used in the simulations and conservative shock tube lengths were chosen to allow for the uncertainties in the driver gas slug length at rupture. Further research into the tuned operation of such a large free-piston driver would allow for an improved estimation of the optimal shock and acceleration tube lengths, and hence test times, for each operating condition.

This study has shown that, when targetting scramjet flight conditions in an expansion tube, relatively low driver sound speeds are required in order to provide an adequate sound speed ratio across the driver-gas/test-gas interface to suppress noise transmission to the test flow. These low driver sound speeds correspond to approximately room temperature helium. This suggests that the use of a large free-piston driver may be superfluous for generating scramjet test flows in an expansion tube. Though when targetting high-enthalpy superorbital conditions, the high sound speed capabilities of the free-piston driver would offer substantial performance benefits.

Secondary diaphragm

Currently operational expansion tubes such as the X2 facility utilise light materials for the secondary diaphragm. Simulations have shown that the inertial effects of this secondary diaphragm material should be included to describe more accurately the flow processes in such a facility. The high pressures associated with proposed operating conditions of the RHYFL-X facility mean that the secondary diaphragm must be able to maintain a pressure differential of over 1 MPa, as opposed to less than 10 kPa for standard operating conditions in other expansion tubes. This would require the use of a significantly stronger, thicker material. Albeit the pressures would scale in proportion to the size of the large secondary diaphragm and peripheral shearing is expected, the behaviour of the diaphragm during the rupture process on this much larger scale is only speculative. Variations in the rupturing, and hence expansion, process may affect the test flow in ways that are not accounted for in the current simulations.

Nozzle

The inviscid axisymmetric simulations of the nozzle showed that a contoured nozzle could successfully expand an inviscid hypersonic flow. The simulation results however were quite sensitive to the accuracy to which the profile of the nozzle was defined. Insufficient resolution of the nozzle contour meant that shock/pressure waves were generated at certain points in the nozzle profile. The viscous simulation used the same nozzle profile resolution that was shown to be successful in the inviscid simulations. Further work needs to be done to determine the effects that machining tolerances would have on the performance of such a nozzle. The axisymmetric viscous simulations also indicated that the nozzle has the effect of increasing the duration of steady test time. Additional research is required to adequately describe the precise mechanisms behind this phenomenon and the extent to which it is applicable for other operating conditions.

Appendix A

Input file for 5-species air model

Listed below is the `air.chm` input file used in the finite-rate chemistry simulations.

air.chm

```
# air.chm

# Reference:
# Gupta, R.N., Yos, J.M., Thompson, R.A. and Lee, K-P. (1990)
# A Review of Reaction Rates and Thermodynamic and Transport
# Properties for an 11-species Air Model for Chemical and
# Thermal Nonequilibrium Calculations to 30 000K.
# NASA RP-1232
#
# 06-Sept-2003

SPECIES poly
   He N2 N O2 O NO
END

REACTIONS  saim  cms
N2 + N2 <=> 2 N + N2    k_f   1.92e17     -0.5    1.131e5
                        k_b   1.09e16     -0.5    0.0
N2 + N  <=> 2 N + N     k_f   4.15e22     -1.5    1.131e5
                        k_b   2.32e21     -1.5    0.0
N2 + O2 <=> 2 N + O2    k_f   1.92e17     -0.5    1.131e5
```

```
                        k_b   1.09e16     -0.5    0.0
N2 + O <=> 2 N + O      k_f   1.92e17     -0.5    1.131e5
                        k_b   1.09e16     -0.5    0.0
N2 + NO <=> 2 N + NO    k_f   1.92e17     -0.5    1.131e5
                        k_b   1.09e16     -0.5    0.0
O2 + O  <=> 2 O + O     k_f   3.61e18     -1.0    5.94e4
                        k_b   3.01e15     -0.5    0.0
O2 + N  <=> 2 O + N     k_f   3.61e18     -1.0    5.94e4
                        k_b   3.01e15     -0.5    0.0
O2 + O2  <=> 2 O + O2   k_f   3.61e18     -1.0    5.94e4
                        k_b   3.01e15     -0.5    0.0
O2 + N2  <=> 2 O + N2   k_f   3.61e18     -1.0    5.94e4
                        k_b   3.01e15     -0.5    0.0
O2 + NO  <=> 2 O + NO   k_f   3.61e18     -1.0    5.94e4
                        k_b   3.01e15     -0.5    0.0
NO + N2  <=> N + O + N2 k_f   3.97e20     -1.5    7.56e4
                        k_b   1.01e20     -1.5    0.0
NO + N   <=> N + O + N  k_f   3.97e20     -1.5    7.56e4
                        k_b   1.01e20     -1.5    0.0
NO + O2  <=> N + O + O2 k_f   3.97e20     -1.5    7.56e4
                        k_b   1.01e20     -1.5    0.0
NO + O  <=>  N + O + O  k_f   3.97e20     -1.5    7.56e4
                        k_b   1.01e20     -1.5    0.0
NO + NO  <=> N + O + NO k_f   3.97e20     -1.5    7.56e4
                        k_b   1.01e20     -1.5    0.0
NO + O  <=> O2 + N      k_f   3.18e9       1.0    1.97e4
                        k_b   9.63e11      0.5    3.6e3
N2 + O  <=> NO + N      k_f   6.75e13      0.0    3.75e4
                        k_b   1.5e13       0.0    0.0
END
```

Appendix B

L1D input files

This appendix lists the following L1D input files:

- B.1 - `s506_10hold_noneq.Lp`: for the inviscid finite-rate chemistry simulation of the low-enthalpy X2 condition s506.
- B.2- `s506_10hold.Lp`: for the inviscid equilibrium chemistry simulation of the low-enthalpy X2 condition s506.
- B.3 - `s833_10hold_noneq.Lp`: for the inviscid finite-rate chemistry simulation of high-enthalpy X2 condition s833.
- B.4 - `s833_10hold.Lp`: for the inviscid equilibrium chemistry simulation of the high enthalpy X2 condition s833.
- B.5 - `RX1_10hold_inviscid.Lp`: for the inviscid equilibrium chemistry simulation of RHYFL-X condition RX-1.
- B.6 - `RX1_10hold_viscous.Lp`: for the viscous equilibrium chemistry simulation of RHYFL-X condition RX-1.
- B.7 - `RHYFLX_nozzle_inv.Lp`: for the inviscid equilibrium chemistry simulation of the RHYFL-X nozzle condition .

B.1 s506_10hold_noneq.Lp

s506_10hold_noneq.Lp

```
#L1d-3.0   low-enthalpy condition (s506) with finite-rate chemistry
0 22 1              test_case, gas_index, fr_chem
3 0 1               nslug, npiston, ndiaphragm
1.9e-03   250000    max_time, max_steps
1.0e-9   0.2        dt_init, CFL
2 2 0.0             Xorder, Torder
3                    n_dt_plot
0.0     0.05e-3  5.0e-6    t_change, dt_plot, dt_his
5.0e-4  0.01e-3  5.0e-6    t_change, dt_plot, dt_his
1.25e-3 0.1e-3   1.0e-6
11                  hnloc
1.550                       hxloc[0]
1.786                       hxloc[1] 3 locations along shock tube
2.021                       hxloc[2]
2.350                       hxloc[3] secondary diaphragm location
2.352                       hxloc[4] just after sec diaphragm location
2.944                       hxloc[5]
3.454                       hxloc[6]
4.504                       hxloc[7] 5 locations along acceleration tube
5.019                       hxloc[8]
6.680                       hxloc[9]
7.400                       hxloc[10], acceleration tube exit
tube definition follows:
500    1            n, nseg
-0.115  0.085  0    xb[0], Diamb[0], linear[0]
7.450  0.085  0
0                   nKl
296.0  0            Tnominal, nT
Secondary Diaphragm [0]
0 45.0e3 10.0e-6 0.0 0.0
1 R 0.0
2 L 0.0
slug 0: Compressed helium
70  0 1 1.03        nnx, to_end_1, to_end_2, strength
900 0 0.002 0.008   adaption
1  0                viscous, adiabatic
V  0.0              left boundary : wall with zero velocity
S  1 L              right boundary: test gas slug 1
1                   hn_cell
1                   hx_cell[0]
-0.115 0.0 26.0e6 0.0 2100.0 Initial: x1, x2, p, u, T
1.0 0.0 0.0 0.0 0.0 0.0                 species mass fraction
slug 1: Air test gas
500  0 1 1.03       nnx, to_end_1, to_end_2, strength
1200 0 0.002 0.006  adaption
0 0                 viscous, adiabatic
S 0 R               left boundary :slug 0: helium driver gas slug
SD 2 L 0            right boundary: accel gas slug with diapragm 0, slug 2
7                   hn_cell
300                    hx_cell[1]
400                 hx_cell[2]
420                    hx_cell[3]
440                    hx_cell[4]
460                    hx_cell[5]
480                    hx_cell[6]
495                    hx_cell[7]
0.00 2.35 7.5e3 0.0 296.0 Initial: x1, x2, p, u, T
0.0 0.78 0.0 0.22 0.0 0.0                   species mass fraction
slug 2: Air accelerator gas
300  0 0 0.0        nnx, to_end_1, to_end_2, strength
2200 1 0.01 0.020   adaption
0 0                 viscous, adiabatic
SD 1 R 0            left boundary : test gas slug 1 with diaphragm 0
```

```
F                    right boundary: free end of accel tube
1                    hn_cell
1                    hx_cell[8]
2.35 7.45 30.0 0.0 296.0 Initial: x1, x2, p, u, T
0.0 0.78 0.0 0.22 0.0 0.0                    species mass fraction
```

B.2 s506_10hold.Lp

s506_10hold.Lp

```
#L1d-3.0   robs condition with equil chemistry (look up tables)
0 96 0               test_case, gas_index, fr_chem
3 0 1                nslug, npiston, ndiaphragm
1.9e-03   250000     max_time, max_steps
1.0e-8   0.35        dt_init, CFL
2 2 0.0              Xorder, Torder
3                     n_dt_plot
0.0     0.05e-3  5.0e-6    t_change, dt_plot, dt_his
5.0e-4  0.01e-3  5.0e-6    t_change, dt_plot, dt_his
1.25e-3 0.1e-3   1.0e-6
11                   hnloc
1.550                        hxloc[0]
1.786                        hxloc[1] 3 locations along shock tube
2.021                        hxloc[2]
2.350                        hxloc[3] secondary diaphragm location
2.352                        hxloc[4] just after sec diaphragm location
2.944                        hxloc[5]
3.454                        hxloc[6]
4.504                        hxloc[7] 5 locations along acceleration tube
5.019                        hxloc[8]
6.680                        hxloc[9]
7.400                        hxloc[10], acceleration tube exit
tube definition follows:
500    1             n, nseg
-0.115  0.085  0     xb[0], Diamb[0], linear[0]
7.450  0.085  0
0                    nKl
296.0  0             Tnominal, nT
Secondary Diaphragm [0]
0 45.0e3 10.0e-6 0.0 0.0
1 R 0.0
2 L 0.0
slug 0: Compressed helium
70  0 1 1.03         nnx, to_end_1, to_end_2, strength
900 0 0.002 0.008    adaption
1  0                 viscous, adiabatic
V  0.0               left boundary : wall with zero velocity
S  1 L               right boundary: test gas slug 1
1                    hn_cell
1                    hx_cell[0]
-0.115 0.0 26.0e6 0.0 2100.0 Initial: x1, x2, p, u, T
0.0 0.0 1.0 0.0 0.0                  species mass fraction
slug 1: Air test gas
500  0 1 1.03        nnx, to_end_1, to_end_2, strength
1200 0 0.002 0.006   adaption
0 0                  viscous, adiabatic
S 0 R                left boundary :slug 0: helium driver gas slug
SD 2 L 0             right boundary: accel gas slug with diapragm 0, slug 2
7                    hn_cell
300                     hx_cell[1]
400                  hx_cell[2]
420                     hx_cell[3]
440                     hx_cell[4]
460                     hx_cell[5]
480                     hx_cell[6]
```

```
495                     hx_cell[7]
0.00 2.35 7.5e3 0.0 296.0 Initial: x1, x2, p, u, T
1.0 0.0 0.0 0.0 0.0                     species mass fraction
slug 2: Air accelerator gas
300  0 0 0.0          nnx, to_end_1, to_end_2, strength
2200 1 0.01 0.020     adaption
0 0                   viscous, adiabatic
SD 1 R 0              left boundary : test gas slug 1 with diaphragm 0
F                     right boundary: free end of accel tube
1                     hn_cell
1                     hx_cell[8]
2.35 7.45 30.0 0.0 296.0 Initial: x1, x2, p, u, T
1.0 0.0 0.0 0.0 0.0                     species mass fraction
```

B.3 s833_10hold_noneq.Lp

s833_10hold_noneq.Lp

```
#L1d-3.0   s833 with finite-rate chemistry
0 22 1              test_case, gas_index, fr_chem
3 0 1               nslug, npiston, ndiaphragm
1.4e-03   250000    max_time, max_steps
1.0e-8   0.15       dt_init, CFL
2 2 0.0             Xorder, Torder
2                    n_dt_plot
0.0     0.2e-3  1.0e-5    t_change, dt_plot, dt_his
0.4e-3  1.0e-5  1.0e-6    t_change, dt_plot, dt_his
11                  hnloc
1.550                       hxloc[0]
1.786                       hxloc[1]
2.021                       hxloc[2]
2.350                       hxloc[3] secondary diaphragm location
2.906                       hxloc[4]
3.158                       hxloc[5]
3.410                       hxloc[6]
4.460                       hxloc[7]
4.975                       hxloc[8]
6.830                       hxloc[9]
7.440                       hxloc[10]
tube definition follows:
500    1            n, nseg
-0.121  0.085  0    xb[0], Diamb[0], linear[0]
7.450   0.085  0
0                   nKl
296.0  0            Tnominal, nT
Secondary Diaphragm [0]
0 45.0e3 10.0e-6 0.0 0.0
1 R 0.0
2 L 0.0
slug 0: Compressed helium
100  0 1 1.03       nnx, to_end_1, to_end_2, strength
900 0 0.002 0.008   adaption
1  0                viscous, adiabatic
V  0.0              left boundary : wall with zero velocity
S  1 L              right boundary: test gas slug 1
1                   hn_cell
1                   hx_cell[0]
-0.121 0.0 26.0e6 0.0 2100.0 Initial: x1, x2, p, u, T
1.0 0.0 0.0 0.0 0.0 0.0                 species mass fraction
slug 1: Air test gas
600  0 1 1.05       nnx, to_end_1, to_end_2, strength
1200 0 0.002 0.006  adaption
0 0                 viscous, adiabatic
S 0 R               left boundary :slug 0: helium driver gas slug 0
SD 2 L 0            right boundary: accel gas slug with diapragm 0, slug 2
```

```
6                   hn_cell
500                 hx_cell[1]
520                    hx_cell[2]
540                    hx_cell[3]
560                    hx_cell[4]
580                    hx_cell[5]
595                    hx_cell[6]
0.00 2.35 2.4e3 0.0 296.0 Initial: x1, x2, p, u, T
0.0 0.78 0.0 0.22 0.0 0.0           species mass fraction
slug 2: Air accelerator gas
300  0 0 0.0        nnx, to_end_1, to_end_2, strength
2200 1 0.01 0.020   adaption
0 0                 viscous, adiabatic
SD 1 R 0            left boundary : test gas slug 1 with diaphragm 0
F                   right boundary: free end of accel tube
1                   hn_cell
1                   hx_cell[7]
2.35 7.45 0.933 0.0 296.0 Initial: x1, x2, p, u, T
0.0 0.78 0.0 0.22 0.0 0.0           species mass fraction
```

B.4 s833_10hold.Lp

s833_10hold.Lp

```
#L1d-3.0   shot 833 with equil chemistry (look up tables)
0 96 0              test_case, gas_index, fr_chem
3 0 1               nslug, npiston, ndiaphragm
1.4e-03   250000    max_time, max_steps
1.0e-8   0.15       dt_init, CFL
2 2 0.0             Xorder, Torder
2                   n_dt_plot
0.0     0.2e-3  1.0e-5    t_change, dt_plot, dt_his
0.4e-3  1.0e-5  1.0e-6    t_change, dt_plot, dt_his
11                  hnloc
1.550                       hxloc[0]
1.786                       hxloc[1]
2.021                       hxloc[2]
2.350                       hxloc[3] sec diaph location
2.906                       hxloc[4]
3.158                       hxloc[5]
3.410                       hxloc[6]
4.460                       hxloc[7]
4.975                       hxloc[8]
6.830                       hxloc[9]
7.440                       hxloc[10]
tube definition follows:
500    1            n, nseg
-0.121  0.085  0    xb[0], Diamb[0], linear[0]
7.450   0.085  0
0                   nKl
296.0  0            Tnominal, nT
Secondary Diaphragm [0]
0 45.0e3 10.0e-6 0.0 0.0
1 R 0.0
2 L 0.0
slug 0: Compressed helium
```

```
100  0 1 1.03        nnx, to_end_1, to_end_2, strength
900 0 0.002 0.008    adaption
1  0                 viscous, adiabatic
V  0.0               left boundary : wall with zero velocity
S  1 L               right boundary: test gas slug 1
1                    hn_cell
1                    hx_cell[0]
-0.121 0.0 26.0e6 0.0 2100.0 Initial: x1, x2, p, u, T
0.0 0.0 1.0 0.0 0.0                  species mass fraction
slug 1: Air test gas
600  0 1 1.05        nnx, to_end_1, to_end_2, strength
1200 0 0.002 0.006   adaption
0 0                  viscous, adiabatic
S 0 R                left bound: slug 0 helium driver gas
SD 2 L 0             right bound: slug 2 accel gas, diaph 0
500                  hx_cell[1]
520                     hx_cell[2]
540                     hx_cell[3]
560                     hx_cell[4]
580                     hx_cell[5]
595                     hx_cell[6]
0.00 2.35 2.4e3 0.0 296.0 Initial: x1, x2, p, u, T
1.0 0.0 0.0 0.0 0.0                    species mass fraction
slug 2: Air accelerator gas
300  0 0 0.0         nnx, to_end_1, to_end_2, strength
2200 1 0.01 0.020    adaption
0 0                  viscous, adiabatic
SD 1 R 0             left bound: slug 1 test gas, diaph 0
F                    right bound: free end of accel tube
1                    hn_cell
1                    hx_cell[7]
2.35 7.45 0.933 0.0 296.0 Initial: x1, x2, p, u, T
1.0 0.0 0.0 0.0 0.0                    species mass fraction
```

B.5 RX1_10hold_inviscid.Lp

RX1_10hold_inviscid.Lp

```
#L1d-3.0 Inviscid RHYFL-X condition RX-1 with equil chemistry
0 96 0               test_case, gas_index, fr_chem
3 0 1                nslug, npiston, ndiaphragm
18.0e-03   250000     max_time, max_steps
1.0e-8   0.35        dt_init, CFL
2 2 0.0              Xorder, Torder
3                     n_dt_plot
0.0     2.0e-4   5.0e-6   t_change, dt_plot, dt_his
7.0e-3  1.0e-5   2.0e-6    t_change, dt_plot, dt_his
8.0e-3  1.0e-4   2.0e-6
7                    number of history cells
2.0                 hxloc[0]
6.0                 hxloc[1]
9.5                 hxloc[2]
```

```
15.0                hxloc[4]
20.0                hxloc[5]
25.0                hxloc[6]
30.0             hxloc[7] end of acceleration tube
300    3            n, nseg
-2.0  0.6  0     xb[0], Diamb[0], linear[0]
-0.05 0.6  0
0.0   0.2  0
30.0  0.2  0
0                   nKl
296.0  0            Tnominal, nT
Secondary Diaphragm [0]
0 2790.0e3 10.0e-6 0.0 0.0
1 R 0.0
2 L 0.0
slug 0: Compressed helium
400  0 1 1.1         nnx, to_end_1, to_end_2, strength
900 0 0.002 0.008   adaption
1  0                viscous, adiabatic
V  0.0              left boundary : wall with zero velocity
S  1 L              right boundary: slug 1 test gas
1                   hn_cell
1                   hx_cell
-2.0 0.0 250.0e6 0.0 150.0 Initial: x1, x2, p, u, T
0.0 0.0 1.0 0.0 0.0                  species mass fraction
slug 1: Air test gas
3000  0 1 1.03        nnx, to_end_1, to_end_2, strength
3700 0 0.002 0.006  adaption
0 0                 viscous, adiabatic
S 0 R               left bound: slug 0 helium driver gas
SD 2 L 0            right bound: slug 2 accel slug, diaph 0
1                   hn_cell
1                   hx_cell
0.00 10.0 1860.0e3 0.0 296.0 Initial: x1, x2, p, u, T
1.0 0.0 0.0 0.0 0.0                  species mass fraction
slug 2: Air accelerator gas
1667  0 0 0.0        nnx, to_end_1, to_end_2, strength
1800 1 0.008 0.040   adaption
0 0                 viscous, adiabatic
SD 1 R 0            left boundary : diaphragm
F                   right boundary: end of tube
1                   hn_cell
1                   hx_cell
10.0 30.0 700.0 0.0 296.0 Initial: x1, x2, p, u, T
1.0 0.0 0.0 0.0 0.0                  species mass fraction
```

B.6 RX1_10hold_viscous.Lp

RX1_10hold_viscous.Lp

```
#L1d-3.0 Viscous RHYFL-X condition RX-1 with equil chemistry
0 96 0              test_case, gas_index, fr_chem
```

```
3 0 1                nslug, npiston, ndiaphragm
20.0e-03   250000    max_time, max_steps
1.0e-8   0.35        dt_init, CFL
2 2 0.0              Xorder, Torder
3                     n_dt_plot
0.0     2.0e-4   5.0e-6   t_change, dt_plot, dt_his
7.0e-3  1.0e-5   2.0e-6    t_change, dt_plot, dt_his
8.0e-3  1.0e-4   2.0e-6
8                    number of history cells
2.0                 hxloc[0]
6.0                 hxloc[1]
9.5                 hxloc[2]
10.0                 hxloc[3] secondary diaphragm location
15.0                 hxloc[4]
20.0                 hxloc[5]
25.0                 hxloc[6]
30.0              hxloc[7] end of acceleration tube
tube definition follows:
300    3             n, nseg
-2.0  0.6  0     xb[0], Diamb[0], linear[0]
-0.05 0.6  0
0.0   0.2  0
30.0  0.2  0
0                    nKl
296.0  0             Tnominal, nT
Secondary Diaphragm [0]
0 2790.0e3 10.0e-6 0.0 0.0
1 R 0.0
2 L 0.0
slug 0: Compressed helium
400  0 1 1.1          nnx, to_end_1, to_end_2, strength
900 0 0.002 0.008   adaption
1  0                 viscous, adiabatic
V  0.0               left boundary : wall with zero velocity
S  1 L               right boundary: slug 1 test gas
1                    hn_cell
1                    hx_cell
-2.0 0.0 250.0e6 0.0 150.0 Initial: x1, x2, p, u, T
0.0 0.0 1.0 0.0 0.0                  species mass fraction
slug 1: Air test gas
3000  0 1 1.03        nnx, to_end_1, to_end_2, strength
3700 0 0.002 0.006  adaption
1 0                  viscous, adiabatic
S 0 R                left boundary: slug 0 helium driver gas
SD 2 L 0             right boundary: slug 2 accel gas, diaph 0
1                    hn_cell
1                    hx_cell
0.00 10.0 1860.0e3 0.0 296.0 Initial: x1, x2, p, u, T
1.0 0.0 0.0 0.0 0.0                    species mass fraction
slug 2: Air accelerator gas
1667  0 0 0.0        nnx, to_end_1, to_end_2, strength
1800 1 0.008 0.040   adaption
```

```
2 0                  viscous, adiabatic
SD 1 R 0             left boundary : diaphragm
F                    right boundary: end of tube
1                    hn_cell
1                    hx_cell
10.0 30.0 700.0 0.0 296.0 Initial: x1, x2, p, u, T
1.0 0.0 0.0 0.0 0.0                    species mass fraction
```

B.7 RHYFLX_nozzle_inv.Lp

RHYFLX_nozzle_inv.Lp

```
#L1d-3.0 RHYFL-X inviscid nozzle condition with equil chemistry
0 96 0                test_case, gas_index, fr_chem
3 0 1                 nslug, npiston, ndiaphragm
16.0e-03   250000     max_time, max_steps
1.0e-8   0.35         dt_init, CFL
2 2 0.0               Xorder, Torder
3                      n_dt_plot
0.0     5.0e-4   5.0e-6   t_change, dt_plot, dt_his
5.5e-3  1.0e-5   2.0e-6    t_change, dt_plot, dt_his
7.5e-3  1.0e-4   2.0e-6
6                     hnloc
1.0                  hxloc[0]
6.0                  hxloc[1]
12.0                  hxloc[2] diaphragm location
20.0                  hxloc[3]
26.0                  hxloc[4]
32.0                  hxloc[5] end of accel tube
tube definition follows:
500    3              n, nseg
-2.0  0.6  0      xb[0], Diamb[0], linear[0]
-0.05 0.6  0
0.0   0.2  0
32.0  0.2  0
0                     nKl
296.0  0              Tnominal, nT
Secondary Diaphragm [0]
0 2040.0e3 10.0e-6 0.0 0.0
1 R 0.0
2 L 0.0
slug 0: Compressed helium
400  0 1 1.03           nnx, to_end_1, to_end_2, strength
900 0 0.002 0.008    adaption
1  0                  viscous, adiabatic
V  0.0                left boundary : wall with zero velocity
S  1 L                right boundary: slug1 (air test gas),
1                     hn_cell
1                     hx_cell
-2.0 0.0 250.0e6 0.0 320.0 Initial: x1, x2, p, u, T
0.0 0.0 1.0 0.0 0.0                   species mass fraction
slug 1: Air test gas
3000  0 1 1.03       nnx, to_end_1, to_end_2, strength
3400 0 0.002 0.006  adaption
0 0                   viscous, adiabatic
S 0 R                 left boundary :slug 0 (he driver)
SD 2 L 0              right boundary: slug2 (accel slug), diaph 0,
1                     hn_cell
1                     hx_cell
0.00 12.0 784.0e3 0.0 296.0 Initial: x1, x2, p, u, T
1.0 0.0 0.0 0.0 0.0                     species mass fraction
slug 2: Air accelerator gas
```

```
1667  0 0 0.0        nnx, to_end_1, to_end_2, strength
1800 1 0.008 0.040  adaption
0 0                 viscous, adiabatic
SD 1 R 0            left boundary : slug1 (test gas), diaph 0
F                   right boundary: free end of tube
1                   hn_cell
1                   hx_cell
12.0 32.0 662.0 0.0 296.0 Initial: x1, x2, p, u, T
1.0 0.0 0.0 0.0 0.0                   species mass fraction
```

Appendix C

MB-CNS input files

This appendix lists the following MB-CNS input files:

- C.1 - `nozzle_inviscid.sit`: for the inviscid axisymmetric simulation of the contoured hypersonic nozzle.
- C.2 - `rhyflx_acceltube.sit`: for the viscous axisymmetric simulation of 11 m of RHYFL-X acceleration tube. This is Part 1 of 2 simulations that simulated the entire acceleration tube and nozzle.
- C.3 - `rhyflx_tubenozzle.sit`: for the viscous axisymmetric simulation of 9 m of RHYFL-X acceleration tube with contoured nozzle placed on the end. This is Part 2 of 2 simulations that simulated the entire acceleration tube and nozzle.

C.1 nozzle_inviscid.sit

nozzle_inviscid.sit

```
# nozzle_inviscid.sit
# Inviscid axisymmetric simulation of the contoured hypersonic nozzle for the
# RHYFL-X facility.

# Define contour of the nozzle block in the x-y plane.
BEGIN_GEOMETRY
   NODE a 0.00000     0.1
   NODE b 0.0399022   0.101179
   NODE c 0.0723912   0.102219
   NODE d  0.118567   0.103872
   NODE e 0.179594   0.106287
   NODE f  0.256234   0.109602
   NODE g 0.348202   0.113901
   NODE h   0.45675   0.119318
   NODE i   0.58185   0.125904
   NODE j  0.724629   0.133733
   NODE k  0.886097   0.142837
   NODE l   1.06744   0.153206
   NODE m   1.27054   0.164814
   NODE n   1.49799   0.177588
   NODE o  1.75342   0.191392
   NODE p   2.04216   0.205974
   NODE q    2.37172    0.220782
   NODE r   2.75669   0.234929
   NODE s   3.21166   0.246975
   NODE t   3.74964   0.255766

   NODE a0 0.000 0.0
   NODE t0 3.74964 0.0

   SPLINE at 19 a b c d e f g h i j k l m n o p q r s t
   LINE a0t0 a0 t0
   LINE a0a a0 a
   LINE t0t t0 t

   # Define the boundaries
   POLYLINE north0 1 + at
   POLYLINE east0  1 + t0t
   POLYLINE south0 1 + a0t0
   POLYLINE west0  1 + a0a

END_GEOMETRY

BEGIN_FLOW
   # Gas and flow properties - perfect gas with gamma of 1.4
   GAS_TYPE PERF_AIR_14
   # Initial conditions in nozzle - p, u, v, T, sp0, sp1, sp2, sp3, sp4
   GAS_STATE accel_gas 662.0 0.0 0.0 296.0 1.0 0.0 0.0 0.0 0.0
   # Uniform inflow properties - p, u, v, T, sp0, sp1, sp2, sp3, sp4
   GAS_STATE inflow    120.0e3 4150.563 0.0 560.0 1.0 0.0 0.0 0.0 0.0

   # Set the boundary discretisation before building the block
   DISCRETISE north0 1800  0 0 0.0
   DISCRETISE east0  42   0 1 1.05
   DISCRETISE south0 1800  0 0 0.0
   DISCRETISE west0  42   0 1 1.05

   # Inflow and outflow boundaries
   BOUNDARY_SPEC west0 SUP_IN inflow
   BOUNDARY_SPEC east0 SUP_OUT 296.0

   # Define blocks with a common boundary
   BLOCK b0 + north0 + east0 + south0 + west0
```

```
   # Assign the initial gas states
   FILL_BLOCK b0 accel_gas

END_FLOW

BEGIN_CONTROL
   TITLE rhyflx nozzle inviscid
   CASE_ID 0
   AXISYMMETRIC
   INVISCID
   FLUX_CALC ausmdv
   MAX_TIME  5.0e-3
   MAX_STEP  200000
   TIME_STEP 1.0e-8
   CFL       0.4

   DT_PLOT   0.5e-4
   DT_HISTORY 2.0e-6

   HISTORY_CELL b0 900 3
   HISTORY_CELL b0 900 10
   HISTORY_CELL b0 1350 3
   HISTORY_CELL b0 1350 10
   HISTORY_CELL b0 1800  3
   HISTORY_CELL b0 1800 10
   HISTORY_CELL b0 1800 30

END_CONTROL

# Name the output files and build them.
BEZIER_FILE nozzle_inviscid.bez
PARAM_FILE nozzle_inviscid.p
BUILD

EXIT
```

C.2 rhyflx_acceltube.sit

rhyflx_acceltube.sit

```
# RHYFL-X nozzle condition
# Simulation of 11m of acceleration tube
# Assume turbulent flow in all blocks

# Set up four rectangles in the (x,y)-plane to form acceleration tube.
BEGIN_GEOMETRY
   NODE a 0.00 0.1
   NODE b 2.00 0.1
   NODE c 5.00 0.1
   NODE d 8.00 0.1
   NODE e 11.0 0.1
   NODE a0 0.00 0.0
   NODE b0 2.00 0.0
   NODE c0 5.00 0.0
   NODE d0 8.00 0.0
   NODE e0 11.0 0.0

   LINE ab a b
   LINE bc b c
   LINE cd c d
   LINE de d e
   LINE a0b0 a0 b0
   LINE b0c0 b0 c0
   LINE c0d0 c0 d0
```

```
   LINE d0e0 d0 e0
   LINE a0a a0 a
   LINE b0b b0 b
   LINE c0c c0 c
   LINE d0d d0 d
   LINE e0e e0 e

   # Define the boundaries of each block
   POLYLINE north0 1 + ab
   POLYLINE east0  1 + b0b
   POLYLINE south0 1 + a0b0
   POLYLINE west0  1 + a0a
   POLYLINE north1 1 + bc
   POLYLINE east1  1 + c0c
   POLYLINE south1 1 + b0c0
   POLYLINE north2 1 + cd
   POLYLINE east2  1 + d0d
   POLYLINE south2 1 + c0d0
   POLYLINE north3 1 + de
   POLYLINE east3  1 + e0e
   POLYLINE south3 1 + d0e0

END_GEOMETRY

BEGIN_FLOW
   # Gas and flow properties - use Look-Up Table generated from CEA data.
   GAS_TYPE LUT_MIX
   # Initial properties of accel gas (p, u, v, T, sp0, sp1, sp2, sp3, sp4)
   GAS_STATE accel_gas 662.0 0.0 0.0 296.0 1.0 0.0 0.0 0.0 0.0

   # Set the boundary discretisation before building the blocks
   DISCRETISE north0 1131  0 0 0.0
   DISCRETISE east0  42   0 1 1.05
   DISCRETISE south0 1131  0 0 0.0
   DISCRETISE west0  42   0 1 1.05
   DISCRETISE north1 1697  0 0 0.0
   DISCRETISE east1  42   0 1 1.05
   DISCRETISE south1 1697  0 0 0.0
   DISCRETISE north2 1697  0 0 0.0
   DISCRETISE east2  42   0 1 1.05
   DISCRETISE south2 1697  0 0 0.0
   DISCRETISE north3 1697  0 0 0.0
   DISCRETISE east3  42   0 1 1.05
   DISCRETISE south3 1697  0 0 0.0

   # Inflow and outflow boundaries
   BOUNDARY_SPEC east3 SUP_OUT
   BOUNDARY_SPEC west0 transient_uni
   BOUNDARY_SPEC north0 FIXED_T 296.0
   BOUNDARY_SPEC north1 FIXED_T 296.0
   BOUNDARY_SPEC north2 FIXED_T 296.0
   BOUNDARY_SPEC north3 FIXED_T 296.0

   # Define blocks with a common boundary
   BLOCK b0 + north0 + east0 + south0 + west0
   BLOCK b1 + north1 + east1 + south1 + east0
   BLOCK b2 + north2 + east2 + south2 + east1
   BLOCK b3 + north3 + east3 + south3 + east2

   CONNECT_BLOCKS b0 east b1 west
   CONNECT_BLOCKS b1 east b2 west
   CONNECT_BLOCKS b2 east b3 west

   # Assign the initial gas states
   FILL_BLOCK b0 accel_gas
   FILL_BLOCK b1 accel_gas
```

```
   FILL_BLOCK b2 accel_gas
   FILL_BLOCK b3 accel_gas

END_FLOW

BEGIN_CONTROL
   TITLE rhyflx simulation - just acceleration tube
   CASE_ID 0
   TURBULENT b0
   TURBULENT b1
   TURBULENT b2
   TURBULENT b3
   AXISYMMETRIC
   VISCOUS
   FLUX_CALC ausmdv
   MAX_TIME  5.0e-3
   MAX_STEP  200000
   TIME_STEP 1.0e-8
   CFL       0.5

   DT_PLOT   0.5e-4
   DT_HISTORY 2.0e-6

   HISTORY_CELL b0 1130 3
   HISTORY_CELL b0 1130 10
   HISTORY_CELL b1 1696 3
   HISTORY_CELL b1 1696 10
   HISTORY_CELL b2 1696 3
   HISTORY_CELL b2 1696 10
   HISTORY_CELL b3 1696 3
   HISTORY_CELL b3 1696 10
   HISTORY_CELL b3 1696 42
END_CONTROL

# Name the output files and build them.
BEZIER_FILE rhyflx_acceltube.bez
PARAM_FILE rhyflx_acceltube.p
BUILD

EXIT
```

C.3 rhyflx_tubenozzle.sit

rhyflx_tubenozzle.sit

```
# RHYFL-X nozzle condition
# Simulation of 9m of acceleration tube with nozzle placed on end
# Assume turbulent flow in all blocks

# Set up 3 rectangles in the (x,y)-plane with nozzle attached.
BEGIN_GEOMETRY
   NODE b 2.00 0.1
   NODE c 5.00 0.1
   NODE d 8.00 0.1
   NODE e 11.0 0.1
   NODE f 11.0399022   0.101179
   NODE g 11.0723912   0.102219
   NODE h  11.118567   0.103872
   NODE i  11.179594   0.106287
   NODE j  11.256234   0.109602
   NODE k  11.348202   0.113901
   NODE l   11.45675   0.119318
   NODE m   11.58185   0.125904
```

```
NODE n  11.724629   0.133733
NODE o  11.886097   0.142837
NODE p   12.06744   0.153206
NODE q   12.27054   0.164814
NODE r   12.49799   0.177588
NODE s   12.75342   0.191392
NODE t   13.04216   0.205974
NODE u   13.37172   0.220782
NODE v   13.75669   0.234929
NODE w   14.21166   0.246975
NODE x   14.74964   0.255766

NODE b0 2.00 0.0
NODE c0 5.00 0.0
NODE d0 8.00 0.0
NODE e0 11.0 0.0
NODE x0 14.74964 0.0

LINE bc b c
LINE cd c d
LINE de d e
SPLINE ex 19 e f g h i j k l m n o p q r s t u v w x
LINE b0c0 b0 c0
LINE c0d0 c0 d0
LINE d0e0 d0 e0
LINE e0x0 e0 x0
LINE b0b b0 b
LINE c0c c0 c
LINE d0d d0 d
LINE e0e e0 e
LINE x0x x0 x

# Define the boundaries of each block
   POLYLINE north1 1 + bc
   POLYLINE east1  1 + c0c
   POLYLINE south1 1 + b0c0
   POLYLINE west1  1 + b0b
   POLYLINE north2 1 + cd
   POLYLINE east2  1 + d0d
   POLYLINE south2 1 + c0d0
   POLYLINE north3 1 + de
   POLYLINE east3  1 + e0e
   POLYLINE south3 1 + d0e0
   POLYLINE north4 1 + ex
   POLYLINE east4  1 + x0x
   POLYLINE south4 1 + e0x0


END_GEOMETRY

BEGIN_FLOW
   # Gas and flow properties - use Look-Up Table generated from CEA data.
   GAS_TYPE LUT_MIX
   # Initial properties of accel gas (p, u, v, T, sp0, sp1, sp2, sp3, sp4)
   GAS_STATE accel_gas 662.0 0.0 0.0 296.0 1.0 0.0 0.0 0.0 0.0

   # Set the boundary discretisation before building the blocks
   DISCRETISE north1 1697  0 0 0.0
   DISCRETISE east1  42   0 1 1.05
   DISCRETISE south1 1697  0 0 0.0
   DISCRETISE west1  42   0 1 1.05
   DISCRETISE north2 1697  0 0 0.0
   DISCRETISE east2  42   0 1 1.05
   DISCRETISE south2 1697  0 0 0.0
   DISCRETISE north3 1697  0 0 0.0
   DISCRETISE east3  42   0 1 1.05
```

```
   DISCRETISE south3 1697  0 0 0.0
   DISCRETISE north4 2018  0 0 0.0
   DISCRETISE east4  42   0 1 1.05
   DISCRETISE south4 2018  0 0 0.0



   # Inflow and outflow boundaries
   BOUNDARY_SPEC east4 SUP_OUT
   BOUNDARY_SPEC west1 FIXED_T 296.0
   BOUNDARY_SPEC north1 FIXED_T 296.0
   BOUNDARY_SPEC north2 FIXED_T 296.0
   BOUNDARY_SPEC north3 FIXED_T 296.0
   BOUNDARY_SPEC north4 FIXED_T 296.0

   # Define blocks with a common boundary
   BLOCK b1 + north1 + east1 + south1 + west1
   BLOCK b2 + north2 + east2 + south2 + east1
   BLOCK b3 + north3 + east3 + south3 + east2
   BLOCK b4 + north4 + east4 + south4 + east3

   CONNECT_BLOCKS b1 east b2 west
   CONNECT_BLOCKS b2 east b3 west
   CONNECT_BLOCKS b3 east b4 west

   # Assign the initial gas states
   FILL_BLOCK b1 accel_gas
   FILL_BLOCK b2 accel_gas
   FILL_BLOCK b3 accel_gas
   FILL_BLOCK b4 accel_gas

END_FLOW

BEGIN_CONTROL

TITLE rhyflx simulation - acceleration tube and nozzle
CASE_ID 0
TURBULENT b1
TURBULENT b2
TURBULENT b3
TURBULENT b4
AXISYMMETRIC
VISCOUS
FLUX_CALC ausmdv
MAX_TIME  6.0e-3
MAX_STEP  200000
TIME_STEP 1.0e-8
CFL       0.5

DT_PLOT   1.0e-4
DT_HISTORY 2.0e-6

HISTORY_CELL b1 1696 3
HISTORY_CELL b1 1696 10
HISTORY_CELL b2 1696 3
HISTORY_CELL b2 1696 10
HISTORY_CELL b3 1696 3
HISTORY_CELL b3 1696 10
HISTORY_CELL b3 1696 42
HISTORY_CELL b4 1009  3
HISTORY_CELL b4 1009 10
HISTORY_CELL b4 1009 30
HISTORY_CELL b4 1514 3
HISTORY_CELL b4 1514 10
HISTORY_CELL b4 1514 30
HISTORY_CELL b4 2018 3
HISTORY_CELL b4 2018 10
HISTORY_CELL b4 2018 30
```

```
END_CONTROL

# Name the output files and build them.
BEZIER_FILE rhyflx_tubenozzle.bez
PARAM_FILE rhyflx_tubenozzle.p
BUILD

EXIT
```

Appendix D

C Codes

This appendix lists the C code for the following programs:

- D.1 - `unsteady_exp.c`: A program to calculate the enthalpy and pressure ratios across an unsteady expansion process based on ideal perfect gas.
- D.2 - `2_diaph_exp_tube.c`: A program that calculates the fill conditions and flow properties within a standard 2-diaphragm expansion tube assuming ideal perfect gas.
- D.3 - `2_diaph_plot.c`: A program that calculates the fill conditions and flow properties within a standard 2-diaphragm expansion tube for a range of primary and secondary shock speeds. Calculations assume ideal perfect gas.
- D.4 - `3_diaph_plot.c`: A program that calculates the fill conditions and flow properties within a superorbital 3-diaphragm expansion tube for a range of primary, secondary and tertiary shock speeds. Calculations assume ideal perfect gas.
- D.5 - `x2_transition.c`: A quasi-steady-state program that simulates the transition process of the compound piston in the driver of the X2 expansion tube. Calcuates the transient heat transfer to the piston and buffer material during this transition process.

D.1 unsteady_exp.c

unsteady_exp.c

```
/*********************************************************/
/* Program unsteady_exp.c                                */
/* Written by Ben Stewart 16 Dec 2003                    */
/*                                                       */
/* Analytically calculates the enthalpy and pressure     */
/* ratios across an unsteady expansion with air as       */
/* the working gas                                       */
/* Assummes perfect gas properties                       */
/*                                                       */
/*********************************************************/

#include <stdlib.h>
#include <ctype.h>
#include <stdio.h>
#include <math.h>

#define sq(x)               ((x)*(x))  /* squares a value        */

FILE *outfile1, *outfile2;

int i;
double
       gamma2 = 1.4,
       H_ratio,H_ratio1,H_ratio2,H_ratio3,
       P_ratio,P_ratio1,P_ratio2,P_ratio3,
       M7;

main()
{
 outfile1 = fopen("H_ratio.out","w");
 outfile2 = fopen("P_ratio.out","w");

for(i=2;i<16;i++)
 {
 printf("i=%d\n",i);
 M7 = i;

       /*********** Enthalpy Ratio *********************/

 H_ratio1 = gamma2*(gamma2-1.0)/(gamma2+1.0);
 H_ratio2 = (1.0/(gamma2-1.0) + sq(M7)/2.0);
 H_ratio3 = sq((1.0 + (gamma2 - 1.0)/2.0 * sqrt(2.0/(gamma2*(gamma2-1.0))))
                / (1.0 + (gamma2-1.0)/2.0 * M7) );
 H_ratio = H_ratio1 * H_ratio2 * H_ratio3;


       /*********** Pressure Ratio *********************/

 P_ratio1 = pow((1.0 + (gamma2 - 1.0)/2.0 * sqrt((2.0/(gamma2*(gamma2-1.0)))))
                 / (1.0 + (gamma2-1.0)/2.0 * M7),(2.0*gamma2)/(gamma2-1.0)) ;
 P_ratio2 = pow( (1.0 + 1.0/gamma2), gamma2/(1.0-gamma2));
 P_ratio3 = pow( (1.0 + (gamma2-1.0)*sq(M7)/2.0), gamma2/(gamma2-1.0));
 P_ratio = P_ratio1 * P_ratio2 * P_ratio3;


       /*********** Print values to the screen *********/

 printf("H ratio = %f\n",H_ratio);
 printf("P ratio = %f\n\n",P_ratio);

       /*********** Print values to files     **********/

 fprintf(outfile1,"%f %f\n",M7,H_ratio);
```

```
  fprintf(outfile2,"%f %f\n",M7,P_ratio);
}
        /*********** Close files ***********************/
fclose(outfile1);
fclose(outfile2);
}
```

D.2 2_diaph_exp_tube.c

2_diaph_exp_tube.c

```
/*********************************************************/
/* Program 2_diaph_exp_tube.c                             */
/* Initiall written by Ben Stewart 16 Nov 1999             */
/*                                                       */
/* Analytically calculates the conditions through         */
/* the rupture of 2 diaphragms in an expansion tube.       */
/* Assumming perfect gas properties.                             */
/*********************************************************/

#include <stdlib.h>
#include <ctype.h>
#include <stdio.h>
#include <math.h>

#define sq(x)                ((x)*(x))  /* squares a value        */

int i;

double       /*** set gas properties **/
               /** 1: driver gas  **/
               /** 2: test gas   **/
               /** 3: accel gas ***/

       gamma1=1.67,gamma2=1.4,gamma3=1.4,    /*He,Air,Air*/
       gas_const1=2077.0,gas_const2=287.0,gas_const3=287.0,

       T1,T2,T3,T4,T4a,T5,T6,T7,
       rho7,
       a1,a2,a3,a4,a4a,a5,a6,a7,
       P1,P2,P3,P4,P4a,P5,P6,P7,TOTAL_P7,
       M1,M2,M3,M4,M4a,M5,M6,M7,
       U2,U3,U4,U4a,U2_prime,U5,U6,U6_prime,U7,
       shock1,shock2;
main()
{

        /** Set Initial Conditions **/
                /******/
 T1=T5=296.0;
 P4=250.0e6;         /*Rupture Pressure*/
 T4=500.0;          /*Rupture Temperature*/
 shock1=2400.0; /*Primary shock speed*/
 shock2=7217.0; /*2nd shock speed */

 M4a=1.0;          /*area change at throat - */
                /*M=0 for constant area, M=1 for large area ratio*/

 printf("\n\nBurst conditions     -   P4=%4.1fMPa T4=%4.1fK\n",P4/1.0e6,T4);
 printf("Primary Shock Speed      -   %4.1f\n",shock1);
 printf("Secondary Shock Speed    -   %4.1f\n",shock2);
 printf("Initial gas temperature  -   %4.1fK\n\n\n",T1);

 a4=sqrt(gamma1*gas_const1*T4);



 a1=sqrt(gamma2*gas_const2*T1);
 M1=shock1/a1;

        /**  calculate conditions at throat **/
 T4a=T4/(1.0+(gamma1-1.0)/2.0*sq(M4a));
 P4a=P4/(pow(T4/T4a,(gamma1)/(gamma1-1.0)));
 a4a=sqrt(gamma1*gas_const1*T4a);
 U4a=M4a*a4a;
```

```
      /** Calculate Conditions Across Shock **/
M2=sqrt((sq(M1)+2.0/(gamma2-1.0))/(2.0*gamma2*sq(M1)/(gamma2-1.0)-1.0));
T2=T1*((1.0+(gamma2-1.0)*sq(M1)/2.0)/(1.0+(gamma2-1.0)*sq(M2)/2.0));
a2=sqrt(gamma2*gas_const2*T2);
U2_prime=M2*a2; /* Velocity of gas w.r.t shock*/

      /** Velocity Across Interface **/
U3=U2=shock1-U2_prime;

      /** Calculate Conditions Across Unsteady Expansion **/
a3=a4a+U4a*(gamma1-1.0)/2.0-U3*(gamma1-1.0)/2.0;
M3=U3/a3;
T3=sq(a3)/(gamma1*gas_const1);
P2=P3=P4a*pow((a3/a4a),(2.0*gamma1/(gamma1-1.0)));

      /** Calculate Original Pressure in Tube **/
P1=P2/((1.0+gamma2*sq(M1))/(1.0+gamma2*sq(M2)));



      /************ 2nd Diaphragm ************/

a5=sqrt(gamma3*gas_const3*T5);
M5=shock2/a5;

      /** Calculate Conditions Across Shock **/
M6=sqrt((sq(M5)+2.0/(gamma3-1.0))/(2.0*gamma3*sq(M5)/(gamma3-1.0)-1.0));
T6=T5*((1.0+(gamma3-1.0)*sq(M5)/2.0)/(1.0+(gamma3-1.0)*sq(M6)/2.0));
a6=sqrt(gamma3*gas_const3*T6);
U6_prime=M6*a6;         /* Velocity of gas w.r.t shock*/

      /** Velocity Across Interface **/
U7=U6=shock2-U6_prime;

      /** Calculate Conditions Across Unsteady Expansion **/
a7=a2+U2*(gamma2-1.0)/2.0-U7*(gamma2-1.0)/2.0;
M7=U7/a7;
T7=sq(a7)/(gamma2*gas_const2);
P6=P7=P2*pow((a7/a2),(2.0*gamma2/(gamma2-1.0)));

      /** Calculate Original Pressure in Tube **/
P5=P6/((1.0+gamma3*sq(M5))/(1.0+gamma3*sq(M6)));
TOTAL_P7=P7*pow((1.0+(gamma2-1.0)*sq(M7)/2.0),(gamma2/(gamma2-1.0)));
rho7=P7/(gas_const2*T7);



      /*******Printing to screen ********/

printf("    /*****************************************************/\n\n");

printf("         (3)              (2)              (1)            \n");
printf("       Expanded       Shock Processed     Shock Tube \n");
printf("      Driver Gas         Test gas            Fill    \n");
printf(" P     %3.2f kPa         %3.2f kPa        %3.2f kPa \n"  ,
                                                 P3/1000.0,P2/1000.0,P1/1000);
printf(" T     %3.2f K           %3.2f K          %3.2f K \n"  ,T3,T2,T1);
printf(" u     %3.2f m/s         %3.2f m/s         -       \n"  ,U3,U2);
printf(" a     %3.2f m/s         %3.2f m/s        %3.2f m/s \n"  ,a3,a2,a1);

printf("\n ratio of a3/a2 -- %3.2f (should be less than 0.8)\n\n", a3/a2);

printf("         (7)              (6)              (5)            \n");
printf("       Expanded       Shock Processed     Acceleration \n");
printf("       Test Gas       Accelerator gas       Tube Fill    \n");
printf(" P     %3.3f kPa         %3.3f kPa        %3.3f Pa \n"  ,
```

```
                                                P7/1000.0,P6/1000.0,P5);
 printf(" T     %3.2f K           %3.2f K          %3.2f K \n"  ,T7,T6,T5);
 printf(" u     %3.2f m/s         %3.2f m/s         -      \n"  ,U7,U6);
 printf(" a     %3.2f m/s         %3.2f m/s        %3.2f m/s \n\n"  ,a7,a6,a5);

 printf("    /*****************************************************/\n\n");

                        /***** Approx Pitot pressure *****/
 printf(" Pitot(region7) = %6.2f kPa\n\n",0.92*P7/(287.0*T7)*U7*U7/1000.0);


}
               /*********** End of Program ************/
```

D.3 2_diaph_plot.c

2_diaph_plot.c

```
/*********************************************************/
/* Program 2_diaph_plot.c                                */
/* Written by Ben Stewart 20 Dec 1999                    */

/* Analytically calculating the conditions through       */
/* the rupture of 2 diaphragms in an expansion tube.     */
/* Cycles through a range of primary and secondary       */
/* shock speeds and calculates the flow conditions for   */
/* each combination                                      */
/*                                                       */
/* Assummes perfect gas properties                       */



#include <stdlib.h>
#include <ctype.h>
#include <stdio.h>
#include <math.h>

#define sq(x)               ((x)*(x))  /* squares a value        */

FILE *outfile2;

int i;

double
       gamma1=1.67,gamma2=1.4,gamma3=1.4,/*He,Air,Air*/
       gas_const1=2077.0,gas_const2=287.0,gas_const3=287.0,
       T1,T2,T3,T4,T4a,T5,T6,T7,
       rho7,
       a1,a2,a3,a4,a4a,a5,a6,a7,
       P1,P2,P3,P4,P4a,P5,P6,P7,TOTAL_P7,
       M1,M2,M3,M4,M4a,M5,M6,M7,
       U2,U3,U4,U4a,U2_prime,U5,U6,U6_prime,U7,
       shock1,shock2;
main()
{
outfile2 = fopen("file2.out","w");

        /** Initial Conditions **/
                /******/
T1=T5=296.0;
P4=250.0e6;
T4=500.0;
shock1=2200.0;
shock2=7217.0;
M4a=1.0; /*area change at throat*/
printf("\n\nBurst conditions -   P4=%4.1fMpa  T4=%4.1fK\n",P4/1.0e6,T4);
printf("Final Shock Speed   -   shock2 = %5.1fm/s\n",shock2);
printf("Init gas temp    -   T1 = %4.1fK\n",T1);
a4=sqrt(gamma1*gas_const1*T4);
a1=sqrt(gamma2*gas_const2*T1);

for(i=1;i<30;i++)
{

M1=shock1/a1;

        /**********  Calculate Conditions at Throat **********/
T4a=T4/(1.0+(gamma1-1.0)/2.0*sq(M4a));
P4a=P4/(pow(T4/T4a,(gamma1)/(gamma1-1.0)));
a4a=sqrt(gamma1*gas_const1*T4a);
U4a=M4a*a4a;
```

```
        /********* Calculate Conditions Across Primary Shock ***********/
M2=sqrt((sq(M1)+2.0/(gamma2-1.0))/(2.0*gamma2*sq(M1)/(gamma2-1.0)-1.0));
T2=T1*((1.0+(gamma2-1.0)*sq(M1)/2.0)/(1.0+(gamma2-1.0)*sq(M2)/2.0));
a2=sqrt(gamma2*gas_const2*T2);

U2_prime=M2*a2;   /***** Velocity of gas w.r.t shock *******/

U3=U2=shock1-U2_prime;  /********** Velocity Across Interface *********/


        /******* Calculate Conditions Across Unsteady Expansion **********/
a3=a4a+U4a*(gamma1-1.0)/2.0-U3*(gamma1-1.0)/2.0;
M3=U3/a3;
T3=sq(a3)/(gamma1*gas_const1);
P2=P3=P4a*pow((a3/a4a),(2.0*gamma1/(gamma1-1.0)));


        /******** Calculate Original Pressure in Tube **********/
P1=P2/((1.0+gamma2*sq(M1))/(1.0+gamma2*sq(M2)));




        /*************** 2nd Diaphragm ***************/

a5=sqrt(gamma3*gas_const3*T5);
M5=shock2/a5;


        /*********** Calculate Conditions Across Shock **************/
M6=sqrt((sq(M5)+2.0/(gamma3-1.0))/(2.0*gamma3*sq(M5)/(gamma3-1.0)-1.0));
T6=T5*((1.0+(gamma3-1.0)*sq(M5)/2.0)/(1.0+(gamma3-1.0)*sq(M6)/2.0));
a6=sqrt(gamma3*gas_const3*T6);
U6_prime=M6*a6; /********** Velocity of gas w.r.t shock***********/

U7=U6=shock2-U6_prime; /********* Velocity of accel and test gas **********/


        /********* Calculate Conditions Across Unsteady Expansion *********/
a7=a2+U2*(gamma2-1.0)/2.0-U7*(gamma2-1.0)/2.0;
M7=U7/a7;
T7=sq(a7)/(gamma2*gas_const2);
P6=P7=P2*pow((a7/a2),(2.0*gamma2/(gamma2-1.0)));


        /******* Calculate Fill Pressure in Accelerator Tube ************/
P5=P6/((1.0+gamma3*sq(M5))/(1.0+gamma3*sq(M6)));
TOTAL_P7=P7*pow((1.0+(gamma2-1.0)*sq(M7)/2.0),(gamma2/(gamma2-1.0)));
rho7=P7/(gas_const2*T7);


        /****************** Printing to file *****************/

fprintf(outfile2,"%f %f %f %f %f %f\n",
      shock1,TOTAL_P7/P4,T7,a7,rho7,P7);

 shock1 = shock1 + 100.0 ;
}

        /*********** close files *************/
fclose(outfile2);

}         /*************** End of Program *****************/
```

D.4 3_diaph_plot.c

3_diaph_plot.c

```
/*********************************************************/
/* Program 3_diaph_plot.c                                */
/* Written by Ben Stewart 20 Jan 2000                    */
/*                                                       */
/* Analytically calculates the conditions through        */
/* the rupture of 3 diaphragms in an ideal expansion.    */
/* tube.                                                 */
/* Cycles through a range of primary and secondary       */
/* shock speeds and calculated the test conditions       */
/* for each combination.                                 */
/* Assumming perfect gas properties                      */
/*********************************************************/

#include <stdlib.h>
#include <ctype.h>
#include <stdio.h>
#include <math.h>

#define sq(x)                ((x)*(x))  /* squaring a value        */

FILE *outfile1;

int i,i_max=25,j,j_max=25;

double
       gamma1=1.67,gamma2=1.67,gamma3=1.4,gamma4=1.4,  /*He,He,Air,Air*/
       gas_const1=2077.0,gas_const2=2077.0,
       gas_const3=287.0,gas_const4=287.0,
       T1,T2,T3,T4,T4a,T5,T6,T7,T8,T9,T10,
       rho7,rho10,
       a1,a2,a3,a4,a4a,a5,a6,a7,a8,a9,a10,
       P1,P2,P3,P4,P4a,P5,P6,P7,P8,P9,P10,TOTAL_P7,TOTAL_P10,
       M1,M2,M3,M4,M4a,M5,M6,M7,M8,M9,M10,
       U2,U3,U4,U4a,U2_prime,U5,U6,U6_prime,U7,U9,U10,U9_prime,
       shock1,shock2,shock3;
main()
{
outfile1 = fopen("file1.out","w");

        /********* Initial Conditions ************/
                  /******/
T1=T5=T8=296.0;
P4=250.0e6;
T4=500.0;
shock1=1300.0;
shock2=2200.0;
shock3=7217.0;
M4a=1.0; /*area change at throat*/
printf("\n\nBurst conditions   -  P4=%4.1f MPa  T4=%4.1f K\n\n\n",P4/1.0e6,T4);
a4=sqrt(gamma1*gas_const1*T4);
a1=sqrt(gamma2*gas_const2*T1);

printf("generating 3D output file suitable for Tecplot, file1.out\n\n\n\n");

fprintf(outfile1,"VARIABLES = shock1, shock2, P0, T, a, rho, p\n");
fprintf(outfile1,"ZONE I = %d, J = %d, F = point\n",i_max-1,j_max-1);

for(i=1;i<i_max;i++)
{

M1=shock1/a1;

        /**********  calculate conditions at throat ***********/
```

```
T4a=T4/(1.0+(gamma1-1.0)/2.0*sq(M4a));
P4a=P4/(pow(T4/T4a,(gamma1)/(gamma1-1.0)));
a4a=sqrt(gamma1*gas_const1*T4a);
U4a=M4a*a4a;


        /********** Calculate Conditions Across Primary Shock **********/
M2=sqrt((sq(M1)+2.0/(gamma2-1.0))/(2.0*gamma2*sq(M1)/(gamma2-1.0)-1.0));
T2=T1*((1.0+(gamma2-1.0)*sq(M1)/2.0)/(1.0+(gamma2-1.0)*sq(M2)/2.0));
a2=sqrt(gamma2*gas_const2*T2);
U2_prime=M2*a2; /***** Velocity of gas w.r.t shock *********/


        /******** Velocity Across Driver/Driver Gas Interface **********/
U3=U2=shock1-U2_prime;

        /**** Calculate Conditions Across First Unsteady Expansion ****/
a3=a4a+U4a*(gamma1-1.0)/2.0-U3*(gamma1-1.0)/2.0;
M3=U3/a3;
T3=sq(a3)/(gamma1*gas_const1);
P2=P3=P4a*pow((a3/a4a),(2.0*gamma1/(gamma1-1.0)));


        /**** Calculate Fill Pressure in Secondary Driver Tube *****/
P1=P2/((1.0+gamma2*sq(M1))/(1.0+gamma2*sq(M2)));



        /*************** 2nd Diaphragm *****************/

a5=sqrt(gamma3*gas_const3*T5);
M5=shock2/a5;


        /****** Calculate Conditions Across Secondary Shock **********/
M6=sqrt((sq(M5)+2.0/(gamma3-1.0))/(2.0*gamma3*sq(M5)/(gamma3-1.0)-1.0));
T6=T5*((1.0+(gamma3-1.0)*sq(M5)/2.0)/(1.0+(gamma3-1.0)*sq(M6)/2.0));
a6=sqrt(gamma3*gas_const3*T6);
U6_prime=M6*a6; /******* Velocity of gas w.r.t shock ********/


        /********* Velocity Across Interface **********/
U7=U6=shock2-U6_prime;


        /********* Calculate Conditions Across Second Unsteady Expansion ********/
a7=a2+U2*(gamma2-1.0)/2.0-U7*(gamma2-1.0)/2.0;
M7=U7/a7;
T7=sq(a7)/(gamma2*gas_const2);
P6=P7=P2*pow((a7/a2),(2.0*gamma2/(gamma2-1.0)));


        /********** Calculate Original Pressure in Shock Tube **********/
P5=P6/((1.0+gamma3*sq(M5))/(1.0+gamma3*sq(M6)));
TOTAL_P7=P7*pow((1.0+(gamma2-1.0)*sq(M7)/2.0),(gamma2/(gamma2-1.0)));
rho7=P7/(gas_const2*T7);


  /******************* Third Diaphragm *******************/


a8=sqrt(gamma4*gas_const4*T8);
M8=shock3/a8;

        /*********** Calculate Conditions Across Secondary Shock **********/
M9=sqrt((sq(M8)+2.0/(gamma4-1.0))/(2.0*gamma4*sq(M8)/(gamma4-1.0)-1.0));
T9=T8*((1.0+(gamma4-1.0)*sq(M8)/2.0)/(1.0+(gamma4-1.0)*sq(M9)/2.0));
```

```
a9=sqrt(gamma4*gas_const4*T9);
U9_prime=M9*a9; /****** Velocity of gas w.r.t shock *********/

        /**** Velocity Across Test Gas/ Accelerator Gas Interface ********/
U10=U9=shock3-U9_prime;



        /***** Calculate Conditions Across Third Unsteady Expansion *****/
a10=a6+U6*(gamma3-1.0)/2.0-U10*(gamma3-1.0)/2.0;
M10=U10/a10;
T10=sq(a10)/(gamma3*gas_const3);
P9=P10=P6*pow((a10/a6),(2.0*gamma3/(gamma3-1.0)));

        /******** Calculate Fill Pressure in Accelerator Tube *********/
P8=P9/((1.0+gamma4*sq(M8))/(1.0+gamma4*sq(M9)));
TOTAL_P10=P10*pow((1.0+(gamma3-1.0)*sq(M10)/2.0),(gamma3/(gamma3-1.0)));
rho10=P10/(gas_const3*T10);



/****************** Printing to file ****************/

fprintf(outfile1,"%f %f %f %f %f %f %f\n",
      shock1,shock2,TOTAL_P10/P4,T10,a10,rho10,P10);

 shock1 = shock1 + 100.0 ;

 if(i==(i_max-1))
   {
   shock2 = shock2 + 100.0;
   shock1 = shock1 - 100.0*i;
   j = j + 1;
   if(j<j_max)
      {i=0;}
   }

} /*end of i loop*/

fclose(outfile1);

}   /****************** End of Program *****************/
```

D.5 x2_transition.c

x2_transition.c

```
/*****************************************************************/
/* Program X2_transition.c                                       */
/* Written by Ben Stewart, February, 2003                        */
/*                                                               */
/* Simulates the transition process of the 2-stage               */
/*  compound piston in the X2 Expansion Tube.                       */
/*                                                               */
/*****************************************************************/

#include<stdlib.h>
#include<ctype.h>
#include<stdio.h>
#include<math.h>

#define sq(x)        ((x)*(x))        /* squares a value        */
#define PI        3.141593        /* value of PI               */

FILE *outfile1;

int i,j,count,heat;

double P1,P1_prime,P2,P2_prime,P3,Pr,start_P,
      T1,T2,Temp,temp,start_T,
      vol_1,vol_2,vol_1prime,vol_2prime,start_vol,
      mass_1,mass_2,mass_1prime,mass_2prime,resid_mass,m_dot,m_dot_prime,
      start_mass,
      rho_1,rho_2,rho_3,
      pist_1_vel,pist_2_vel,resid_vel,vel,
      Re,Re_1,Pr_No,h,h_1,heat_transfer,heat_lost,heat_in_1,heat_in_2,
      heat_1,heat_2,
      A1,A2,Re_area1,Re_area2,h_area1,h_area2,
      head_loss,energy,
      E_1,E_1prime,E_2,E_2prime,start_E1,start_E2,C_v,C_p,
      area_1,area_2,resid_area,
      b_layer,
      force1,force2,net_force,shear,shear_work,
      x,vol_reservoir,vol_reservoir_prime,
      Mach_no,loss,time,C1,C2,C3,new_gap,k,mew,
      T_wall[4000],T_wall_1[4000],dist[4000],q[4000];


double delta_t          = 2.0e-6,
      R                = 2077.0,
      g                = 9.81,
      Kc        = 0.1,
      gama        = 1.67,               /* set gas and material properties */
      f                = 0.013,
      eff_dia        = 0.019,
      rho_poly        = 1250.0, c_poly = 1675.0, k_poly = 0.29,
      rho_steel        = 7800.0, c_steel = 470.0, k_steel=700.0;


double buffer_length         = 0.270,
      buffer_outer        = 0.230,
      buffer_inner        = 0.110,
      bore_1                = 0.273,
      dia_eff                = 0.1031,
      sec_stage                = 2.100,        /* Set geometry details */
      pist2_dia                = 0.091,
      pist2_length        = 0.306,
      pist1_length        = 0.200,
      pist_1                = 12.27,
      pist_2                = 20.27;


double F_friction=100.0; /*estimated friction acting on piston*/
```

```
void swap(void);
void quasi_steady(void),piston_vel(void),
               transient_heat(void),other_heat(void);
void write_to_file(void);



          /********** Beginning of main program ************/
main()

{

 /********************** OPEN FILES *****************************/

 outfile1=fopen("file1.out","w");




 /******************** CALCULATE GEOMTRY  ***********************/

 area_1        = PI*(sq(bore_1/2.0)-sq(pist2_dia/2.0));
 area_2        = PI*sq(pist2_dia/2.0);
 resid_area = PI*(sq(buffer_inner/2.0)-sq(pist2_dia/2.0));
 vol_1        = PI*(sq(bore_1/2.0)-sq(buffer_outer/2.0))*buffer_length +
                area_1*pist2_length;
 vol_2        = PI*(sq(buffer_inner/2.0)*buffer_length
                  + sq(dia_eff/2.0)*0.045) + area_2*sec_stage;
 start_vol = vol_1+vol_2;

 vol_reservoir=0.277;



 /*****************  Set Initial Conditions  *******************/
   x=0.0;
   T_wall[0]         = T_wall_1[0] = 296.0;
   q[0]                = 0.0;
   dist[0]        = 0.000120;
   start_P        = P1 = P2 = 137000.0;
   Pr                = 1.05e6;
   start_T        = T1 = T2 =296.0;
   C_v                = 3116.0;
   C_p               = 5192.6;
   heat_lost         = heat_1 = 0.0;
   pist_1_vel         = pist_2_vel = 47.0;
   rho_1        = rho_2 = P1/(R*T1);
   mass_1        = vol_1*rho_1;
   mass_2        = vol_2*rho_2;
   start_mass         = mass_1*mass_2;
   start_E1=E_1 = mass_1*C_v*T1;
   start_E2=E_2 = mass_2*C_v*T2;

        /**** print out initial conditions to screen ****/

printf("\n Initial Conditions\n");
printf(" P = %8.1fPa, T = %4.1fK, piston vel = %3.1fm/s\n"
        ,P1,T1,pist_1_vel);



 /********* Calculate properties at initial time step ***********/

 x        = x+delta_t*pist_2_vel;
 i          = 1;
 time        = ((double)(i)*delta_t);
 vol_1prime = (pist2_length-x)*area_1 +
              PI*(sq(bore_1/2.0)-sq(buffer_outer/2.0))*buffer_length;
 vol_2prime = vol_2-(area_2*delta_t*pist_2_vel);
```

```
m_dot        = 0.0;
P1_prime = P1*pow(vol_1/vol_1prime,gama);
P2_prime = P2*pow(vol_2/vol_2prime,gama);

E_1        = E_1+P1_prime*area_1*pist_1_vel*delta_t;
E_2        = E_2+P2_prime*area_2*pist_2_vel*delta_t;
T1        = E_1/(mass_1*C_v);
T2        = E_2/(mass_2*C_v);
net_force = Pr*(area_1+area_2)-(P1_prime*area_1)
               -(P2_prime*area_2)-F_friction;
pist_1_vel = pist_2_vel = pist_1_vel+(net_force/(pist_1+pist_2)*delta_t);
swap();

rho_1        = P1/(R*T1);
rho_2        = P2/(R*T2);
Mach_no = sqrt((pow((P1/P2),(gama-1.0)/gama)-1.0)*2.0/(gama-1.0));
temp        = T1/(1.0+(gama-1.0)*sq(Mach_no)/2.0);
vel        = Mach_no*sqrt(gama*R*temp);
rho_3        = rho_1/pow((1.0+(gama-1.0)/2.0*sq(Mach_no)),1.0/(gama-1.0));
m_dot        = vel*resid_area*rho_3;
energy        =m_dot*C_v*T1*delta_t;



/*****************************************************************/
/***** Start the quasi-steady state movement of the piston  *******/
/*****************************************************************/

heat = 1; /** Flag for heat transfer -
                /** 1 - heat transfer, else no heat transfer **/
if(heat==1)
        printf("\n  Calculating Heat Transfer......\n\n");
else
        printf("\n  Neglecting Heat Transfer.......\n");
```

```
      /****** When length of protruding inner piston in greater ******/
      /***************** than the buffer length ********************/

if(pist2_length>buffer_length)
{

 /**perform steady state calculations up to when the **/
 /**piston reaches the end of the buffer**/
 while((x+delta_t*pist_2_vel)<buffer_length)
  {
   quasi_steady();
   piston_vel();
   write_to_file();
  }

 /**perform steady state calculations up to when the outer piston hits buffer **/
 while((x+delta_t*pist_2_vel)>buffer_length &&
                          (x+delta_t*pist_2_vel)<pist2_length)
  {
   /** calculate gap between piston and wall **/
   /** at start of 2nd stage compression tube**/
   new_gap = 0.0095-0.0095*(x-0.270)/0.045;
   resid_area = PI*(sq(pist2_dia/2.0+new_gap)-sq(pist2_dia/2.0));
   quasi_steady();
   piston_vel();
   write_to_file();
  }

 /** set new vol_2 equal to the original vol_2 minus the **/
 /** volume consumed by the length of the inner piston **/
 vol_2        = PI*(sq(buffer_inner/2.0)*buffer_length + sq(dia_eff/2.0)*0.045)
```

```
        + area_2*sec_stage - area_2*pist2_length;

 /** set velocity of outer piston to zero as it has hit the buffer **/
 pist_1_vel=0.0;


/** ideal compression for remaining small region up **/
/** to when piston has inserted into 2nd stage compression tube**/
 while((x+delta_t*pist_2_vel)>pist2_length && (x+delta_t*pist_2_vel)<0.315)
  {
   x = x+delta_t*pist_2_vel;
   i = i+1;
   dist[i-1] = x;
   time = (double)(i+2)*delta_t;
   m_dot = Mach_no = vel = 0.0; /**because piston has now sealed gap**/
   vol_2prime = vol_2-delta_t*pist_2_vel*area_2;
   P2_prime = pow(vol_2/vol_2prime,gama)*P2;
   T2        = pow(P2_prime/P2,(gama-1.0)/1.0)*T2;
   rho_2 = pow(P2_prime/P2,1.0/gama)*rho_2;
   vol_2 = vol_2prime;
   P2 = P2_prime;
   E_2        = rho_2*vol_2*C_v*T2;
   write_to_file();
   pist_2_vel = pist_2_vel - (P2*area_2)/pist_2*delta_t;
  }

}


       /******** When length of protruding inner piston in less *********/
      /******************* than the buffer length **********************/


if(pist2_length<=buffer_length)
 {
 /** perform steady-state calculations for length **/
 /** of protruding piston (until outer piston hits buffer) **/
 while((x+delta_t*pist_2_vel)<pist2_length)
  {
  quasi_steady();
  piston_vel();
  write_to_file();
  }


 /** ideal compression for remaining region up to when piston **/
 /** has inserted into 2nd stage compression tube**/
 while((x+delta_t*pist_2_vel)>pist2_length && (x+delta_t*pist_2_vel)<0.315)
  {
  x = x+delta_t*pist_2_vel;
  i = i+1;
  time        = (double)(i+2)*delta_t;
  m_dot = Mach_no = vel = 0.0; /**because piston has now sealed gap**/
  vol_2prime = vol_2-delta_t*pist_2_vel*area_2;
  P2_prime = pow(vol_2/vol_2prime,gama)*P2;
  T2 = pow(P2_prime/P2,(gama-1.0)/1.0)*T2;
  rho_2 = pow(P2_prime/P2,1.0/gama)*rho_2;
  vol_2 = vol_2prime;
  P2 = P2_prime;
  E_2 = rho_2*vol_2*C_v*T2;
  write_to_file();
  pist_2_vel = pist_2_vel - (P2*area_2)/pist_2*delta_t;
  }

 }


  /****** print  final properties to screen ******/
printf(" Final conditions\n");
```

```
printf(" P1=%8.1fPa, T1=%4.1fK\n",P1,T1);
printf(" P2=%8.1fPa, T2=%4.1fK\n",P2,T2);
printf(" piston velocity = %3.1fm/s\n\n",pist_2_vel);


/*********************  CLOSE FILES  ******************************/

fclose(outfile1);
}    /********** END OF MAIN PROGRAM ************/

/** swap properties with newly calculated properties **/
void swap(void)
{
P1        = P1_prime;
P2        = P2_prime;
vol_1        = vol_1prime;
vol_2        = vol_2prime;
}

/** steady-state calculation of properties in each time step **/
void quasi_steady(void)
{
x        = x+delta_t*pist_2_vel;
i        = i+1;
time        = (double)(i)*delta_t;

mew = 1.458e-6*pow(temp,3.0/2.0)/(temp+110.4); /*Sutherlands Viscosity*/
Re = rho_3*vel*x/mew; /*calculate Reynolds number for surface of buffer*/
Re_1 = rho_3*fabs(vel-pist_2_vel)*x/mew; /* Reynolds No with respect to */
                                         /* moving piston */

/* Calculate boundary layer size */
if(Re<500000.0)
       b_layer=5.48*x/pow(Re,0.5); /*expression for laminar b.l. size */
  else
      b_layer=0.382*x/pow(Re,1.0/5.0); /*turbulent b.l.*/

vol_1        = vol_1-(area_1*delta_t*pist_1_vel);
vol_2        = vol_2-(area_2*delta_t*pist_2_vel);
mass_1        = mass_1-(m_dot*delta_t);
mass_2        = mass_2+(m_dot*delta_t);
k        = 0.141+2.38e-4*temp; /* thermal conductivity */
Pr_No        = C_p*mew/k; /*Prandtl number*/

/** Calculate heat transfer coefficients to the **/
/** buffer (h) and inner piston (h_1) **/
if(Re<=500000.0)
  {
  /**laminar**/
  h        = 0.332*pow(Pr_No,-2.0/3.0)*rho_3*C_p*vel*pow(Re,-0.5);
  h_1        = 0.332*pow(Pr_No,-2.0/3.0)*rho_3*C_p*
           fabs(vel-pist_2_vel)*pow(Re_1,-0.5);
  }
  else
    {
    /**turbulent**/
    h        = pow(Pr_No,0.333)*(0.037*pow(Re,0.8)-871.0)*k/x;
    h_1= pow(Pr_No,0.333)*(0.037*pow(Re_1,0.8)-871.0)*k/x;
    }

 /** calculate transient heat transfer levels **/
transient_heat();

 /** calculate shear force and the work done by the shear force **/
shear        = rho_3*sq(vel)*0.0225*pow(mew/(rho_3*vel*b_layer),0.25);
shear_work = shear * 2.0*PI*(buffer_inner+pist2_dia)*x*vel*delta_t;
```

```
 /** calculate energy in both regions **/

E_1 = E_1 + P1*area_1*pist_2_vel*delta_t - m_dot*delta_t*C_v*T1;

if(heat==1)
   E_2 = E_2 + P2*area_2*pist_2_vel*delta_t + m_dot*delta_t*C_v*temp
         - heat_transfer-shear_work;
   else
     E_2 = E_2 + P2*area_2*pist_2_vel*delta_t + m_dot*delta_t*C_v*temp;

/** calculate heat lost to the walls in regions 1 and 2 **/
other_heat();

/** calulate new gas properties **/
T1        = (E_1-heat_1)/(mass_1*C_v);
T2        = (E_2-heat_2)/(mass_2*C_v);
rho_1        = mass_1/vol_1;
rho_2        = mass_2/vol_2;
P1        = rho_1*R*T1;
P2        = rho_2*R*T2;
P3        = P2;

/** calculate Mach number of flow between regions 1 and 2 **/
Mach_no= sqrt((pow((P1/P3),(gama-1.0)/gama)-1.0)*2.0/(gama-1.0));

/** determine gas properties based on the Mach number **/
if(Mach_no<1.0)
 {
 temp        = T1/(1.0+(gama-1.0)/2.0*sq(Mach_no));
 vel        = Mach_no*sqrt(gama*R*temp);
 rho_3        = rho_1/pow((1.0+(gama-1.0)/2.0*sq(Mach_no)),1.0/(gama-1.0));
 }
 else /** choked flow M=1 **/
   {
   Mach_no=1.0;
   temp = T1/(1.0+(gama-1.0)/2.0*sq(Mach_no));
   vel        = Mach_no*sqrt(gama*R*temp);
   /*rho_3 = rho_1/pow((1.0+(gama-1.0)/2.0*sq(Mach_no)),1.0/(gama-1.0));*/
   rho_3 = rho_1/pow(T1/temp,1.0/(gama-1.0));
   }


/**calculate mass-flow and energy transfered between regions in each time step **/
m_dot        = vel*rho_3*((0.0095-(2.0*b_layer/8.0))/0.0095)*resid_area;
energy        = energy + m_dot*C_v*temp*delta_t;

}

 void piston_vel(void)
{
 /*calculate changes in volume and pressure due to piston movement*/
vol_reservoir_prime = vol_reservoir + pist_1_vel*delta_t*PI*sq(0.115);
Pr = Pr*pow(vol_reservoir/vol_reservoir_prime,gama);

 /* calculate net_force acting on piston and change in piston velocity*/
net_force = Pr*(area_1+area_2)-(P1*area_1)-(P2*area_2)-F_friction;
pist_1_vel = pist_2_vel = pist_1_vel + (net_force/(pist_1+pist_2)*delta_t);
}


        /*************** Transient Heat Transfer ********************/
void transient_heat(void)
{
 dist[i-1]=x;
```

```
       /** calculate heat transfer to new exposed **/
     /** portion of buffer and piston            **/
if((dist[i-1])<buffer_length)
  {   /** if x = less than buffer length **/
   q[i-1] = h*PI*buffer_inner*(dist[i-1]-dist[i-2])*(temp-T_wall[0]) +
            h_1*PI*pist2_dia*(dist[i-1]-dist[i-2])*(temp-T_wall_1[0]);
  }
  else /** if piston has moved beyond end of buffer and   **/
         /** is in contracting region at start of 2nd stage **/
   {
   q[i-1] = h*2*PI*(pist2_dia/2.0+new_gap)*(dist[i-1]-dist[i-2])
                          *(temp-T_wall[0])   +
            h_1*PI*pist2_dia*(dist[i-1]-dist[i-2])*(temp-T_wall_1[0]);
   }

if((i-2)>0)
 {
   /** calculate heat-transfer levels to the other sections of buffer**/
   /** and piston which have already been exposed to the flow **/
 for(j=(i-2);j>0;j--)
  {
  if((dist[j])<buffer_length)
     {  /** if x = less than buffer length **/
      q[j] = h*PI*buffer_inner*(dist[j]-dist[j-1])*(temp-T_wall[j]) +
             h_1*PI*pist2_dia*(dist[j]-dist[j-1])*(temp-T_wall_1[j]);
     }
     else /** if piston has moved beyond end of buffer **/
          /** and is in contracting region at start of 2nd stage**/
       {
       q[j] = h*2.0*PI*(pist2_dia/2.0+new_gap)*(dist[j]-dist[j-1])
                           *(temp-T_wall[j]) +
              h_1*PI*pist2_dia*(dist[j]-dist[j-1])*(temp-T_wall_1[j]);
       }
  }
 }
}


heat_transfer=0.0; /** set heat-transfer for this time step to zero **/


/** add up individual heat-transfer rates for each **/
/** section multiplied by the time-step duration **/
for(j=0;j<1;j++)
  {
  /** total heat transfer for this section **/
  heat_transfer = heat_transfer+q[j]*delta_t;
  }

 /** total heat (energy) lost to buffer and piston so far**/
heat_lost = heat_lost + heat_transfer;


       /** calculate new temperatures of newly exposed **/
    /** sections of buffer and piston **/
          /** (T_wall[] = buffer temp, T_wall_1[]=piston temp) **/

T_wall[i-1] = T_wall[0] + 2.0/sqrt(PI)*h*(temp-T_wall[0]) *
                           sqrt(delta_t)/sqrt(rho_poly*c_poly*k_poly);
T_wall_1[i-1] = T_wall_1[0] + 2.0/sqrt(PI)*h_1*(temp-T_wall_1[0]) *
                           sqrt(delta_t)/sqrt(rho_steel*c_steel*k_steel);


       /** calculate new temperatures of all other sections **/
    /**                  of buffer and piston **/
```

```
   if((i-2)>0)
    {
     for(j=(i-2);j>0;j--)
       {
       T_wall[j] = T_wall[j] + 2.0/sqrt(PI)*h*(temp-T_wall[j]) *
                               sqrt(delta_t)/sqrt(rho_poly*c_poly*k_poly);

    /** melting temperature of the buffer material has been set to 500K **/
             /** ie. cant get any hotter than this **/
             if(T_wall[j]>500.0)
                               {T_wall[j]=500.0;}




       T_wall_1[j] = T_wall_1[j] + 2.0/sqrt(PI)*h_1*(temp-T_wall_1[j]) *
                           sqrt(delta_t)/sqrt(rho_steel*c_steel*k_steel);
       }

    }
}
        /*************** End of Heat Transfer Section ******************/


void other_heat(void)
{
        /****************** Heat lost in region 1 *********************/
mew        = 1.458e-6*pow(T1,3.0/2.0)/(T1+110.4);
k        = (0.141+2.38e-4*T1);
Pr_No        = C_p*mew/k;
A1        = area_2 +
          (buffer_length+pist2_length-x)*PI*bore_1 +
         PI*pist2_dia*(pist2_length-x) +
          PI*buffer_outer*buffer_length;
Re_area1 = rho_1*pist_1_vel*(buffer_length+pist2_length-x)/mew;
if(Re_area1<500000.0)
  {
  h_area1 = 0.332*pow(Pr_No,-2.0/3.0)*rho_1*C_p*pist_2_vel*pow(Re,-0.5);
  }
  else
   {
   h_area1 = pow(Pr_No,0.3333)*(0.037*pow(Re_area1,0.8)-871.0)*k/0.15;
   }
heat_1        = h_area1*A1*(T1-296.0)*delta_t;
heat_in_1 = heat_in_1 + heat_1;


        /****************** Heat lost in region 2 ************************/

mew        = 1.458e-6*pow(T2,3.0/2.0)/(T2+110.4);
k        = (0.141+2.38e-4*T2);
Pr_No        = C_p*mew/k;
A2        = PI*pist2_dia*2.100 + PI*buffer_inner*buffer_length;
Re_area2 = rho_2*pist_2_vel*1.200/mew;
if(Re_area2,500000.0)
  {
  h_area2 = 0.332*pow(Pr_No,-2.0/3.0)*rho_2*C_p*pist_2_vel*pow(Re,-0.5);
   }
   else
    {
    h_area2 = pow(Pr_No,0.3333)*(0.037*pow(Re_area2,0.8)-871.0)*k/2.1;
    }
heat_2        = h_area2*A2*(T2-296.0)*delta_t;
heat_in_2 = heat_in_2 + heat_2;
}
```

```
void write_to_file(void)
{
fprintf(outfile1,"%f %f %f %f %f\n",x,P2,T2,Mach_no,pist_1_vel);
}

        /**** End of Program ****/
```

References

[1] R. J. Stalker. *Space Travel - Why Is It So Expensive?* The Australian Academy of Technological Sciences and Engineering - FOCUS, No. 109 (Nov/Dec 1999).

[2] F. S. Billig. *Propulsion Systems from Takeoff to High-Speed Flight.* AIAA Progress in Astronautics and Aeronautics **137, Chapter 1**, 21 (1991).

[3] D. R. Buttwsorth, P. A. Jacobs, and T. V. Jones. *Simulation of Oxford University Gun Tunnel Performance using Quasi-One-Dimensional Model.* Shock Waves **11**, 377 (2002).

[4] R. J. Bakos and J. I. Erdos. *Optimizing Pressure Recovery in a Detonation Driven Reflected Shock Tunnel.* International Symposium on Shock Waves, Paper 5999 (1997).

[5] C. J. Doolan. *A Two-Stage Free-Piston Driver for Hypervelocity Expansion Tubes.* Ph.D Thesis, Department of Mechanical Engineering, The University of Queensland (1997).

[6] R. A. Jones and P. W. Huber. *Toward Scramjet Aircraft.* A technology report, Hypersonic Propulsion Branch, NASA Langely Research Center. pp 38-48 (1978).

[7] R. J. Stalker. *Scaling laws and the launch vehicle market.* In *Seventh National Space Engineering Symposium, Canberra*, pp. 119–129 (The Institute of Engineers, Australia, 1992).

[8] B. S. Stewart, R. G. Morgan, P. A. Jacobs, and D. Jenkins. *The RHYFL Facility as a High Performance Expansion Tube for Scramjet Testing.* AIAA Paper 2000-2595 (2000).

[9] W. Chinitz, J. Erdos, O. Rizkalla, G. Anderson, and M. Bushnell. *Facility Opportunities and associated Stream Chemistry Considerations for Hypersonic Air-Breathing Propulsion.* Journal of Propulsion and Power **10**(1), 6 (1994).

[10] R. J. Stalker and R. G. Morgan. *Parallel hydrogen injection into a constant area high enthalpy flow.* A.I.A.A. Journal **20**(10), 1468 (1982).

[11] R. J. Stalker and R. G. Morgan. *Supersonic hydrogen combustion with a short thrust nozzle.* Combustion and Flame **57**, 55 (1984).

[12] J. Tamagno, R. J. Bakos, M. Pulsonetti, and J. I. Erdos. *Hypervelocity Real Gas Capabilities of GASL's Expansion Tube (HYPULSE) Facility.* AIAA Paper 90-1390 (1990).

[13] R. J. Bakos, J. Calleja, J. I. Erdos, M. Sussman, and G. Wilson. *An Experimental and Computational Study Leading to New Test Capabilities for the HYPULSE Facility with a Detonation Driver.* AIAA Paper 96-2193 (1996).

[14] R. J. Bakos, J. Calleja, J. I. Erdos, A. H. Auslender, M. Sussman, and G. J. Wilson. *An Experimental and Computational Study Leading to New Test Capabilities for the HYPULSE Facility with a Detonation Driver.* AIAA Paper 96-2193 (1996).

[15] R. C. Rogers, A. T. Shih, C. Y. Tsai, and R. O. Foelsche. *Scramjet Tests in a Shock Tunnel at Flight 7, 10 and 15 Conditions.* AIAA Paper 2001-3241 (2001).

[16] R. O. Foelsche, R. C. Rogers, C. Y. Tsai, R. J. Bakos, and A. T. Shih. *Hypervelocity Capability of the HYPULSE Shock-Expansion Tunnel for Scramjet Testing.* ISSW23 paper 1047 (2001).

[17] R. J. Bakos and J. I. Erdos. *Options for Enhancement of the Performance of Shock-Expansion Tubes and Tunnels.* AIAA Paper 95-0799 (1995).

[18] M. Kendall. *A Study of High-Enthalpy, Entropy-Raising Drivers for Impulse Facilities.* PhD Thesis, Department of Mechanical Engineering, The University of Queensland (1998).

[19] P. Hurdle and A. Rolland. *RHYFL - A Tool for Attaining Hypersonic Flight.* THRESHOLD, Rockwell International (6), 42 (1990).

[20] W. R. B. Morrison and R. J. Stalker. *Exporting Hypervelocity Technology.* In *Fifth National Space Engineering Symposium, Canberra*, pp. 14–26 (The Institute of Engineers, Australia, 1989).

[21] J. D. Anderson. *Hypersonic and High Temperature Gas Dynamics* (McGraw Hill, New York, 1989).

[22] C. Park. *Evaluation of Real-Gas Phenomena in High-Enthalpy Impulse Test Facilities: A Review.* Journal of Thermophysics and Heat Transfer **11**(1), 330 (1997).

[23] C. Park. *Evaluation of Real-Gas Phenomena in High-Enthalpy Aerothermal Test Facilities: A Review.* Journal of Thermophysics and Heat Transfer **11**(3), 330 (1997).

[24] D. S. Babikian, N. K. J. M. Gopaul, and C. Park. *Measurement and Analysis of Nitric Oxide Radiation in an Arcjet Flow.* Journal of Thermophysics and Heat Transfer **8**(4), 737 (1994).

[25] C. S. Park, M. E. Newfield, D. G. Fletcher, and T. Gokcen. *Spectroscopic Measurements of Shock-Layer Flows in an Arcjet Facility.* Journal of Thermophysics and Heat Transfer **13**(1), 60 (1999).

[26] A. R. Mohammad, L. H. Mack, S. Arepalli, and C. D. Scott. *Characterization of Plenum Spectra in an Arcjet Wind Tunnel.* Journal of Thermophysics and Heat Transfer **11**(3), 339 (1997).

[27] R. J. Bakos, R. G. Morgan, and J. Tamagno. *Effects of Oxygen Dissociation on Hypervelocity Combustion Experiments.* AIAA Paper 92-3964 (1992).

[28] R. A. Crawford and R. P. Rhodes. *Hypersonic Propulsion Simulation Capability Utilizing MHD Augmented Arc-Heater Flow.* AIAA Paper 90-2505 (1990).

[29] J. T. Best, T. P. Fetterhoff, M. L. Laster, and J. L. Jordan. *RDHWT/MARIAH II Hypersonic Wind Tunnel Research Program Update.* AIAA Paper 2001-1859 (2001).

[30] K. N. C. Bray. *Evaluation of the Hypersonic Gun Tunnel.* ARS Progress in Astronautics and Rocketry. Academic Press, New York pp. 547–700 (1962).

[31] B. E. Richards and K. R. Enkenhaus. *Hypersonic Testing in the VKI Longshot Free-Piston Tunnel.* AIAA Journal **8**(6), 1020 (1970).

[32] R. J. Stalker and N. R. Mudford. *Unsteady Shock Propagation in a Steady Flow Nozzle Expansion.* Journal of Fluid Mechanics **241**(6), 525 (1992).

[33] R. J. Bakos. *An Investigation of Test Flow Nonequilibrium Effects on Scramjet Combustion.* Ph.D Thesis, Department of Mechanical Engineering, The Univeristy of Queensland (1994).

[34] R. J. Stalker, A. Paull, and A. J. Neely. *Comparitive Features of Free Piston Shock Tunnel and Expansion Tube Facilities.* Tenth National Aero-Space Plane Technology Symposium, Paper 241 (April 1991).

[35] J. Blanks. *Initial Calibration of the AEDC Impulse Facility.* AEDC Technical Report TR-95-36, Arnolds Engineering Development Center, Arnolds Air Force Base. (1996).

[36] R. J. Stalker. *Hypervelocity aerodynamics with chemical non-equilibrium.* Annual Review of Fluid Mechanics **21**, 37 (1989).

[37] E. L. Resler and D. E. Bloxsom. *Very High Mach number Flows by Unsteady Flow Principles.* Limited Distribution Monograph, Graduate School of Aeronautical Engineering, Cornell University (1952).

[38] R. L. Trimpi. *A preliminary theoretical study of the expansion tube, a new device for producing high-enthalpy short-duration hypersonic gas flows.* NASA Technical Report R-133 (1962).

[39] R. G. Morgan. *Superorbital Expansion Tubes.* 21st International Symposium of Shock Waves, Paper 9000 (1997).

[40] R. G. Morgan. *Free piston driver expansion tubes.* Chapter 4.3, Handbook of Shock Waves, Academic Press (2000).

[41] J. I. Erdos, R. J. Bakos, and A. Castrogiovanni. *Dual Mode Shock-Expansion/Reflected-Shock Tunnel.* AIAA paper 97-0560 (1997).

[42] R. J. Stalker. *Development of a Hypervelocity Wind Tunnel.* Aeronautical Journal of the Royal Aeronautical Society. **26**, 374 (1972).

[43] A. J. Neely and R. G. Morgan. *The Superorbital Expansion Tube concept, experiment and analysis.* Aeronautical Journal **98**(973), 97 (1994).

[44] R. G. Morgan and R. J. Stalker. *Double Diaphragm Driven Free Piston Expansion Tube.* In *Proceedings of the 18th International Symposium on Shock Waves.*, pp. 1031–1038 (Springer-Verlag, 1991).

[45] R. G. Morgan. *A review of the use of Expansion Tubes for creating superorbital flows.* AIAA Paper 97-0279 (1997).

[46] A. Paull and R. J. Stalker. *Test Flow Disturbances in an Expansion Tube.* Journal of Fluid Mechanics **245**, 493 (1992).

[47] R. G. Morgan. *Development of X3, a superorbital Expansion Tube.* AIAA Paper 2000-0558 (2000).

[48] A. Anderson, A. Kumar, and J. I. Erdos. *Progress in Hypersonic Combustion Technology with Computation and Experiment.* AIAA Paper 90-5254 (1990).

[49] O. Sudnitsin. *Design and Testing of Expansion Tube with Area Change.* Masters Thesis, Department of Mechanical Engineering, The University of Queensland (1999).

[50] G. Wilson. *Time-Dependent Quasi-One-Dimensional Simulations of High Enthalpy Pulse Facilities.* AIAA Paper 92-5096 (1992).

[51] P. A. Jacobs. *Numerical Simulation of Transient Hypervelocity flow in an Expansion Tube.* Computers Fluids **23**(1), 77 (1994).

[52] G. Wilson, S. Myles, and R. J. Bakos. *Numerical Simulations of the Flow in the HYPULSE Expansion Tube.* NASA Technical Memorandum 110357, NASA. (1995).

[53] A. Sasoh, Y. Ohnishi, K. Koremoto, and K. Takayama. *Operation, Design and Performance of a Free-Piston Driven Expansion Tube.* AIAA Paper 99-0825 (1999).

[54] P. A. Jacobs. *Single-block Navier-Stokes integrator.* ICASE Interim Report 18 (1991).

[55] P. A. Jacobs. *A computer program for the simulation of transient compressible flows.* Departmental Research Report 1996-10, Department of Mechanical Engineering, University of Queensland (1996).

[56] P. A. Jacobs. *A computer program for the simulation of transient compressible flows.* Departmental Research Report 1998-07, Department of Mechanical Engineering, University of Queensland (1998).

[57] C. J. Doolan and R. G. Morgan. *A Two Stage Free-Piston Driver for Expansion Tubes.* AIAA Paper 96-0854 (1996).

[58] J. P. Holman. *Heat Transfer - Seventh Edition, in SI units.* McGraw-Hill Books, Singapore, (1992).

[59] R. A. Palmer. *Measurement of Heat Transfer in Superorbital Flows.* Ph.D Thesis, Department of Mechanical Engineering, The University of Queensland (1999).

[60] B. J. McBride and S. Gordon. *Computer Program for Calculation of Complex Chemical Equilibrium Compositions and Applications. II Users Manual and Program Description.* NASA Reference Publication 1311, National Aeronautics and Space Administration (1994).

[61] M. Wegener, M. Sutcliffe, and R. G. Morgan. *Optical Study of a Light Diaphragm Rupture Process in an Expansion Tube.* Shock Waves Journal **10**, 167 (2000).

[62] M. Kendall, R. G. Morgan, and P. J. Petrie-Repar. *A study of free-piston double diaphragm drivers for expansion tubes.* AIAA Paper 97-0985 (1997).

[63] J. J. Jones and J. A. Moore. *Exploratory Study of Performance of the Langely Pilot Model Expansion Tube with a Hydrogen Driver.* Technical Report D-3421, NASA (1966).

[64] C. G. Miller. *Operational Experience in the Langley Expansion Tube with Various Test Gases.* Technical Memorandum 78637, NASA (1977).

[65] C. G. Miller. *Experimental Perfect-Gas Study of Expansion Tube Flow Characteristics.* Technical Paper 1317, NASA (1978).

[66] G. T. Roberts, R. G. Morgan, and R. J. Stalker. *Influence of Secondary Diaphragm on Flow Quality in Expansion Tubes.* In *Proceedings of the 19th International Symposium on Shock Waves*, pp. 203–208 (Springer-Verlag, 1995).

[67] A. Paull. *Report on the Commissioning of the expansion tube PISTL.* Technical report, Hypersonic Airbreathing Propulsion Branch of NASA Langley Research Center (1996).

[68] K. V. Haggard. *Freestream Temperature, Density and Pressure Measurements in an Expansion Tube Flow.* Technical Note D-7273, NASA (1978).

[69] M. J. Hayne. *Hypervelocity Flow Over Rear-ward-Facing Steps.* Ph.D Thesis, Division of Mechanical Engineering, The Univeristy of Queensland (2004).

[70] M. M. Macrossan, H. H. Chiu, and D. J. Mee. *A Test Facility for Hypervelocity Rarefied Flow.* In *Proceedings of the 22nd International Symposium on Rarefied Gas Dynamics.* (2000).

[71] R. G. Morgan. *Personal Communications.* (2004).

[72] P. A. Jacobs. *Numerical Simulation of Transient Hypervelocity Flow in an Expansion Tube.* Computers Fluids **23**(1), 77 (1994).

[73] V. Wheatley. *Modelling Low-Density Flow in Hypersonic Impulse Facilities.* Masters Thesis, Department of Mechanical Engineering, The University of Queensland (2001).

[74] H. Mirels. *Test Time in Low Pressure Shock Tubes.* Physics of Fluids **6**(9), 1201 (1963).

[75] C. J. Doolan and P. A. Jacobs. *Modeling mass entrainment in a quasi-one-dimensional shock tube code.* AIAA Journal **34**(6), 1291 (1996).

[76] M. Sutcliffe. *The Use of an Expansion Tube to Generate Carbon Dioxide Flows Applicable to Martian Atmoshperic Entry Simulations.* Ph.D Thesis, Department of Mechanical Engineering, University of Queensland (2000).

[77] O. Rizkalla. *A System of High Temperature Equilibrium Chemistry Subroutines.* Technical report, GASL (1991).

[78] D. T. Pratt. *Studies in Convection, Volume II.* Launder BF (ed), Academic Press, New York (1976).

[79] R. Gollan. *Finite-Rate Chemistry Package.* Department of Mechanical Engineering Report 09/03, The University of Queensland (2003).

[80] R. N. Gupta, J. M. Yos, R. A. Thompson, and K. P. Lee. *A Review of Reaction Rates and Thermodynamic and Transport Properties for an 11-Species Air Model for Chemical and Thermal Equilibrium Calculations to 30 000 K.* NASA Reference Publication 1232, National Aeronautics and Space Administration (1990).

[81] R. J. Bakos and R. G. Morgan. *Chemical Recombination in an Expansion Tube.* A.I.A.A. Journal **32**(6), 1316 (1994).

[82] R. S. M. Chue, R. J. Bakos, C. Y. Tsai, and A. Betti. *Design of shock-free expansion tunnel nozzle in HYPULSE.* Shock Waves **13**, 261 (2003).

[83] O. Sudnitsin and R. G. Morgan. *Steady expansion nozzle in super-orbital flows.* 21st International Symposium on Shock Waves, Paper 5474 (1997).

[84] C. E. Smith. *The Starting Process in a Hypersonic Nozzle.* Journal of Fluid Mechanics **24**(4), 625 (1966).

[85] P. A. Jacobs and C. M. Gourlay. *An Interactive Method-of-Characteristics Program for Gas-dynamic Calculations.* The International Journal of Applied Engineering Education **7**(3), 242 (1991).

[86] P. A. Jacobs. *IMOC: Interactive Method-of-Chacteristics for Two-Dimensional Supersonic Flow..* Departmental Research Report 2000-03, Department of Mechanical Engineering, University of Queensland (2000).

[87] B. S. Stewart, P. A. Jacobs, and R. G. Morgan. *The Starting Process of an Expansion Tube nozzle.* The 23rd International Symposium on Shock Waves (2001).

[88] R. L. Trimpi and L. B. Callis. *A perfect-gas analysis of the expansion tunnel, a modification to the expansion tube.* NASA Technical Report R-233, NASA Langley Research Center. (1965).

[89] R. S. M. Chue, R. J. Bakos, and C. Y. Tsai. *Design and Calibration of an Expansion Tunnel Nozzle in HYPULSE.* Proceedings of the 7th International Workshop on Shock Tube Technology (2000).